An Investigation into the Effect of Modular Taper Design in Total Hip Replacements on Engagement, Motion and Fretting Corrosion

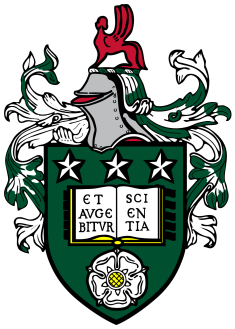

Abigail Wade

Institute of Functional Surfaces
School of Mechanical Engineering
University of Leeds

Submitted in accordance with the requirements for the degree of *Doctor of Philosophy*

December 2023

This work is dedicated to Professor Anne Neville. A true role model who will continue to inspire me for the rest of my life.

Declaration

The candidate confirms that the work submitted is her own and that appropriate credit has been given where reference has been made to the work of others.

This copy has been supplied on the understanding that it is copyright material and that no quotation from the thesis may be published without proper acknowledgement.

The right of Abigail Wade to be identified as Author of this work has been asserted by her in accordance with the Copyright, Designs and Patents Act 1988.

Abigail Wade
December 2023

Papers Contributing to this Thesis

Wade, A. et al. (2020) 'Geometric Variations of Modular Head-Stem Taper Junctions of Total Hip Replacements', Medical Engineering & Physics, 83, pp. 34–47. doi: 10.1016/j.medengphy.2020.07.017.

This paper forms a large basis of Chapter 3.

Wade, A. et al. (2021) 'Importance of surgical assembly technique on the engagement of 12/14 modular tapers', Proc IMechE Part H: J Engineering in Medicine. doi: 10.1177/09544119211053066.

This paper contributes to the methodology presented in Chapter 4.

Wade, A. et al. (2021) 'How Angular Mismatch and Surface Topography in Modular Head-Stem Taper Junctions in Total Hip Replacements Affects Fretting-Corrosion and Motion Under Uni-Axial Loading', pending.

This drafted manuscript is constructed largely from Chapter 5.

Wade, A. et al. (2021) 'The effect of angular mismatch and surface topography on the motion and fretting corrosion response of the modular taper junction in total hip replacements subject to a simulated walking gait', pending.

This drafted manuscript is constructed largely from Chapter 6.

Acknowledgements

The first thank you has to go to my family. Elizabeth Wade, the guiding hand of reason when there was none to be found, a rationaliser of the seemingly irrational. John Wade, for making sure I went on frequent bike rides helping to bring some perspective back into my life when it was lost. My sisters and brother who were always there when I needed them the most.

The next special thank you has to go to Dr Dominic Jones, a massive technical and emotional support through my PhD. Without his electrical engineering expertise, analytical mind, guiding hand and 'can do' attitude, I would have been lost.

I would like to thank all the technicians and especially Tony, Mick, Graham and Camille. Without them work in the laboratories would have been simply impossible.

To my supervisory team, including MatOrtho Ltd and particularly Dr Simon Collins for helping me kick start my career in intellectual property. To Dr Bryant and Dr Beadling, for teaching me to trust in my own thought process and key life lessons which have helped shape me into a stronger, better person than I was before I started this process. To Kim Matthews for always being on the end of the phone and to Claire, to whom I wish every success in her future endeavours.

And to all others whose names I have not mentioned. I am sincerely grateful.

Abstract

Modularity, and more specifically that between the head and stem in total hip replacements (THR), is ubiquitous in THR systems, with a key advantage of allowing surgeons to select components intra-operatively for restoration of natural hip function. However, modular interfaces are susceptible to fretting corrosion due to micro-scale motions in a corrosive environment that presents a crevice geometry, referred to in the field as mechanically assisted crevice corrosion. Mechanically assisted crevice corrosion or fretting corrosion has been, and continues to be, associated with higher than acceptable revision rates as a result of adverse soft tissue reactions to ion and debris generated at interfaces, such as the head-stem modular taper interface.

There is wide variation in modular taper design in THR, including taper length, taper angle, angular mismatch, surface topography and the head-stem material couple. However, decades of research into the effect of design on fretting corrosion has failed to draw consistent conclusions, save for high level conclusions such as long smooth tapers perform better than short rough ones.

The aim of this thesis was to systematically investigate the role of taper design variables on performance outcomes, in this case fretting corrosion. To start, fifty-one modular tapers from five manufactures were geometrically and topographically assessed to quantify intra and inter manufacturer variation. These observations, in conjunction with current national joint registry trends, were used to inform prototype samples using standard and beyond standard preclinical testing methodologies that better represent patient biomechanics. In-situ electrochemical and micro motion methodologies were also developed to quantify degradation processes in real-time. This study investigated the roles of angular mismatch and roughness on fretting corrosion, the effect of head assembly force was also studied.

Seating mechanics and disassembly force were largely found insensitive to angular mismatch and surface topography. An increase in current, subsidence (when the heads were assembled to low assembly forces) and micro motion was seen with increasing axial load during simulation studies. The use of a more complex biomechanical loading methodology (ISO 14242-1) did not result in an increase in current compared to a uniaxial loading methodology. At a greater head assembly force of 7 kN resulted in lower currents, subsi-

dence and micro motion compared to when the heads were assembled to 2 kN . Generally, the samples with increased roughness presented greater currents than the smoother samples across the different loading scenarios (e.g. in the uniaxial study, the smooth matched samples presented an average current of 2.0 ± 0.6 μA compared to the rough smooth samples 14.7 ± 5.1 μA), indicating a higher susceptibility to fretting corrosion. This was not associated with a greater level of motion. Across the different simulation studies, the distally engaged samples (-0.089 ± 0.004 °) presented the lowest current compared to proximally engaged samples (0.118 ± 0.013 °) and matched samples (0.017 ± 0.004 °) of equivalent surface topography. Additionally, the distal samples presented a level of motion similar to the matched samples of equivalent surface topography.

Findings from this investigation suggests that taper design parameters of a rough male taper surface topography and a proximal angular mismatch, specified for ceramic heads, should not be directly translated over to metal head couples as per current clinical practice. Rather, this investigation suggests that smoother, distally engaged samples assembled to a high assembly force may help minimise degradation products generated at the head-stem taper modular interface in metal head couples. The inclusion of a more complex simulated walking gait loading scenario (ISO 14242-1) over the uniaxial simulated loading scenario may not be a valuable improvement to short-term, high throughput experimental studies.

Future work will investigate the effect of patient derived gaits and different daily living activities on the performance of modular tapers to better simulate that occurring in-vivo. The short-term test methodology developed in this project will also be used assess a greater number of samples in order to determine which combination of features best optimise the modular taper junction.

Table of Contents

List of Figures

List of Tables

Nomenclature

Greek Symbols

α	Cone angle of conical asperity (deg)

Acronyms / Abbreviations

α_1	Angle of Rotation in x-z plane
α_2	Angle of Rotation in y-z plane
δ	Tangential Displacement (mm)
S_a	Arithmetic Mean of Roughness Profile
S_k	Core Roughness Depth
S_{ku}	Kurtosis
S_{pd}	Peak Density
S_{sk}	Skewness
S_z	Maximum Profile Height
AA	Adduction-Abduction
AF	Axial Force
$ALTR$	Adverse Local Tissue Reactions
AP	Anterior-Posterior
CCD	Centrum Collum Diaohyseal
CE	Counter Electrode
CMM	Coordinate Measurement Machine

E Elastic (or Young's) Modulus (Pa)

EAS Electrochemically Active Species

E_b Breakdown Potential

E_{corr} Corrosion Potential (V)

E_p Passivation Potential

E_r Repassivation Potential

FE Flexion-Extension

GSR Gross Slip Regime

I_{corr} Exchange Corrosion Current Density (A cm^2)

IE Internal-External Rotation

$MHRA$ Medicines and Healthcare products Regulatory Agency

ML Medial-Lateral

MoM Metal-on-Metal

MSK Musculoskeletal

NJR National Joint Registry

OCP Open Circuit Potential

PBS Phosphate Buffered Saline

PSR Partial Stick Regime

Q Tangential Force (N) / Charge (C)

RMM Roundness Measurement Machine

SR Stick Regime

THR Total Hip Replacement

VSI Vertical Scanning Interferometry

WE Working Electrode

ZRA Zero Resistance Ammeter

Chapter 1

Introduction

1.1 Motivation for Research

There are over 1.7 billion people worldwide with a Musculoskeletal (MSK) condition [9]. MSK conditions affect muscles, bones, joints, tendons and ligaments which can have serious implications on mobility and dexterity. According to the World Health Organisation, MSK conditions are the major cause of morbidity throughout the world, heavily influencing health and quality of life with a great cost burden on health systems [10]. Osteoarthritis accounts for around 20 % of MSK disorders worldwide and is the loss of articular cartilage at joints which can cause pain, stiffness and sometimes loss of function [9, 10]. Joint replacement can be an effective solution which involves removing the affected areas and replacing them with a protheses. Within the UK, there were over 215,000 primary hip and knee replacements undertaken in 2019 alone, approximately 94 % were undertaken as a treatment for Osteoarthritis [11].

The total hip replacement (THR), as it is known today, was developed by Sir John Charnley in the 1960s and was composed of a polytetrafluorethylene cup, cemented into the prepared acetabulum and a stainless steel femoral monobloc component, also cemented into place [12, 13]. Developments seen in THR systems implanted today include: uncemented components, use of ceramics at the head-cup bearing interface and modularity within components. Within the UK, 104, 002 hip replacements were undertaken in 2019, 64 % included a cemented femoral component [11]. The most common head-cup bearing material remains to be metal-on-polymer at 55 % of THR implanted in 2019 followed by ceramic-on-polymer at 38 %, demonstrating a general increasing trend year-on-year. Use of metal-on-metal (MoM) bearings contributes only 0.7 % of bearing articulations. This is largely attributed to the higher than expected revision rates identified in 2010 by the National Joint Registry (NJR) [14] and subsequent alerts issued by the Medicines and

Healthcare products Regulatory Agency (MHRA). Figure 1.1a shows the THR developed by Charnley and Figures 1.1b and c illustrate two of the most common THR systems implanted in 2019. Although the overall system appears to have made little development from that of Charnley's, one key difference is the increase in the number of components, facilitated by a more modular system.

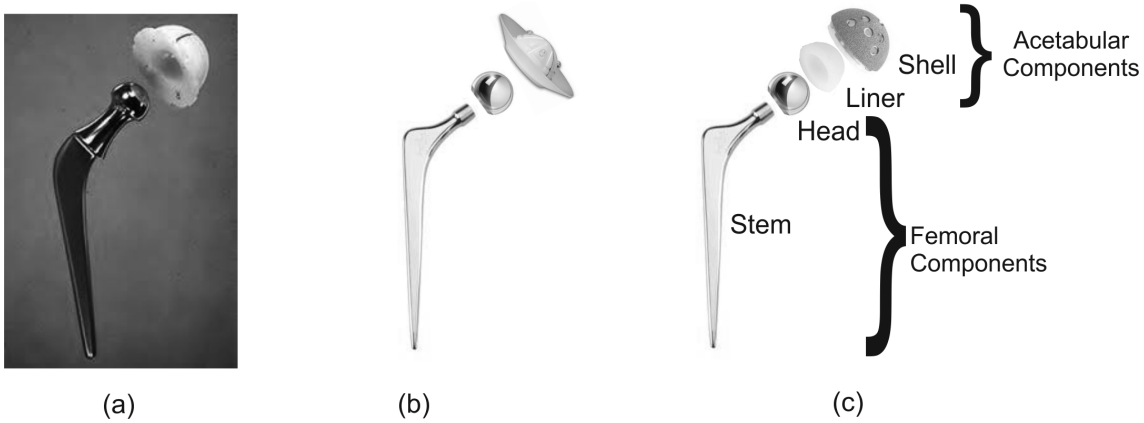

Fig. 1.1 Illustrations of THR (a) invented by Sir John Charnley in the mid-1900s and the most commonly implanted systems in the UK in 2019: (b) cemented system and (c) cemented stem coupled with cementless cup [11].

Introduced in the 1970s, the modular taper is a 'self-locking' interference fit connection, that allowed the separation of the once monobloc femoral stem into two separate components, the femoral stem and head. Modularity within orthopaedic devices is considered highly advantageous by allowing surgeons greater flexibility intra-operatively [15]. For example, head-stem modularity, is achieved by a tapered cone-in-cone modular junction (shown in Figures 1.1b and c between the head and stem) and are present in almost all femoral components implanted today. This allows the bearing head to be made of a different material from the stem, e.g. a ceramic head for improved wear properties coupled with a metallic femoral stem for more appropriate mechanical properties [16]. This is facilitated by the use of a taper cone-in-cone compressive fit. Different head sizes and offsets can be used to balance soft tissues, restoring equal leg length and a natural gait [17, 18]. It also offers the ability to retain well fixed femoral stems while replacing the head, reducing the risk of morbidity, bone loss and soft tissue damage [19]. This has been recorded to occur in around 45 % of revision surgeries in Sweden [20].

The push for increased modularity also saw the introduction of neck modularity in the 1990s, offering even greater intra-operative flexibility [21]. However, after problems associated with mechanical failure and severe degradation leading to the recall of modular neck stems in July 2012, they are not often implanted in the present day. Hence, moving from a monobloc femoral stem to a modular one has not been without its challenges.

Modular interfaces have been found to allow fluid ingress and motion on the micro-scale, giving rise to corrosion and wear degradation mechanisms [22, 23]. Degradation products have been associated with adverse local tissue reactions (ALTR), presented in patients as pain followed by instability [24–27].

Interest in wear and corrosion products causing ALTR was brought to the forefront by MoM bearing articulations and also highlighted other possible generation sites such as modular interfaces [28]. According to the NJR [11], the implantation of MoM bearing articulations makes up a very small proportion of hip replacements but ALTR to particulate debris is still highlighted as one of the more prominent reasons for revision, making up 13 % of all revisions, of which the head-stem junction is one possible generation source. A study by Ridon et al. [29] compared matched cohorts of MoM THR with resurfacings (no modular femoral stem). They found that almost 30 % of the THR cohort underwent revision due to adverse reactions to metal debris compared to 0 % for the resurfacing cohort, highlighting that the head-stem interface would appear to be a prominent site for degradation product production. Additionally, a recent experimental study by Bhalekar et al. [30] found that the wear of the CoCrMo femoral heads arose mainly from the internal taper, further highlighting the importance of the taper junction as a possible degradation product generation site for ALTR.

Degradation products such as wear and corrosion products that can go on to cause ALTR and other inflammatory responses are created at interfaces, where the head-stem interface is but one possible generation site. Hence, the clinical problem that can be attributed to the head-stem taper junction in isolation is not fully understood. That said, a study by Matthies et al [31] found that in large head metal-on-metal retrieval implants, the average material lost from the taper interface was in the region of 2.3 mm^3 whilst the bearing interface was found to experience around a 5.4 mm^3 volume material loss, these volumes being in close agreement with another study that reported 1.03 mm^3 of material loss from the taper interface compared to 6.36 mm^3 of material loss from a metal-on-metal bearing interface [32]. Hence, over twice the volume of material loss was experienced at the bearing interface compared to that at the taper interfaces, indicating that although the large diameter metal-on-metal bearing interfaces may have posed a more prominent clinical problem in the past, the clinical problem caused by the head-stem modular interface is not insignificant. Additionally, degradation debris generated from the taper junction has been reported as being different in morphology and composition compared to that generated at the articular surface, the nature of the debris generated at the taper junction having been reported to trigger a more severe host reaction compared to that generated at the bearing interface [32, 33].

Furthermore, problems associated with the introduction of modularity in THR have been known since the 1990s [28]. Researchers have spent over 25 years studying factors affecting performance and how this occurs, mostly failing to draw consistent conclusions. These factors can be summarised into three categories: the patient (i.e. biomechanics and weight), the implant (i.e. properties and materials) and assembly (i.e. surgical technique). One of the few individual factors that have been found to consistently affect taper performance by experimental studies in the laboratory, was assembly of the head and stem. However, this is a highly variable surgical process. Intra-operatively, the surgeon will fit the stem into the inter-medullary canal of the femur and assemble the femoral head onto the stem before creating a compressive fit at the taper junction by applying an impaction force to the head using an impactor and mallet. The impaction process can differ significantly, with different surgeons using a different number of impacts achieving highly variable peak forces measured to be anywhere between 1 (light blow) to 20 (heavy blow) kN, with an average of around 7 kN, 3 and a half times higher than that used to assembly heads in most preclinical simulation studies [34–36]. Patient factors such as weight, how active they are, biological reactions and the quality of the bone stock can all play roles in modular head-stem taper degradation [37]. Hence, the effect of a wide variation in modular junction design on this highly complex, multi-factorial system that can span multiple disciplines, has meant that there is a lack of common understanding of what the head-stem modular interface should look like. Controlled, in-vitro investigations into the effects of different design parameters, systematically investigating how each design parameter interacts with different factors offers a strong tool into helping identify what these tapers should look like.

1.2 Aims and Objectives

The modular taper design variables that affect performance have not been systematically investigated. The aim of this thesis was to pre-clinically investigate the relationship between clinically relevant modular taper design parameters and fretting corrosion performance. The influence of a range of design and assembly factors on modular taper fretting corrosion was investigated to ascertain if modular taper interfaces can be optimised to reduce the occurrence of fretting corrosion.

It was hypothesized that modular junction design parameters that increased conformity (e.g., angular mismatch and ‘smoother’ surface topography) would increase engagement of the modular taper junction, and therefore reduce the amount of motion experienced at the taper interface for reduced fretting corrosion and thus, improve performance compared to modular junction designs with lower conformity.

To achieve the aim and test the hypothesis, the project was broken down in to the following objectives:

1. measure a variety of modular tapers currently on the market in clinically available THR in terms of geometry and topography to determine the range of variation in different taper designs and manufacturing tolerances, and identify key taper design parameters and create representative samples for experimental investigation of their effect on engagement, motion and fretting corrosion;

2. investigate the engagement distribution and strength of the representative samples with varying angular mismatch and surface topography of that seen in the clinically available samples, by developing controlled assembly and disassembly tests beyond that of ISO 7206-10, including measuring seating mechanics and disassembly force, and identifying, a relationship, if any, between angular mismatch and surface topography with seating mechanics and disassembly force;

3. develop a short-term test protocol based on current experimental standard methodologies and systematically assess the pre-clinical relative performance of the representative samples with varying angular mismatch and surface topography in terms of fretting corrosion and motion, by developing in-situ electrochemical and motion measurement techniques to better understand mechanisms in real-time, and using head-stem reconstructions of the taper junction subject to uniaxial dynamic loading;

4. further develop the short-term test protocol developed in the previous objective to include beyond standard biomechanical testing that is a more realistic simulation of the working conditions in-vivo, the testing protocol being able to accommodate the aforementioned in-situ electrochemical and motion measurement techniques, further systematically assessing the pre-clinical relative performance in terms of motion and fretting corrosion of the representative samples with varying surface topography and angular mismatch.

1.3 Thesis Organisation

This thesis has been divided into 7 chapters with Chapter 7 aiming to conclude the project and provide a general discussion with reflection on outcomes and future opportunities.

Chapter 2: Presents a comprehensive review of current literature that investigated the effects of taper design in THR, identifying any gaps in the current knowledge and understanding, and identifies how modular tapers performance is currently assessed

Chapter 3: Details the results of geometry and topography measurements from a range of clinically available head and stem taper interfaces, identifying design parameters for investigation

Chapter 4: Investigates the engagement of representative samples by measuring geometry and topography and conducting assembly-disassembly experiments

Chapter 5: Investigates the fretting corrosion and motion response of the taper junction subject to incremental uniaxial dynamic loading when the samples were assembled to 2 kN

Chapter 6: Describes the developed method of how the fretting corrosion and motion response was measured subject to more complex loading compared to a uniaxial profile and conducts an investigation when the heads were assembled to 2 and 7 kN

Chapter 7: Overall discussion highlighting the main findings across the project, its limitations and future work.

Chapter 2

Literature Review

2.1 Introduction

There are a number of degradation mechanisms at work in the modular head-stem taper junction interface of total hip replacements (THR). Many of the mechanisms interact with one another and can span multiple disciplines including chemical, mechanical and biological [38]. The multi-disciplinary nature results in a very complex problem that is not yet fully understood. The effect of a wide variation in taper designs on this highly complex system, is further complicated by surgeon and patient factors. As such, there is a lack of common understanding on how different taper design parameters affect clinical performance.

This section first explores the clinical demands and problems associated with modular THR, then go on to look at some of the key degradation mechanisms identified by literature, and finally investigating the current state of the art on studies that look at the effect of taper design on performance. This included investigation and critical analysis of experimental methodologies developed to date.

2.2 The Hip Joint

The natural hip is one of the largest and most heavily loaded joints in the body with an impressive range of motion, making it quite the challenge to replace from a bioengineer's point of view [39]. In simplified terms, the hip connects the femur and pelvis with a non-perfect ball and socket joint consisting of a cartilage lined femoral head and acetabulum [40], see Figure 2.1 for a schematic of the hip joint. It is well adapted to satisfy the every day demands of walking, sitting, standing, jumping and running. To provide an

appreciation of this complex joint that has developed and evolved over millions of years, a few of the properties and their key functions will be highlighted.

Firstly, the acetabulum (aided by the labrum) is a deep socket within which the femoral head articulates, allowing for good joint stability and enables a large range of motion [41]. Cartilage covers the articular surfaces and it is a porous structure that is hydrated with synovial fluid produced by the synovial membrane. Together, the cartilage and synovial fluid provide effective lubrication in both dynamic and static loading conditions [42]. Ligaments, including those that make up the joint capsule, play a key role in joint mobility and stability [43]. The acetabulum opening is orientated obliquely forwards (anteriorly), sideways (laterally) and downwards (inferiorly), while the adjoining femoral head (and neck) is located laterally from the acetabulum, biomechanically advantageous for bipedal locomotion [44, 45].

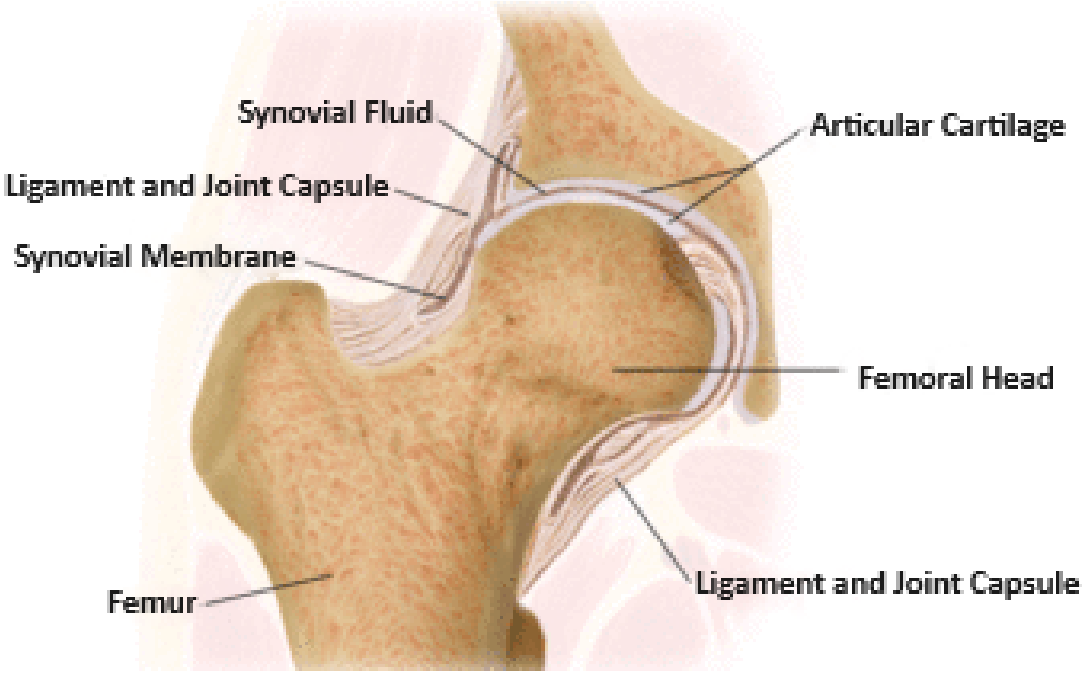

Fig. 2.1 Schematic showing the anatomy of the natural hip. Image was taken from [46].

In addition to the bone and ligament anatomy, there are many different muscles that act around the hip to allow it to rotate in all directions while bearing the weight of the body [41]. This poses a significant engineering problem as it creates a very complex loading profile. The types of mechanical loads experienced at the taper junction include: bending moments in three dimensions, torsion, compressive and tensile axial loads [39, 6]. These are dynamic loads and can exceed body weight by almost a factor of four [6]

2.2.1 Synovial Fluid

Synovial fluid is a key aspect that the bioengineer has to consider when replacing the hip joint. Like most features of the human body, synovial fluid has multiple roles including lubrication, metabolic and regulatory functions [47]. Healthy synovial fluid is a viscous, non-Newtonian fluid and largely consists of blood plasma with some of the larger protein molecules being filtered out and with additional proteins and molecules such as hyaluronic acid bring secreted into the synovial cavity. However, the composition, and thus the properties, can be altered by disease or joint injury [47, 48].

Table 2.1 summarises the component parts of synovial fluid and their concentrations reported by literature in a healthy joint and those affected by disease, and more specifically osteoarthritis and rheumatoid arthritis. A major component of synovial fluid is the protein composition, with the largest portion considered to be albumin followed by globular proteins (globulins) [47]. Albumin is a carrier protein that can form molecular complexes due to its electrostatic properties and is closely related to pH, the solvent-solute interaction, and the presence of ions in synovial fluid [49]. Healthy synovial fluid has been found to present a pH of 7.434 ±0.017 [50] whilst disease has been found to alter synovial fluid pH due to the associated inflammatory response. For example, joints affected by osteoarthritis have been reported to present a pH in the region of 7.4 - 8.16 [50, 51], and joints affected with rheumatoid arthritis with a pH of 7.207 ±0.1 [50].

Two molecules present in synovial fluid thought to be particularly important to lubrication include lubricin and hyaluronic acid (hyaluronan). In diseased joints, the protein concentration is consistently reported by literature to increase, whilst hyaluronic acid and lubricin have been reported in some instances to decrease (Table 2.1). There are some contrasting findings on the effect of disease on concentrations of these component parts, for example Ludwig et al. [52] reported that the concentration of hyaluronan was found to increase but not significantly in patients that presented osteoarthritis compared to healthy patients. In contrast, a review paper by Hui et al. [47] reported that patients with osteoarthritis generally present a lower concentration of hyaluronan ranging from 1.2 to 2.2 mg/mL.

Studies that have investigated the constituent parts of synovial fluid often focus on a few components, for example Ludwig et al. [52] focused on hyaluronan and lubricin, and few provide a holistic understanding of all the component parts and their concentrations. An aspect of synovial fluid often neglected to be quantified, particularly by recent studies, is that of the inorganic components of synovial fluid. A review study by Harsha and Joyce [53] reported the inorganic component concentrations of healthy synovial fluid, citing Wright [54] as the source (see Table 2.1). Given that synovial fluid is an ultra filtrate of

blood plasma [55], the concentrations of the inorganic components as reported by Harsha and Joyce [53] are in good agreement with a study by Briggs [56]. Briggs [56] found the concentration of the inorganic components of blood plasma to be 3.55 mg/mL chloride, 3.17 mg/mL sodium, 0.196 mg/ml potassium, 0.098 mg/ml calcium and 0.025 mg/ml magnesium. Additionally, the compositions included in Table 2.1 are not an exhaustive list but rather an appreciation of the component parts of this complex fluid, for example, blood serum includes phosphorous in the concentrations of between 3.4 and 4.5 mg/dl in adults [57].

Table 2.1 Components of synovial fluid and their concentrations in healthy joints and those affected by osteoarthritis and rheumatoid arthritis.

Study		Healthy	Osteoarthritis	Rheumatoid arthritis
Levick [58]	total proteins	19 ±1.2 mg/mL		50 ±4.8 mg/mL
	albumin	12 ±1.4 mg/mL		19.1 ±1.3 mg/mL
	alpha, beta, hapto-globulins	8.1 ±0.4 mg/mL		19 ±1.2 mg/mL
	transferrin			1.4 mg/mL
	orosomucoid			0.8 mg/mL
	hyaluronate	3 mg/mL		1 mg/mL
Levick and McDonald [59]	Albumin	40-45%		
	hyaluronan	3 mg/mL		
Historical controls as reported by Mazzucco et al. [60]	proteins	15-25 mg/mL	29-39 mg/mL	36-54 mg/mL
	phospholipids	0.1 mg/mL	0.2-0.3 mg/mL	1.5-3.7 mg/mL
	hyaluronic acid	1-4 mg/mL	0.7-1.1 mg/mL	0.8-1.5 mg/mL
Brannan and Jerrard [61]	glucose	95–100 % of blood serum		
Elsaid et al. [62]	lubricin	0.3 - 0.5 mg/mL		
Ludwig et al. [52]	lubricin	0.287 ±0.032 mg/mL	0.147 ±0.028 mg/ml	
	hyaluronan	0.54 ±0.09 mg/ml	0.73 ±0.08 mg/ml	
Wright [54] as cited by Harsha and Joyce [53]	water	970 mg/mL		
	proteins	17 mg/mL		
	chloride	3.8 mg/mL		
	sodium	3.3 mg/mL		
	potassium	0.16 mg/mL		
	calcium	0.06 mg/mL		
	hyaluronan	3.2 mg/mL		

2.2.2 Biomechanics of the Hip

An early study by Greenwald and O'Connor [63] in 1971 measured the load transmitted through 51 natural hips obtained from deceased patients, and subject to a simulated walking gait scaled to the respective estimated patient's body weight. Peak loads transferred through the hip were reported to be in the region of 3200 N (assuming acceleration due to gravity to be 9.81 ms^{-2}). The transfer of this load was determined to be distributed over slightly less than three quarters of the nominal femoral head-acetabulum interface, and more specifically, distributed around the periphery of the fovea (a depression in the femoral head accommodating a ligament attached to the femoral head and acetabulum), as shown in Figure 2.2. A key strength of this study was the use of a natural joint for the determination of transferred load. On the other hand, key limitations of this study arise from the simulated nature of the applied load as opposed to being biomechanically loaded in-vivo and the use of Ringer's solution to simulate synovial fluid.

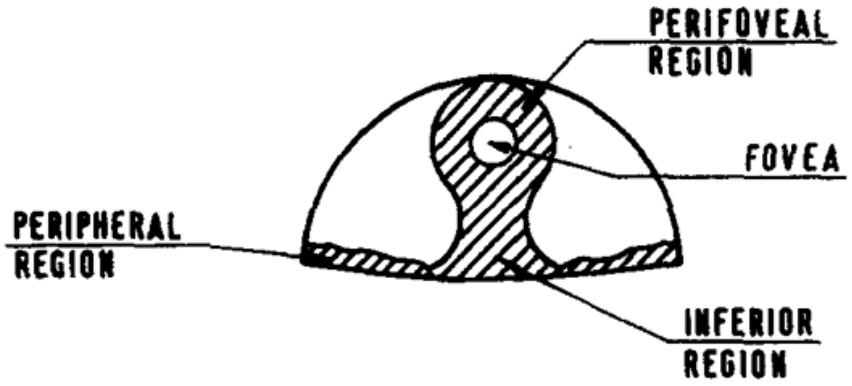

Fig. 2.2 Schematic showing the areas of no contact between the natural femoral head and acetabulum afforded by this view from a medial side view of the femoral head. Image taken from [63].

Whilst Greenwald and O'Connor [63] assumed the frictional interaction to be negligible in the transfer of load through the hip joint, Unsworth et al. [64] published their work on the frictional behaviour of the natural hip four years later. The 'coefficient of friction' (μ), as defined by Equation 2.1, was determined using a pendulum with human joints lubricated with synovial fluid as the bearing at the centre of rotation. The coefficient of friction was found to be variable with normal load (n) and rotational velocity altering the lubrication mechanism. With that said, the coefficient of friction was found to be between 0.01 and 0.03 under steady state conditions and thus a 0.3 and 0.9 Nm torque at an applied normal load of 1500 N and 20 mm radius femoral head.

$$\mu = \frac{\tau}{n \times r_{ball}} \tag{2.1}$$

Where:

- μ is the coefficient of friction;
- τ is the frictional torque;
- n is the normal load; and
- r_{ball} is the radius of the femoral head.

Together Greenwald and O'Connor [63] and Unsworth et al. [64] provide an estimation of the sorts of forces and frictional torques experienced at the natural hip, however, a key limitation of these studies is the lack of in-vivo biomechanical loading. In 1967 and 1978, Paul [65] and Crowninshield et al. [5], respectively, published their work on the forces and moments that act about the hip of healthy patients. These studies used inverse dynamics with the aid of motion capture techniques and load plates to calculate the forces experienced at the natural hip. Paul [65] reported the hip joint resultant force to demonstrate a twin-peak waveform over the course of single walking cycle. Peak forces of this twin-peak waveform were found to be approximately 4 times that of the patients body weight with the main component acting vertically down. Crowninshield et al. [5] agreed with Paul [65] in that a twin-peak pelvic contact force was recorded in the vertical direction (the largest component) with peak forces in the region of between 2 and 5 times body weight. Crowninshield et al. [5] also presented the moments experienced at the hip, however, these were calculated relative to a reference frame located in the centre of the pelvis.

A more recent study compared to that of Paul [65] and Crowninshield et al. [5], and a seminal study in the biomechanical loading of the hip joint was that of Bergmann et al. [6]. This was achieved by sensorising a total hip replacement with strain gauges and implanting them into four patients. Figure 2.3 shows a schematic of the load vectors in three dimensions that were measured. Biomechanical loading of the femoral head was found to apply bending moments in the three anatomical planes, with the greatest acting vertically down due to body weight (F_z), see Figure 2.3.

Firstly, comparing the forces measured during walking for a 75 and 100 kg person by Bergmann et al. [6] to the forces presented by Greenwald and O'Connor [63], Paul [65] and Crowninshield et al. [5]; Bergmann et al. [6] reported a peak resultant force (F) of 1800 N and 3900 N for a 75 and 100 kg person, respectively. Greenwald and O'Connor

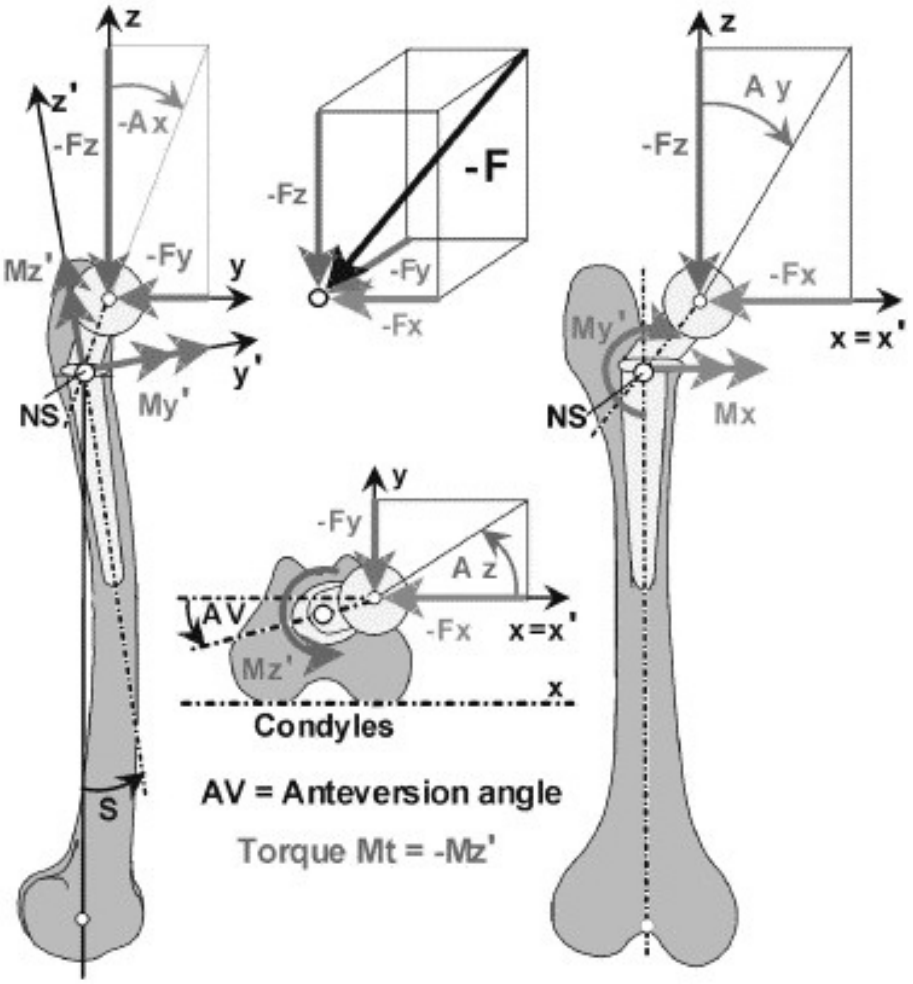

Fig. 2.3 Schematic of the loading vectors of a total hip replacement subject to in-vivo loading. Image taken from [66].

[63] measured load of 3200 N, falling within this range of Bergmann et al. [6]. Dividing Bergmann et al. [6]'s force by body weight and acceleration due to gravity would result in values of 2.4 and 3.9, comparable to that presented Paul [65] and Crowninshield et al. [5] as mentioned above.

Bergmann et al. [6] advanced on the Greenwald and O'Connor [63]'s and Paul [65]'s walking simulation and also measured a verity of daily living activities. These loading vectors were dynamic, and found to reach peak magnitudes of almost 4000 N in F_z, 1000 N in F_y, 900 N F_x and 70 Nm M_z for a person that weighs 100 kg [6]. Normal daily activities included walking, going up and down stairs, standing on one leg, knee bending and stumbling. Figure 2.4 shows how forces can be dynamic over different daily living actives of a 100 kg person, and specifically the contact force (F) and torsional moment (M_z). Bergmann et al. [6] also found that people considered to be more active achieved

2,553,400 walking cycles a year. Almost double that number of people considered to have a 'normal' activity profile with 1,369,300 walking cycles a year.

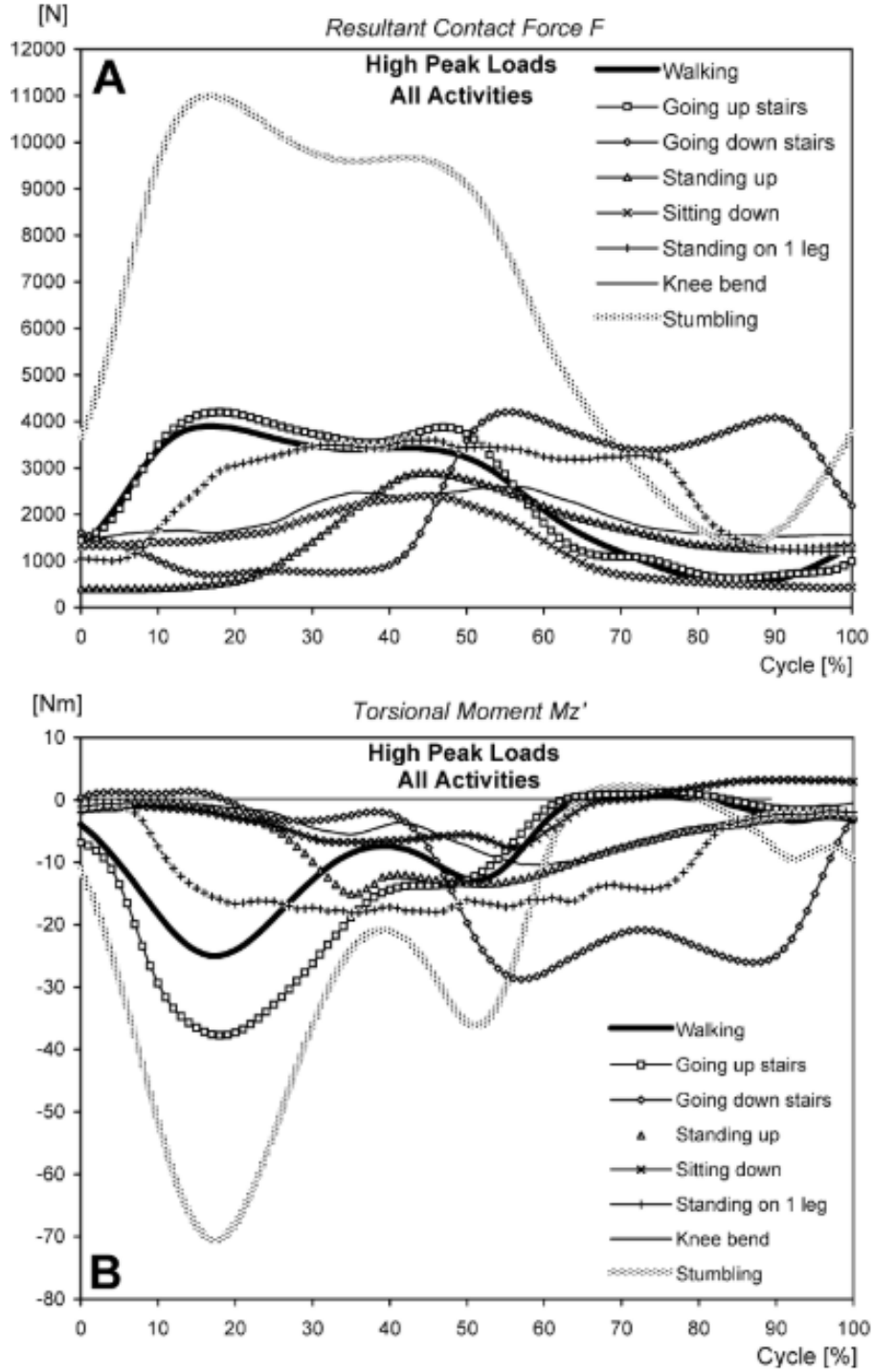

Fig. 2.4 (A)Resultant contact forces (F) and (B) torsional moments (M_z) for a 100 kg person during different daily activities. Image taken from [6].

A key strength of the study by Bergmann et al. [6] was that sensors were placed such that direct measurement of actual forces experienced at the hip were taken. A key

limitation of this study was the low samples size with only four subjects that were all over the age of 50, providing limited insight into the full demographic. The natural hip was also replaced with this sensorised prosthesis which may slightly alter the biomechanical loading from that of a natural hip joint.

A more recent study by Lunn et al. [67] employed a larger sample group with 132 patients. Lunn et al. [67] used a motion capture laboratory (a ten camera Vicon system, Vicon MX, Oxford, UK) with the aid of load plates (two load plates, AMTI, Watertown, MA) like that of Paul [65] and Crowninshield et al. [5], but also used The *AnyBody* Modelling System software which is informed by a cadaveric dataset. A limitation of Lunn et al. [67]'s methodology was that the forces experienced at hip were that predicted from the kinematic data (captured using motion capture), the ground reaction force (captured using the load plates) and The *AnyBody* Modelling System software, and not a direct measure like that of Bergmann et al. [6]. Nevertheless, Lunn et al. [67] reported strong agreement between their results and those of Bergmann et al. [68], with Lunn et al. [67] measuring a 2400 N peak resultant contact force compared to 2100 N of Bergmann et al. [68] for a comparable body weight of 78 kg.

In any event, both Bergmann et al. [6] and Lunn et al. [67] are measurements of loads experienced at a THR and not the natural hip joint. However, forces reported by Bergmann et al. [6] and Lunn et al. [67] were found comparable to the early work that employed natural hip joints, as detailed above. Looking now to more recent studies to understand the difference of loading experienced by a natural hip joint and a THR. Aqil et al. [69] and Li et al. [70], measured the forces being transmitted through the hip joint of healthy patients and patients with osteoarthritis in one hip. Aqil et al. [69] measured the ground reaction force of healthy patients, patients with osteoarthritis in one hip before surgery and the same patients after surgery. Before surgery, a discrepancy in the ground reaction force, and thus the force transferred through the hip joint, between osteoarthritic leg compared to the non-affected leg was found to be 1.29 and 1.45 body weight normalised force, respectively. After THR surgery this discrepancy was almost eliminated with measurements of the ground reaction force to be 1.36 times that of body weight for the affected hip and 1.38 for the non-affected hip. However, these ground reaction forces after THR were found to be greater than that of the healthy control with 1.3 times that of body weight for each leg. Figure 2.5 shows the normalised ground reaction force as a function of time (the author believes the x-axis Figure 2.5a to be incorrectly labelled) over one walking cycle for healthy patients, patients with osteoarthritis in one hip before surgery and the same patients after surgery. The biomechanics shown in Aqil et al. [69] would indicate a comparability between the biomechanics experienced by a THR and that of the natural hip, save for a

small scaling factor and a larger discrepancy between the two peak forces of the 'twin peak' walking profile compared to the someone with healthy hip joints.

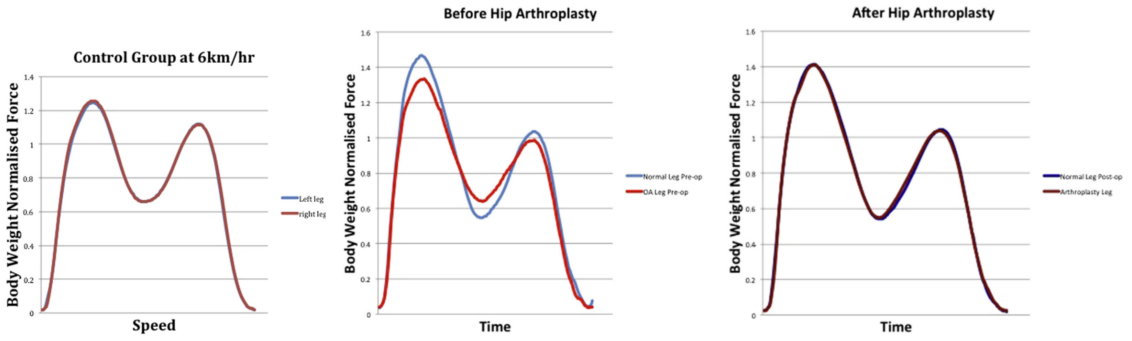

Fig. 2.5 (Normalised ground reaction forces for (a) healthy patients, (b) patients of osteoarthritis in one leg before THR surgery and (c) after. Image taken from [69].

Li et al. [70] on the other hand measured the hip contact force using the same experimental methodology as Lunn et al. [67], i.e., the use of a motion capture laboratory equipped with a load plates and the *AnyBody* Modelling System Software. Like that of Lunn et al. [67], Li et al. [70] reported a close agreement with Bergmann et al. [66]. In contrast to Lunn et al. [67], Li et al. [70] did not find an increased hip contact force in patients that underwent THR, as found by Aqil et al. [69], but did also suggest a discrepancy between the two peak forces (of the twin-peak waveform) of the patients that underwent THR, not seen in the healthy patients. This is shown in Figure 2.6 which shows the normalised contact force for body weight over the course of one walking cycle for a healthy patients (Normal), patients that underwent THR (THR-O) and that of a simulated walking gait defined by ISO 14242-1 [8] used by pre-clinical studies. The ISO 14242-1 [8] is in close agreement with that of a healthy patients hip contact force. Further discussion on the differences between the ISO walking gait profile and that found in-vivo can be found in Section 2.7.1.

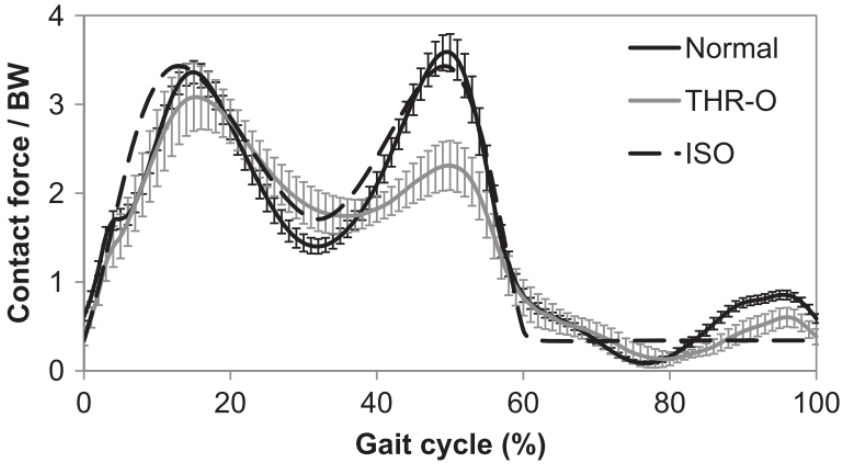

Fig. 2.6 The normalised contact force by body weight reported by Li et al. [70] in normal healthy patients, patients that underwent THR and the ISO 14242-1 [8] waveform. Image taken from Li et al. [70].

Considering the frictional contribution to the loading of a THR in-vivo, Unsworth et al. [71], using the same pendulum machine with a human joint fulcrum as before, measured the friction of a total hip replacement and were found to be between five and fifteen times that of natural healthy human joint (μ0.05-0.30). However, it is lower in friction compared to a natural joint severely affected by rheumatoid arthritis (μ0.4). Indicating that a THR experience a greater loading contribution due to frictional interactions at the bearing interface compared to healthy natural joints.

2.3 The Total Hip Replacement

The most common reason for joint replacement surgery is due to osteoarthritis, other reasons include rheumatoid arthritis, avascular necrosis, trauma and other inflammatory joint problems [72]. According to the World Health Organisation (WHO), musculoskeletal or rheumatic diseases are the major cause of morbidity throughout the world, heavily influencing health and quality of life with a great cost burden on health systems [10]. Hip replacement surgery is considered an effective treatment and involves removing affected areas and replacing it with a prostheses. The standard procedure for THR involves the removal of the femoral head, hollowing out of the intramedullary canal, into which a femoral stem is fixed, and preparing the acetabulum for receipt of a socket [73–75]. Fixation of the femoral stem in the intramedullary canal and the socket in the prepared acetabulum today, is either by way of bone cement (cemented) or osseointegration directly onto the stem (uncemented). Figure 2.7 shows a schematic of an implanted THR with the relevant hip anatomy.

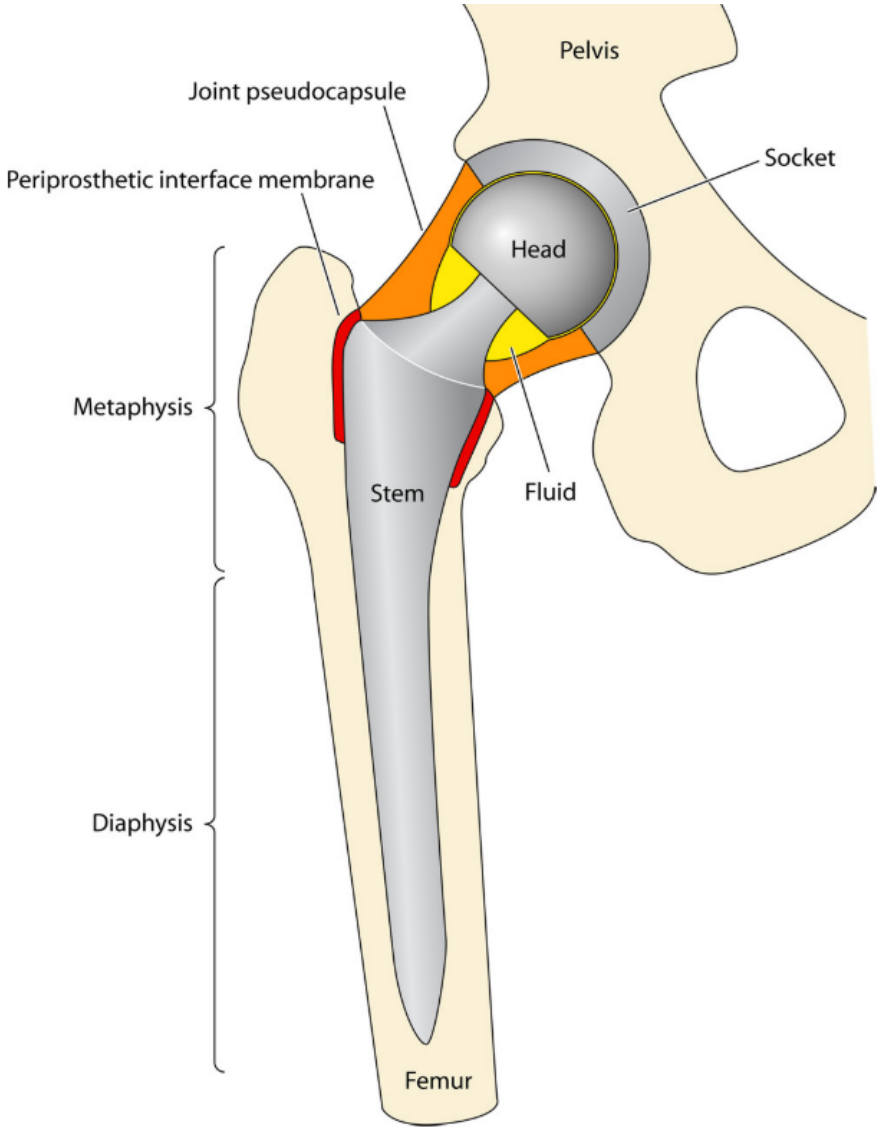

Fig. 2.7 Schematic of an implanted THR with respect to relevant bony anatomy, image taken from [76].

The earliest recorded hip replacement was by Glück in 1891, who used ivory to replace the femoral head; while the 1950s to 1960s saw great advancement due to the work of Charnley and McKee [39, 13]. Charnley, introduced a single stainless-steel femoral component articulating against a polyethylene acetabular cup held in place using bone cement which went on to become the gold standard. While McKee's design consisted of a cobalt chrome alloy metal-on-metal (MoM) articulation. This first generation MoM articulation design fell in popularity in the 1970s due to pain and component loosening requiring revision, presenting a 10 % failure rate after only 4 years [77, 78].

Total hip replacements as we know them today have been in use since the early 1960s, and was considered to be the most successful orthopaedic surgery of its generation [77, 12]. Despite the high success rate of THR surgery, replacing a natural hip that has developed

and evolved over millions of years is still a challenge. There are many factors that must be taken into account when designing a THR system, including: biocompatibility, lubrication of the bearing surfaces, mechanical integrity under biomechanical loading, mechanical and chemical degradation resistance, range of motion, joint stability, fixation of the protheses, the body's response to stress according to Wolff's law and the ability to re-balance the soft tissues of the hip [40, 12, 79]. Figures 2.8a and b show two of the most commonly implanted uncemented stems of 2022 in the UK according to the 19th NJR [80], namely the Corail stem (DePuy Synthes, Johnson and Johnson Med Tech) and the Accolade II stem (Stryker). Figures 2.8c and d show two of the most commonly implanted cemented stems, namely the Exeter v40 stem (Stryker) and C-Stem AMT stem (DePuy Synthes, Johnson and Johnson Med Tech).

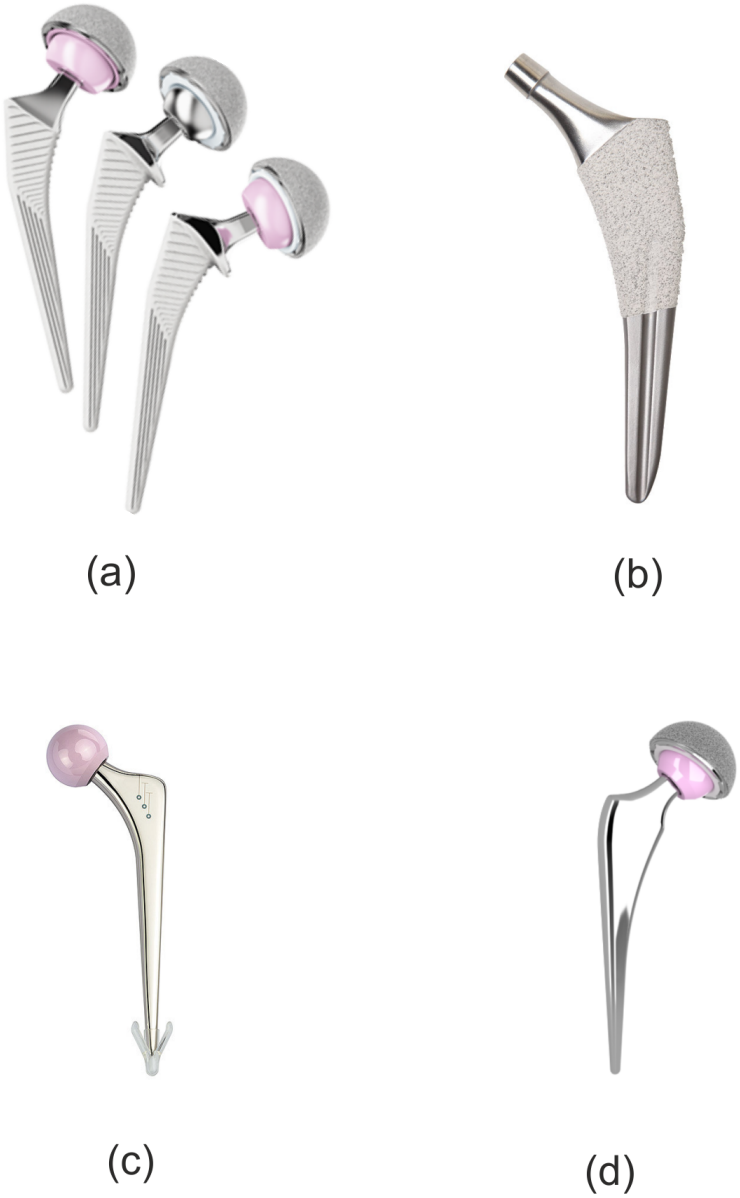

Fig. 2.8 (Most commonly implanted uncemented and cemented stems in 2022 according to the 19th NJR [80]: a) Corail (uncemented), b) Accolade II, c) Exeter v40 (cemented) and d) C-Stem AMT (cemented). Images taken from [81], [75], [82] and [83] to create images a, b, c and d, respectively.

Stem modularity is an innovation that has been made and was first successfully introduced by way of head-stem modularity in the 1970s to allow a ceramic heads to be used at the bearing material [21, 84]. This was followed by the introduction of yet another modular interface, the neck-stem interface in the 1990s. Although head-stem modularity can be found in almost all THR systems implanted today, modular neck stems are not widely implanted due to problems associated with mechanical failure and severe degradation, leading to infection (which will be discussed in more detail in Section 2.4). This was

demonstrated by a recall of modular neck designs in July 2021, as reported in Krishnan et al. [21].

The push for increased modularity was to provide surgeons with increased intra-operative flexibility, allowing surgeons to fine-tune the final prothesis for each specific patient. More specifically, this is achieved by providing a selection of dimensions to help restore the centre of rotation of the hip with the centre of the femoral head and to help better match the anatomy of the patient, particularly important where the femur may be severely deformed [21, 84, 85]. Other benefits include allowing for part revision of the stem during revision surgery, such that well-fixed components can be left in place, smaller incision surgical techniques allow and the possibility for reduced inventory (although this appeared not to be the case in practice as reported by Collier et al. [86]) [21].

2.3.1 Reasons for Revision of THR

Although the National Health Service (NHS) indicates that THR are designed to last for 15 years [73], a study published in The Lancet reported that patients and surgeons can expect a total hip replacement to last for 25 years in 58 % of patients [87]. This was determined by performing a meta-analysis of journal articles and data from six different national joint registries [87]. Therefore, a successful THR can be considered to be one that outlast the patient or, according to the NHS, one that is in-situ for greater than 15 years. That said, THR can fail and may need to be revised. Reasons for needing to revise primary THR include [80]:

- **Aseptic Loosening.** This is loosening of implants from the bone without signs of infection [88, 89]. The process leading to aseptic loosening is predominantly associated with the formation of particles at both sliding and fretting interfaces of joint replacements which causes a cellular response leading to bone resorption, a process also known as osteolysis (lysis). The risk factors associated with aseptic loosening include: poor initial fixation and loss of fixation over time whether that be mechanical or biological particle-induced osteolysis [90].

- **Osteolysis.** As introduced above, the primary mechanism for osteolysis is one of a particle induced cellular response leading to bone resorption which in some cases can then go on to lead to aseptic loosening [91, 92]. As such, the risk factors are similar to ascetic loosening, including improper initial fixation and loosening over time associated with the formation of a synovial-like membrane between implant and bone, ageing, stress shielding, any possible migration and fluid pressure within the synovial-like membrane [92].

- **Adverse Soft Tissue Reaction to Particulate Debris.** Adverse soft tissue reaction to particulate debris or adverse local tissue reaction (ALTR), is caused by an inflammatory response to implant wear and corrosion products, and most notably, metal wear and corrosion products [93]. The inflammatory response can lead to pseudotumours, inflammation of the synovial membrane and soft tissue degradation [93]. Although ALTR has gained traction as an identified reason for revision, the NJR [80] reports that data prior to 2008 are likely to be an underestimate as it was not available as an indication for revision. Risk factors include: increased patient mobility, time in-situ, malpositioning of implants by the surgeon and the use of large diameter metal heads [93].

- **Infection.** Bacterial infection can occur in total hip replacements leading to revision surgery. Increase risk of infection has been associated with patients with medical complications such as rheumatoid arthritis and obesity; other risk factors also include infection via the surgical incision site, longer surgery duration and a longer hospital stay [94].

- **Unexpected Pain.** Pain can be a good indicator that a THR is not functioning correctly, such that pain as a reason for revision surgery is not usually cited alone in the vast majority of cases [80]. In other words, pain may be the presenting symptom yet the underlying cause may be something else such as ALTR [95].

Figure 2.9 shows a plot of the indications for single-stage revision between 2013 and 2022 in the UK. The most common reason for revision is aseptic loosening followed by lysis and adverse soft tissue reaction to particulate debris.

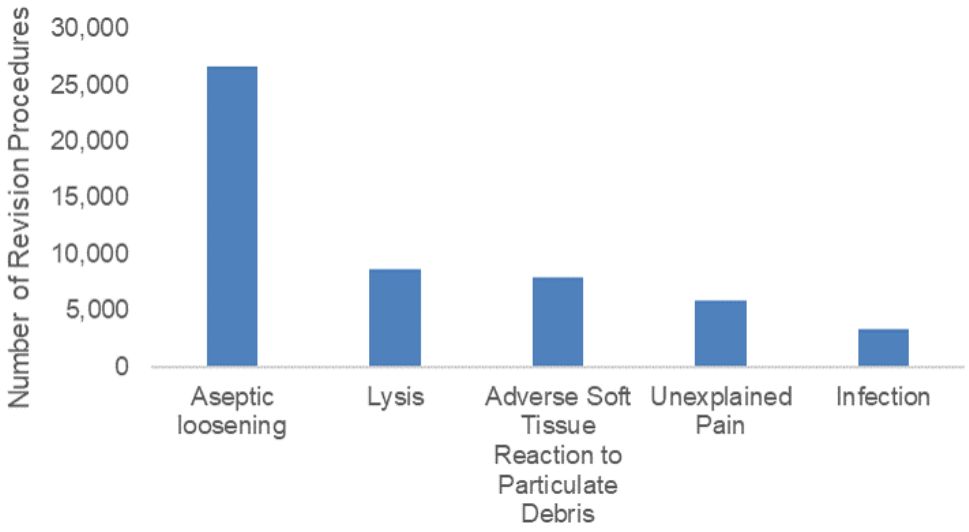

Fig. 2.9 A graph showing the reasons for the number of single-stage revisions between 2013 and 2022 in England, Wales, Northern Ireland, the Isle of Man and Guernsey. Data taken from the NJR [80].

Degradation products such as wear and corrosion products have been identified as key contributors to the reason why some hip replacements require revision, these products are created at interfaces. Figure 2.10 shows the locations of the typical interfaces in THR with annotations summarising the wear and corrosion mechanisms occurring at each of these interfaces. The modular taper junction is but one interface at which wear and corrosion products are created.

Initially, interest in wear and corrosion products causing adverse local tissue reactions was associated with metal-on-metal bearing articulations but it also highlighted other possible interfaces such as modular interfaces [28]. In 2014, the European Commission published a report on the risk of metal-on-metal joint replacements, identifying the taper junction as an important particle and ion generation site [97]. This report also highlighted a gap in knowledge and pre-clinical research aimed at investigating the influence of relevant taper parameters on wear and corrosion [97]. Interest in this area has intensified following the publication of EU regulation updates, stating that a requirement for approval on the EU market includes demonstrating that the risks posed by degradation products produced by medical devices is as small as possible [98]. Further intensification arises from the publication of an opinion by the EU Committee for Risk Assessment, stating that the risk category for a commonly used metallic alloy is to be increased [99].

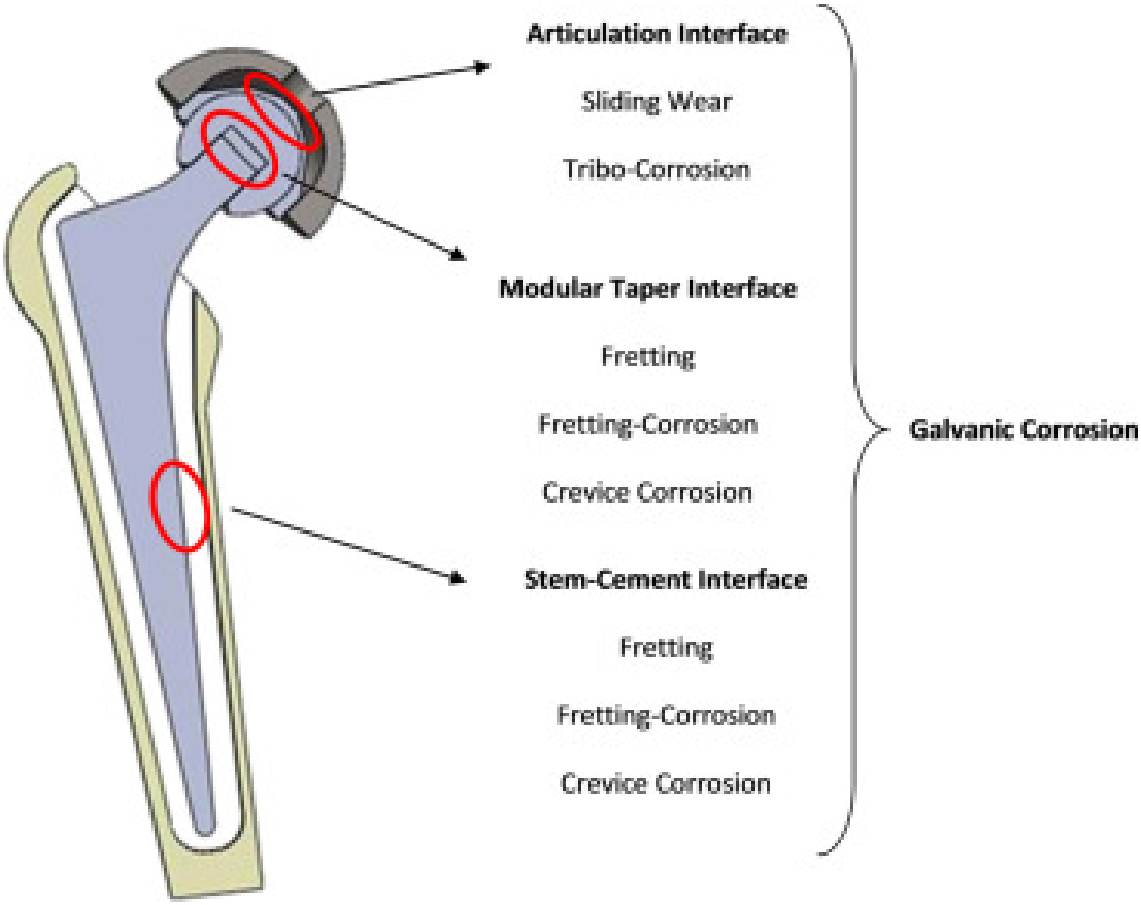

Fig. 2.10 Annotated pictorial representation of the interfaces and summary of the degradation mechanisms that occur at this interfaces. Image taken from the [96].

2.4 Modular Head-Stem Tapers in THR

This next section will now focus more specifically on THR modularity, including an overview of the clinical implications and the insight into the demands placed on the modular head-stem taper junction.

2.4.1 Clinical Implications of Modularity in THR

Modular taper junctions allow for fluid ingress and motion at the interface. This leads to a complex multidisciplinary degradation mechanism, often referred to as fretting corrosion or mechanically assisted crevice corrosion that will be discussed in more detail in the next section. Wear and corrosion products created at the taper junction are commonly associated with ALTR presented in patients as pain followed by instability due to loosening of the implants [24–27]. Figure 2.11 shows an example of head-stem taper corrosion and evidence of ALTR during a revision surgery replacing the metal head with a ceramic one with a titanium insert. More specifically, Figures 2.11 A and B show the implants with

black flake-like corrosion products [100] whilst Figure 2.11 C shows a pale mass typical of pseudotumour formation [101].

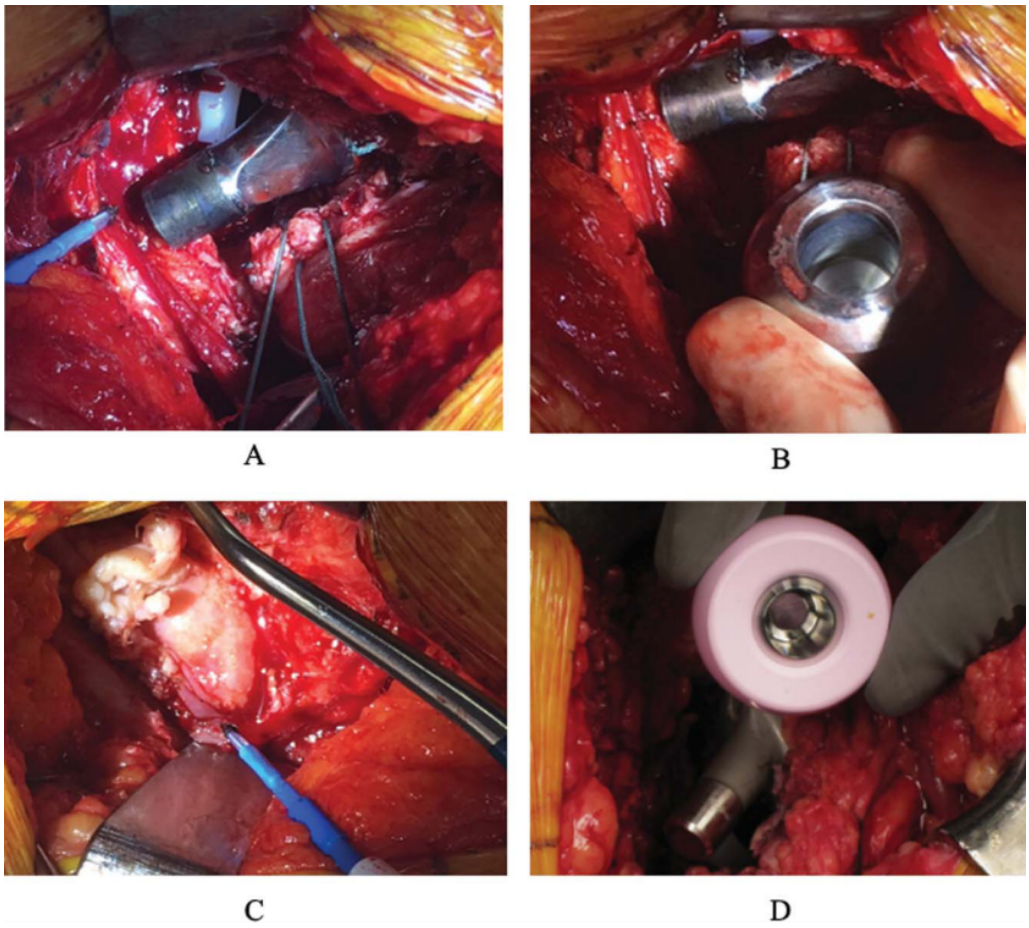

Fig. 2.11 Photographs showing mechanically assisted crevice corrosion at the modular taper junction showing (A) the male taper (B) femoral head taper, (C) adverse local tissue reactions and (D) the replacement of a ceramic femoral head in conjunction with a titanium adapter sleeve. Image taken from [100].

Differentiating the sources of wear and corrosion that cause ALTR can be difficult, and so the clinical importance of the taper interface in isolation can be difficult to determine. With that said, Ridon et al. [29] compared matched cohorts of THR with resurfacing (no modular femoral stem). They found that almost 30 % of the THR cohort underwent revision due to adverse reactions to metal debris compared to 0 % for the resurfacing cohort, suggesting that the taper, between the head and stem, could be one of the prominent interfaces for metal ion and debris release. However, it should be noted that the head-stem modular taper junction is not the only interface that differs between a resurfacing and THR. Resurfacings lack the femoral stem which sits within the intermedullary canal and so this study does not definitively identify the head-stem modular junction as a clinical concern but does provide a good indication. Xia et al. [102] on the other hand, went further

than Ridon et al. [29] and analysed the size, shape, distribution and composition of the metal particles retrieved from the tissue surrounding metal-on-metal hip resurfacings (one metal-on-metal interface, the bearing interface), large diameter metal-on-metal THR (two metal-on-metal interfaces, the bearing interface and the head-stem modular taper junction), and dual modular neck total hip replacements (one metal-on-metal interface, the neck-stem modular taper junction) using electron microscopy techniques. The lowest volume of particle release was by the dual modular taper system, however, was associated with the most severe host reaction, followed by the metal-on-metal THR and finally the resurfacing. This indicated that the nature of the particles produced at the taper junction, which has been found to differ in morphology and composition from the bearing interface [32, 102], can engender a more severe reaction compared to particles produced at the bearing interface.

In addition, an indication of the clinical importance of the taper interface can be shown by several recent case studies that specifically identify the head-stem taper as the cause for revision surgery [27, 103–105]. Nevertheless, between 2014 and 2022, 11 % of all single-stage revision procedures in the UK were due to ALTR [106], of which an interface contributing to the production of wear and corrosion products associated with ALTR, is the head-stem taper junction.

2.4.2 The Head-Stem Modular Taper Junction

The modular taper in THR (Figure 2.12b) was based on a 'self-locking' Morse Taper (Figure 2.12a). Invented in the 1860s, the Morse Taper is composed of a female conical taper (spindle) and a male taper (toolholder), where the presence of an acute taper angle is important in creating a tight fit under axial compression. It allows machine parts for drills, lathes and milling machine to be changed quickly without compromising torque transmission. The original Morse taper achieved a sufficient interference fit by designing the two interfaces to be highly conforming, smooth, hard (usually case hardened steel), long and with a slight taper angle of around 2 °[107–109, 16].

THR tapers (Figure 2.12b) on the other hand tend to be much shorter with a higher taper rate (i.e. shorter with a greater taper angle), often presenting a threaded finish and a level of angular mismatch (i.e. the difference in cone angle between the female and male taper), in order to create specific contact regions [16, 110]. More specifically, clinically available '12/14' (denoting the smallest and largest diameter of the taper) head-stem modular tapers have been found to vary in terms of: taper length between 10.5 and 15.0 mm, taper diameter between 12.6 to 12.7 mm at 1 mm distal from the proximal flat, taper angle between 5.55 and 5.8 °and surface topography mean roughness amplitude (R_a) by 0.49 and 13.65 µm [110].

THR head-stem modular tapers also differ between material couples with all hip replacement system implanted today in the UK comprising metal stems with either ceramic or metal heads [106]. More specifically, around 65 % of THR currently implanted in the UK present a metal head coupled with a metal stem i.e. a metal-on-metal contact at the modular taper [111]. Ceramic heads coupled with a metal stem are responsible for around 35 % of THR implanted today, but present an increasing tend, meaning that the percentage of ceramic heads is only set to rise. The most commonly implanted components in the UK would indicate the following possible specific material head-stem couples [106]:

- Orthinox Stainless Steel stem (trade name for high-nitrogen stainless steel) coupled with a high-nitrogen stainless steel head [112];
- high-nitrogen stainless steel stem with a CoCr (Cobalt Chromium alloy) head [112];
- high-nitrogen stainless steel stem with a BIOLOX Delta (trade name for alumina yttria-stabilized tetragonal zirconia [113]) ceramic head [112];
- TiAl6V4 (titanium alloy) stem with a BIOLOX Delta ceramic head [81, 114];

Metal alloys and ceramics biomaterials make up the femoral head and stem. The term biomaterial is used to describe materials that come into contact with living tissue and are thus considered biocompatible i.e., in use, they perform an appropriate host response [115]. Almost all stem materials are manufactured from metallic alloys given their high strength, toughness (resistance to fracture), balance between stiffness and elasticity, ductility and high yield strength [116]. There is an increasing tend in the use of ceramic femoral heads [106] due to their hard yet brittle nature [117]. The next subsections aim to cover three commonly implanted metal alloys and the ceramic material BIOLOX delta used to manufacture ceramic femoral heads. More detailed comparisons of material couple selection in the performance of the head-stem modular taper are covered in more detail in later sections.

Stainless Steel Alloy

Stainless steel is an iron based alloy with more than 50 % mass iron, over 10.5 % mass chromium and other elements such as molybdenum, copper, titanium, niobium and nitrogen to help improve the material properties [116]. Stainless steels predominantly owe their corrosion resistance, and thus their ability to resist reaction in physiological conditions, to the formation of a chromium oxide passive layer on the surface [118], further enhanced by the addition of the aforementioned additional elements [116].

Conventionally, 316L Stainless steel is used in orthopaedic implants, standardised by ASTM F138 for medical implants [119] with less than 0.03 weight % carbon (the 'L' in 316L Stainless Steel represents 'low carbon'), 17-19 weight % chromium, 13-15 weight % nickel, less than 2 weight % manganese, 2.25-3.00 molybdenum, less than 0.5 weight % copper, less than 0.75 weight % silicon and less than 0.1 weight % nitrogen [120]. The use of high nitrogen stainless steels, standardised by [121], is now common place with nitrogen content between 0.25 mass fraction % [121] giving rise to superior fatigue strength and improved corrosion resistance [120].

Cobalt Chromium Alloys

Like stainless steels, cobalt based alloys have long been used in orthopaedics [122–124] due to their good material properties such as a high yield stress, toughness and superior corrosion resistance, increased stiffness (240 GPa elastic modulus compared to 210 GPa [2]) and superior hardness compared to stainless steels [116]. The most commonly implanted cobalt alloy today, is that of Cobalt Chromium Molybdenum (CoCrMo) with greater than 50 mass % cobalt, 27-30 mass % chromium, 5-7 mass % molybdenum, defined by standards including ASTM75-18 [125], ISO5832-6 [126] and ISO5832-4 [127].

Titanium Alloys

Titanium alloys, traditionally developed for aerospace applications, have been implanted as early as 1996 [128] and are now commonly implanted in a range of medical implants including total hip replacements, and more specifically, femoral stems and acetabular shells [116]. They present superior corrosion resistance and biocompatibility compared to stainless steels due to the formation of titanium oxide, good specific strength and lower elastic modulus compared to stainless steel and chromium alloys yet poor torsional strength. A widely implanted titanium alloy in total hip replacements is Ti-6Al-4V standardised by ISO 5832-3 [129] comprising mostly titanium, between 5.5-6.75 mass fraction % aluminium, 3.5-4.5 mass fraction % vanadium among other elements with less than 0.3 mass fraction %.

Ceramics

Alumina oxide was one of the first ceramics successfully implanted into patients in 1971 by Pierre Boutin with his ceramic-on-ceramic cup-head bearing interface [130]. Ceramics used in total hip replacements are good materials for bearing interfaces as they are very hard, resistant to wear, have high wettability for good lubrication and are biocompatible

[131]. However, ceramics are poor under tension, brittle and not very tough, limiting their applicability due to the risk of component fracture [132]. Ceramics have seen significant improvements over the years with the latest generation providing increased toughness to ceramics with the introduction of BIOLOX ®delta. The increased toughness was realised through the uniform distribution of yttria-stabilized tetragonal zirconia particles (25 %) in an alumina oxide matrix (75 %) along with the addition of chromium and strontium oxide in a small percentage of less than 1 % [130].

In addition to taper design parameters, including head-stem material choice, the biomechanical loading profile is very different from that experienced in Morse tapers. Morse tapers are designed to transmit high torques under a dominant compressive axial load, whereas the head-stem taper in-vivo experiences a complex loading profile that is cyclic in nature [6]. With reference back to Section 2.2.2, where a more detailed understanding of the loading profile transferred through the hip joint can be found, the primary force is that due to body weight with a large component acting in compression along the taper axis, however, there are off-axis loads whose effect on taper performance is largely unknown within the literature.

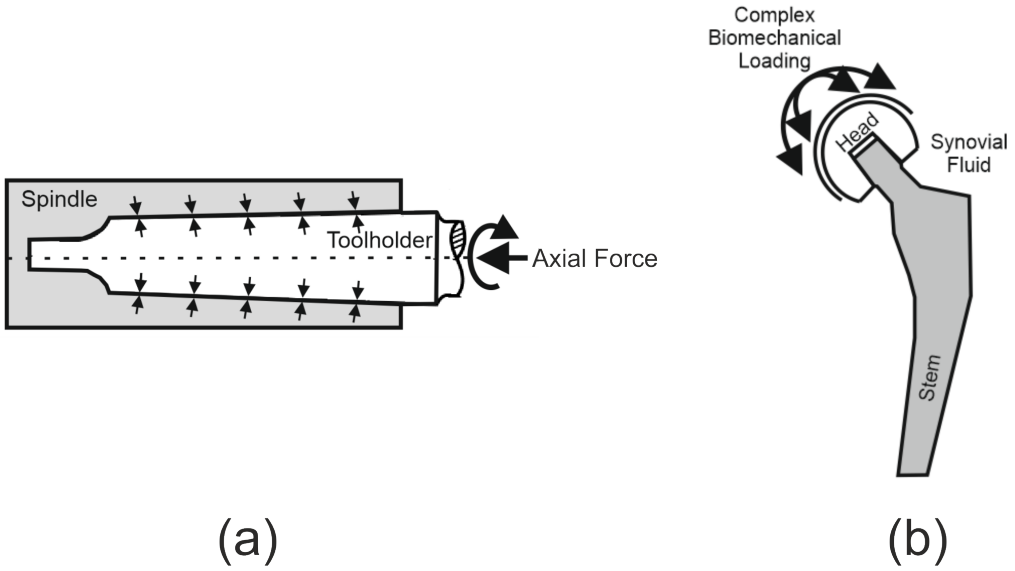

Fig. 2.12 Schematic of (a) traditional Morse Taper compared to (b) a THR head-stem taper junction.

2.4.3 Surgical Assembly of Modular THR

During surgery, after the femoral stem has been fitted into the intramedullary canal of the femur, the femoral head is assembled onto the stem. The head is seated on the stem and an compressive interference fit between the head (female taper) and stem (male taper) is

created with a mallet. Figure 2.13 shows the impaction process during a study by Wendler et al. [133] that measured the surgical assembly force in-situ.

Fig. 2.13 In-situ measurement of the surgical assembly force on human cadavers. Image taken from [133]

Studies that investigated the assembly forces applied by surgeons report that this is a highly variable uncontrolled process. Scholl et al. [34] measured the impaction force, velocity and number of impacts exerted by eight orthopaedic surgeons on a bench top model of a femur. They found that the average impaction force was 14,855 ± 6758 N over a range of between 6 and 24 kN, the average impaction velocity was 4.8 ± 1.6 m/s with most surgeons using three blows of increasing velocity to seat the head, the minority used one large blow in the region of 25,014 N. Although Scholl et al. [34] showed a large variation in the assembly process between surgeons, no statistical difference was found with varying surgical experience. Heiney et al. [35] reported a much lower average force used by surgeons of varying experience of 4,409 ± 660 N with no statistical difference between surgeons of varying experience. A possible explanation of the discrepancy between the impaction force reported by Scholl et al. [34] and Heiney et al. [35] was that whilst Scholl et al. [34] measured force using a piezoelectric instrumented hammer, Heiney et al. [35] only estimated force using a pressure sensitive film by correlating colour density with

force. Wendler [133] instrument both prothesis and hammer with piezoelectric sensors and reported an assembly force of 2037.2 N ± 724.9 N ranging from 822.5 N to 3835.2 N with no significant differences between male and female surgeons and surgical experience. An explanation as to why Wendler [133] reported lower assembly forces compared to Scholl et al. [34], despite using similar measurement systems, was that Wendler [133] accounted for the compliance of the patient's body by performing these studies on cadavers. With that said, these studies suggest that assembly forces applied by surgeons can be anywhere between 1-20 kN and often greater than the 2 kN adopted by many in-vitro studies as stipulated by ISO 7206-10 [134]. For reference, a 2 kN impaction force is equivalent to around two and a half average human males in the UK momentarily standing on the femoral head.

2.4.4 Biomechanical Loading of the Modular Junction in THR

The head-stem taper in THR transmits loads applied to the femoral head, to the stem. The forces applied to the head as shown in Figure 2.3, and those applied during the surgical assembly process [135], cause stress to be experienced at the interface facilitating fretting corrosion. Figure 2.14 shows a schematic of the forces applied to the femoral head as per the coordinate system used by Bergmann et al. [6] (please refer to Figure 2.3).

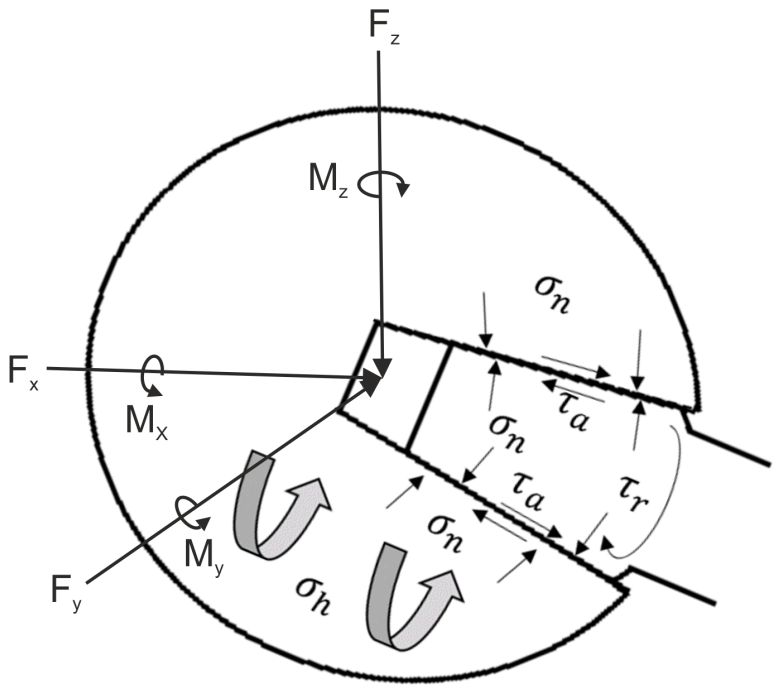

Fig. 2.14 Schematic of forces acting about the taper junction using the same coordinate system as Bergmann et al. [6], and stresses experienced at the interface between male and female taper. Where θ_n is the normal stress, θ_h is the hoop stress, τ_a is the shear stress in the axial direction and, τ_r is the shear stress in the circumferential direction.

Finite element studies often calculate the contact pressure at the interface subject to simulated loading conditions. Figure 2.15 shows the contact pressure (equivalent to the normal stress θ_n of Figure 2.14) experienced at the taper interface at different assembly forces and subject to a 4 kN uniaxial force acting vertically down due to body weight (F_z). Figure 2.15 demonstrates how contact pressure can present an asymmetric pattern with increased stress at diagonally opposite locations of the taper. Other FEA studies also show that contact pressure varies over the interface due to variations in taper design parameters [136] and loads applied to the hip joint through surgical assembly [137, 138] and during different daily activities [139]. For example, less conforming tapers have been found to present greater contact stresses over a reduced area [140, 136, 141], increased surgical assembly forces were also found to increase contact pressure but over an increased area [137, 138] and more extreme activities of daily living such as stair climbing compared to walking, present an increased contact pressure with an enhanced asymmetric distribution [139]. As such, the biomechanical loading of the femoral head and the taper interface, although linked, does differ.

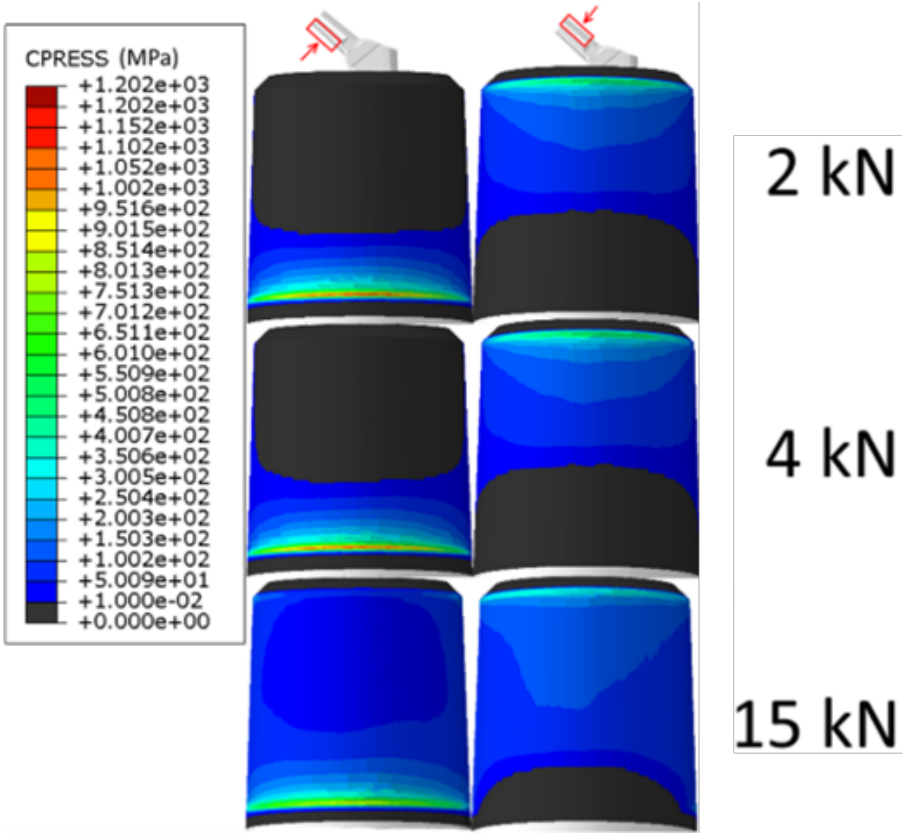

Fig. 2.15 Heat map of Contact pressure in MPa of the taper interface subject to uniaxial loading in the F_z direction and with a magnitude of 4 kN when the femoral head is assembled to 2kN, 4kN and 15 kN. Image adapted from Bitter et al. [137].

2.5 Degradation Mechanisms

Thus far, the thesis has covered the clinical context for THR, implications of THR and clinical failure, modular THR as a technology and the biomechanics of THR. The next section aims to cover the engineering mechanisms occurring at modular interfaces in THR whilst the following sections look at how head-stem modular variables affect engineering degradation mechanisms including how this is assessed.

The most consistently supported degradation mechanism in the literature describes a synergy between fretting and corrosion i.e. fretting corrosion or mechanically assisted crevice corrosion [22].

2.5.1 Fretting

Fretting involves relatively small-amplitude oscillatory movement between two surfaces, which are typically considered stationary, resulting in material loss. Depending on the working conditions, different fretting regimes can be achieved and are associated with

different degradation mechanisms [142]. The regime is dependent on a number of different variables including the contact compliance governed by the modulus of elasticity (E) and the coefficient of friction. However, within a given contact this is predominately determined by normal load (W) and tangential force (Q) or displacement (δ) [143].

Considering a point contact, like that between a spherical and a flat surface, Figure 2.16 summarises the material response under the three different regimes. The stick regime (SR), associated with an elastic response, shown by a linear relationship between Q and δ and negligible damage [142]. The partial slip regime (PSR) demonstrates both slip and stick at the interface. There is a central stick region with sufficient contact pressure to resist relative movement, surrounded by an annular slip region with insufficient contact pressure to resist movement, as predicted by Mindlin [144]. Substantial plastic deformation occurs at the contact shown by the hysteresis loop in the Q vs δ graph, this is focused at the boundary between slip and stick. The PSR is often associated with fretting fatigue crack formation due to cyclic loading of contacting asperities. The gross slip regime (GSR) occurs when the whole contact experiences slip shown by the increase in δ without an increase in Q. The GSR is more commonly associated with fretting wear. The different mechanisms of how material is lost through wear and fatigue will be discussed in more detail below.

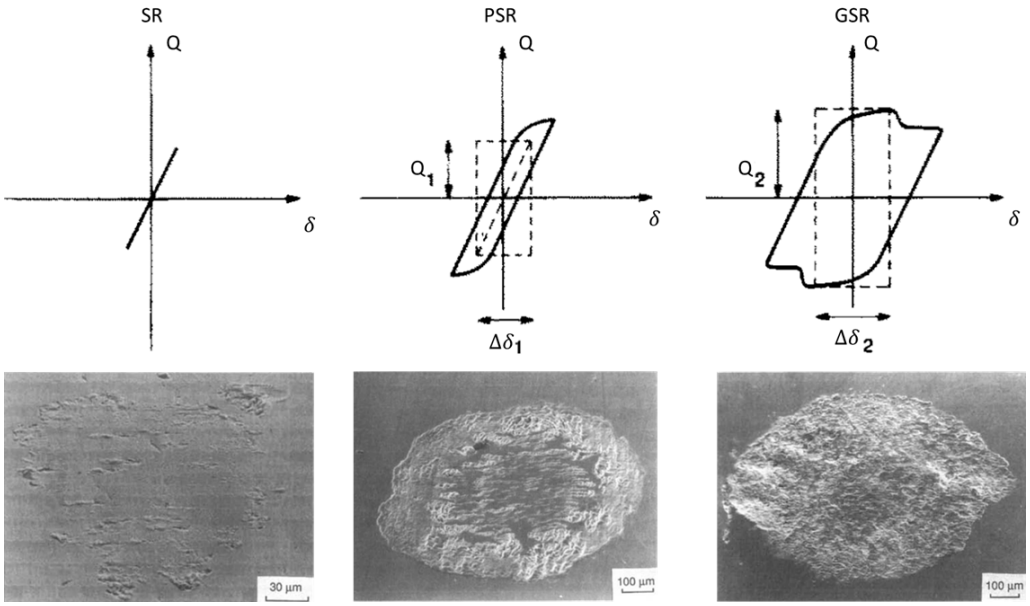

Fig. 2.16 Characteristic fretting loops (Q vs δ graphs) of the SR, PSR and GSR and examples of the wear scars typical of each regime considering a Hertzian contact. Images taken from [142]

Transition from SR to PSR and to GSR can be achieved by either increasing δ above critical amounts to overcome the contacts compliance under a constant W or, decreasing W below critical amounts with a constant δ. One important point to note here is that the

rate of material loss can actually decrease with an increase in W by altering the regime and reducing slip at the interface [143].

Adhesive Wear

Adhesive wear is especially important to consider in metallic contacts due to the presence of free electrons which are able to transfer at contacting asperities, facilitating adhesion [145]. Figure 2.17 shows a schematic of the wear mechanism. Upon contact it is thought that there is a sufficient normal load concentrated at the contacting asperity to facilitate plastic deformation (Figure 2.17a to b), leading to 'junction growth'. Plastic flow as one surface moves relative to the other can case the junction to cold weld [146, 147]. Depending on the strength of this junction, failure can occur within material leading to the creation of a wear particle (Figure 2.17c).

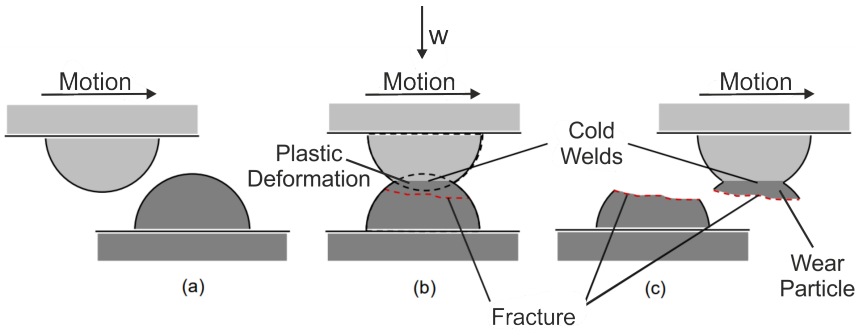

Fig. 2.17 Schematic of adhesive wear (a) before, (b) during and (c) after contact. Image adapted from [148].

Although the majority of THR currently implanted in the UK feature a metal head coupled with a metal stem i.e. a metal-on-metal contact at the modular taper [111]. Ceramic heads coupled with a metal stem are responsible for around 35 % of THR implanted today, can also experience adhesion attributed to bonding between the metal cations and oxygen in the ceramic [149]. However, abrasive wear is very important to consider due to the large disparity in hardness between ceramics and metals. Other complicating factors for both types of contact in THR include the presence of surface oxides (that form readily on biocompatible metals) and contaminants which generally serve to reduce adhesion by separating the surfaces [145].

Abrasive Wear

Abrasive wear occurs when a hard asperity of a contact surface (two-body abrasion) or separate particle (three-body abrasion) slides over another surface [145]. Depending on the materials involved, shape of the asperity or abrading particle, material loss can

be a result of: micro-cutting, micro-fractures, fatigue of repeated ploughing and grain detachment. Micro-cutting represents a more classic model of this mechanism and upon which theoretical models have been built. Figure 2.18 shows a schematic of the model presented by Rabinowicz et al.[150] to relate wear volume (V) to normal load (W), sliding distance (L), surface hardness (H) and asperity or particle shape (α).

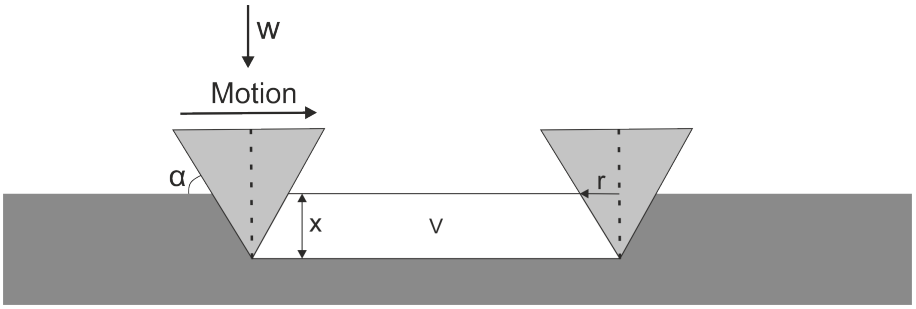

Fig. 2.18 Schematic of abrasive wear showing the hard conical asperity (with a cone angle of α) removing material (of volume V) from the softer surface with a depth of x and normal load W.

The model predicts that wear volume produced by a single asperity is directly proportional to W and L, and inversely proportional to hardness (H). See Equation 2.2. The equation can be rearranged to resemble Archard's, where K is a function of the asperities geometry assuming all the material displaced by the asperity is lost.

$$V = \frac{WLcot(\alpha)}{\pi H} \tag{2.2}$$

[150]

Abrasive wear is especially important to consider when ceramic heads are used due to the large disparity in hardness. Third-body abrasion also has a role to play due to contaminants or wear particles trapped in the taper junction.

Fatigue Wear

Fatigue wear is a result of cyclic stress variations over a long period of time leading to surface initiated cracks that can propagate forming a wear particle [145]. Unlike most wear mechanisms, material loss due to fatigue can occur at a contact that may not experience sliding e.g. rolling contacts and in situations were the surfaces are completely separated by a film of lubrication. However, in THR fatigue wear is a result of relative motion between the two surfaces, see Figure 2.19. The first step is crack initiation which occurs at a weak point such as a slip plane (Figure 2.19a). This crack is then able to propagate along the slip

plane with successive loading cycles (Figure 2.19 b) which can eventually lead to fracture and particle detachment (Figure 2.19 c) [151].

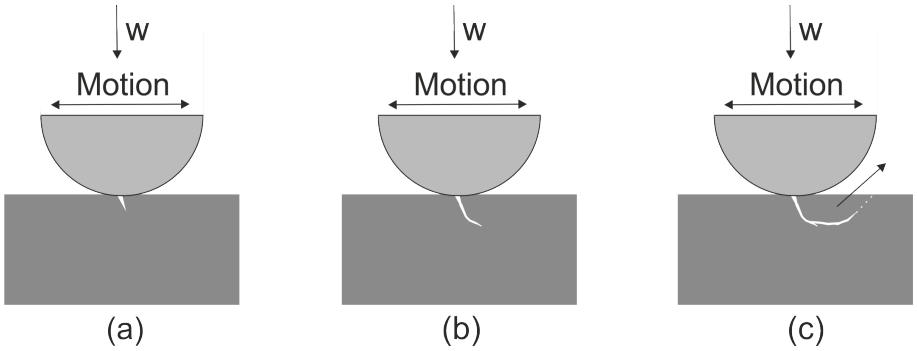

Fig. 2.19 Schematic of fatigue wear showing (a) crack initiation, (b) crack formation and (c) particle detachment.

Biocompatible metals, such as those used in THR, spontaneously form an oxide layer. In some cases, this can act to increase fatigue wear due to the formation of an oxide layer within newly formed cracks, provided enough oxygen is available [145]. Another complicating factor, is the high affinity for hydrogen of certain bio-metals used in THR leading to hydrogen embrittlement that could have implications on the crack mechanism [152].

2.5.2 General Corrosion

Corrosion refers to the deterioration of material due to (electro)chemical reactions within the environment [145, 153]. Corrosion of metals occurs when metal atoms (M) within an aqueous solution oxidise, releasing electrons (e^-), forming a metal ion which is then able to enter the solution [154] (Equation 2.3). Likewise, the metal ions can reduce back into the metal substrate by reacting with the valence electrons near the surface.

$$M \rightleftharpoons M^{n+} + ne^- \tag{2.3}$$

Metal substrates within an aqueous electrolyte have millions of oxidation and reduction reaction sites forming a dynamic equilibrium [155]. This dynamic equilibrium is affected by the presence of electrochemically active species (EAS) that can react with electrons and discharge the surfaces of metals promoting the release of metal ions from the surface (corrosion). Equation 2.4 demonstrates how a common EAS such as oxygen can be reduced by excess electrons in an aerated, basic or alkaline solution.

$$2H_2O + O_2 + 4e^- \rightarrow 4OH^- \tag{2.4}$$

This metal-electrolyte interface is commonly modelled as an Electrical Double Layer (EDL) shown in Figure 2.20. This consists of some oxidised metal ions held close to the negatively charged surface by the excess electrons, but separated from the substrate by water molecules. This figure also shows how EAS can diffuse into the EDL and discharge the surface from the diffuse layer, driving the release of metal ions to maintain equilibrium.

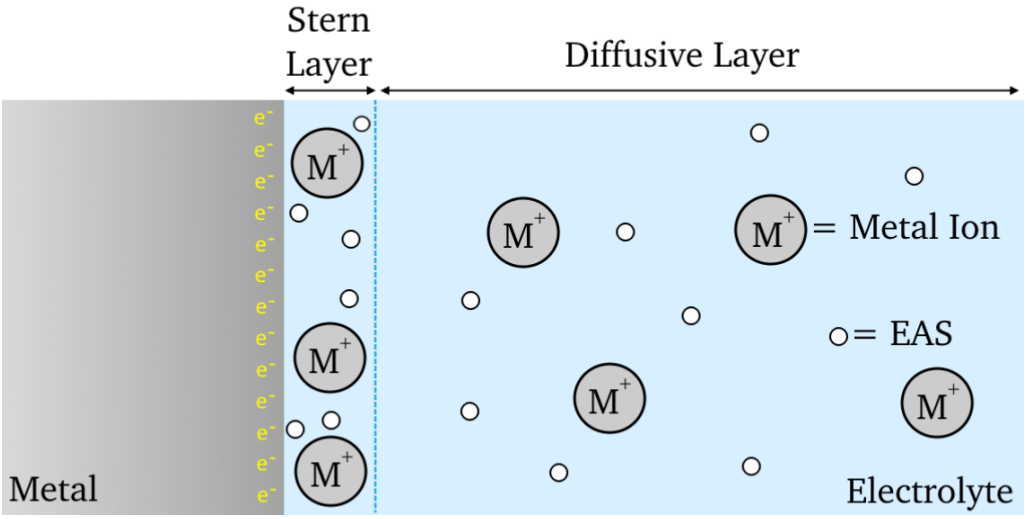

Fig. 2.20 Illustration of the electrical double layer (EDL). Image taken from [156].

This charge separation in the EDL produces a potential difference that cannot be measured directly [155]. The use of a reference electrode (RE) makes this possible by measuring the voltage across the two, providing a potential difference of the electrode of interest with respect to the RE, also known as the Open Circuit Potential (OCP). The OCP changes with EDL composition (i.e. concentration and type of products, reactants and EAS). Likewise, the EDL changes with an applied voltage. This relationship is detailed mathematically by the Nerst equation shown in Equation 2.5.

$$E = E^0 - (RT/nF)ln[(a_p)/(a_r)] \tag{2.5}$$

Where:

E is the cell potential under specific conditions (V)

E_0 is the cell potential under standard conditions (V)

R is the ideal gas constant (8.314 J /mol)

T is the temperature in Kelvin (K)

n is the number of electrons stated in the half cell reaction (e.g. Equation 2.3)

F is Faraday's constant (C/mol)

a_p is the chemical activity of the products

a_r is the chemical activity of the reactants

Different metals have different tendencies to either oxidise or reduce. These tendencies can be measured as a potential difference under standard conditions, against a hydrogen electrode and ranked in the electrochemical/galvanic series [154]. The more positive potentials indicate more noble metals due to their reluctance to form ions. Whereas, a more negative potential indicate more active metals that would suggest a higher propensity to form ions and corrode. However, this series has its limitations in predicting corrosion resistance, as is the case for metals used in orthopaedic implants. Implants resist corrosion and are biocompatible as their surfaces readily oxidise in-vivo [157]. This oxide layer is a very thin nanometre thick protective passive layer which prevents the continuous uniform corrosion by blocking metal ion transfer into the solution [158, 159]. However, metals that have a propensity to readily oxide and form this protective passive oxide layer are susceptible to more localised corrosion mechanisms, such as crevice corrosion.

2.5.3 Crevice Corrosion

Crevice corrosion is one of the most commonly cited chemical degradation mechanisms said to take place in the taper junctions of Total Hip Replacements, and can be considered to be a contributory mechanism of mechanically assisted crevice corrosion [22, 23]. Crevice corrosion is important in the context of the head-stem modular taper junction, as the transport of fluid in and out of the junction is restricted through a small gap at the opening of the taper junction. This crevice geometry can cause fluid stagnation for crevice corrosion of which Oldfield and Sutton [160] were the first to develop a detailed description of the fundamental mechanism and will be briefly explained here below.

Initially, both oxidation (anodic) and reduction (cathodic) reactions happen freely over the surface [160]. The annular gap at the taper can hinder the diffusion of oxygen into the interface, resulting in depletion over time. The next step in Oldfield and Sutton's [160] mechanism is marked by a concentration difference of the solution within the interface compared to outside. This sets up a preferential anodic site within the crevice

and cathodic site outside, where valence electrons are still free to react with oxygen. In order to maintain equilibrium, the anodic reactions within the interface is driven with a detrimental ratio of cathodic to anodic surface area. This is free to continue until the local solution becomes saturated in the metal hydroxide (the overall reaction of Equations 2.3 and 2.4). Precipitation of metal hydroxides reduces the amount of hydroxide ions from the solution, generating hydrogen ions reducing the pH (Equation 2.6). The excess cations (e.g. hydrogen and metal ions) can cause migration out of the crevice and attract anions (e.g. chloride ions) in. Metal chlorides can then form (Equation 2.7), competing with the metal hydroxides within the passive film which are less strongly bonded to the oxide matrix influencing passivity of the protective film [159]. Additionally, metal chlorides also form hydrochloric acid (Equation 2.8) further decreasing pH.

$$M^{2+} + 2H_2O \rightarrow M(OH)_2 + 2H^+ \tag{2.6}$$

$$2Cl^- + M^{2+} \rightarrow M(Cl_2) \tag{2.7}$$

$$M(Cl_2) + H_2O \rightarrow M(OH)_2 + HCl \tag{2.8}$$

The next stage of the model is marked by the passive layer breaking down due to a decrease in pH, as per the associated Pourbaix diagram. In other words, this is when the local solution becomes aggressive enough to breakdown the passive oxide layer within the crevice. Once the passive layer is broken the reaction is autocatalytic, repeating the Equations 2.3, 2.4 and 2.6 to 2.8, continuing the production of metal ions. This is the fourth and final stage, which will continue until the crevice geometry is broken.

The Oldfield and Sutton [160] model considered the crevice geometry and its influence on corrosion. The two parameters important to consider are the crevice gap (gap at the opening of the taper) and depth. A narrower crevice opening and deeper crevice would predict a more aggressive crevice geometry. The passive oxide layer also plays a significant role in this model by preventing the occurrence of the fourth stage. Passive oxide layers depend on the metal alloy composition any defects and, the oxide grain structure [159, 154].

2.5.4 Fretting Corrosion

Fretting is intimately linked to corrosion, mainly attributed to the continuous mechanical disruption of the passive layer [161]. Brown et al. [23], was one of the first to employ the use of an electrolytic cell to measure the electrochemical response due to the constant depassivation and repassivation of the oxide layer within the taper junction during dynamic simulation.

Mechanically assisted crevice corrosion was a term coined by Gilbert et al. [22] to umbrella the complex interaction between fretting and corrosion, and any interaction they may have within the modular taper junctions in orthopaedic devices. In summary, this involves the constant mechanical abrasion during biomechanical loading and subsequent repassivation of a spontaneously formed 2-10 nm thick surface oxide layer present on all passive biomedical alloys. The repeated disruption of the oxide layer exposes the metal substrate, resulting in liberation of metal ions that can be either be released into the electrolyte, or react with oxygen to form a metal oxide. Figure 2.21 shows a schematic of this process and illustrates how surface deformations and slip planes due to dislocations near the surface can disrupt the surface oxide and affect its passivity. This occurs within a crevice geometry that can hinder the movement of corrosion reactants and products which can initialise and sustain accelerated corrosion [38].

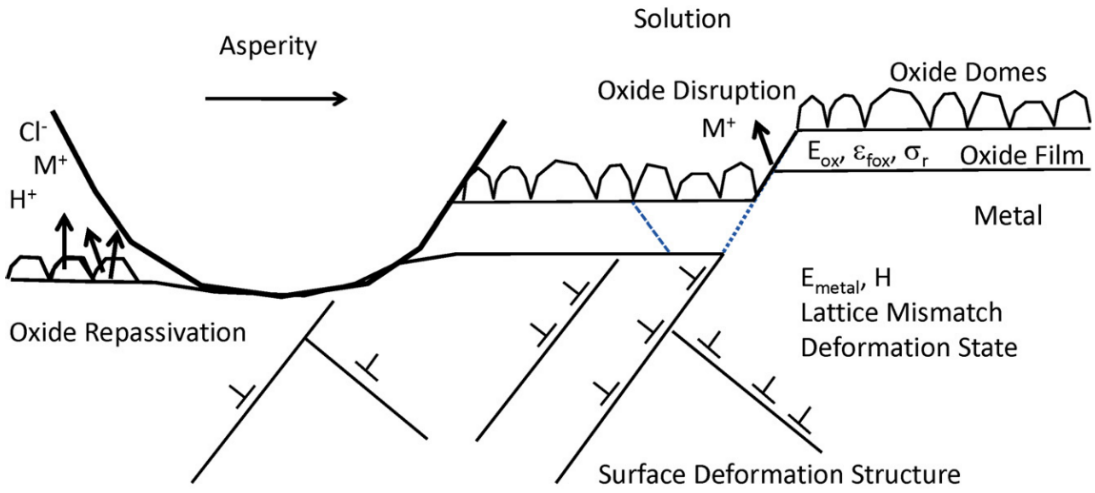

Fig. 2.21 Schematic of the coined term Mechanically Assisted Corrosion (MAC), demonstrating the mechanical removal of oxide layer that spontaneously repassivates and subsurface deformation and dislocations as a result of the fretting action. Images taken from [38].

The term ‘mechanism’ for mechanically assisted crevice corrosion also covers other interacting factors which can be broadly grouped into mechanical, chemical and biological factors, as illustrated in Figure 2.22. Although, Figure 2.22 does help evoke the understanding that the problem is a web with many interacting factors that can span multiple

disciplines, it should be noted that the interactions may not be limited to those as indicated in the diagram. For example, the 'bulk mechanics' category also plays a direct role in the mass transport in and out of the taper junction, where bending experienced at the taper junction can force fluid out, and pull fluid into, the taper interface [162]. Additionally, taper design parameters which have been found to affect mechanically assisted crevice corrosion are not explicitly represented in Figure 2.22. It could be that this is captured in the Surface Mechanics category under asperity contact abrasion and adhesion, however, design parameters could also have a direct impact on 'transport phenomena', for example, angular mismatch has been shown to at least in part seal the taper interface from fluids, minimising the fretting corrosion response [4], yet does not appear to be captured in this figure.

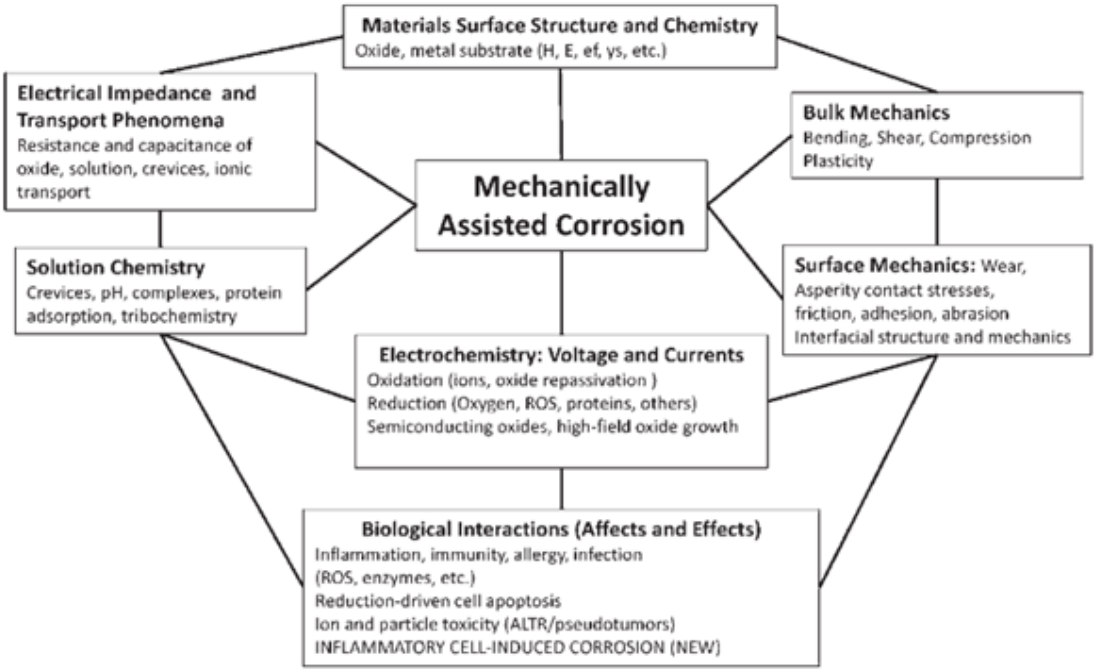

Fig. 2.22 Illustration of the complex, multi-disciplinary nature of mechanically assisted crevice corrosion. Images taken from [38].

Although the proposed mechanism for mechanically assisted crevice corrosion goes some way to explaining the degradation mechanism occurring within the taper junction of orthopaedic devices, it is generally accepted that there is an incomplete understanding.

2.6 Clinical Studies

Problems associated with the introduction of modular tapers in THR have been known since the 1990s [28]. Researchers have spent over 25 years studying factors affecting

performance and how these occur, mostly failing to draw consistent conclusions. These factors can be summarised into three categories: the patient (i.e. biomechanics and weight), the implant (i.e. properties and materials) and surgical (i.e. assembly and implantation). The effect of a wide variation in taper designs on this highly complex, multi-factorial system, further complicated by surgeon and patient factors, has meant that there is a lack of common understanding of what the ideal head-stem taper interface should look like.

Retrieval studies of medical implants are invaluable as they provide unequivocal links to clinical performance. They are capable of capturing a patients biological response to the implant in addition to quantifying and characterising degradation. In the past, retrieval studies have provided regulatory agencies, surgeons, patients, manufacturers, and in some instances evidence during litigation proceedings, with vital information on the failure modes of different implants. The results of such studies also inform further research and development and the results of such studies used to validate experimental and computational studies. In terms of the modular taper junction in THR, retrieval studies have been used by researchers to investigate the clinical implications of different modular taper design parameters, identifying clinical trends, which will be covered in more detail in the following Sections.

Despite the valuable information provided by retrieval studies, they do present their limitations. Firstly, results are normally limited to surface analysis post retrieval, only providing information at a single point in time. Information on how the modular taper interfaces degrade overtime is lost. Hence, retrieval studies are limited in helping to elucidate degradation mechanisms in-vivo. Secondly, analysis is normally limited to failed implants and control over when implants are retrieved is limited, introducing experimental bias into the results. The activity, biological environment, surgical assembly can differ significantly from patient-to-patient, introducing variability into experimental design. Pre-implantation information is also limited with no implant specific interface measurements pre-implantation for comparison. Finally, there can also be logistical difficulties in obtaining samples and further ethical implications and difficulties in the management of retrieved samples.

2.6.1 Clinical Assessment Methodologies

Retrieval studies generally involve analysing either both or one of the taper interfaces after the implants have been retrieved from a patient, normally following revision surgery. The interfaces are assessed in a number of different ways, including a semi-quantitative scoring system, where a score is assigned based on visual evidence of fretting and corrosion using

a criteria. The Goldberg scoring system and associated criteria are detailed below in Table 2.2.

Table 2.2 Criteria for fretting and corrosion scores according to the Goldberg scoring system [1]

Severity	Score	Criteria
None	1	No visible corrosion observed No visible signs of fretting observed
Mild	2	<30% of taper surface discoloured or dull Single band or bands of fretting scars involving three or fewer machine lines on taper surface
Moderate	3	>30% of taper surface discoloured or dull, or <10% of taper surface containing black debris, pits, or etch marks Several bands of fretting scars or single band involving more than three machine lines
Severe	4	>10% of taper surface containing black debris, pits, or etch marks Several bands of fretting scars involving several adjacent machine lines, or flattened areas with nearby fretting scars

Other studies measure the material loss using surface analysis such as coordinate measurement machines (CMM) and roundness measurement machines (RMM) [163, 164]. Material loss is calculated by inferring a 'pristine' interface from regions that appear unaffected (e.g. they present evidence of machining marks) or superimposing a 'pristine' surface where there are no unaffected areas, and then subtract the actual interface, allowing the volume and linear material loss to be calculated. Figure 2.23 shows how Morlock at al. [165] calculated material loss (red volume in the far right image) by superimposing a 'pristine' geometry (far left) on a model (middle right) of the worn retrieved modular taper (middle left).

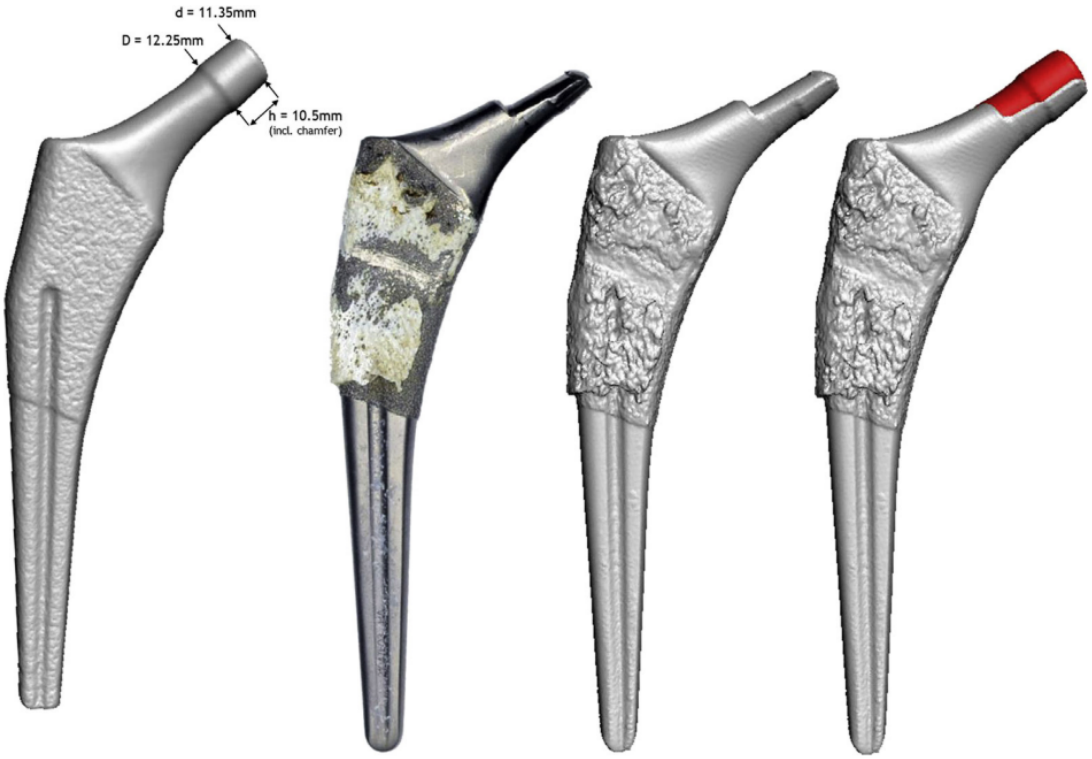

Fig. 2.23 Pictorial representation of the method used by Morlock et al. 2.23 to determine material loss indicated in red of the far right image from superimposing a pristine geometry (far left) onto a three dimensional representation (middle right) of the worn retrieved samples (middle right). Image taken from [165].

The strengths of the scoring system compared to measuring material loss is that it is easy to implement and has been found to be repeatable between different examiners, despite its subjective nature [166]. Determining the material loss using CMM and RMM techniques can be difficult in instances of a highly worn surface where the 'pristine' surface can be difficult to establish leading to less accurate measures of degradation. The limitations of the discrete scoring system is that it can lack precision and is a subjective assessment. That said, a study has found a correlation between the scoring system and material loss measurements [166]. A recent study by McCarty et al. [167] attempted further developed the Goldberg scoring system by developing a six-point scoring system with clearer, more extensive criteria descriptions, claiming to improve the intra-assessor's repeatability of novice assessors and provide strong correlation between measured material loss and the new grading system.

There are a number of different taper design parameters that have been found to affect the performance based on retrieval studies, including the head diameter, head offset, flexural rigidity based on bulk mechanical material properties and geometrical dimensions, surface topography, taper length and taper angle.

2.6.2 Head Diameter and Head Offset

Retrieval studies have found that an increased head diameter [168–171] and head offsets [168, 172, 165, 171, 173] are associated with greater evidence of fretting corrosion and material loss. More specifically, Langton et al. [168] measured the material loss of the head-stem taper junctions from one manufacturer that presented a metal-on-metal head-cup material articulation. They found material loss rates to be unaffected by wear to the head articular surface, yet to increase with an increase in head offset. This was attributed to an increased effective lever arm, increasing the bending moments experienced at the taper junction. The effective lever arm is the distance from the centre of the femoral head and taper junction, thus affected by both head offset and femoral head diameter [168]. This increase in effective lever arm was also seen in metal-on-polyethylene articulations, shown by studies reporting that an increased head diameter [169, 170, 172] and head offset [173, 171] were associated with increased visual wear (as per a Goldberg or Goldberg-like 4-point scoring system) and also attributed to an increased effective lever arm.

The effective lever arm and how this varies with head offset is shown schematically in Figure 2.24. An increased head offset places the centre of the head (and about which forces and moments act) more proximal to the taper junction, and in some instances, beyond (as per the far right diagram in Figure 2.24). On the other hand, more negative head offsets push the centre of the head more distal with respect to the taper junction (as per the far left diagram in 2.24). Hence, the location of the centre of the head with respect to the taper junction can alter the bending moments, stress and micro motion experienced at the taper junction. Figure 2.24) shows how compressive stress can differ at the interface due to body weight acting in the direction as indicated by the arrows. Greater compressive stress is indicted by yellow shading extending further from the interface whilst red indicates a lack of compressive stress and separation of the surfaces.

The role of the lever arm was further corroborated by Morlock et al. [165] who found corresponding varying wear patterns with the applied bending moments with varying head offsets. In terms of what this means clinically, the NJR [11] indicates a proportional increase in 32 mm diameter heads and a proportional decrease in 28 mm suggesting a push towards larger diameter heads, whilst head offset is determined by the surgeon to best fit specific patients.

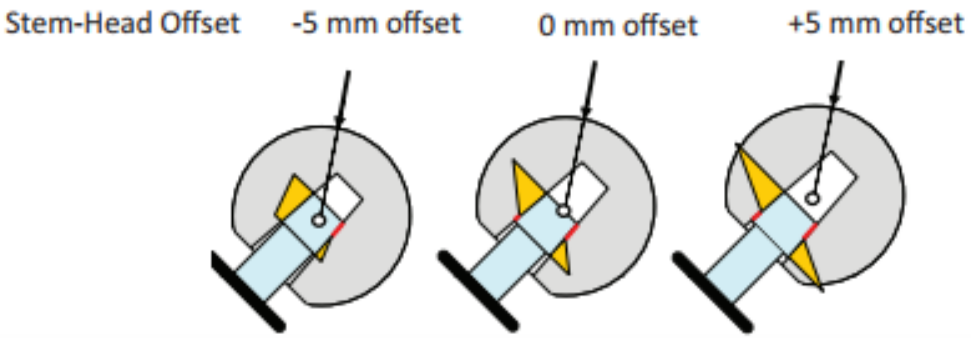

Fig. 2.24 Compressive radial stress distributions (yellow) at the taper interface, plotted on a radial axis and with regions of separation shown in red along the axial axis due to body weight. Images taken from [135]

Some retrieval studies present conflicting findings like that presented by Arnholt et al. [170] and Nassif et al. [174]. Arnholt et al. [170] found that head offset was not associated with an increased fretting score whilst head diameter was. Whereas, Nassif et al. [174] found that fretting and corrosion score and material loss did not correlate with head diameter nor lateral head offset. One possible explanation as to why Nassif et al. [174] presented conflicting findings was that it was underpowered, assessing only 26 stems which included stems from four different manufacturers. As such, it is more strongly supported that increased head diameter and offset are associated with increased taper degradation, primarily attributed to increased bending moments. Arnholt et al. [170] on the other had primarily set out to investigate the role of surface topography with little detailed on how the relationship between head diameter and head offset were determined.

Increased frictional torques have also been reported to be associated with greater head diameters [175] supported by in-vitro findings [176]. Friction due to articulation at the bearing interface is transmitted through the head-stem taper junction to the stem which may also play a role in taper degradation. This friction, when applied at a perpendicular distance from the centre of the head, and thus the taper junction, can create torque (turning moments), transmitted through the taper junction. Hence greater head diameters act to increase the effective lever arm.

2.6.3 Flexural Rigidity

Generally, it has been found that over time, male taper designs have decreased in flexural rigidity (FR) owed to lower elastic moduli (E) of femoral stems for reduced stress shielding and narrower diameters (D) for an increased range of motion [2]. The equation used by Goldberg et al. [1] and Porter et al. [2] for flexural rigidity is detailed by Equation 2.9;

where E is the elastic modulus of the stem and Diameter is the diameter of the male taper at the point of contact with the female taper, assimilated to the centroid of the male taper.

$$FR = E \times I = E\left(\frac{\pi(D)^4}{64}\right) \tag{2.9}$$

However, a decrease in flexural rigidity is associated with an increase in evidence of fretting corrosion [1, 172, 170, 177, 178]. This was shown by an early study by Goldberg et al. [1] who conducted a large multi-centre retrieval study, visually assessing and grading the taper interfaces using their 4-point grading system Table 2.2. It was thought that, the ability for modular THR systems to resist elastic strains is important to the magnitude of motion at the taper interface, and thus, the ability to resist fretting corrosion. Additionally, Goldberg et al. [1] also implicated the differences in stiffness of the a Ti6Al4V stem and a CoCr head, giving rise to relative motion at the taper interface. Whilst Goldberg et al. [1] conducted a large study, that was not selective based on total hip replacement design or reason for revision, more recent studies by Higgs et al. [172], Arnholt et al [170] and Keo et al. [177] undertook visual analysis using a 4-point grading system on polymer-on-metal THR, also reporting that a decrease in flexural rigidity led to an increase in visual signs of degradation. This effect of flexural rigidity was also noted in ceramic head couples by El-Zein et al. [178] who investigated two different taper designs, a '12/14' and a v40 (akin to a '12/14' taper that is specific to a single manufacturer). They found that the v40 tapers presented greater visual effects of degradation using a 4-point scoring system, and attributed this to v40 tapers being more flexible.

Although, Equation 2.9 indicates that flexural rigidity is a function of the diameter of the male taper, geometry external to the taper junction could affect motion of the system [179]. Additionally, and although the aforementioned studies cite the explanation of a reduced flexural rigidity giving rise to greater degradation, motion translated to the taper junction is not an aspect explicitly captured by Equation 2.9.

2.6.4 Material Couple Selection

Different materials not only have an implication on the bulk mechanical properties but the surface and corrosion properties also. There are a number of different material combinations for head-stem couples in THR, including:

- Ceramic Head (commonly yttria-stabilised zirconia toughened Alumina, Biolox Delta)-Stainless Steel Stem (commonly high nitrogen stainless steel ISO 5832-9 [121] but more traditionally 316L-Stainless Steel)
- Ceramic-Cobalt Chromium Molybdenum alloy (or CoCrMo, according to ISO 5832-6 [180])
- Ceramic-Titanium alloy (commonly Ti6Al4V according to ISO 5832-3 [181])
- CoCrMo-Stainless Steel
- CoCrMo-CoCrMo
- CoCrMo-Titanium alloy

According to the NJR [11] over 70 % of femoral stems currently implanted are manufactured from stainless steel. The most common head-cup bearing material is metal-on-polymer at 55 % followed by ceramic-on-polymer at 38 %. This indicates that the most commonly implanted head-stem material couples currently implanted are CoCrMo heads on stainless steel stems, followed by ceramic heads on stainless steel stems.

Material selection can have competing, and sometimes conflicting implications on wear and corrosion mechanisms. Table 2.3 summarises some key mechanical and corrosion properties of some typical metals used in THR. Greater values of elastic moduli indicate an increased resistance to bending (i.e. stiffer) and greater yield strength indicates that the material is better able to sustain greater tensile stresses before deforming plastically. In terms of corrosion, a more positive E_{corr} value indicates an increased resistance to produce metal ions and suggests an increased resistance to corrosion and a more positive I_{corr} indicates an increased transfer of electrons also indicating an increased corrosion rate. For example, Ti6AL4V has been found to present a higher resistivity to static corrosion compared to CoCrMo as indicated by the more positive E_{corr} and lowest I_{corr}, but a lower elastic modulus, which can reduce the flexural rigidity associated with increased fretting corrosion at the taper junction.

Table 2.3 Summary of key mechanical and corrosion properties of common metal alloys used in biomedical devices. Mechanical properties for metallic biomaterials, including elastic moduli as recited by Porter et al. [2], yield strength according to the American society for testing and materials committee F-4 recommendation and corrosion properties as found by Songür et al. [3].

Alloy	Elastic Moduli GPa	Yield Strength MPa	E_{corr} V Vs Ag/AgCl	I_{corr} μA cm $^{-2}$
316L Stainless Steel	210	190-690	-0.233	0.987
Cobalt Chromium Molybdenum (Wrought)	240	517-827	-0.156	0.23
Titanium (Ti-6Al-4V)	112	825-869	-0.129	0.199

Understanding these interdependent and often competing interactions between fretting and corrosion can be difficult. Retrieval studies that investigated the system response of various head-stem couples, indicate that generally:

- CoCrMo-CoCrMo and Titanium alloy-Titanium alloy couples tend to perform better than CoCrMo-Ti couples [86, 1, 171]
- Ceramic-on-metal tended to performed better then metal-on-metal groups [182, 183, 178]

Although CoCrMo heads coupled with stainless steel stems are the most commonly implanted material couples in the UK today, retrieval studies appear to be primarily focused at CoCrMo and Titanium alloys. This is despite stainless steel not presenting the most preferable mechanical nor corrosion properties, as indicated in Table 2.3.

2.6.5 Surface Topography and Taper Length

Without any standardisation, there is a wide variation in modular taper design in current clinically available THR. Taper length has been found to vary by almost 5 mm and surface topography by almost a whole magnitude [110, 184]. The large variation in surface topography can largely be attributed to the presence, or lack of, a ‘threaded’ texture. This was introduced to create a roughness amplitude of between 6 and 20 μm, specified by

CeramTec for use with ceramic heads [185]. The increased roughness was introduced to allow greater plastic deformation to help minimise any stress concentrations that may lead to burst fracture in ceramic heads. However, a 'threaded' male taper has been adopted in metal head couples with little to no design rationale to the author's knowledge. Figure 2.25 illustrates the variation in surface topography and taper length of two different stem designs.

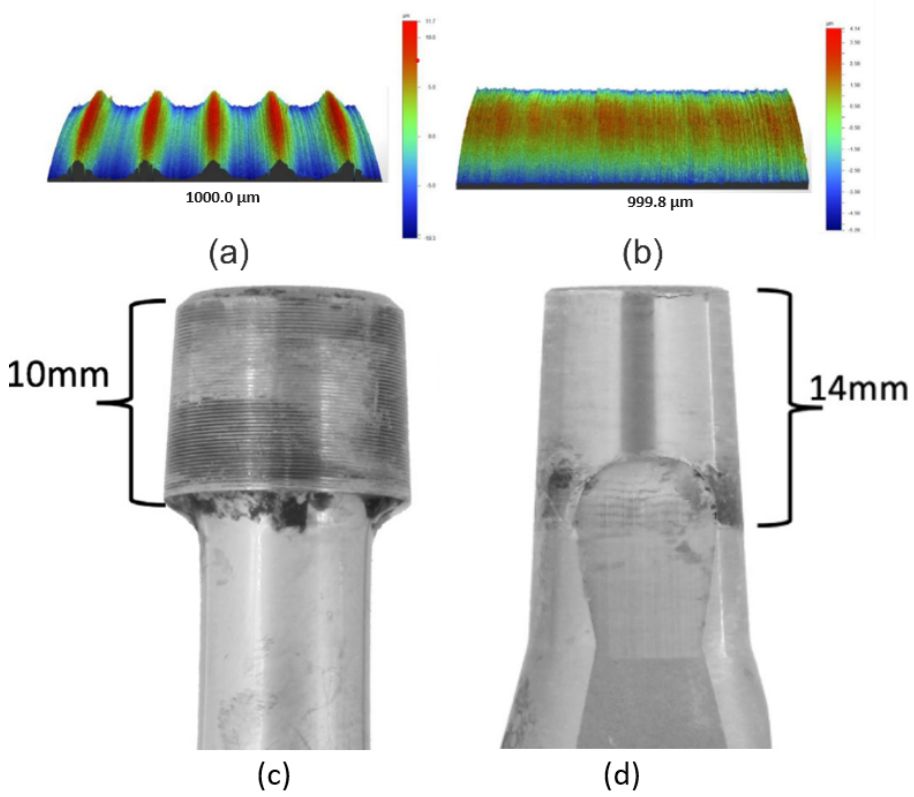

Fig. 2.25 Surface topography of a (a) threaded Corail (scale -10.3 to 11.7 µm) and (b) non-threaded SROM (scale -5.29 to 4.14 µm) both with sample length 1 mm, image taken from [184]. Taper length of the (a) Corail and (b) SROM stems, images taken from [186].

Retrieval studies have shown that longer tapers tend to perform better than shorter ones but this is in conjunction with a smoother surface topography [186, 187, 164]. This was attributed to long smooth tapers more evenly distributing contact stress at the interface. Additionally, shorter male tapers could introduce the distal male taper to be seated within the female taper, causing a possible stress concentrations and crevice geometries.

When considering surface topography and taper length as single design parameters, there are conflicting findings within the literature. Namely, a study by Whittaker et al. [163] reported that an increased surface topography roughness was linked to increased material loss, while Arnholt et al. [170, 188] reported that the presence of a 'thread' on the male taper did not affect material loss or visible evidence of fretting and corrosion.

Furthermore, two retrieval studies reported an increased susceptibility to degradation with longer tapers, with one reporting this in conjunction with a greater diameter [174, 177] while another reported that a decrease in engagement length was linked with an increase in fretting score [170]. These studies highlight the uncertainty surrounding a single design variable and how interacting factors of this complex problem can result in seemingly conflicting findings. This contributory nature of other factors was also demonstrated by Kop et al.[189] who looked at both head-stem and neck-stem modular interfaces and reported that CoCrMo alloy necks with a threaded finish presented more visible effects of degradation compared smooth CoCrMo stems, but found the opposite with Titanium modular neck components.

As discussed in Chapter 1, the most common head bearing material is metal followed by ceramic, with ceramic heads presenting in increasing trend year-on-year [11]. This suggests an increasing trend of rougher male tapers due to the requirements set out by *CeramTec*.

2.6.6 Taper Angle and Angular Mismatch

The effect and taper angle and angular mismatch has not been extensively investigated using retrieval studies. One possible explanation for this could be the inability to measure the precise taper and angular mismatch prior to implantation.

In terms of taper angle, Morse's original design criteria was only a slight taper, whereas taper in THR tend to be much greater and vary between different manufacturers even in instances where they are considered the same type. For example, '12/14' head-stem tapers vary between 5.60 and 5.80 ° [110]. In contrast to Morse's original design criteria, a study by Kao et al. [177] reported that tapers with a greater taper angle resulted in increased evidence of fretting and corrosion.

Furthermore, taper junction in cutting applications are designed to be as conforming as possible. Angular mismatch between male and female taper is a key conformity determining factor. However, head-stem taper junctions often present a designed angular mismatch. A retrieval study by Kocagöz et al. [190] reported that there was no correlation between angular mismatch and visual evidence of fretting corrosion.

2.6.7 Head Assembly

Surgical variables, and more specifically, intraoperative head assembly has been implicated in contributing to taper degradation. To date, studies into the effect of head assembly tend to be restricted to pre-clinical experimental studies, most likely due to the difficulty in

measuring and monitoring head assembly during surgery. However, a recent retrieval study by Bormann et al. [191] found that eccentric head seating had a noticeable impact on the extent of imprinting at head taper surfaces, which could be attributed to taper degradation. Figure 2.26 shows an area of no contact attributed to non-uniform head assembly.

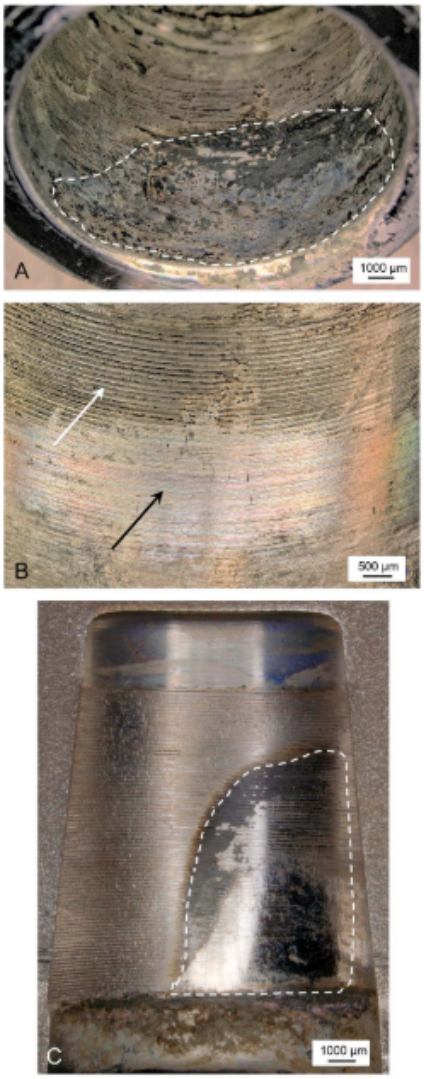

Fig. 2.26 A-C Optical images of a female taper presenting evidence of eccentric head assembly, before cleaning (A), after cleaning (B) and after sectioning (C) with dashed lines indicating a portion of no contact. Image taken from Bormann et al. [191].

Although Bormann et al. [191] has made progress in developing a clinical link between intraoperative head assembly and taper degradation, eccentric assembly is only inferred as a possible cause for the observations shown in Figure 2.26. As such, a definitive link between assembly and taper performance has yet to be established.

2.6.8 Summary

Retrieval studies generally indicates that greater head diameters, greater offsets, reduced flexural rigidity and long-smooth tapers tend to perform better. There are conflicting findings in the effect of taper length and surface topography as single design parameters. Additionally, there are limited investigations into the effect of taper angle and angular mismatch.

Retrieval studies that investigate the effect of taper design are invaluable, providing unequivocal links to their long-term clinical performance. However, they do present limitations in terms of being limited in what can be measured and controlled. More specifically, measurements and analyses are limited to after the retrieval has been effected, normally after it has failed. This presents limited insight into degradation as a function of time and into the different failure mechanisms. Furthermore, there are many factors of the investigation that cannot be controlled, making comparisons between different designs difficult. In-vitro experimental studies on the other hand, allow for greater experimental control but do require clinical validation which can be provided by retrieval studies.

2.7 Pre-Clinical Studies

2.7.1 Pre-Clinical Dynamic Simulation Assessment Methodologies

In-vitro tests provide a very strong tool in assessing taper performance by facilitating real-time measurements. However, currently the biological environment cannot be fully recreated in-vitro, where many studies have not been able to recreate the level of degradation seen in-vivo [38]. Aspects not fully considered by in-vitro head-stem simulation studies include:

- The interaction of biological processes. For example, inflammatory cells, Fenton chemistry and the availability of oxygen within the body are thought to vary significantly from that simulated in-vitro with large implications on the degradation mechanism [192–194].
- Simulations studies are often restricted to uniaxial dynamic loading with some recent studies employing ISO 14242 Part 1 [8] walking gait profile loading. However, even the ISO [8] walking gait profile can be considered conservative compared Bergmann et al. [6]'s patient derived gaits across various different daily living activities.
- THR are often in-situ for over 15 years. In comparison, long-term dynamic simulation studies normally takes somewhere in the region of two months with over

5 million cycles, thought to be equivalent to 5 years in-situ [195]. In comparison, a patient considered to have a 'normal' activity profile would present around 20.5 walking cycles over a 15 year life-span of an implant. Hence, long-term performance for implants is not fully considered during in-vitro simulation studies.

One of the earliest studies investigating the taper junction experimentally was that conducted by Brown et al. [23] in 1995. This involved immersing the taper junction in a saline solution which was electrically connected to a large surface area counter electrode via a Zero Resistance Ammeter (ZRA). The taper junction was then dynamically loaded. If upon dynamic loading the passive oxide was disrupted, a charge generated on the samples would then flow to the fully passivated counter electrode, resulting in a current that can be measured by ZRA. In 1998, three years following this study by Brown et al. [23], ASTM F1875-98 "Standard practice for fretting corrosion testing of modular implant interfaces: hip femoral head-bore and cone taper interface" [196] was published which largely formed the basis of most pre-clinical dynamic simulations studies going forward. Figure 2.27 shows a schematic of an experimental setup taken from ASTM 1875-98 [196] for one of the two methods of assessment detailed by the standard. In this instance, an ammeter measuring current, is connected to the sample (working electrode, WE) and cathode (counter electrode, CE) and the only interface that is exposed to the solution is that of the taper, facilitated by a seal.

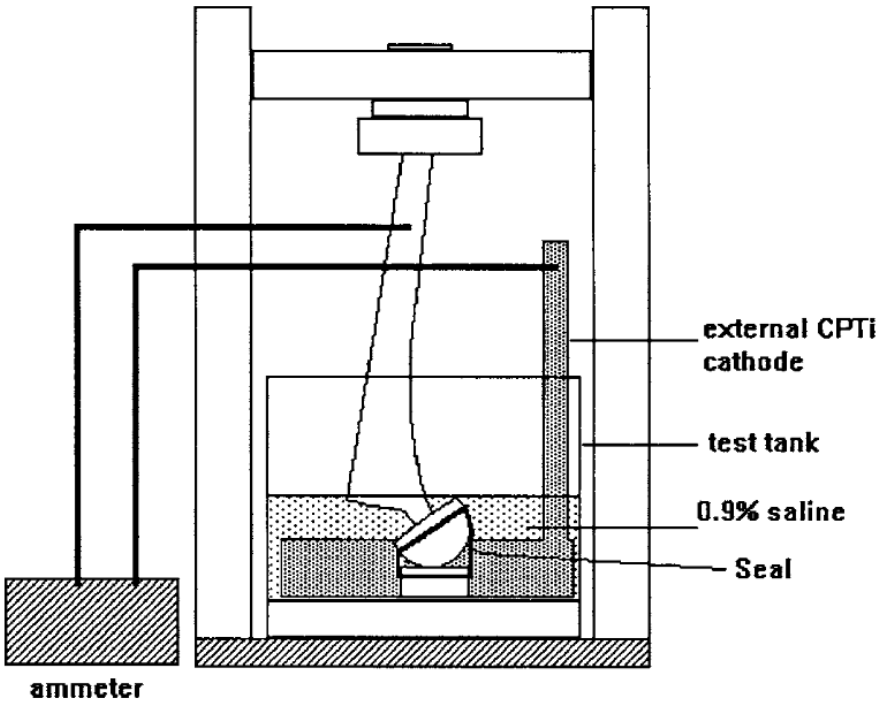

Fig. 2.27 A suggested experimental setup of uniaxial fretting corrosion tests according to ASTM 1875-98 [196].

With an orientation as shown in Figure 2.27, the samples are uniaxially dynamically loaded. The load cycling between 0.3 and 3 kN. ASTM 1875-98 [196] details two main test methodologies subject to uniaxial loading are summarised in Table 2.4.

Table 2.4 ASTM F1875-98 fretting test conditions and measurements [196].

	Summary of Method	Analysis
Method I	Long term testing to 10 million cycles at 5 Hz to study damage mechanisms using chemical and surface analysis	Chemical analysis of test fluid characterisation of particulate debris. Optical microscopy and SEM of interfaces
Method II	Short term evaluation to 1 million cycles at 1Hz to evaluate design differences using electrochemisty	**Procedure A** saturated calomel electrode OCP Potentiostatic or cyclic polarization **Procedure B** large surface area counter electrode zero resistance ammeter (ZRA)

Chemical analysis of the soluble ions released into the electrolyte has been achieved previously with the use of Inductively Coupled Plasma Mass Spectrometry (ICP-MS) techniques [197]. This is a multi-elemental analysis technique, identifying the ionic species and their respective concentrations of samples taken periodically throughout simulation.

Measurement of Open Circuit (OCP) against a reference electrode allows a semi-quantitative understanding of when this passive layer has been disrupted during dynamic loading. The OCP is the potential established between the working electrode (the metallic surface to be studied) and the environment, with respect to a reference electrode, which is placed in the electrolyte close to the working electrode [155]. A sudden decrease in OCP upon the onset of loading, and recovery upon the removal/halting of a dynamic load is associated with the disruption of the passive, discharging metal alloy-electrolyte interface and then its recovery.

Applying a voltage away from the OCP alters the anodic and cathodic reaction rate, allowing the measurement of an electrical current that can be used to better understand the reaction kinetics and corrosion rates. Within ASTM 1875-98 [196], this is achieved in three ways, Zero Resistance Ammeter (ZRA), potentiostatic and cyclic polarisation measurements. The amount of metal released due to electrochemical corrosion can then be estimated using Faraday's law, see Equation 2.10.

$$m = \frac{MQ}{nF} \tag{2.10}$$

Where:

m is the corrosive mass loss from the working electrode

M is the Atomic Mass

n is the Valence Number

F is Faraday's Constant (96,490 C/mol)

Q is the charge transfer (C)

In potentiostatic tests a selected potential is imposed on the metal across the WE and reference electrode (RE), current is measured across the WE and CE i.e. a three-electrode set-up. Depending on the potential applied (+ve anodic, -ve cathodic vs OCP) the anodic and cathodic currents can be evaluated. Current is a direct measure of metallic ion loss, where integration of current with respect to time allows charge (Q) to be calculated. Then using Faraday's law, mass loss due to corrosion can be calculated as it is directly proportional to charge.

Cyclic polarisation can be used to assess a metal's susceptibility to localised corrosion. Figure 2.28 shows a schematic of a typical cycling polarisation curve of a passive metal. The potential is 'swept' anodically until a set current density is reached which represents substantial stable pitting, and then a return scan is performed, sweeping back cathodically. The passivation potential (E_p) occurs when the current density either decreases or becomes constant for a finite period. The breakdown potential (E_b) occurs at a rapid onset of current and the region between E_p and E_b is known as the passive region. Repassivation potential (E_r) occurs when the return cathodic scan intersects back across the passive region. Figure 2.28 illustrates a typical cyclic polarisation curve, however, they can look quite different depending on the material, geometry, topography and experimental setup [155, 198, 199].

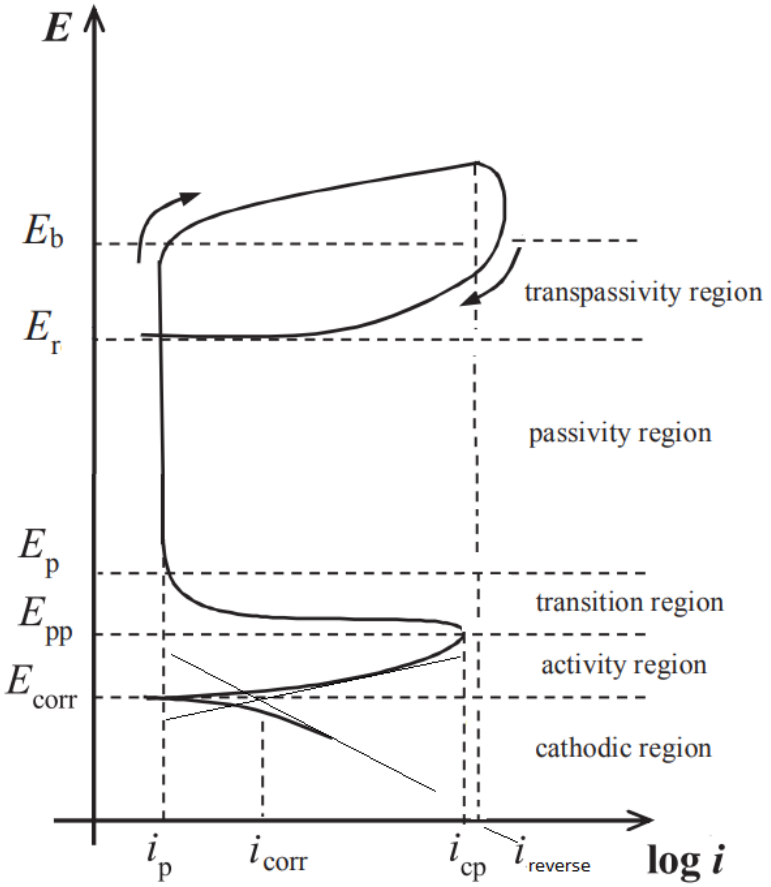

Fig. 2.28 Annotated cyclic polarisation curve. Image adapted from [200]

Although electrochemical methods to quantify fretting corrosion can be a very powerful analytical tool, applying a potential or current away from the equilibrium of a system takes the simulation a step away from that which occurs in-vivo. The electrolyte used to model the biological environment is important when trying to understand how different tapers might perform. The test fluids specified by ASTM1875-98 [196] include a NaCl solution at 0.9 % and a proteinaceous solution at 10 % calf serum and 0.9 % NaCl. The NaCl solution is indicated as being suitable for comparative studies and the proteinaceous solution more suitable for studies investigating degradation mechanisms.

While many studies employ the use of phosphate buffered saline (PBS) solutions to simulate ion concentrations present in most biological fluids, the introduction of calf serum into PBS solutions adds to the simulation models due to the presence of proteins including albumin and globulin, which have been found to alter the tribochemistry of implant surfaces [201–204]. Table 2.5 summarises some of the key components of PBS and bovine calf serum and their concentrations compared to human synovial fluid. PBS is the most commonly used test fluid in the literature as it can simulate the key inorganic components of biological fluids with a representative pH. It can also simulate the osmotic properties of biological fluids while being relatively inexpensive and easy to store and

dispose of. However, PBS is missing the organic components present in synovial fluid. Bovine calf serum solution, derived from the blood of cattle, does include the organic constituents of their blood and can be readily obtained for laboratory use with the correct storage, use and disposal management. Given that synovial fluid is an ultra filtrate of blood plasma [55], bovine calf serum should be a good simulations fluids, however there are some differences. Firstly, the total protein concentration is greater than that of synovial fluid with greater levels of albumin and globulins, bovine calf serum does not present molecules such as hyaluronic acid and lubricin secreted by the synovial membrane [47, 205]. These differences between bovine calf serum and synovial fluid, including the different concentrations of proteins and the lack of molecules secreted by the synovial membrane has been reported to alter the corrosion and tribology of these biomedical implants [206, 47].

Table 2.5 The main components reported by literature, their concentrations and pH of commonly used simulated biological fluids compared to synovial fluid.

PBS [207, 208] (g/L)		Bovine calf serum [208, 209]		Human synovial fluid [58, 60, 62, 53]	
		proteins	36-38 g/l	proteins	15-25 mg/mL
		albumin	17-23 g/L	albumin	12 ±1.4 mg/mL
		α,β,γ globulins	20 g/L	α, β, hapto - globulins	8.1 ±0.4 mg/mL
		hemoglobin	113 mg/L		
		glucose	550-1250 mg/L	glucose	95–100% of blood serum levels
				hyaluronic acid	1-4 mg/mL
		fibonectin	35 mg/L	lubricin	0.3 - 0.5 mg/mL
		creatine	27.3-31 mg/L	Phosph-olipids	0.1 mg/mL
Sodium Chloride	8	Na+	142 mmol/L	Sodium	3.3 mg/mL
Potassium Chloride	0.2	Cl-	155 mmol/L	Chloride	3.8 mg/mL
sodium phosphate dibasic	1.44	Ca+	3-3.4 mol/L	Calcium	0.06 mg/mL
potassium phosphate monobasic	0.24	K+	11mol/L	Potassium	0.16 mg/mL
		Urea	160-260 mg/L		
pH	7.4	pH	6.5-8.5 [210]	pH	7.434 ±0.017 [50]

Another environmental difference between that of the in-vitro experimental compared to in-vivo, is that the experimental studies are conducted exposed to the atmosphere. An early study by Mortia et al. [192] suggests that the much reduced availability of oxygen within the body, compared to any biological simulated solution, causes a large difference in degradation in-vivo compared to in-vitro. Oxygen is a key reactant in corrosion of medical implants and its availability has not yet been considered by in-vitro studies.

Developments in Pre-Clinical Dynamic Simulation Assessment Methodologies

Motion measurement during simulation at the taper interface has provided another layer of information. The two techniques that have been used to measure motion at the interface include non-contacting displacement sensors based on eddy current principle and image correlation [211–215, 34]. The most commonly used technique is that using eddy currents as the transducer mechanism. This has been achieved under uniaxial loading using between two to four sensors [211–214]. Figure 2.29 shows a schematic of an integrated electrochemical cell with two non-contacting displacement sensors for uniaxial dynamic loading.

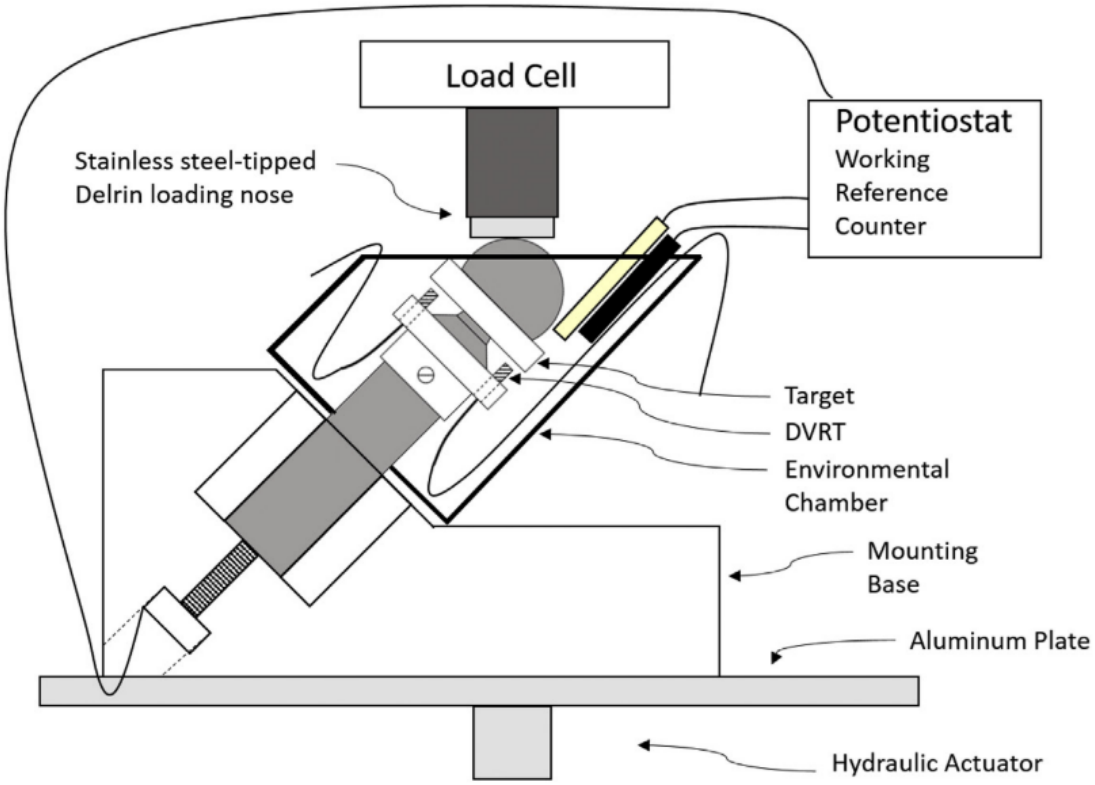

Fig. 2.29 Experimental setup of uniaxial fretting-corrosion testing incorporating both electrochemical and motion measuring capabilities. Image taken from [211]

Image correlation techniques provide a number of different benefits to eddy current sensors, including removing much of sensing equipment from the samples which can be cumbersome. However, this a relatively new technique in measurement of motion at the taper interface, with significant increase in expense and complexity for accurately resolving motions in three dimensions for a sufficient period of time [216].

Long and short term tests as detailed in Table 2.4 can take around a month/fortnight to complete respectively. Development of incremental short-term tests has been used as an efficient way to undertake comparative investigations [211, 217, 218]. The major benefit of this methodology is the assessment of tapers under a greater range of realistic loads, as informed by Bergmann et al. [6] which can be performed in a short time frame, more suitable for high resolution real-time electrochemistry and motion measurements. The key disadvantage is the limitation in understanding it can provide in the long and even medium term.

A key difference between in-vivo and in-vitro working environments is the more complex biomechanical loading compared to the simplified uniaxial profile. In-vitro simulation for measurement of taper interfaces has been largely limited to uniaxial loading. Possible reasons for this include the requirement for isolating the electrolyte surrounding the taper from the bearing surface, and avoiding any collisions between the assembly and sensing equipment, and theoretically, obscuring the camera's line of sight of the components. The most applicable standard for more complex loading to test THR systems is detailed in ISO 14242-1 [8], which is still considered to be on the conservative side compared to patient derived gaits and other daily activities such as stair climbing [6].

A recent study by Wight et al. [7] measured the fretting corrosion subject to a incrementally scaled loading profile of that detailed in ISO 14242-1 [8]. In summary, this was a double peak axial compressive load with flexion-extension, abduction-adduction and internal-external rotation. The peak axial load incremented in 100 N steps from 100N to 1,100N, and steps of 200 N from 1,100 N to 3,300 N, thus incrementally increasing the frictional torque acting about the head. Figure 2.30 shows a schematic of the experimental setup employed by Wight et al. [7]. Although the only metal-metal interface was that of the taper junction, it was noted that the bearing head was in contact with the polyethylene socket. This bearing interface being subject to sliding wear would likely contribute to the electrochemical response and so was not isolated to the taper junction.

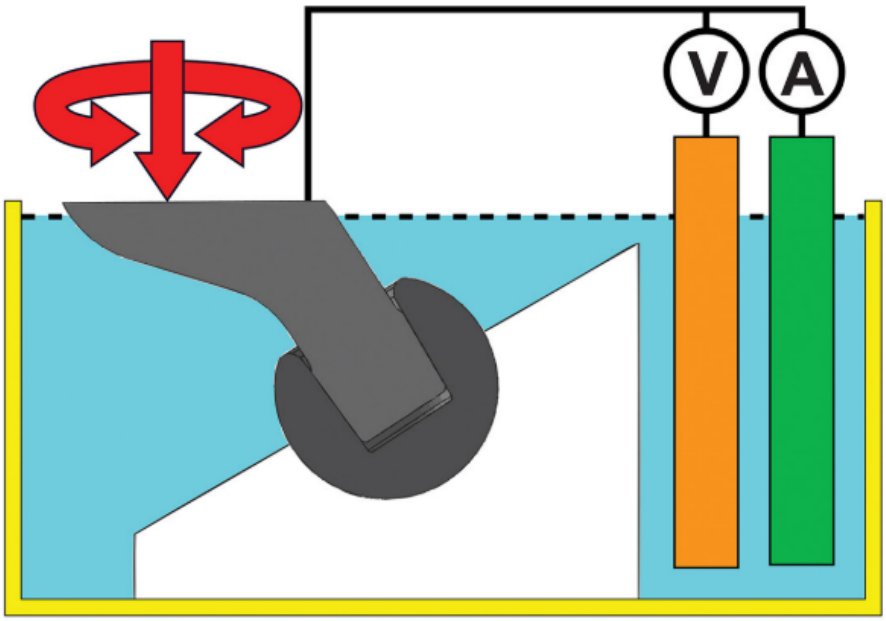

Fig. 2.30 A schematic illustrating the experimental setup of Wright et al.[7] that employed a more complex loading profile whilst measuring the electrochemical response, showing: the test sample (grey) and polyethylene socket (white) in a saline (blue) filled test chamber (yellow) with flexible cap (dotted line) containing reference electrode (orange) and counter electrode (green) connected to the test sample and subject to applied load (red). Image taken from Wright et al.[7].

Although torque will intuitively increase with increased compressive axial load, this was not measured by Wight et al. [7]. Haider et al. [219] measured the torque and calculated the subsequent resultant torque from a metal-on-polymer bearing couple using the experimental arrangement as shown in Figure 2.31 when subject to the loading profile as defined in ISO 14242-1 [8]. Resultant torque was calculated by resolving the forces and moments measured by a 6-degree-of-freedom load cell about the bearing head. Peak resultant torques acting around the head were found to be in the region of 3.6 Nm (as calculated from a frictional factor read from a graph) for metal-on-polymer bearing interfaces were completely immersed in diluted bovine serum.

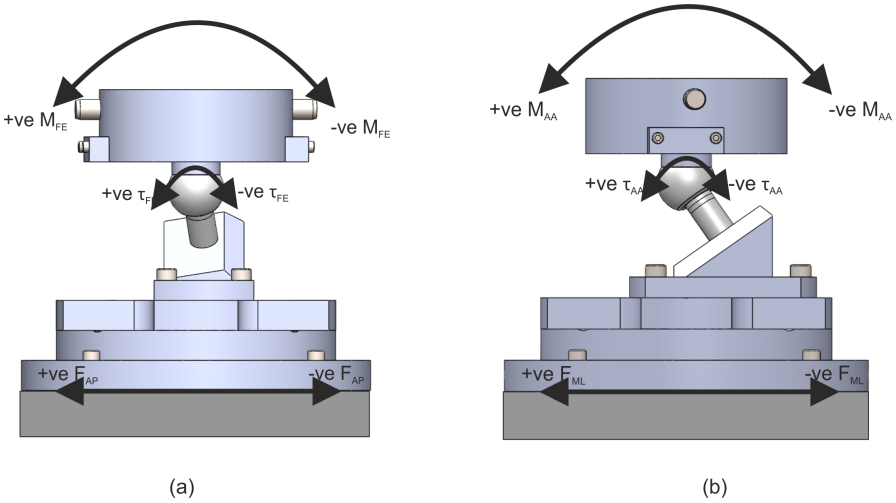

Fig. 2.31 Diagrams showing the forces and moments applied during testing of a study conducted by Haider et al. [219].

However, it should be appreciated that the ISO 14242-1 [8] was largely based on the work of Paul [65] who calculated the hip contact forces using a motion capture system and a load plate of healthy patients and not of those who had undergone THR. However, as discussed in Section 2.2.2, there are some marginal disparates between the forces transmitted through a THR and that of a healthy joint during walking [69, 70] and a greater differences between a walking gait and different daily living activities [6, 220]. Figure 2.32 shows the resultant hip contact force as predicted by Lunn et al. [220], stratified across different daily living activities and compared to that of the ISO walking gait loading scenario [8]. Whilst there is comparability in the waveforms shown in Figure 2.32a of the different walking gaits (including the ISO walking gait [8]), there were differences in peak resultant hip contact force. A greater difference in the waveform from the ISO walking gait [8] were seen in Figure 2.32b during squatting, lunging, sitting and standing.

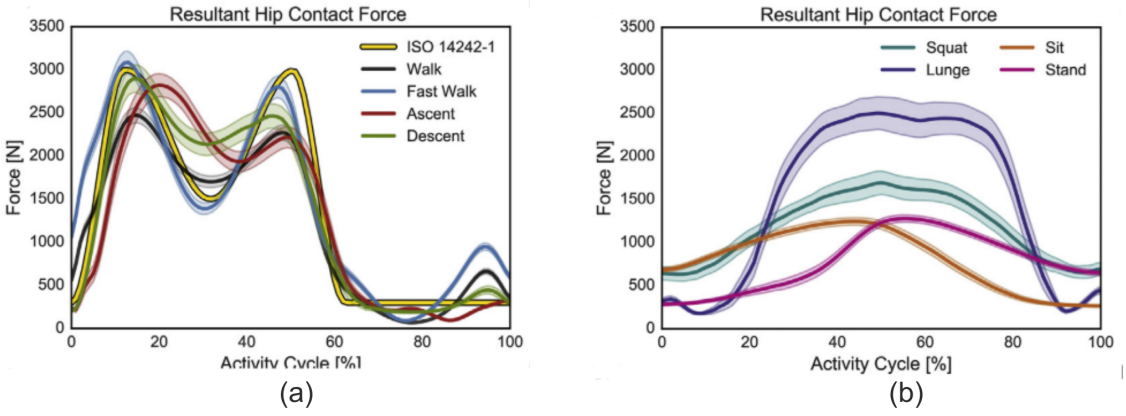

Fig. 2.32 Resultant hip contact forces predicted by Lunn et al. and stratified across different activities of daily living. Figures adapted from [220].

2.7.2 Effective Lever Arm

Using ZRA electrochemical measurement methods, Brown et al. [23] found that samples with a greater head offset presented greater current measurements, indicating a greater proportion of oxide layer disruption. This indicated that greater head offsets were more susceptible to fretting corrosion than smaller offset, in-line with that seen in retrieval studies. A more recent study carried out by Panagiotidou et al. [221] investigated the effect of head offset according to ASTM F1875-98 [196] using potentiostatic methods. Greater currents were found with greater head offsets, indicating a greater proportion of passive oxide layer disruption.

Ouellette et al. [222] also investigated the effect of head offset and head. This study measured both the electrochemical and motion response subject to incremental uniaxial dynamic loading and found that increased head offset was associated with greater currents and micro motion, indicating increased passive oxide layer disruption. It was also noted that this study employed a Design of Experiments approach to investigate the effect of seven different parameters, suggesting that head offset has a prominent effect compared to other parameters such as surface topography and angular mismatch.

Wight et al. [7] was one of the first studies to publish their work on assessing taper degradation subject to more complex loading compared to the more common uniaxial loading profiles used previously. Although larger diameter heads were found to be more susceptible to fretting corrosion, this was not attributed to frictional torque. This suggests that the bending moments experienced at the interface could play a larger role in taper degradation, as suggested in retrieval studies. Additionally, this study appeared to use ZRA electrochemical techniques where the bearing interface was exposed to the electrolyte contributing to the electrochemical response.

2.7.3 Flexural Rigidity

The study by Panagiotidou et al. [221] also investigated the effect of different material combinations and found that titanium stems showed the highest corrosion currents compared to CoCrMo when coupled with a CoCrMo head. Although the reason for this was not explored in the study, one possible explanation could be due to the lower elastic modulus of the titanium stems allowing more elastic deformation translating into greater micro motion and therefore passive oxide layer disruption, as hypothesised by retrieval studies. This was in contrast to Ouellette et al. [222]. A CoCrMo head on either a CoCrMo and titanium alloy stem has little to no correlation with the fretting corrosion or motion response.

A more recent study by Haschke et al. [213] measured the motion at the taper junction subject to uniaxial dynamic loading using six non contacting motion sensor using eddy-current formation at the transducer mechanism. Use of six motion measurement sensors allowed motions in three-dimensions to be characterised. This study found that less rigid tapers lead to increased micro motion between the head and stem. Motion measured by sensors included both elastic strain and relative motion at the taper junction. Relative motion at the taper junction was isolated by subtracting the measurements from an equivalent monobloc, as this is what is thought to contribute to fretting corrosion.

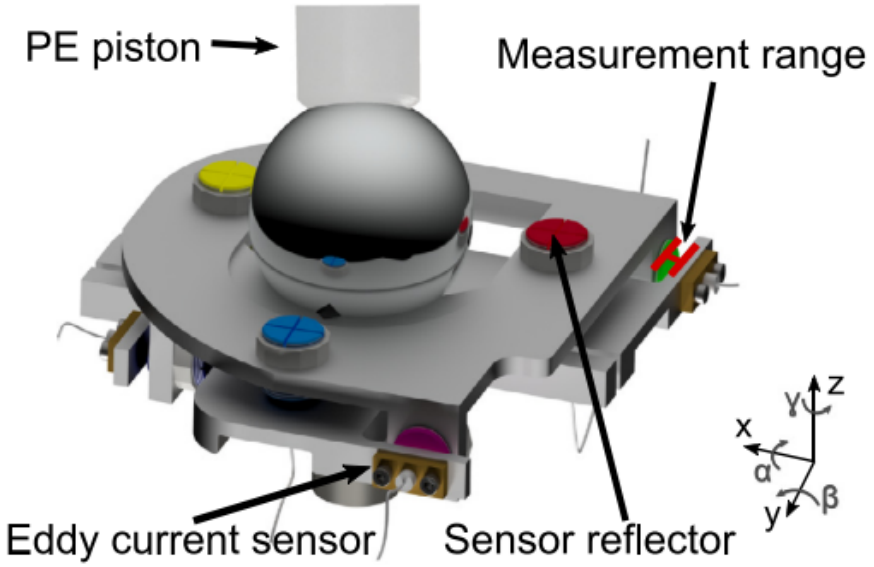

Fig. 2.33 Motion measurement setup used by Haschke et al. [213] that used six non-contacting displacement sensors.

2.7.4 Material Couple

Hallab et al. [223] investigated the effect of ceramic heads versus CoCrMo heads using electrochemical methods and measured the metal release into the test solution using a graphite furnace Zeeman atomic absorption spectrophotometer. Although both material combinations demonstrated evidence of passive oxide layer disruption, greater metal release (approximately 11-fold increase in Co and 3-fold increase in Cr) was associated with CoCrMo heads compared to ceramic. One possible explanation for superior performance of the ceramic head was that the ceramic head component does not undergo corrosion or contribute to compliance at the contact. Another explanation was that the ceramic head was better able to 'key into' the softer metal stem.

Halleb et al. [223] findings was also in-part supported by Rowen et al. [224], finding that ceramic head couples with a v40 (type of taper junction) presented a lower current

response compared to a CoCrMo head. However, an alternative '12/14' taper with a different geometry presented very comparable currents between ceramic and CoCrMo head couples, indicating a possible interaction with taper design.

Furthermore, using electrochemical techniques, Gilbert et al. [225] found that CoCrMo heads on stainless steel stems were more susceptible to fretting corrosion than CoCr heads on CoCr stems. This is interesting as CoCrMo heads on stainless steel stems is the most commonly implanted head-stem material according to the NJR [11].

2.7.5 Surface Topography and Taper length

Retrieval studies indicate that an increased roughness amplitude with shorter taper lengths were associated with increased fretting corrosion. This was supported in-vitro where Panagiotidou et al. [185] found that at low to moderate assembly forces, longer tapers with a smoother topography might perform better than shorter ones with a rougher topography [185]. However, they reported that this might not be the case for high assembly forces, in excess of 8 kN. This highlights the importance of how interacting factors can affect the fretting corrosion response. An earlier paper by the same research group reported that 'rough' threaded-type surface topography presented evidence of oxide layer disruption, while the 'smooth' non-threaded did not for tapers of the same length [226]. This supports the retrieval study by Whittaker et al. [163] reporting surface topography as a single design parameters affected fretting corrosion.

In contrast, a recent study by Ouellette et al. [222] undertook a Design of Experiments approach to investigate the effect of seven different parameters, reporting little to no correlation of surface topography with fretting corrosion and motion. At the other end of the spectrum Kretzer et al. [197] investigated the metal ion and particle release using mass spectroscopy methods and reported that an increase in release with smoother male neck-stem tapers. Where the smoothest taper with a 'total surface roughness' of 1.28 µm presented a 44 ± 45 µg release compared to the roughest with a 'total surface roughness' of 12.15 µm presented a 12 ± 7 µg release.

A more recent study by Mueller at al. [4] also measured the metal ion release and found an increase in ion release with a reduction in taper length, which is in contrast to the general consensus of retrieval studies. This finding was attributed to a lesser fluid volume inside the crevice compared to longer tapers. However, the clinical implications of this, especially on the long term performance of implants remains to be shown. Additionally, this study found that although taper roughness does not reveal any significant influence on ion release, surface topography morphology did. Surface topography with a reduction

in protruding peaks above the core roughness amplitude i.e. a more plateau-like surface, resulted in a reduction in metal ion release.

2.7.6 Angular Mismatch

Like retrieval studies, there appear to be limited experimental studies investigating the effect of angular mismatch. In agreement with retrieval studies, Ouellette et al. [222] reported little to no correlation between angular mismatch in the range of ± 0.2 ° and fretting corrosion. This suggests that the range of angular mismatch present in THR might not be as clinically relevant as other parameters that affect fretting corrosion. In contrast, a recent study by Mueller at al. [4] found that angular mismatch did have a significant effect on metal ion release. More specifically, the more proximal the angular mismatch, the greater release of metal ions. This was attributed to fluid being able to move in and out of the taper junction more freely than those with a distal angular mismatch.

There have been a greater number of computational studies reporting increased contact stress, motion and predicted wear with an increase in angular mismatch [141, 136, 227]. Additionally, there was a difference in behaviour depending on the angular mismatch and if it created a proximal (contact concentrated at the centre of the head, Figure 2.34a) or distal engagement (contact concentrated at the taper opening, Figure 2.34b). Distal engagements were reported to be present smaller taper opening gaps, thought to help resist corrosion related degradation [139]; a theory what has since been supported by Mueller at al. [4].

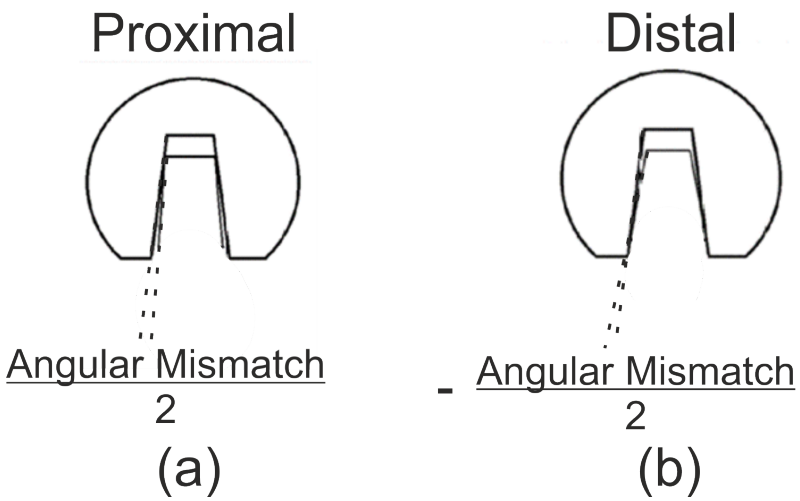

Fig. 2.34 Schematic of angular mismatch creating a (a)proximal contact and a (b) distal contact.

There does appear to be a disparity between the outcomes of the few retrievals and experimental studies with that of the computational studies. Possible reasons for this

include limitations of modelling complex conforming fretting corrosion contact in-silico and a distinct lack of controlled systematic retrieval and experimental studies. While there are limitations in undertaking a controlled investigation using retrieval studies, developments in preclinical techniques that allow real-time measurements of fretting corrosion and motion provide a powerful tool for future studies. One aspect of the complex degradation problem at the taper junction that has been accounted for computationally, is the use of a more complex biomechanical loading profile compared to the uniaxial profile used to date in experimental studies.

2.7.7 Head Assembly

Head assembly is a large variable during surgery that is not characterised or quantified and so is not validated parameter able to predict clinical performance. However, head assembly is one of the few individual factors that has been found to consistently affect taper performance in-vitro [228, 211, 229, 217, 185, 212, 230, 222, 231–233]. In summary, the studies demonstrated that increasing the assembly force of these 'self-locking' tapers increased: seating displacement [228, 211, 212, 218], disassembly force [229, 228, 230, 231, 233], engagement [232, 138], deformation at the interface [232, 138], and in the short to medium term, a reduction in the amount of motion [211, 212] and fretting corrosion [211, 222, 217, 185, 218].

Despite a high sensitivity to assembly, some studies when investigating the performance of different taper junction designs in-vitro tend to use a 2 kN axial force to comply with ISO 7206-10 [134], often under quasi-static conditions. Studies investigating the assembly forces applied by surgeons suggest a peak force of anywhere between 1-20 kN can be achieved, with an average of around 7 kN, much higher than 2 kN and very different to the quasi-static conditions employed by most studies [34–36].

2.7.8 Summary

Generally, pre-clinical studies support the findings of retrieval studies. That is, an increase in effective lever arm, decreased flexural rigidity and shorter rougher tapers were associated with increased fretting corrosion. Similarly, conflicting findings, or an unclear understanding, surround surface topography, taper length and angular mismatch. In contrast to retrieval studies, pre-clinical studies found a strong link between head assembly force fretting corrosion and motion, a parameter that is controlled in-vivo.

Pre-clinical studies offer a powerful analytical tool. However, some simplifications include simulation being limited to uniaxial loading. Assuming that tapers are designed

to operate under high compressive forces, high off-axis to taper axial force ratios that are dynamic and complex in nature could have possible implications in terms of taper performance. Furthermore, the pre-clinical studies demonstrate how different taper parameters interact, making understanding of a single design parameter difficult. For example, Panagiotidou et al. [185] found that long smooth tapers performed better at low to moderate assembly forces, but this was not necessarily the case at high assembly.

2.8 Simplified Pin-on-Disk Studies

Although pre-clinical dynamic studies using full reconstructions of the modular taper junction have provided a means of controlled investigation into different design parameters, the modes and mechanisms of how individual design parameters affect taper degradation are not yet fully understood. The lack of full understanding of how the different taper design parameters affect degradation can be attributed, at least in part, to the conformity of the taper junction. In conforming contacts, many different contacting asperities can each have differing local working conditions, and thus how material is lost from surfaces may differ within a single taper junction. Simplified pin-on-disk studies provide one tool for investigating a single point contact, proving greater control over the local working condition for investigating degradation mechanisms on a more fundamental level. Figure 2.35 shows how single asperity contacts within a taper interface can be modelled using a simplified Hertzian contact.

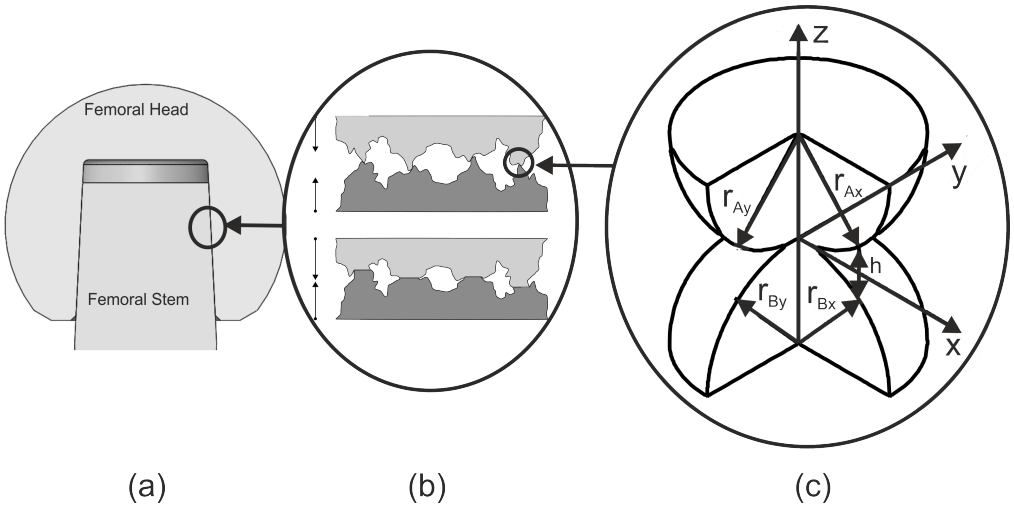

Fig. 2.35 Schematic of a contacting interface going down the length scales from (a) geometrical form, (b) contacting asperities showing deformation upon contact and (c) schematic showing a Hertzian contact model of two elastic spheres that can be used to predict the contact area at asperities.

A better fundamental understanding of degradation mechanisms can then be used to help explain what is seen in more complex dynamic studies using full reconstructions of the modular taper junction and also retrieval studies. A key limitation of pin-on-disk studies is that they do not have direct clinical applicability. More specifically, findings of pin-on-disk studies can be used to investigate hypotheses of degradation mechanisms; these tested hypotheses can then be used to help explain what is seen in more complex studies, hence they have indirect applicability which is open to interpretation.

2.8.1 Methodology

The fretting motions of a single point contact have been achieved using tribometers, an example of which is shown in Figure 2.36. The example tribometer setup shown in Figure 2.36 includes an actuator to produce oscillatory tangential displacements of the disk, a vertical (z-stage) actuator that controls the normal load (W) applied through the pin and a three-electrode electrochemical cell to measure the electrochemical response.

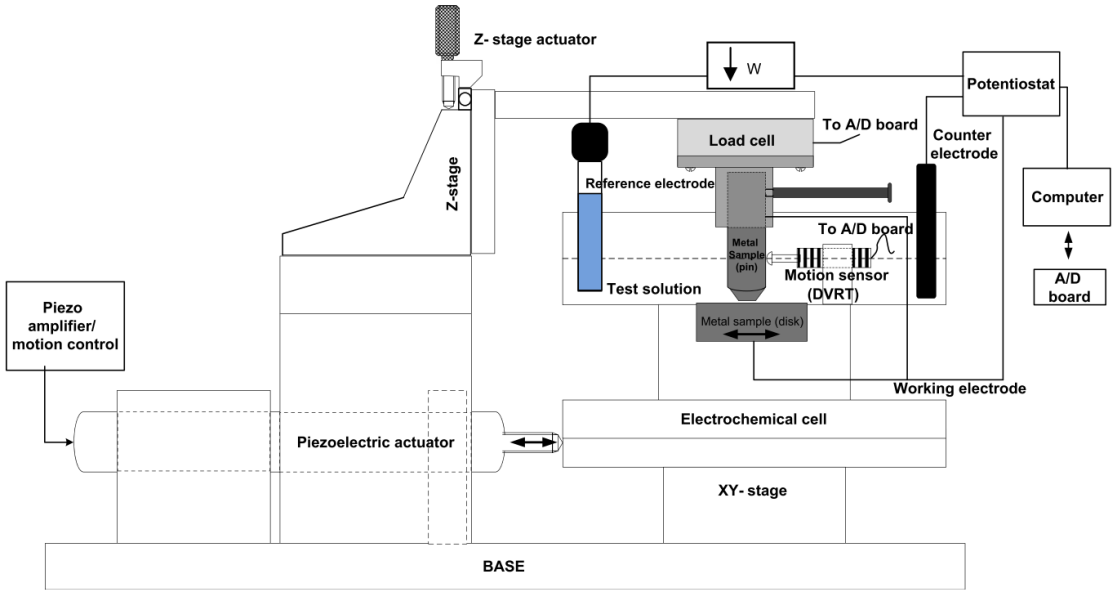

Fig. 2.36 Schematic showing the experimental set up of a pin-on-disk study actuated by a tribometer and instrumented with an electrochemical cell. Image taken from [234].

As shown in Figure 2.36, tribometers can be instrumented with three electrode electrochemical cells, other measurements include pre- and post- surface analysis and continuous solution sampling. Such electrochemical, surface and solution analysis methodologies include those discussed in Section 2.7.

One of the key advantages of simplified pin-on-disk tribometer studies includes accurate control of the actual contact area (A). As shown in Figure 2.35b, the actual area of contact

is very different from that of the apparent area by virtue of surface roughness (micron scale asperities). Considering a single contacting asperity junction in isolation (i.e., a point contact), actual area of contact can be predicted by Hertzian theory of deformation between two elastic spheres (Figure 2.35c). Where actual contact area (A) is proportional to applied normal load (W) as detailed by Equation 2.11, assuming no plastic deformation [235].

$$A = \left(\frac{3WR}{4E'}\right)^{1/3} \tag{2.11}$$

Where:

R = Effective radius (m)

E' = Effective modulus (Pa)

The effective radius can be calculated from Equations 2.12 to 2.13.

$$\frac{1}{R} = \frac{1}{R_x} + \frac{1}{R_y} \tag{2.12}$$

$$\frac{1}{R_x} = \frac{1}{r_{Ax}} + \frac{1}{r_{Bx}} \tag{2.13}$$

$$\frac{1}{R_y} = \frac{1}{r_{Ay}} + \frac{1}{r_{By}} \tag{2.14}$$

The effective modulus can be calculated from Equation 2.15.

$$E' = \frac{2E_A E_B}{(1-{v_a}^2)E_B + (1-{v_b}^2)E_A} \tag{2.15}$$

The mean contact pressure (p_{mean}) of a Hertzian contact can be determined by Equation 2.16. Resolving Equations 2.11 and 2.16, mean contact pressure is proportional to the cubed route of normal force. Hence, increasing normal force increases contact area yet also causes an overall increase in contact pressure.

$$P_{mean} = \frac{W}{\pi A^2} \tag{2.16}$$

As discussed in Section 2.5.1 and shown in Figure 2.16, a Hertzian fretting contact in the PSR presents a central stick region surrounded by an outer slip annulus, as predicted by Mindlin [144]. The ratio of the central stick radius (a') to the overall contact radius (A) can be used to determine which fretting regime occurred. Assuming a Hertzian contact, Mindlin's elastic model for fretting contacts can be applied, Equation 2.17. Where a ratio of stick radius to contact radius of zero would indicate critical GSR conditions and a value greater than zero but less than one would indicate PSR. Finally, a ratio of one would indicate the SR.

$$\frac{a'}{A} = \left(1 - \frac{Q}{\mu W}\right)^{1/3} \tag{2.17}$$

A major limitation of pin-on-disk studies include the compliance in the tribometer itself. This is particularly important at high normal forces were compliance of the test rig can affect the applied tangential displacement compared to what is actually being transferred to the interface.

2.8.2 Contact Pressure and Displacement Amplitude

Transition between the different fretting regimes for a given contact is governed by normal load and tangential displacement. As predicted by Equation 2.17, an increase in normal load (W), and therefore contact pressure, results in an increase in the ratio of the central stick radius (a') to the overall contact radius (A), tending towards the SR. On the other hand, an increase in tangential displacement (Q) results in a decrease in the ratio of the central stick radius (a') to the overall contact radius (A), tending towards the GSR. Transition from PSR to GSR can be achieved by either increasing tangential displacement above a critical amount to overcome the dominant elastic deformation of the contact under a constant normal load or decreasing normal force below a critical amount with a constant tangential displacement. Figure 2.37a shows normal force versus tangential displacement maps setting out the transition boundaries between the different regimes. Figure 2.37a also indicates an additional fretting regime, the mixed fretting. During constant working conditions, the nature of the contact can vary with increasing number of cycles due to

degradation. This can cause transition from the GSR to the SSR or vice versa around the critical transition points, this is known as the mixed fretting regime [236].

As discussed in Section 2.5.1, the different fretting regimes are associated with different degradation mechanisms. The PSR is often associated with fretting fatigue crack formation due to cyclic loading of contacting asperities and the GSR with fretting wear or particle detachment. Figure 2.37b, like Figure 2.37a shows normal force versus tangential displacement graphs, but maps out the boundaries between the different material responses.

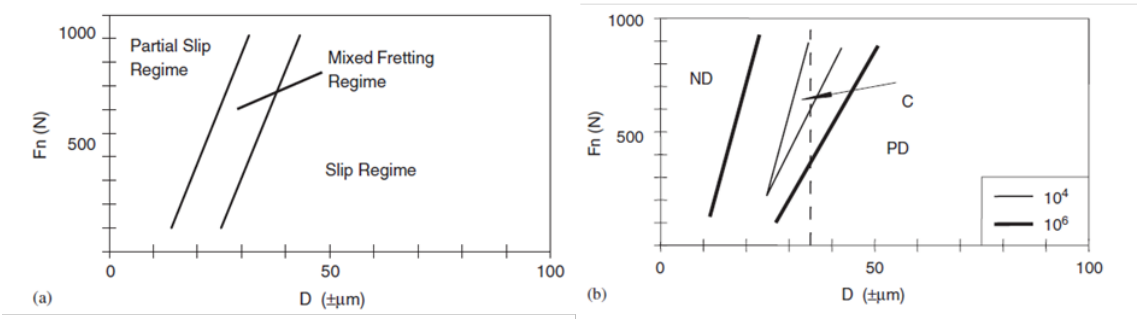

Fig. 2.37 (a) Fretting maps with normal force plotted against slip displacement (a) Running condition fretting map, where Partial Slip Regime is the SSR. (b) Materials response fretting map where ND= no degradation, C = cracking and PD = particle detachment. Image taken from Zhou et al. [143].

In fretting corrosion contacts, the different fretting regimes have also been found to alter the mechanical-chemical response. The mechanical-chemical material loss model as put forward by Watson et al. [237], is explained below.

Total mass loss (M_{total}) is the sum of the mechanical (wear, M_{mech}) and chemical (corrosion, M_{chem}) components, as per Equation 2.18:

$$M_{total} = M_{mech} + M_{chem} \tag{2.18}$$

Each of the mechanical and chemical components each have a pure mechanical and chemical material loss components associated respectively, and synergistic components (Equations 2.19 and 2.20). The synergistic components for the mechanical mass loss will be defined as corrosion enhanced wear (M_{cw}) and the component for chemical material mass loss, wear enhanced corrosion M_{wc}:

$$M_{mech} = M_{wear} + M_{wc} \tag{2.19}$$

$$M_{chem} = M_{corr} + M_{cw} \tag{2.20}$$

A study by Bryant and Neville [238] undertook a pin (CoCrMo)-on-disk (CoCrMo) study that investigated the above mechanical-chemical model as a function of tangential displacement and contact pressure. Figure 2.38 shows a map of the dominant degradation mechanism and fretting regime of the contact as a function of the tangential slip (S) to tangential displacement (D) ratio (S/D) and contact pressure. There was an increased tendency for wear (mechanical) degradation mechanisms to dominate with increased tangential slip displacement and reduced contact pressure, i.e., the GSR. On the other hand, corrosion (chemical) degradation mechanisms tended to dominate with reduced tangential displacement.

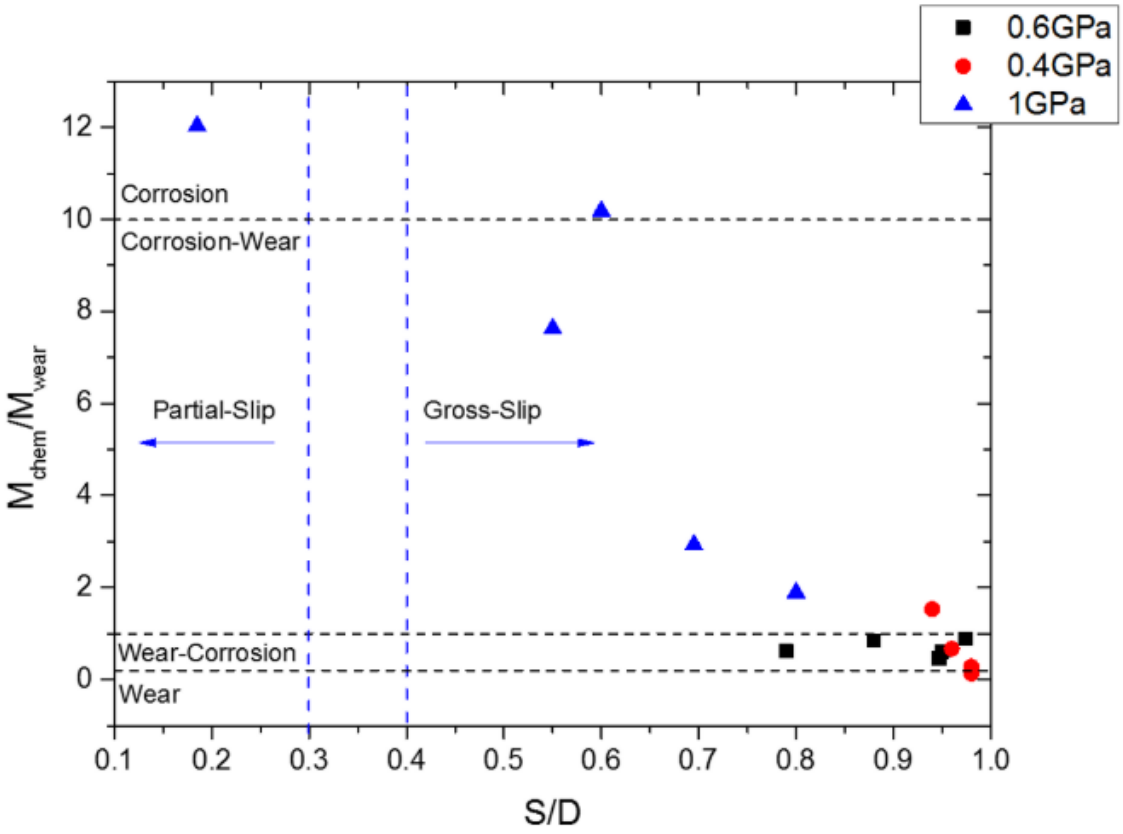

Fig. 2.38 Map of the dominant degradation mechanisms as a function of tangential slip to tangential displacement ratio and contact pressure. Image taken from Bryant et al. [238].

Although the trends noted by Bryant and Neville [238] were only supported by a single data point in some instances i.e., only one data point in the PSR, findings from this study were supported by others. Firstly, the study by Hothi et al. [239] found that the head-stem taper junction presented more corrosion dominant degradation mechanisms compared to the bearing interface that experienced reciprocating sliding. This finding supports that

found by Bryant and Neville [238] of increased wear dominated degradation mechanisms with tangential slip displacement.

Additionally, total mass loss, due to both corrosion, wear and corrosion-wear mechanisms, were found to decrease with an increase in contact pressure and a decrease in tangential displacement, associated with reduced fretting wear and oxide abrasion [238]. This finding is in line with the long standing work of Vingsbo and Söderberg[142] and that of more recent tribocorroion models [240].

Other studies that support the findings of Bryant and Neville [238] is that of Swaminathan et al. [234], the results of which will be discussed below in terms of contact compliance.

2.8.3 Material Couples

The SR is associated with being able to support the tangential displacement by the elastic compliance of the contact. The PSR accommodates tangential displacement by the plastic and elastic compliance of the contact and partial slip of a contact interface. Finally, the GSR supports tangential displacement by the plastic and elastic compliance of the contact and the gross slip at the interface [142]. As such, the elastic and plastic compliance of the different materials also plays a role in what fretting regime is experienced at an interface.

One such study that found different fretting corrosion responses with different material couples was that of Swaminathan et al. [234]. This was a pin-on-disk study that investigated the fretting corrosion response of Ti6Al4V-on-Ti6Al4V, Ti6Al4V-on-CoCrMo and CoCrMo-on-CoCrMo material couple contacts, immersed in PSB using potentiostatic methods. They allowed the samples to reach equilibrium in an open circuit for 10 minutes before applying a fixed potential of 0 V Ag/AgCl, which was justified as being close to typical open circuit potential of these alloys in PBS. However, in comparison to Songür et al. [3] who investigated the corrosion potential of these alloys, reported an open circuit potential of around -0.156 V for CoCrMo and -0.129 V for Ti6Al4V, indicating an over potential of 156 mV and 129 mV was applied by Swaminathan et al. [234] for CoCrMo and Ti6Al4V, respectively.

Referring now to Figure 2.39, a key finding of Swaminathan et al. [234], was that irrespective of material couples, at low contact pressures, current increased with an increase in contact pressure. This was associated with the an increase in oxide abrasion due to increased contact area that overcame the yield point of the surface (i.e., hardness), while the contact was in the GSR. With a further increase in contact pressure, a decrease in current was observed. This was associated with a transition from GSR to the PSR and a

decrease in oxide abrasion as more tangential displacement was accommodated by the material response.

Bringing material couples back into the equation, the point at which current stopped increasing with contact pressure and started to decrease was lower for the more compliant material couples. Furthermore, the most compliant and highest coefficient of friction (i.e., ratio of tangential force to normal force) contact couple of Ti6Al4V-on-Ti6Al4V, presented the greatest increase in current with an initial increase in contact pressure. The weaker and more brittle oxide layer that forms on Ti6Al4V compared to CoCrMo was also implicated in the possible explanation as to why the Ti6Al4V-on-Ti6Al4V couple presented greater currents are lower contact pressures.

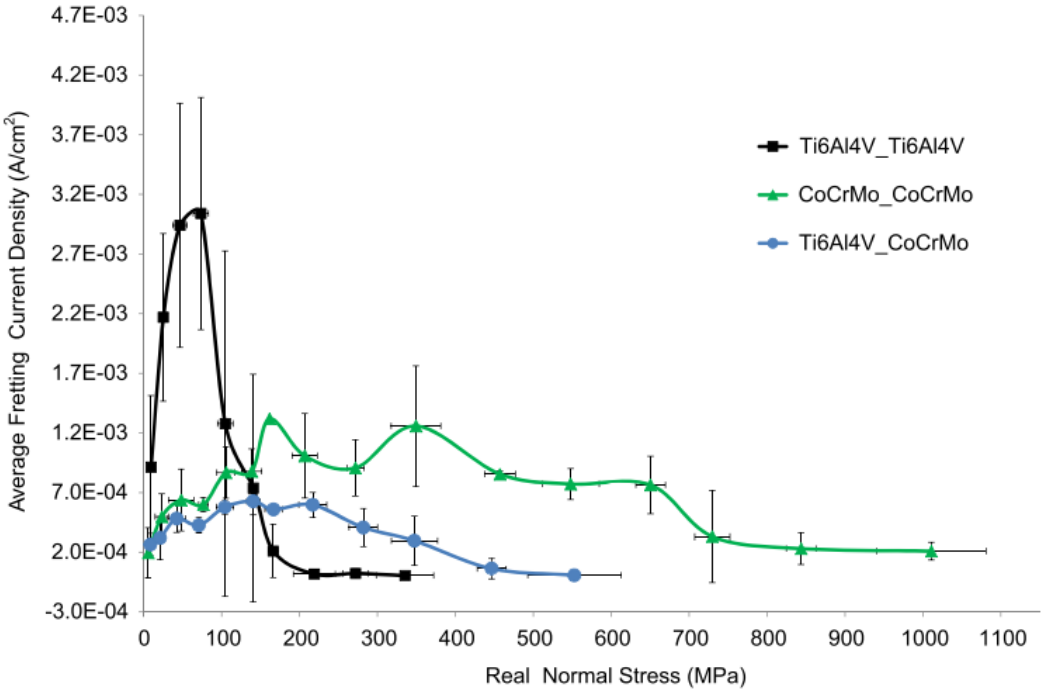

Fig. 2.39 Average fretting current density vs. real normal stress obtained for different alloy combinations. Image taken from [234].

The above trends were also supported by a more recent study by Mali et al. [241] which also investigated stainless steel material couples. More specifically the material couples included 316L stainless steel-on-316L stainless steel, Ti6Al4V-on-316L stainless steel and CoCrMo-on-316L stainless steel (SS316L). Mali et al. [241] found that Ti6Al4V-SS316L demonstrated the highest fretting current densities, attributed to a higher coefficient of friction and a weaker surface oxide film resulting in increased oxide abrasion. On the other hand, couples with CoCrMo and 316L-stainless steel presented lower currents, associated with stronger oxides.

In summary, the surface mechanical properties and corrosion properties are important for fretting corrosion contacts and although Titanium alloys present a higher resistance to static corrosion than CoCrMo, CoCrMo demonstrates a harder, more strongly bonded surface oxide [242]. The ability for the enhanced mechanical properties of the CoCrMo oxide to provide some level of protection against fretting corrosion depends on a number of factors, including which fretting regime is experienced at a given contacting asperity [242, 234, 241]. In other words, the more compliant interfaces such as the Ti alloy interface, can help reduce the level of gross slip if there is a sufficient normal load and small enough tangential displacement, giving rise to the PSR or even SR as opposed to the GSR [234]. However, if the GSR occurs, harder more wear resistant surfaces could offer a greater level of protection.

2.8.4 Surface Topography

As discussed in Swaminathan et al. [234] and Mali et al. [241], the coefficient of friction also plays a role in the fretting corrosion response for a given contact.

Friction is the resistance to motion as one surface moves tangentially over the other [145]. There are different proposed mechanisms of what gives rise to friction in a dry contact. Bowden and Tabor[243] present two mechanisms of dry friction including adhesion between two contacting asperities, and ploughing as the harder asperities penetrate and plastically deform the softer surface. These are simplistic models of a complex surface interaction that occurs on an atomic level [145].

Assuming that friction arises from adhesion, ploughing or a combination thereof, increased contact area would intuitively increase friction. However, as shown pictorially in Figure 2.35, contact area is but a fraction of the apparent area of contact, and is rather a function of normal force (Equation 2.11). It is generally accepted that friction is very much related to the real contact area [244].

Using the Hertzian model of elastic deformation to predict actual contact area (Equation 2.11), frictional force should be proportional to the two-thirds power of the normal load. However, Amonton's first law states that frictional force is directly proportional to the normal load. It is thought that local plastic deformation at asperities upon the application of load occurs to that point at which load can be supported elastically. In practice, as the surface approach one another there is an increase in the number of contacting asperities. Multiple contact points of a real 'rough' surface within a given contact (i.e. Hertzian contact superimposed upon a Hertzian contact) could contribute to a more linear relationship between normal force and frictional force [235, 244]. Note that the proportionality constant is termed the coefficient of friction (μ).

Given the above brief explanation of friction, surface topography (i.e., the shape and density of the contacting asperities) is therefore a parameter thought to affect the fretting corrosion response of an interface. Smith et al. [245] investigated the effect of surface topography of a single point contact by altering the dimensions using potentiostatic methods, and therefore compliance, of a pin which was fretted against a flat disk. This study found that more compliant contacts, by virtue of thin long point contacts, experienced transition from the GSR to the PSR at lower normal forces, and lower currents were measured with contacts in the PSR.

Figure 2.40 shows schematically how the thinner, longer and therefore more compliant contacting asperities are less able to resist deformation and present a lower interfacial slip and thus, less oxide abrasion. On the other hand, the stiffer contacting asperities by virtue of a wider and thicker asperity is better able to resist deformation and hence tangential motions are accommodated by slip at the interface and thus, oxide abrasion.

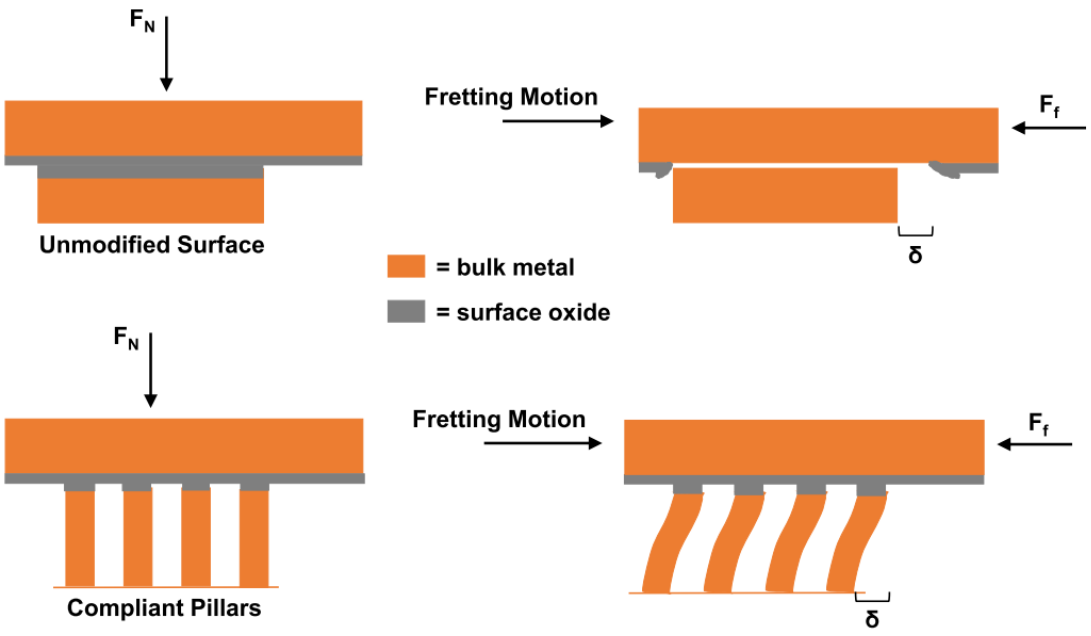

Fig. 2.40 Top diagram showing a schematic of the GSR associated with a less compliant contact interface and associated oxide (grey) abrasion. Bottom schematic with a more compliant contacting interface in either the SR or the PSR with tangential fretting motion being accommodated by the material response. Image taken from [245].

One key limitation of Smith et al. [245] was the short term nature of the study over only 1,600 cycles. Although the more compliant contacts were associated with less oxide abrasion and fretting corrosion, the prevalence of crack formation and fretting fatigue associated with the PSR has been reported to be prominent over a much greater duration [246]. A later study by Smith et al. [247] attempted to address this by conducing a similar investigation to their earlier study but over 1 million cycles under a constant normal force.

They found that the current response was very much associated with slip at the interface, such that before 0.2 million cycles, the high compliance contact (long thin contacts) capable of accommodating the PSR/SR demonstrated smaller currents due to less oxide abrasion. Beyond 0.2 million cycles, the higher compliance contacts did present some slip which was associated with third body oxide debris being trapped in the interface and resulted in an increase in current. The remainder of the study saw that all the compliance groups in the PSR/SR regime, and thus low current measurements. Further to the particle detachment in the high compliance group, surface analysis also found crack formation at the contacting interface. This indicates that although the current response was associated with mechanical abrasion of the surface oxide, degradation for contacts within the PSR is not wholly unavoidable and more prevalent in the long term.

The two studies above by Smith et al. [245, 247] investigated a single points contact with different geometries to alter the contacts compliance. However, the effect of different surface topographies in a conforming contact can alter, not only the shape of a single asperity in isolation, but also the interaction of neighbouring contacting asperities. For example, if surrounding contacts support more of the normal load, the normal load experienced by that asperity is reduced, and thus altering the fretting corrosion response.

Royhman et al. [248] investigated the effect of a machined surface compared to a polished surface of a flat-on-flat fretting contact using potentiostatic methods. This study reported that, although the electrochemical tests showed that the rougher 'threaded' samples were more susceptible to fretting corrosion compared to the 'smooth' samples, the rough also presented a lower dissipated energy (i.e., less inter-facial slip). This lower dissipated energy was said to be indicative of a more compliant contact, suggesting less mechanical damage to the surface which is in contrast with higher currents measured in the electrochemical tests suggesting a greater damage to the passive oxide layer. Upon inspection of the results, it was noticed that although the rougher samples presented much higher contact pressures, all sample groups experienced the GSR. Therefore, the reduced current measured with increased contact pressure due to altering the prevailing fretting regime was not achieved in this study compared to the Smith et al. studies [245, 247].

A gap in the current literature would appear to be if surface topography in the taper junction of THR can be altered to increase the local contact force of a given contacting asperity to achieve the PSR and therefore reduce the susceptibility to fretting corrosion in conforming contacts.

2.8.5 Summary

This section of the literature review looked into simplified pin-on-disk tribometer studies in an attempt to further elucidate the different degradation mechanisms associated with different taper interface design parameters. With clinical and pre-clinical studies generally agreeing that increased fretting corrosion was associated with:

- an increase in effective lever arm;
- a decrease in flexural rigidity; and
- shorter rougher tapers.

On the other hand, clinical and pre-clinical studies generally lacked a common consensus associated with:

- surface topography as a parameter in isolation;
- taper length as a parameter in isolation; and
- angular mismatch.

In contrast, pre-clinical studies found a strong link between head assembly force and fretting corrosion and motion. Whereas head assembly is not a parameter that is controlled intra-operatively, and hence not a parameter found to affect the results in clinical studies. That said, there will be inherent variability in clinical studies due to variations in the surgical assembly process.

Clinical and experimental variability coupled with the complex nature of a compliant fretting contacts means the effect of different taper designs on degradation mechanisms is not yet fully elucidated. Simplified pin-on-disk studies offer greater experimental control to help bridge gaps in understanding from clinical studies and pre-clinical simulation studies using full head-stem reconstructions.

Simplified pin-on-disk studies found that if sufficient normal force and compliance of a contacting asperity can be achieved, such that the PSR or the SR can be achieved, this was associated with reduced oxide abrasion and was an indication that such contacts are less susceptible to fretting corrosion. Compliance of a contacting asperity is governed by the mechanical properties of the bulk material, the surface oxide layer, the bond between the oxide layer and the underlying bulk material and the geometry of the asperities. However, complete elimination of gross-slip from fretting regimes does not eliminate

fretting corrosion at the interface with the PSR being associated with fretting fatigue and more insidious degradation mechanism, more apparent over longer durations.

A limitation of pin-on-disk studies is that there is no direct applicability of the results from more complex studies that use full head-stem reconstructions. Rather, the results can only be used to help construct possible theories on the different degradation mechanisms occurring at the head-stem taper junction in both experimental studies and in-vivo. There is a gap in current literature with sufficient supporting evidence regarding if the taper junction can be adapted to optimise the fretting corrosion response using findings from pin-on-disk studies, and even if it can, what the short, medium and long term effects of doing so are.

2.9 Overall Summary of Current Literature

The aim of this present section, was to review the current literature that investigated the effect of different taper design parameters in the head-stem modular junctions, and establish the state of the art with respect to how they are tested and what the current understanding is of how design parameters affect degradation mechanisms. To do this, the review was split into sections. First, a brief overview was provided of the hip joint, the total hip replacement and then the clinical problem associated with the head-stem modular taper junction. Thereafter, a more focused review was performed of studies that investigated the effect of different taper designs on the performance of the taper junction. This was done by focusing on retrieval studies, after this, pre-clinical simulation studies that employed full reconstructions of the head-stem taper, and finally looking towards simplified pin-on-disk studies to help elucidate specific degradation mechanism associated with different taper designs.

Each of the different types of studies present their own strengths and limitations. Some of the key benefits and limitations are summarised below:

- Retrieval studies:
  - findings have unequivocal links to clinical performance; yet
  - limited experimental control;
- Pre-clinical head-stem simulation studies:
  - good experimental control; yet
  - the in-vivo biological loading environment has not yet been fully recreated; and

  - there are incomplete explanations for all findings due to the complex nature of such a conforming fretting corrosion contact;

- Simplified pin-on-disk studies:

  - extremely good experimental control with simplified contacts for more complete specific explanations; yet
  - they are not directly applicable to full head-stem simulation studies nor retrieval studies.

An area of study that has not been investigated in any great depth in this review is in-silico studies. Computational studies offer even more experimental control over simplified pin-on-disk studies but can be considered over idealised with limited applicability to that seen in practice. A good investigation might employ all four different techniques to investigate a single parameter to help develop more fully supported explanations of their findings.

Between the clinical, pre-clinical full head-stem reconstruction simulation studies and simplified pin-on-disk studies, it was generally agreed that:

- more extreme loading conditions resulted in an increased susceptibility to fretting corrosion associated with greater micro motion and applied loads at the taper interface for increased oxide abrasion experienced at the taper junction, demonstrate by:

  - clinical studies finding increased taper degradation with increased head diameters, head offsets and flexural rigidity;
  - pre-clinical head-stem simulation studies also finding evidence of an increase susceptibility to fretting corrosion with increased effective leaver arm (i.e., head diameter and offset) and flexural rigidity;
  - simplified pin-on-disk studies findings of increased oxide abrasion with increased contact area (a function of applied force) and tangential force/displacement with the contacts in the GSR.

- Longer taper junctions, with smoother surface topography were found to experience less surface oxide abrasion compared to shorter rougher taper junctions, attributed to reduced contact pressure at thread peaks and less micro motion, this was demonstrated by:

  - clinical studies finding less taper degradation with longer and smoother tapers;

  - pre-clinical head-stem simulation studies also reporting reduced evidence of oxide abrasion with longer and smoother tapers; and
  - although pin-on-disk studies cannot directly investigate the effect of taper length and surface topography, support could be assimilated to findings of less oxide abrasion associated with lower normal forces if in the GSR (possibly like that experienced at the contacting asperities of surfaces with smoother surface topography), and smaller tangential displacements (assuming the explanation provided by pre-clinical head-stem simulation studies of longer tapers being better able to resist toggling motions is correct).

Areas of uncertainty surround the effect of surface topography and taper length independently, this was demonstrated by:

- no studies having established an experimental link between taper length and micro motion; and
- studies that employ full head-stem geometries have not yet found if surface topography (individual contact compliance) can be altered to achieve the PSR in a sufficient number of contacting asperities in the conforming taper junction interface to reduce oxide abrasion and thus, the fretting corrosion response.

Other areas of uncertainty surround the clinical effect of head assembly, although pre-clinical studies unanimously agree that greater assembly forces are associated with a reduced susceptibility to fretting corrosion, this is not yet a clinically validated finding.

Taper design parameters that lack experimental research, include annular mismatch and taper angle. In terms of taper angle, there is a large discrepancy between THR head-stem taper angle and that originally intended by Morse. Additionally, there does not appear to be any sort of consensus within the literature about the effect of taper angle. Similarly, there is generally a lack of experimental studies that have investigated the effect of angular mismatch in THR. Although it has been hypothesised that less angular mismatch could help reduce micro motion at the interface (as per computational studies) and therefore result in less oxide abrasion, it is also hypothesised that a distal angular mismatch may help create a seal, inhibiting corrosion.

Given the above referenced lack of clarity, areas of new research to address such gaps in the literature include:

- identifying how, and indeed if, surface topography in conforming head-stem taper junctions can be altered to achieve the PSR so as to reduce the prevalence of oxide

abrasion, including how variations in surface topography influence degradation as a whole i.e., wear, wear-corrosion and corrosion mechanisms;

- investigating, if any, the experimental relationship between taper length, micro motion and fretting corrosion in isolation;
- using full head-stem reconstructions of the taper junction to experimentally investigate the how taper angle influences the compressive fit, micro motion, fretting corrosion and more generally the degradation mechanisms; and
- using the common consensus reached on the effect of angular mismatch by computational studies, investigate the relationship between angular mismatch, taper engagement, micro motion and fretting corrosion.

A common problem when conducting retrieval and in-vitro experimental studies, which is less of a concern in computational studies, is that varying a single design parameter could have competing effects which make it difficult to elucidate the results. For example, comparing the influence of a stem manufactured from Ti6Al4V with a stem manufactured from 316-L stainless steel:

- the overall system compliance of Ti6Al4V, could increased the magnitude of micro motion transferred the taper junction during dynamic loading compared to the stiffer steel alloy, as per [1, 172, 170, 177, 178];
- contact compliance is smaller in Ti6Al4 which may help to engender a higher proportion of contacting asperities in the PSR for reduced oxide abrasion and fretting corrosion, as per [241]; and
- better corrosion resistivity of Ti6Al4V.

Hence, although the areas of research that would prove fruitful in addressing the aforementioned research gaps have been itemised as discrete points, a systematic approach, identifying how each of these factors interact would appear to provide the most impact in informing an optimised taper design.

Chapter 3

Variation of Clinically Available Modular Tapers

3.1 Introduction

Engagement is a key parameter of taper junctions and is sensitive to design and manufacturing tolerances. Historically, great lengths were gone to ensure cylindrical accuracy. For example, from the early 1900s hardening was undertaken for a number of reasons, including: to increase stiffness and to reduce damage due to handling and fretting from mismatched mating surfaces; but primarily for cylindrical accuracy for increased conformity between the two surfaces [108].

Engagement is usually parametrised by angular mismatch, taper length and surface roughness [226, 177, 229, 249, 110, 184]. With a lack of standardisation of tapers in THR, there is a large variation in these design parameters between different manufacturers, that also differ somewhat from taper designs in other industries. One reason for the failed attempts to draw up a suitable standard was the lack of complete characterisation [250].

As the variations in head-stem taper design and manufacturing tolerance are not publicly known, the aim of this study was to fully characterise the variety of modular head-stem tapers currently on the market in clinically available THR in terms of geometry and topography. This was achieved by using two techniques, a coordinate measurement machine, used to measure geometry and any deviations in form, and vertical scanning interferometry (VSI) to capture the characteristics of surface topography. Such techniques have been used by studies such as Mueller at al. [110] and Munir et al. [184] who have previously characterised the geometry and surface topography of taper interfaces in clinically available samples.

Key geometrical parameters identified in previous studies that were also utilised in this present study include taper angle and angular mismatch, key parameters of engagement for taper junctions [107]. Similarly, key surface topography parameters used by previous studies and measured in this present study include mean roughness amplitude, core roughness amplitude, maximum profile height, skewness, kurtosis, peak density and the pitch of male tapers that presented a 'threaded' finish. Other parameters not often used by other studies yet presented in this study include deviation from the 'ideal' cone geometry surface maps generated from the CMM data and peak density captured using VSI data. The use of deviation from the 'ideal' cone was to help span the gap in characterising parameter across the length scales and namely between those measured using the CMM (macro-scale) and VSI (micro-scale). This allowed 'straightness' and 'roundness' to be parametrised, again, key parameters in dictating the conformity at taper junctions used in industry [107]. The methodology in determining these deviation maps was akin to studies that measured volumetric losses using CMM, whereby an 'ideal' cone geometry (or more broadly 'unworn' geometry) is fitted to a point could of data and deviations normal to the surface of this 'ideal' cone was then plotted as a three dimensional surface plot [164, 168, 251].

Outcomes from this study were then used to quantify the range of variation of different taper designs in terms of manufacturing tolerances and design selection of different manufacturers. This variation was then used to inform test sample design for future studies and to allow for a more descriptive link between taper design, engagement, motion and fretting corrosion.

3.2 Materials and Methodology

Geometrical measurements were taken using a coordinate measurement machine (CMM, Legex 322, Mitutoyo, Japan) with an accuracy (maximum possible difference from the true value being measured) being a function of distance travelled, governed by Equation 3.1.

$$T = \frac{0.8 + 0.2L}{100} \tag{3.1}$$

Where:

- T = Length measurement tolerance (µm)
- L = Measuring length (mm)

Topographical measurements were taken using a vertical scanning interferometer (VSI, NPFlexTM, Bruker, USA). The study included twelve different commercially available male tapers and six female tapers, see Table 3.1. Two of the ten male tapers (MT4 and MT5) were manufactured from simplified spigots coupons, whilst all the others were full femoral stems. This meant that MT4 and MT5 were clinical '12/14' tapers manufactured from 14 mm diameter bar stock. VSI was only performed on the male tapers due to the physical limitations of performing scans within a female taper geometry. Manufacturer and product information was kept anonymous for commercial reasons.

Three different types of taper were investigated in this study, namely, 10/12, 12/14 and Type 1. In the instance of the 10/12 and 12/14 tapers, the former number indicates the proximal diameter in mm whilst the latter indicates the distal diameter. The Type 1 taper indicates a manufacturer specific taper junction design. Different manufactures employ different taper designs. Although the design rationale as to why manufacturers select certain design parameters is not publicly known, it is thought that there is a push for narrower tapers for an increased range of motion without impingement to aid stability, balanced with the increased susceptibility of fretting corrosion associated with narrower and more flexible junctions [177, 252].

Table 3.1 Details of clinical samples measured in this study. NB 'Spigot' indicates a spigot coupon, as opposed to a full stem and rough, indicates a visibly 'threaded' type finish.

Male Taper (MT)\ Female Taper (FT)	Manufacturer	Type	Rough (Yes/No)	Collared (Yes/No)	Material	Number of samples
MT 1	A	12/14	Yes	Yes	CoCrMo	2
MT 2	A	12/14	Yes	No	CoCrMo	3
MT 3	A	12/14	Yes	No	Titanium Alloy	1
MT 4	B	12/14 Spigot	Yes	No	CoCrMo	3
MT 5	B	12/14 Spigot	Yes	No	Titanium Alloy	6
MT 6	B	12/14	Yes	No	CoCrMo	1
MT 7	C	12/14	Yes	No	Stainless Steel	8
MT 8	C	10/12	No	No	CoCrMo	8
MT 9	D	12/14	No	No	CoCrMo	1
MT 10	E	Type 1	No	Yes	CoCrMo	1
MT 11	C	12/14	Yes	No	Titanium Alloy	3
MT 12	C	12/14	Yes	Yes	Titanium Alloy	3
FT 1	A	12/14	-	-	CoCrMo	1
FT 2	A	12/14	-	-	CoCrMo	1
FT 3	B	12/14	-	-	CoCrMo	2
FT 4	B	12/14	-	-	Zirconia Toughened Aluminium Oxide	1
FT 5	C	12/14	-	-	CoCrMo	4
FT 6	C	12/14	-	-	CoCrMo	2

3.2.1 Geometry - CMM

The taper surface was scanned using a 1.5 mm diameter ruby with a stylus that was 30 mm long (K651119, Mitutoyo, Japan). A 1.5 mm Ruby was selected as it is hard-wearing and the smallest diameter feasible to reduce the amount of mechanical filtering.

The same measurement strategy was used for both male and female tapers. The flat proximal end of the tapers was used to create the x-y plane in which the origin lay at the centre, as shown in Figure 3.1a and b. The traces consisted of 32 equally spaced vertical traces along the length of the longitudinal axis of the taper (z-axis) and circumferential traces at 0.5 mm spacing between each said circumferential traces. Although each trace was taken as a continuous contour, a pitch (ie., distance between each point of a trace) of 0.1 mm was used. With a maximum diameter of 14 mm, the longest trace was 44mm, providing a maximum accuracy tolerance of 0.096 µm by applying Equation 3.1, affecting the measurements of deviation from the ideal cone. Vertical traces were used to determine angular mismatch, with a trace length of 15 mm affording an accuracy of 0.038 µm.

The circumferential spacing was selected based on being half the recommended spacing between traces when measuring wear of total hip prostheses according to ISO 14242-2 [253]. Thirty-two equally spaced vertical traces were selected as this demonstrated convergence of the calculated taper angle with that calculated using the horizontal traces.

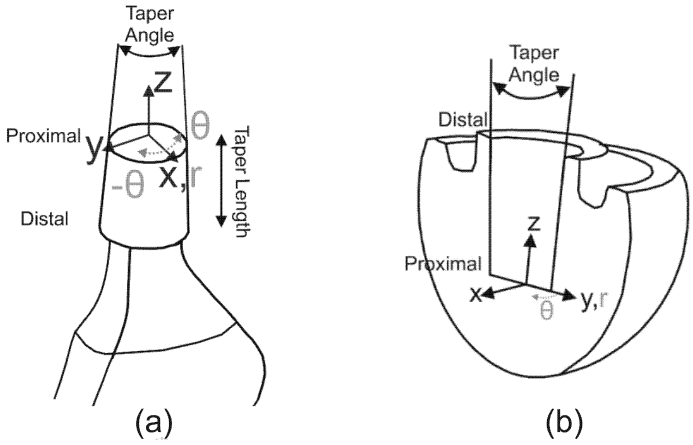

Fig. 3.1 Schematic of the CMM cartesian (black) and cylindrical polar (grey) coordinate systems with respect to the (a) male taper stem geometry and (b) female taper head geometry.

The raw data was exported in 3D cartesian coordinates to allow bespoke analysis using *Matlab* (R2017a, MathWorks, USA). Stems were aligned with the coordinate systems as shown in Figure 3.1a by using the symmetry of the stems in a vice and engineering parallels to minimise the amount of rotation about the z-axis between stem measurements.

Prior to any analysis, the chamfer of the male taper and the proximal clearance area of the female taper was removed from all the data sets. This was achieved by excluding data from the first 1.5 mm of the male tapers (i.e. from z = 0 to z = -1.5 mm) and the first 2 mm of the female taper (i.e. z = 0 mm to z = 2 mm, Figure 3.1c and d). Taper angle (or cone angle) was then calculated independent of any rotation about the x and y axes by using two directly adjacent vertical traces and applying the cosine rule. The first step was to apply a linear regression to each vertical trace to find the relationship between the x, y and z coordinates. These were then used to determine the vector equation of a line before applying the cosine rule to the directly opposite corresponding trace vector (see Figure 3.1c and d). This was repeated and averaged over the sixteen different planes about the taper axis (i.e., using two vertical scans located on direct opposite sides of the taper for a single plane).

Circumferential traces were used to determine deviation from the ideal cone. Tilt about the x and y axes was removed prior to analysis. This was achieved by first finding the relationship between x, y and z coordinates of the centres of each circumferential traces (Figure 3.2a).). Two angles were then calculated from this linear relationship: 1) between the y-z plane and the component of the linear relationship in the x-z plane (α_1, Figure 3.2b) and 2) between the x-z plane and the component of the linear relationship in the y-z plane (α_2, Figure 3.2c). These angles were then used to create two rotation matrices for rotation about the y-axis ($T_{roty(\alpha_1))}$, Equation 3.2) and x-axis ($T_{rotx(\alpha_2)}$, Equation 3.3).

$$T_{roty(\alpha_1))} = \begin{bmatrix} cos(\alpha_1) & 0 & sin(\alpha_1) \\ 0 & 1 & 0 \\ -sin(\alpha_1) & 0 & cos(\alpha_1) \end{bmatrix} \tag{3.2}$$

$$T_{rotx(\alpha_2))} = \begin{bmatrix} 1 & 0 & 0 \\ 0 & cos(\alpha_2) & -sin(\alpha_2) \\ 0 & sin(\alpha_2) & cos(\alpha_2) \end{bmatrix} \tag{3.3}$$

After rotating all the points from the circumferential traces it was then translated to centre all the data about the origin (Figure 3.2d).

Taper angle was calculated by fitting a cone of best fit to the point cloud of data. Hereafter the 'cone of best fit' will be referred to as an 'ideal cone'. The ideal cone was determined by first converting to a cylindrical polar coordinate system, before taking twice the inverse tangent of the gradient coefficient (a) of the linear relationship between radii

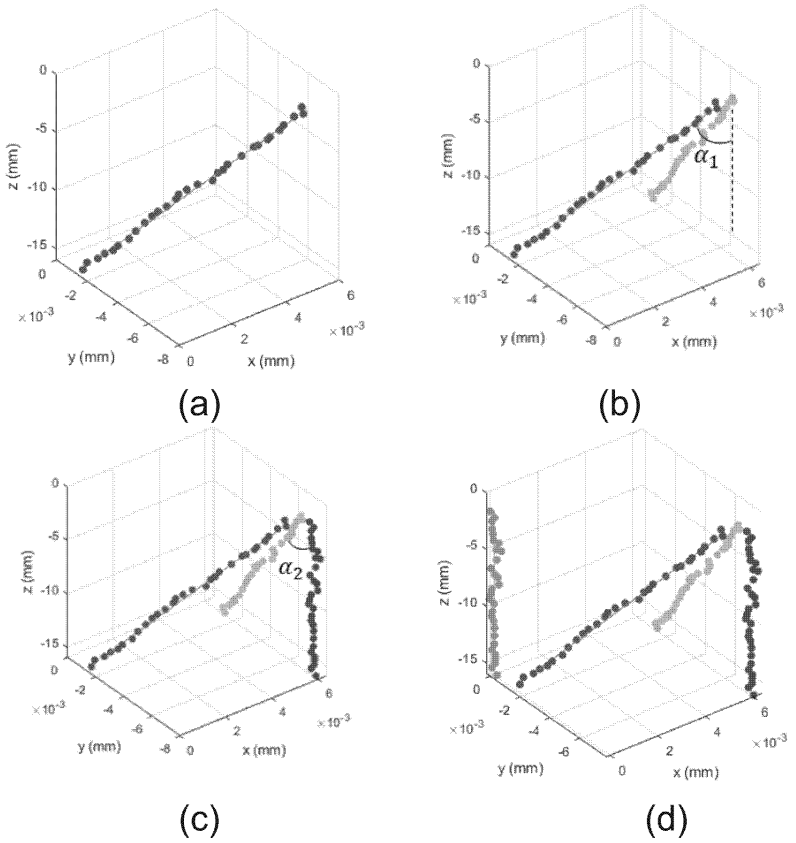

Fig. 3.2 (a) Centres of each circumferential trace and 3D linear regression (b) rotation about the y-axis i.e. in the x-z plane (c) rotation about the x-axis i.e. in the y-z plane and (d) translation about the origin.

(r) and the z-axis, see Figure 3.3a. The full taper length was used as the nominal cone generator for determining deviation from the nominal cone. Still within cylindrical polar coordinates, the ideal cone radii (r_{ideal}) at any given z-value was calculated from the ideal cone generator (defined by the linear equation in Figure 3.3a and b) and taken from r_{actual} for each point within the point cloud (Figure 3.3b). Deviation was then plotted as a surface plot against position around the male taper (θ) and the z-axis of the taper.

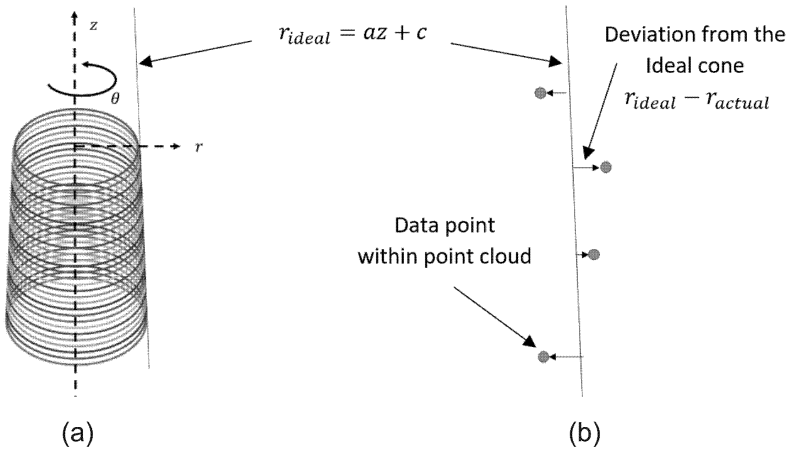

Fig. 3.3 (a) Cylindrical polar coordinate system and (b) schematic of deviation of each point from the cone generator.

Taper angles and deviation from the ideal cone of best fit were also verified with a pre-developed cone analysis software (Sphere Profiler, Redlux, UK). There was less than a 0.0001 °discrepancy in cone angle between the bespoke Matlab analysis and the predeveloped geometry analysis software with matching deviation patterns, see Figure 3.4.

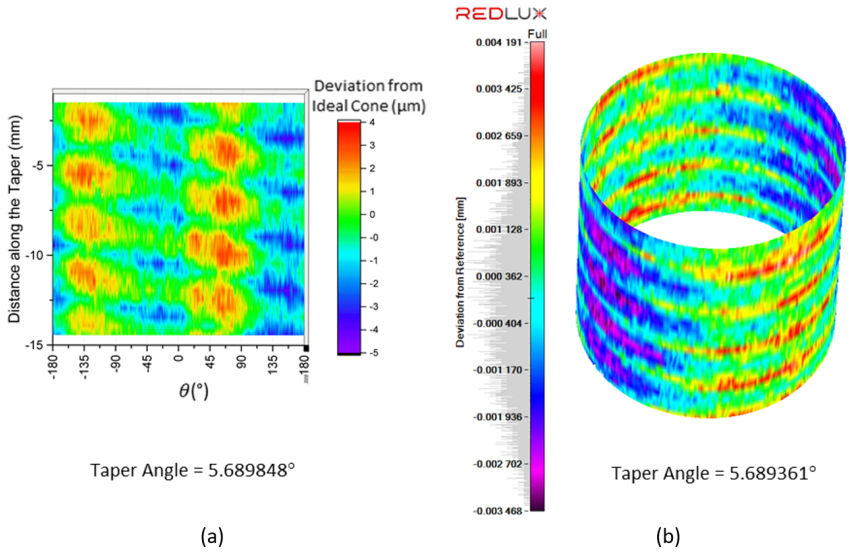

Fig. 3.4 Example of a taper analysed using the (a) bespoke *Matlab* programme and (b) predeveloped *Redlux* analysis.

3.2.2 Surface Topography - VSI

Scans of the male tapers were carried out with a 20× magnification over an area of 2 mm by 0.5 mm square, requiring twenty-two individual measurements to be stitched together for a single scan. Based on CMM findings, VSI scans were taken at proximal and distal

positions, and towards the middle at three different locations around the interface (θ = 0, -45, -90 °) as shown in Figure 3.5.

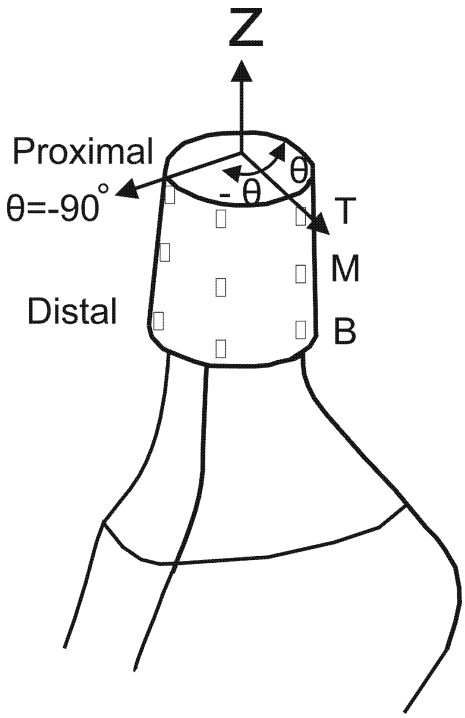

Fig. 3.5 The six locations in which scans were taken on each stem included in the VSI measurement matrix. Where T, M and B stand for Top, Middle and Bottom.

These scans were then analysed using Vision64 (Bruker, USA). Roughness profile traces along the z-axis of each scan were exported to *Matlab* (R2017a, MathWorks, USA) for pitch analysis for all 'rough' male tapers (Table 3.1). Roughness measurements were performed with a cut-off length of 0.8 mm according to ISO 4288 [254]. Certain roughness parameters were selected to describe each surface and it's variations in terms of amplitude, distribution specially and shape. Table 3.2 identifies each parameter with a short description of what that means physically, and reference to any appropriate standards or papers.

Table 3.2 Surface roughness parameters used to fully describe the surface in terms amplitude, spatial distribution and shape

Roughness Parameter	Description	Applicable Standard or Paper
S_a	Arithmetic mean of absolute values from the reference surface for a given sample length.	ISO 4287 [255]
S_p	Largest profile peak height.	ISO 4287 [255]
S_v	Greatest valley depth.	ISO 4287 [255]
S_z	Maximum profile height i.e. sum of Sp and Sv.	ISO 4287 [255]
S_k	Depth of the roughness core profile. Core profile being the roughness profile excluding protruding peaks and deep valleys.	ISO 13565 [256]
S_{sk}	Skewness, describes how much the distribution of the roughness profile is 'skewed' above or below the reference surface i.e. if points a normal distributed $S_{sk} = 0$, if skewed above the mean surface $S_{sk} < 0$ (dominated by valleys) and below $S_{sk} > 0$ (predominately peaks).	ISO 4287[255]
S_{ku}	Kurtosis, describes how evenly data point of the roughness profile are distributed from the reference surface. Where if $S_{ku} > 3$, describes a very narrow distribution about the reference i.e. a 'spikey' surface; and $S_{ku} < 3$, describes a wide distribution about the reference surface tending more towards that of a square profile.	ISO 4287 [255]
S_{pd}	Number of peaks per area i.e. peak density.	ISO 25178 [257]
Pitch	Distance between two adjacent peaks or troughs on rough male tapers.	Munir et al. [184]

3.2.3 Statistics

Data was presented as a mean ± 95 % confidence intervals unless stated otherwise. Taper angles were compared using 1-way analysis of variance followed by the student's t-test. Level of significance was set at p-value of 0.05 for all statistical tests. Analysis was performed using Excel (Microsoft, USA).

3.3 Results

3.3.1 Geometry

Taper Angle

Figure 3.6 shows the calculated male taper angles. Taper Angle varied between male tapers, even those of the apparent same type i.e. the '12/14' male tapers (p-value < 0.05). Statistical difference was seen between the majority of male tapers, including those of the same type and manufacturer, e.g. MT7 and MT11 with MT12. The '12/14' male tapers demonstrated an average taper angle of 5.659 ± 0.013 ° and range of 0.080 ° shown in Figure 3.6a. MT8 ('10/12' taper) and MT10 (Type 1 taper) demonstrated a significantly reduced average angle of 3.070 ° and 3.773 ° respectively (Figure 3.6b and c). Figure 3.6 displays the cone angles and confidence intervals from repeats on separate samples of the same type and the 16 different planes about the z-axis providing an indication of 'roundness'. The smallest confidence intervals belong to spigots (MT4 and MT5) and, MT7.

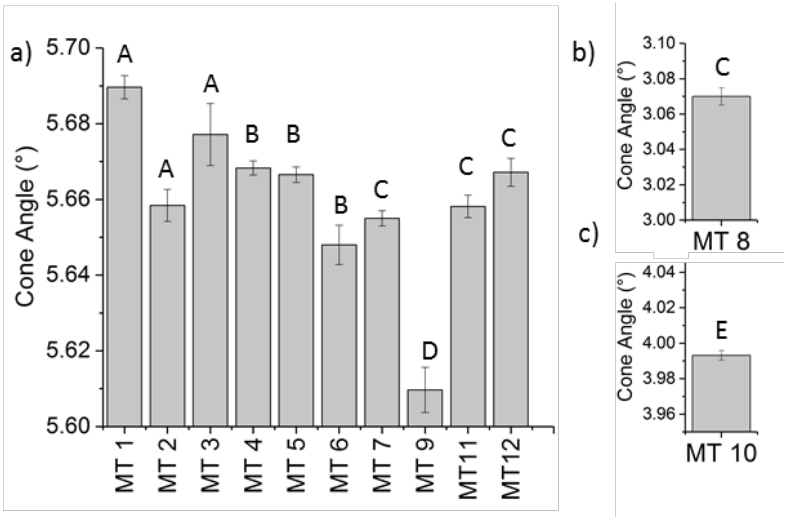

Fig. 3.6 Taper angles of (a) '12/14' male tapers and (b) '10/12' (MT8) and (c) Type 1 (MT10). Letters above each bar indicates the manufacturer. Error bars correspond to the 95 % confidence intervals from the taper angles calculated using the sixteen equally spaced different cones about the z-axis. NB although the scales are very different the range are a consistent 0.1 ° for comparison.

The female taper angles, all of which are '12/14', were different (p-value < 0.05) except FT2 when compared to FT4 (Figure 3.7). The female tapers demonstrated an average larger cone angle of 5.712 ± 0.043 ° and range of 0.130 ° compared to the '12/14' male tapers, providing a predominantly proximal contact between ideal cones. However, FT5 and FT6 from manufacturer C presented a much smaller taper angle. The female tapers presented a similar variation in angle between tapers of the same type compared to the male tapers, shown by the confidence intervals in Figure 3.6 and Figure 3.7.

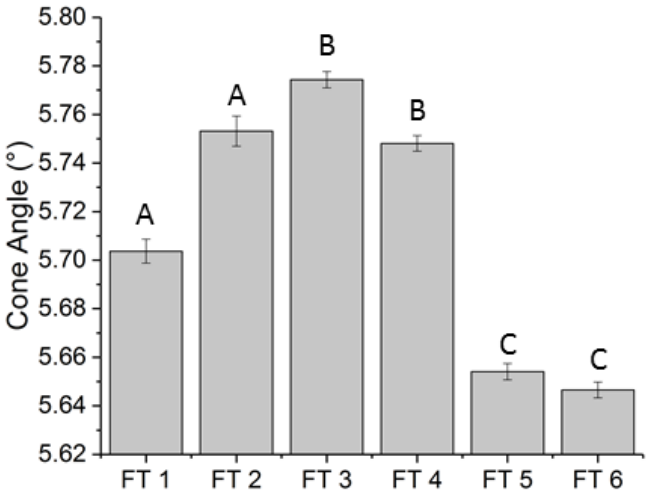

Fig. 3.7 Taper angles of all female tapers. Letters above each bar indicates the manufacturer (see Table 3.1). Error bars correspond to the 95 % confidence intervals from the taper angles calculated using the sixteen equally spaced different cones about the z-axis.

Angular Mismatch

Assuming there was no mixing of female and male tapers between manufacturers, the majority of possible head-stem couples presented a proximal angular mismatch with an average value of 0.023 ± 0.008 ° (Figure 3.8a). However, 69 % of manufacturer C head-stem couples presented a distal mismatch of -0.013 ±0.002 °. The remaining 31 % presented an average mismatch of 0.008 ± 0.002 °. There was significant difference between all manufacturer mismatch angles with a p-value < 0.05 between groups.

Figure 3.8b shows the distribution of angular mismatch for matched manufacturer couples verses mixed manufacturer couples. On average the angular mismatch between the matched and mixed manufacturer couples is similar (0.023 ± 0.008 ° verses 0.043 ± 0.058 °). The mixed manufacturer couples demonstrated a slightly larger average proximal mismatch, greater distribution and range of possible angular mismatches than the matched manufacturer couples.

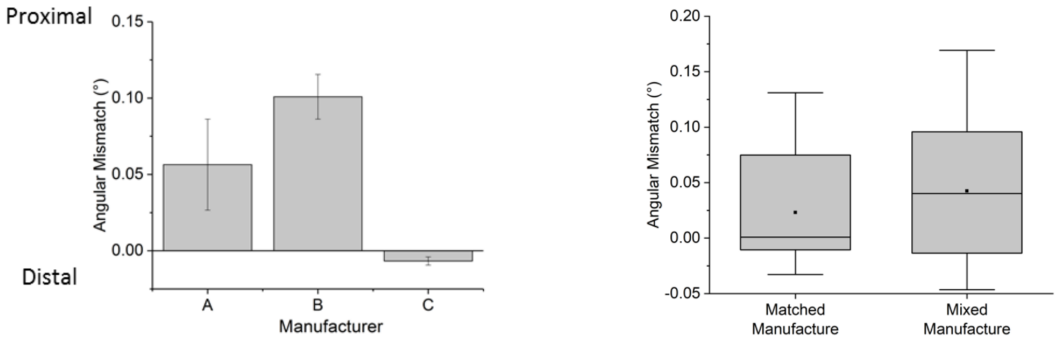

Fig. 3.8 (a) Angular mismatch between cone angles of all matched manufacturer couples, separated by manufacturer. (b) Box plots that demonstrated the spread of angular mismatches for matched manufacturer couples vs mixed manufacturer couples (NB excluding MT8 and MT10), where the mean value has also been indicated by the block square point within each data set.

Deviation from the Ideal Cone

The variation in taper angle around and along the z-axis of the taper (i.e. ‘roundness’ and ‘straightness’) are due to deviations from the ideal cone. Figure 3.9 shows surface deviation patterns for the male tapers. In cases where there was more than one sample per taper for measurement, the same deviation pattern was observed.

Clear ‘threaded’ patterns were seen in: MT3, the spigots (MT4 and MT5), MT6, MT7 and MT12 (Figure 3.9a, b, c, d and e respectively). The largest pitch of 0.286 mm was

measured on MT7, using simple circle geometry a pitch of 0.286 mm would allow a 1.5 mm diameter ruby a circle sagitta of 0.0136 mm. corresponding with great precision to the CMM deviation range of the ideal cone of 0.0136 mm.

Out of 'roundness' in the form of ovality demonstrated by a two sine waves equally distributed around the taper was seen in MT8 and MT10 (Figure 3.9f and g respectively). MT1, MT2 and MT11 demonstrated a deviation pattern characteristic of a 'threaded' taper with ovality (Figure 3.9h, i and j respectively). MT9 presented the smallest deviation range of 0.0035 mm (less than 40 % of the average deviation range of all the male tapers) with a pattern that indicated that there might have been ideal cone fitting mismatch (Figure 3.9k). The location of the major and minor axes of ovality were distributed at the same location relative to the stem geometry for the MT8, MT2 and MT11 tapers. The major axis occurred at approximately $\theta = 0\ ^\circ$ and $\theta = \pm\ 180\ ^\circ$ (in cylindrical polar coordinates) corresponding to the plane of the stem that would allow the smallest second moment of area as shown in Figure 3.1a. The collared MT1 and MT10 presented an oval pattern that was out of phase with MT2 and MT8 (both of which are non-collared) by around 60 °.

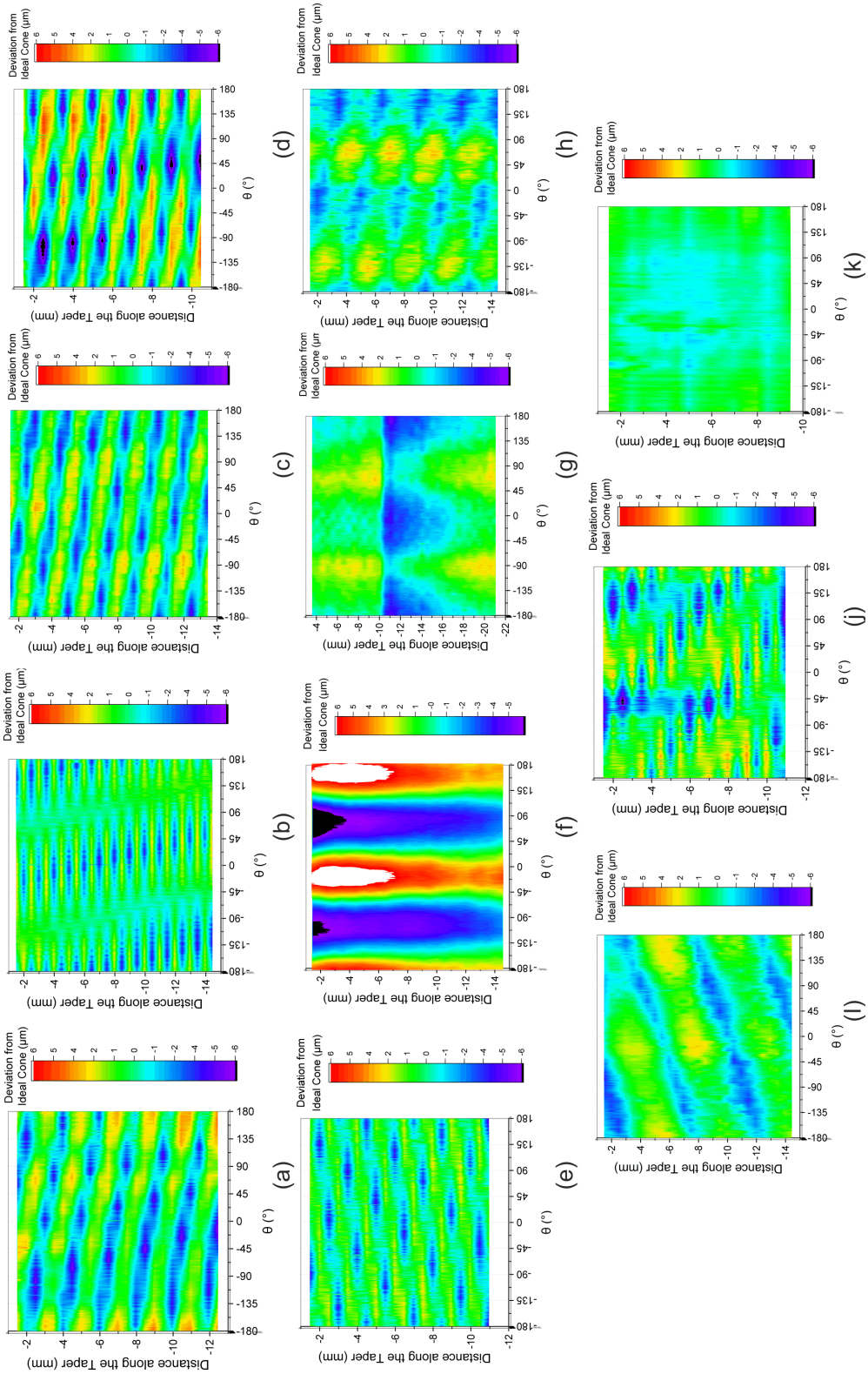

Fig. 3.9 Surface maps of the deviation from the ideal cone in cylindrical polar coordinates for male tapers. (a) MT3 (b) MT4 (c) MT6 (d) MT7 (e) MT12 (f) MT8 (g) MT10 (h) MT1 (i) MT2 (j) MT11 (k) MT9.

The female and male tapers presented a similar range of deviation (10 μm vs 9 μm for male and female tapers respectively) but very different deviation patterns. In cases where there was more than one sample of the same taper for measurement, the same deviation pattern was observed. Figure 3.10 shows the deviation maps from the ideal cone for all the female tapers. Three different patterns were observed in the female tapers. FT1 and the ceramic FT4 tapers presented no repeating patterns around the taper z-axis or along it (Figure 3.10a and b). No repeating patterns were presented in FT1 and FT4 indicating eccentricity that could be a function of ideal cone fitting mismatch. The ceramic taper (FT4) demonstrated the smallest deviation range, around 40 % smaller than other female tapers. The four remaining female tapers presented a third order harmonic around the z-axis of the taper including: FT2, FT3, FT 5 and FT 6 (Figure 3.10c, d, e and f). It was noted that the four female tapers that presented this triple harmonic belonged to all the solid metal heads in this study. FT2 was the only other CoCrMo head in this study that did not present this pattern and was of a separate bearing surface and taper insert (i.e. hollow).

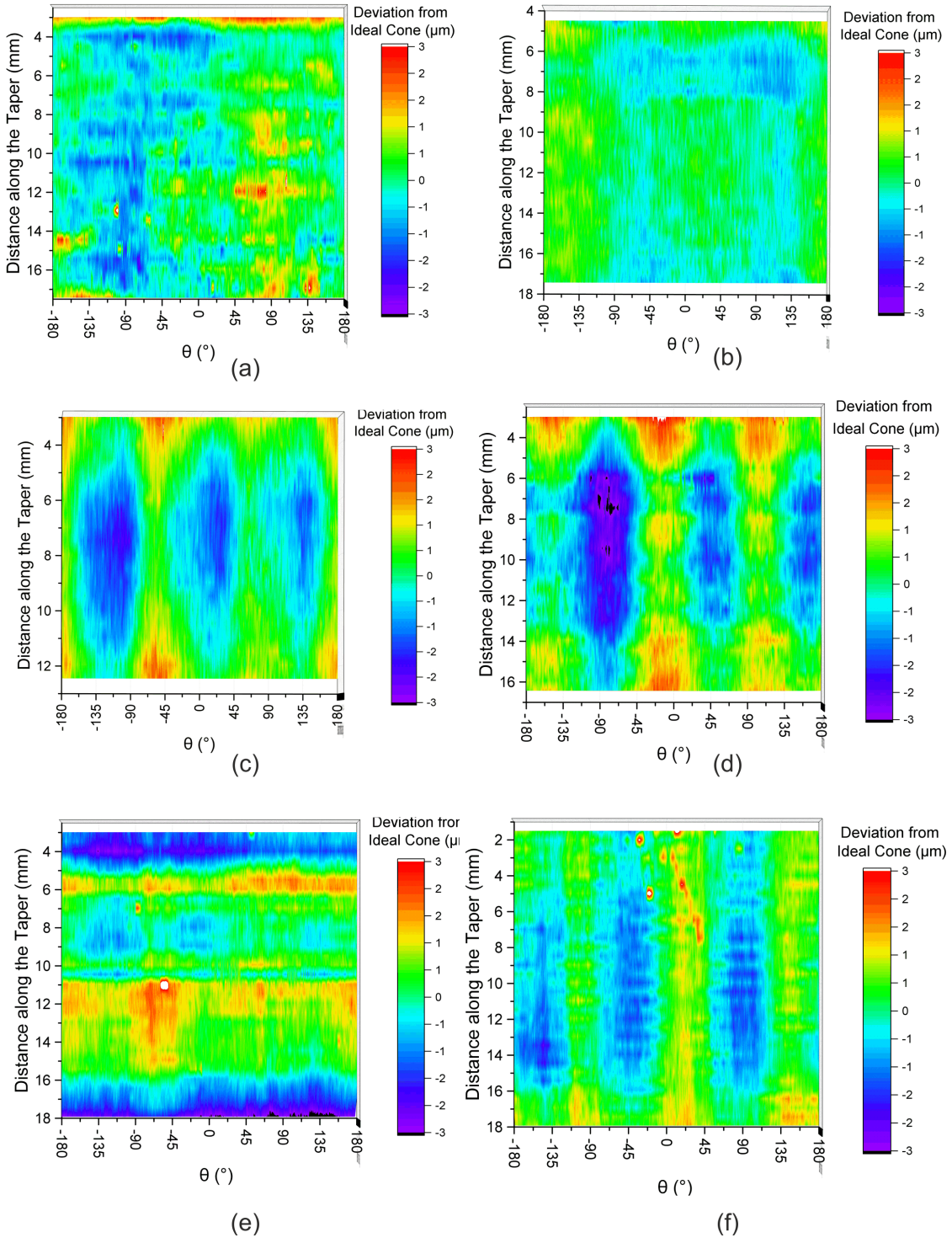

Fig. 3.10 Surface maps of the deviation from the ideal cone in cylindrical polar coordinates for female tapers. (a) FT1, (b) FT4, (c) FT2, (d) FT3, (e) FT5 and (f) FT6.

3.3.2 Surface Topography

There was a wide variation in the surface topography of male tapers, where an example trace of each 12 tapers can be found in Appendix A, Figures A.1 and A.2. The largest

difference was seen between the samples that presented a 'rough' threaded-type texture and those that did not. Figure 3.11 summarises the parameters that characterise the amplitude of the roughness profiles.

The rough male tapers presented an average roughness S_a of 3.16 ± 0.45 µm, whilst the smooth male tapers presented an average S_a of 0.464 ± 0.14 µm . This was also reflected in S_z, where the rough surface finish presented a S_z of 15.62 ± 2.08 µm and the smooth finish presented an S_z 6.86 ± 4.34 µm. However, S_z is the sum of the highest peak and lowest valley over the whole sample area, and is not always representative of the whole surface. S_k can provide a better insight into the average peak-to-trough height over the whole surface as it excludes protruding peaks and valleys. However, it appears to provide an underestimation in average peak-to-trough height for the rough surface finish tapers. The rough male tapers presented an average S_k of 7.60 ± 1.08 µm and the smooth finish 1.43 ± 0.24 µm. Variation in the amplitude parameters was not only a function of if they presented a 'threaded' rough finish or not, but was also seen between stems of the same manufacturer (p-value < 0.05) and between different samples of the same product (p-value < 0.05).

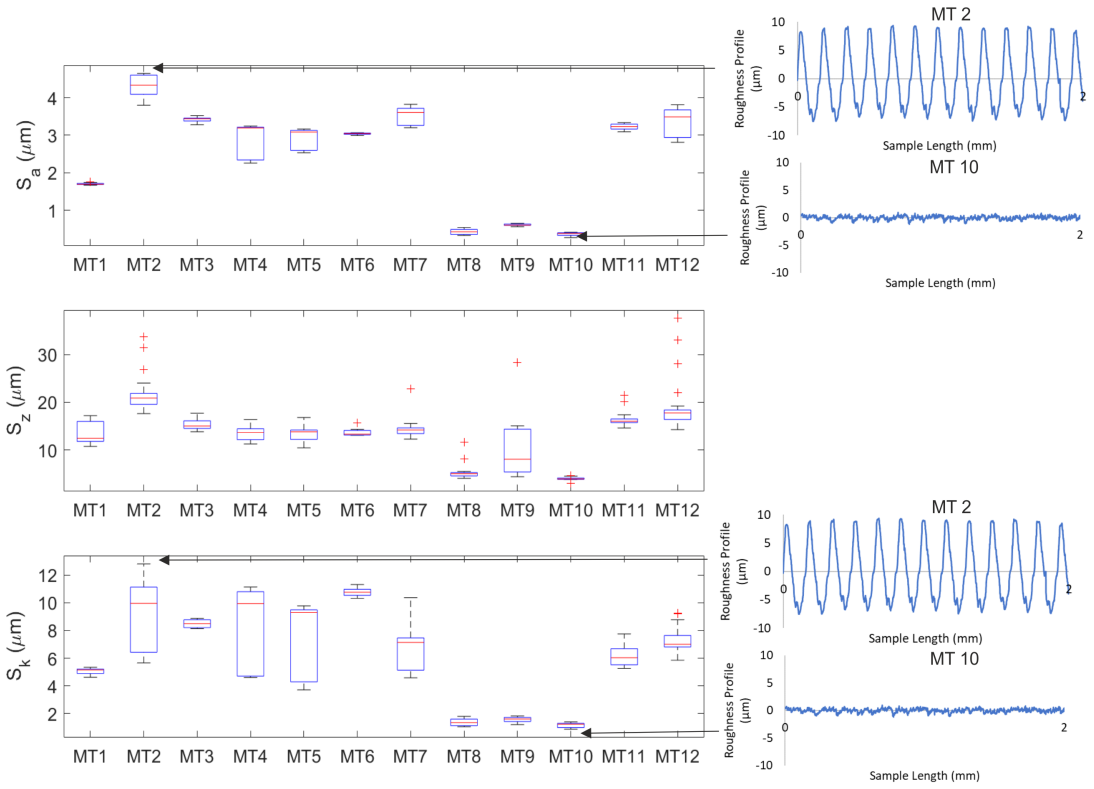

Fig. 3.11 Box plots of statistical surface topography parameters that summarise amplitude, including S_a, S_z and S_k. Example roughness profiles of certain samples are shown to the right that demonstrate range in parameters.

Variation in roughness amplitude was also seen in different locations on the same stem, these have been summarised for all the samples and can be found in Appendix A, Figure A.3 to A.10. S_a was found to vary by 4 ± 2 % depending on the location of the VSI scan for a given stem. Figure 3.12 shows an example of how surface topography amplitude (S_a) varied with respect to the radial position around the taper (Figure 3.12a) and along the taper axis (Figure 3.12b), using MT9 as an example. MT9 presented a difference of 0.03 µm around the stem and 0.02 µm along the stem. Any possible trends in roughness amplitude due to differences in location on the interface were much smaller than variations between stems, and so was not fully investigated.

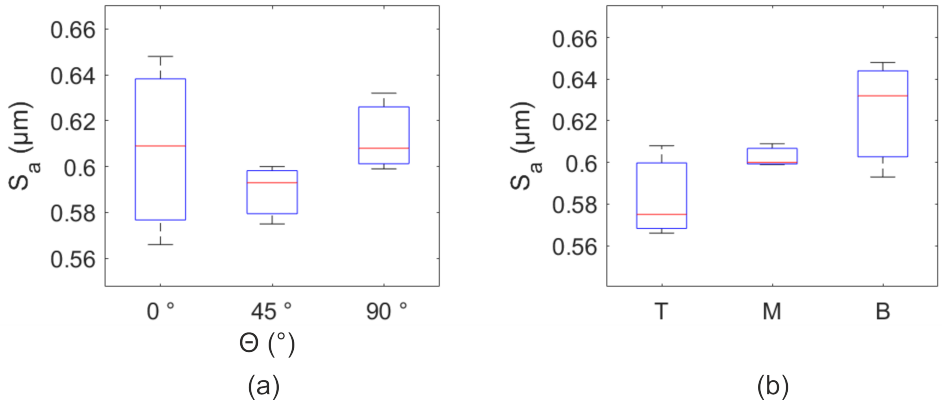

Fig. 3.12 Box plots of S_a as a function of (a) radial position and (b) position along the taper axis for MT9.

Surface topographies also varied in their shape and distribution. Parameters used to characterise this have been summarised in Figure 3.13. S_{sk} and S_{ku} parametrise the skewness and kurtosis of the roughness profiles, respectively. MT2 samples showed the largest skew below the mean roughness line, indicating that the profile was dominated by peaks. MT9 showed the greatest skew above the mean roughness line and the profile was therefore dominated by valleys. Generally, the 'smooth' tapers tended to present a more negative S_{sk} (-0.26 ± 0.296 Vs 0.400 ± 0.179), larger S_{ku} (3.09 ± 0.35 Vs 2.02 ± 0.21) and a greater number of peaks per unit area (3391 ± 323 mm^{-2} Vs 5183 ± 126 mm^{-2}) than the 'rough' tapers. MT7 showed a more normal, yet wide distribution about the mean roughness line with a S_{sk} of 0.188 ± 0.020 and S_{ku} of 1.534 ± 0.02.

Like the amplitude parameters, shown in Figure 3.11, the shape and distribution parameters also presented variation between taper of the same manufacturer (p-value < 0.05), and between different samples of the same product (p-value < 0.05), see Appendix A Figure A.3 to A.10.

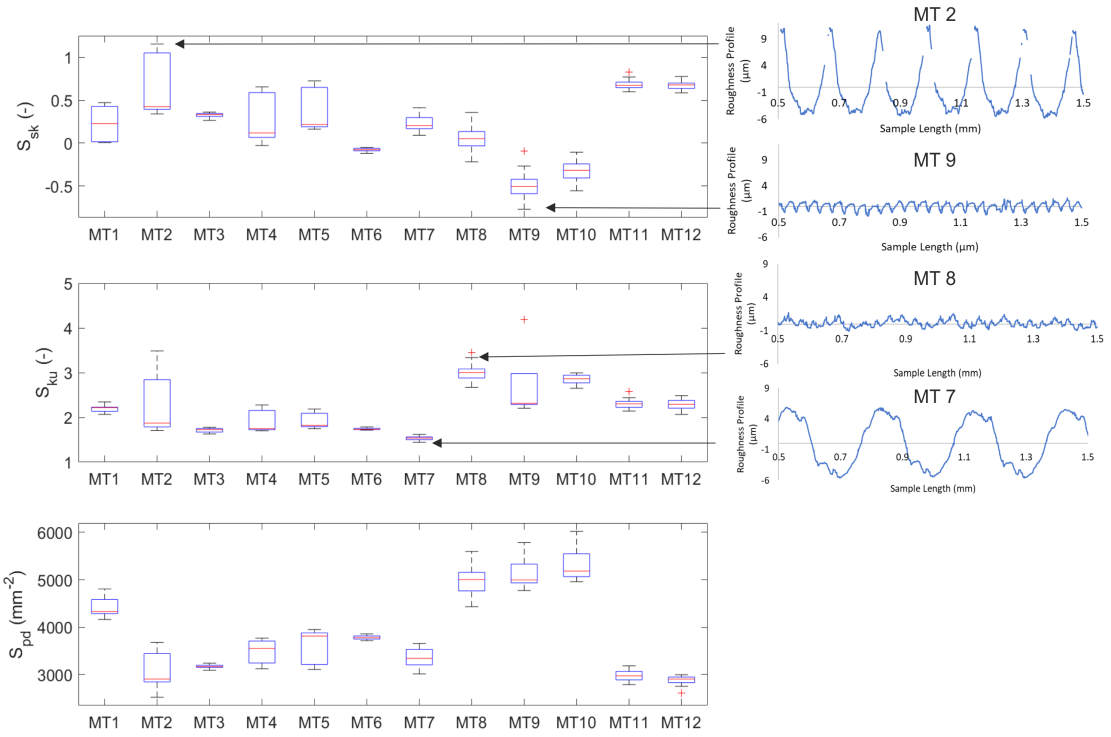

Fig. 3.13 Box plots of statistical surface topography parameters that help characterise the shape of the roughness profile amplitude, including S_{sk}, S_{ku} and S_{pd}. Example roughness profiles of certain samples are shown in the right that demonstrate range in parameters

Some rough male tapers presented a threaded-type finish, with an associated pitch. A maximum difference in pitch between the finest (Figure 3.14a) and coarsest (Figure 3.14b) was found to be 0.15 ± 0.007 mm as shown in Figure 3.14c. There was a significant difference between the different taper types except for between: MT4 and MT5, MT3 and MT6, MT4 and MT11, MT4 and MT12, and MT11 and MT12 (p-value > 0.05). Significant difference was also seen between different products of the same manufacturer. The largest pitch of 0.286 ± 0.007 mm was measured on MT7, using simple circle geometry this pitch would allow a 1.5 mm diameter ruby a circle sagitta of 0.0136 mm corresponding with great precision to the CMM deviation range of the nominal cone of 0.0136 mm (see Figure 3.9d).

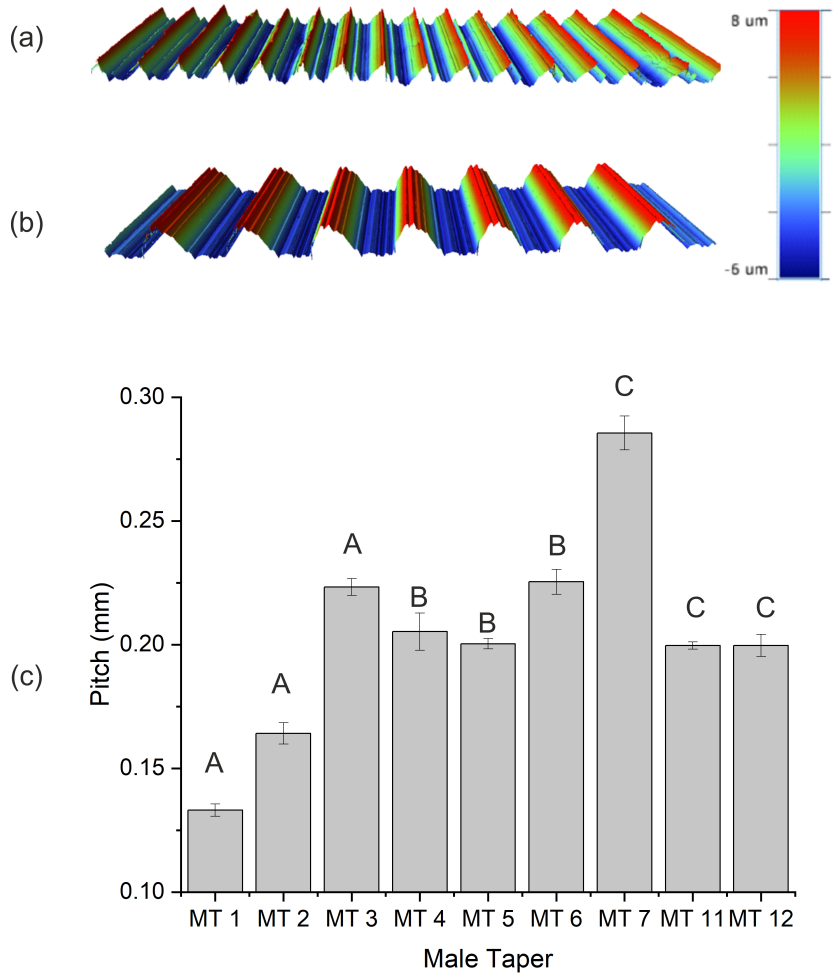

Fig. 3.14 Surface topography 2 x 0.5 mm scan of (a) the finest pitched 'threaded' finish (MT1) and the largest (MT7), (c) average pitch of all the rough male tapers.

3.4 Discussion

This study measured the geometry and topography of a variety of modular tapers currently on the market in clinically available THR. According to the NJR [111], the samples measured represent the taper design in the implants present in well over half the population that have received THR surgery. The largest limitation in assessing variation across the market was derived from the number of repeat samples available for each product. A target minimum of three samples per product was not always possible and the limited number of samples should be taken into account when drawing conclusions from this study, especially where only one was available for measurement.

Geometry and topography were measured using a CMM and VSI techniques. Although previous studies that employed CMM and VSI techniques to measure geometries such as

taper length and taper angle, and statistical surface topography parameters, respectively; to the author's knowledge, this is the first study to help bridge the gap between geometrical form and surface topography. This was achieved by capturing the deviation from geometrical form on the micron-scale while also capturing VSI scans for surface morphology measurements on the micron- to submicron- scale.

One of the challenges faced by this study was the use of two separate measurement techniques to characterise the taper junction across the length scales. A trade-off facing almost all surface topography measurement systems is that between resolution and measurement area, i.e., with increased resolution there is often a reduction in the area that can be measured. One way to overcome this is to use two techniques and map the higher resolution measurements onto that of the lower. This study did this by mapping the VSI measurements onto the CMM measurements. However, the accuracy of this mapping process is limited to high level references, and in this case the etching on the end of proximal flat face of the taper junctions. As such, there is still some gap in characterisation between parameters obtained between the two measurement techniques.

Nevertheless, this study did identify the variation in geometry and surface topography parameters to inform representative samples. More specifically, male and female taper angle and the resulting angular mismatch between matched manufacturer head-stem clinical samples, the amplitude of surface topography and morphology. Furthermore, this study also developed measurement methodologies to characterise the representative samples, including any manufacturing variation that may be present, allowing these variations to be taken account of during subsequent simulation studies.

3.4.1 Taper Angle

Verification of the developed analysis algorithms in this present study was provided by way of comparison with pre-developed software used in previous studies to determine bearing interface geometry and deviation maps [258], please refer to Figure 3.4 for the comparison of taper angle and deviation maps between the two analysis solutions. Further verification that actual taper angle was captured accurately can be determined by looking at other comparable studies which will be discussed in the next paragraph.

One of the first observations was that tapers of the apparent same type (i.e. '12/14') presented different geometries. Variation in the '12/14' male taper cone angles ranged from 5.61 to 5.69 °, for a variation range of 0.08 ° (Figure 3.6a). This compared to that of Mueller et al. [110] that reported a variation range of 0.1 ° (with a range of 5.58 to 5.68 °, as determined from the figures) between manufacturers. Although comparison of the developed algorithm by this present study was not possible with Mueller et al. [110]

who used a purchased software (Imageware 12.2; UGS Corporation, Plano, TX), the close agreement between this present study and that of Mueller et al. [110] offers verification that the actual taper angle was captured correctly.

In terms of the '12/14' female taper cone angles, this study found a variation range of 0.13 ° (5.65 to 5.77 °, Figure 3.7) between manufacturers; in close agreement with Mueller et al. [110] reporting a variation range of 0.2 ° (5.60 to 5.80, as determined from the figures) between manufacturers. One reason for the possible disparity could be that Mueller et al. [110] had access to eight different female tapers from eight different manufacturers, whilst this present study was limited to six. However, the range of female taper angles found by this present study was within that found by Mueller et al. [110], corroborating the verification of the measurement methodology and analysis algorithms developed during this study.

Comparing the non-'12/14' male taper measured in this study, the 'Type 1' male taper (MT10) presented a smaller cone angle than the '12/14' and was within the range measured by Nassif et al. [174]. The '10/12' male taper (MT8) presented the smallest cone angle of 3.07 $\pm$ 0.28 °, closer to that intended by Morse to resist shear stresses of 2.833 °[16]. Tapers with smaller angles, often referred to in the tooling industry as 'shallower' tapers, are used to create a self-lock taper junctions as sufficient compressive stress can be created over the surface of the toolholder (male taper) to allow it to be held in the spindle (female taper) without the need for additional fixtures. In the tooling industry, larger (steeper) taper angles are used in self-releasing situations and can present taper angles of 16.5 °. Self-releasing tapers require the use of a drawbar to apply greater axial force to ensure a sufficient compressive fit is achieved [259]. Hence, although head-stem tapers in THR are greater than that of self-locking tapers used in the tooling industry, they are closer in angle to the self-locking tapers. Head-stem taper junctions in THR are treated as self-locking tapers and the rationale for the selection of specific taper angles (which are greater than that used in the tooling industry) by different manufacturers is not publicly available. One possible reason for why greater taper angles are used in THR could be the limitation imposed by the femoral head and the length of male taper that can be accommodated in the female taper and thus, a steeper taper angle to allow for a shorter taper junction. Additionally, a drive towards shorter taper junctions, which can be helped realised by a steeper taper angle, has been reported to reduce the risk of impingement on the acetabula components for a reduced risk of postoperative instability [2].

Although the design rationale for different taper angles within the tooling industry can vary depending on whether it is a self-locking taper or a self-releasing taper, the design rationale for the selection of different taper angles in THR is not publicly known. Indeed, there is but one retrieval study and no experimental simulation studies to the author's

knowledge that have investigated how taper angle per se influences fretting corrosion at the modular taper interface. The aforementioned retrieval study was that by Kao et al. [177]. Kao et al. [177] found that tapers with smaller cone angles tended to present more severe observable effects of fretting corrosion. Taper angles varied between 2.3 and 5.4 ° and using the Goldberg scoring system (refer to Table 2.2 for details of the criteria) Keo et al. [177] found that for every 1 ° decrease in taper angle, the stem fretting score increased by 0.25 points. This was attributed to micro motion at the interface increasing with less conical and more cylindrical taper geometries. Critiquing the study presented by Kao et al. [177], the Goldberg scoring system provides discrete fretting and corrosion scores of 1, 2, 3 or 4, and so only a 4 °difference in taper angle would be predicted to result in a 1 point difference in score. However, the greatest difference in taper angle of the samples measured was only 3.1 °in the taper angle, and so it could be argued that the relationship identified by Kao et al. [177], albeit statistically significant, is not valid. Additionally, no description of a proposed mechanism, nor citation of earlier work was made to their explanation of increased taper angle is linked to less micro motion and therefore fretting corrosion. In view of the relationship between taper angle and fretting corrosion set forth by Kao et al. [177], this present study presented a maximum difference in male taper angle (between MT1 and MT8) of 2.62 ° and so the Kao et al. [177] would predict a 0.66 point difference in fretting and corrosion score of a categorised semi-quantitative criterion.

Looking now to studies that did not directly investigate the effect of taper angle on fretting corrosion. Ouellette et al. [228] investigated the seating mechanics of two different tapers a ‘9/10’ and a ‘12/14’ taper, and although they did not investigate the effects of taper angle on seating displacement, they did propose a simple model of the effect of taper angle on the seating mechanics. More specifically, Ouellette et al. [228] set forth that smaller taper angles would decrease the taper locking stiffness allowing a greater displacement under the same impaction loads for enhanced taper locking. This contrasts with Kao et al. [177]’s proposal of increased taper angles being associated with less micro motion and thus fretting corrosion.

Taper angle is a system parameter of this conforming interface, it cannot be investigated using simplified studies such as pin-on-disk studies, and requires a full taper reconstruction. As such, there appears to be a distinct lack of studies to provide a conclusive understanding on the effect of taper angle on fretting corrosion of the head-stem taper interface. Valuable further work would include retrieval studies that employ material loss measurements, experimental simulation studies including investigation into the effect of biological fluids, and computational studies. However, investigation of taper angle was outside of the scope of this present project.

This study found that both male and female taper angles also presented differences between products of the same taper type (i.e. of the same manufacturer). Taper angle is arguably the most important manufacturing tolerance to ensure a tight and uniform fit compressive fit. The most applicable standards for tolerances are detailed by ISO 1947 [107] which describes twelve different taper angle tolerance grades from AT1 to AT12. For cones of between 10 to 16 mm in length, the tightest tolerance grade (AT1) prescribes a maximum variance of 10" (0.003 °) in cone angle (AT_α, see Figure 3.15) and 0.4-0.6 µm between the largest and smallest diameter (AT_D) at the end of the cone (at L, see Figure 3.15). At the same taper length the loosest tolerance grade (AT12) prescribes maximum variances of 21'38" (0.36 °) in cone angle and 63-100 µm difference in diameter at L.

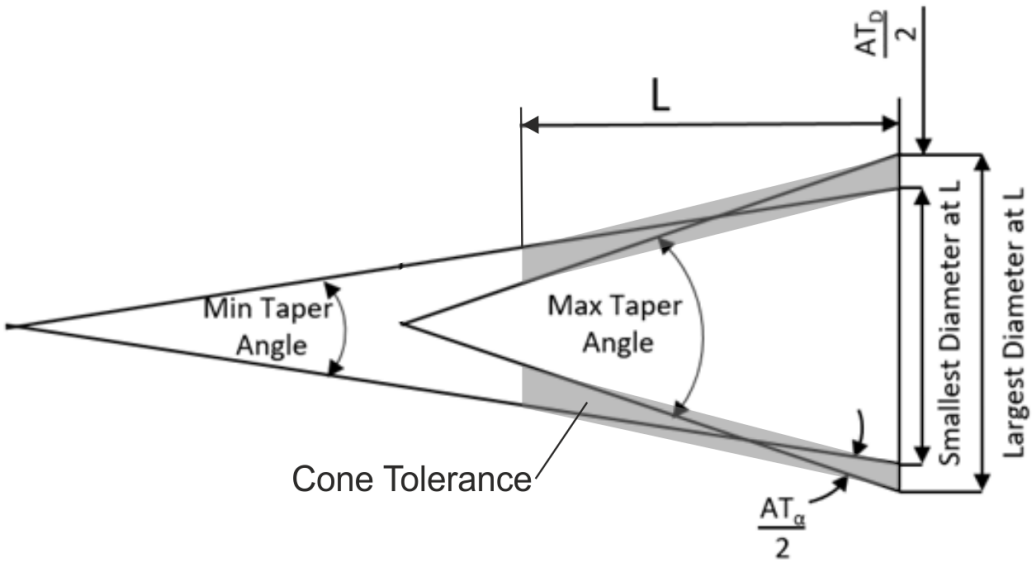

Fig. 3.15 Schematic of the relevant taper tolerances described in ISO 1947 [107].

Current manufacturing tolerances of taper angles in THR are not public knowledge but ranges of measured cone angles of the same type and manufacturer can provide a good indication. Using these and other published measurements of THR tapers, a maximum difference of around 0.05 ° in cone angle and 20 µm in diameter for a given taper design from the same manufacturer has been found [110]. This is in agreement with a paper published in 1998 that reported angular tolerances in the region of 0.06 to 0.1 ° [250]. The diameter may also have been underestimated due to a level of mechanical filtering from the 1.5 mm ruby tipped stylus. This would place clinical tapers closer to the tolerance grade of AT8 (AT_α = 0.057 °, L = 10-16 µm), if not beyond. No manufacturing process will ever be able to produce 'perfect' surfaces, especially not on complex geometrical shapes such as is present in THR. However, this study does suggest that more can be done in the way of

increasing conformity at the interface in THR if tapered interfaces in CNC machines can be routinely manufactured to AT3 tolerance grades or tighter [260].

3.4.2 Angular Mismatch

The measured angular mismatch ranged from -0.04 to 0.13 ° to create either a distal or proximal engagement, respectively. All manufactures presented different angular mismatches, with manufacturer A presenting a mismatch of 0.0565 ±0.030 °, manufacturer B of 0.101 ±0.015 and manufacturer C of -0.007 ±0.003 °(Figure 3.8a). Comparing now to Mueller et al. [110] who reported an angular mismatch of -0.15 to 0.02 °, where a negative angular mismatch indicated a proximal angular mismatch. Thus, the angular mismatch measured by this present study was in close agreement with that measured previously, providing further verification of the developed measurement methodologies and analysis algorithms. However, this present study calculated angular mismatch by subtracting the female taper angle from the male taper angles as per Kocagöz et al [190], different to Mueller et al. [110] who subtracted the male taper angle from the female taper angle. Although this may seem a trivial point, a previous study by Werner et al. [261] has highlighted the confusing variability of definitions used in studies that have investigated fretting corrosion at the head-neck taper junction, and thus, consistency of how parameters are measured and reported should be achieved in the hope of avoiding possible confusion. The majority of studies define a positive angular mismatch as a proximal mismatch and negative as distal, and thus recommendation for angular mismatch to be calculated by subtracting the female taper angle from the male taper angle.

Angular mismatch is not normally parametrised in the tooling industry as it is not a design parameter, but rather a consequence of manufacturing tolerances and so learning and constancy with other industries is limited. In contrast, in the orthopaedic industry, proximal contacts are a design feature of ceramic head couples to ensure most of the stress is experienced by the portion of the head with most material [16]. However, 69 % of manufacturer C head-stem couples presented a distal mismatch of -0.013 ± 0.002 °. In this case, male taper angles were consistent with other ‘12/14’ male tapers (MT7, Figure 3.6a) and female taper angles were smaller compared to other ‘12/14’ female tapers (FT5 and FT6 in Figure 3.7), suggesting mismatch was governed by a smaller female taper angle. The remaining 31 % presented an average mismatch of 0.008 ± 0.006 °, possibly an attempt to achieve a matched contact for metal-on-polymer bearing couples. There was significant difference between all manufacturer mismatch angles with a p-value < 0.05 between groups. Morlock et al. [262] stated that most female taper in metal heads are designed with a similar angles compared to the female taper of ceramic heads, with some

female tapers of metal heads being manufactured to present the same taper angle of the male taper; the present study supporting the latter part of Morlock et al. [262]'s statement.

Despite the mixing of head and stems from different manufacturers being discouraged and classed as 'off-label', one study by Tucker et al [263] reported that this does happen and that it resulted in a higher failure rate. Figure 3.8b shows the distribution of angular mismatch for matched manufacturer couples verses mixed manufacturer couples. On average the angular mismatch between the matched and mixed manufacturer couples is similar. The mixed manufacturer couples demonstrated on average a slightly larger proximal mismatch and greater distribution and range of possible angular mismatches compared to the matched manufacturer couples. The tendency to achieve a proximal mismatch is likely due to the requirement for use with ceramic heads. In summary, depending on which two manufacturers are involved in the mixed head-stem couple, angular mismatch will likely be increased but in very few cases can be decreased. An instance where an increased angular mismatch due to mixing head and stem manufacture was thought to contribute to the requirement of revision surface due to pseudotumour formation was that reported in Chana et al. [103]. The femoral head was a large diameter CoCrMo head with a 12/14 taper manufactured by Smith & Nephew (Warwick, UK) and the male stem was manufactured out of a Beta-Titanium alloy (TMZF) with a v40 male taper (type of 12/14 taper) manufactured by Stryker (New Jersey, US). Using previously reported taper angles from Muller at al. [264], mixing of this particular head stem couple would lead to an angular mismatch of 0.156 ± 0.015 °, compared to a 0.073 ± 0.004 ° mismatched if both tapers where manufactured by Smith & Nephew and 0.06 ± 0.033 ° if both were manufactured by Zimmer. This report highlights the possible clinical implications of different taper designs between manufactures. However, it should be noted that this angular mismatch cannot be solely attributed to the implant failure reported in Chana et al. [103] et al. due to the use of an adapter at the head-stem interface, the large diameter metal-on-metal bearing and the low elastic modulus of TMZF for a decreased flexural rigidity, all thought to contribute to implant failure in this instance.

3.4.3 Deviations in Geometrical Form

Previously, tapers have been parametrised in terms of geometry and surface topography [110, 184]. However, deviation from geometrical form also plays a key role in engagement. This was demonstrated by Witt et al. [232, 265] which found engagement of the two surfaces to be inconsistently distributed. To the author's knowledge, this is the first study to help bridge the gap between geometrical form and surface topography.

Deviations from ideal geometry are normally characterised by 'roundness' and 'straightness' [107], and appeared to be linked to the flexural rigidity of the taper and lower stem geometry. For example the narrowest '10/12' taper (MT 8) presented the greatest out of 'roundness' shown in Figure 3.9f. The pattern demonstrated noticeable ovality, correlating with differences in the second moment of area of the lower stem geometry shown schematically in Figure 3.16. The major axis of the oval occurred at roughly $\theta = 0$ ° and $\theta = \pm 180$ °, which corresponds to the smaller second moment of area of the lower stem geometry. The smaller second moment of area allowing the male taper (workpiece) to flex away from the cutting tool resulting in material above the ideal cone. Figure 3.9f also demonstrated an increase in deviation from the ideal cone towards the proximal end of the taper, consistent with simple engineering beam bending theory principles. Conversely, the spigots (MT4 and MT5) did not present a difference in second moment of area and presented one of the smallest standard deviations in ideal taper angle (Figure 3.6), indicating good dimensional control during manufacture. MT7 presented the smallest variation in taper angle and good dimensional control as shown by the surface deviation maps (Figure 3.9d). It also presented the shortest length for reduced deflection and better control during manufacture.

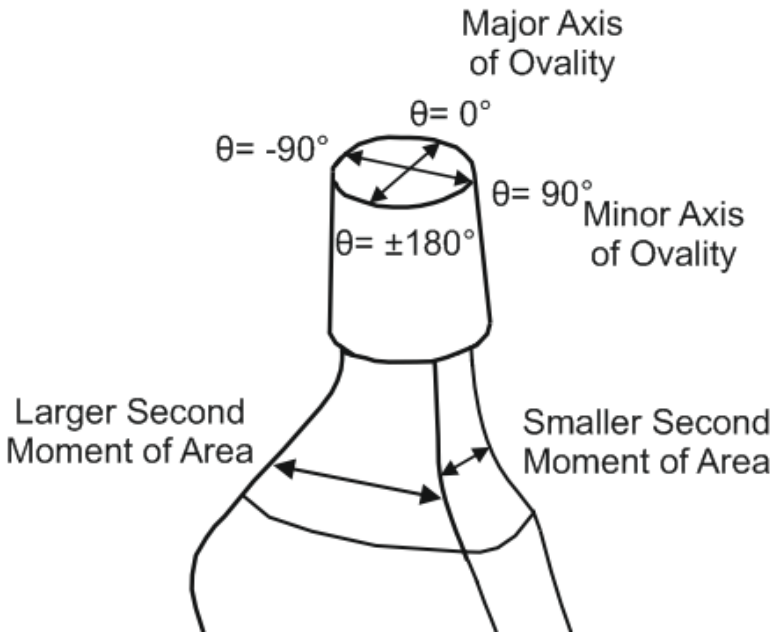

Fig. 3.16 Schematic illustrating how ovality relates to differences in second moments of area of the lower neck geometry.

Ovality was also seen in MT1, MT2, MT10 and MT11 (see Figure 3.9g, h, i and j). Where the non-collared MT2 and MT11 presented ovality where the major axes occurred at $\theta = 0$ ° and $\theta = \pm 180$ ° corresponding to the smaller second moments of area, as was with MT8. However, the collared MT1 and MT10 presented an oval pattern that was out of phase with the non-collared MT2, MT8 and MT11 by around 60 °. One possible

explanation for this is the collar altering the second moments of area from what they would be if they were non-collared. The effect of ovality was investigated using finite elements models by Bitter et al [141] that demonstrated increased motion, contact pressures, and wear compared to a 'perfect' fit.

The female head tapers presented a similar level of 'out of roundness' to the male stem tapers (see Figure 3.7). To date, much of the focus has been on the topography of the male taper and whether 'rough' or 'smooth' male tapers have an implication on performance of the taper junction. However, local deviations from the ideal cone of the female taper will have just as many implications in conformity between the two components.

The four different types of female tapers that presented a third order harmonic (FT2, FT3, FT5 and FT6, see Figure 3.10) were all solid metal heads, whilst the two remaining female tapers were either a hollow metal head (i.e. assembled from a separate bearing surface and taper insert) (FT1) or ceramic (FT4). The smallest cone angle deviation range was presented by the ceramic head (FT4) corresponding to the smallest deviation range from the ideal cone, possibly due to the sintering and grinding processes involved in the manufacture of ceramic heads. Although it is not quite clear where the third order harmonic deviation pattern has come from due to the spherical nature of the head, this is usually attributed to distortion of the work piece by clamping or forces experienced during manufacture [266].

Inaccuracies in manufactured components due to machining and clamping forces on a workpiece with variable stiffness is a problem experienced by other industries such as the aerospace and automotive. Stiffness variability within a given workpiece, and thus variable deflection experienced by the workpiece relative to the cutting tool, can be due to complex geometries and material removal during the machining process. One solution to overcome this problem includes the possible use of adaptive clamping forces, this is where the clamping forces can be adjusted to compensate for variability in component stiffness during machining for geometrical accuracy of the finished component [267]. This methodology could be adopted by orthopaedic manufacturers to eliminate the out of roundness patterns discovered by this present study.

Other implications of these deviations found in this study presented are those of volume loss calculations post in-vitro assessment or from retrievals studies. Calculating the volume of theoretical fluid that fills the space between the surface generated using the CMM surface maps and maximum ideal cone (see Figure 3.17) presented a range of 5-0.5 mm^3 for male tapers and 2.5-11 mm^3 for female tapers. Material loss calculations of retrieved male tapers were within the range 0-0.8 mm^3 and 0.41-25.89 mm^3 for female tapers [268]. Material loss in the Racasan et al. [268] study took into account a threaded surface and any 'barrelling' or 'hogging' form. However, differences in volume loss from other studies

and theoretical mismatch in this study are of comparable scale. Additionally, ovality in the male tapers and the triple peak pattern within the female tapes would not be detected or taken into account on retrieval or damaged tapers.

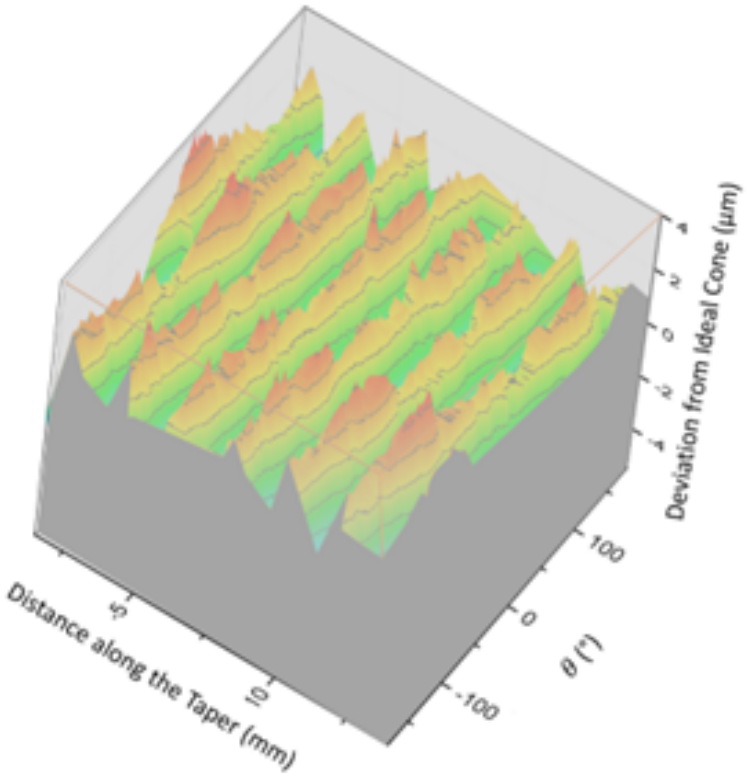

Fig. 3.17 Schematic of theoretical volume of fluid that could fill the space between the actual taper surface and the maximum ideal cone.

To overcome this possible inaccuracy of measured material loss calculations by retrieval studies, pre and post surface analysis and accurate mapping of the as manufactured surface to the worn surface could be adopted. Although this may not be practical for every surgery, special efforts for select samples could be made for studies.

3.4.4 Surface Topography - Male Taper

In other industries, great effort has been expended in order achieve very accurate, smooth conical interfaces. It has been known for parts to undergoing two grinding processes after being turned into shape, allowing for periods of rest to allow the parts to take their final form before finishing [108]. The finishing process of tapers in THR on the other hand, appears to be a turning process, evident from the machining marks on ‘smooth’ (or non-threaded) clinically available tapers as shown in Figure 3.18. With that said, quantitative comparison of roughness amplitudes indicate R_a values of toolholder shanks of 0.803 µm as measured by Zhao et al. [269], compared to the present study where the ‘smooth’ male

tapers presented a smaller S_a of 0.464 ± 0.14 µm. On the other hand, some male tapers present an intended threaded-type finish to increase the roughness amplitude with values of S_a measured by this present study to be 3.16 ± 0.45 µm, greater than that of the toolholder shanks used in the tooling industry. Introduction of a thread was largely attributed to *CeramTec*, a company that manufactures ceramic heads. They specify a roughness of between 6 and 20 μm as reported by Panagiotidou et al. [185].

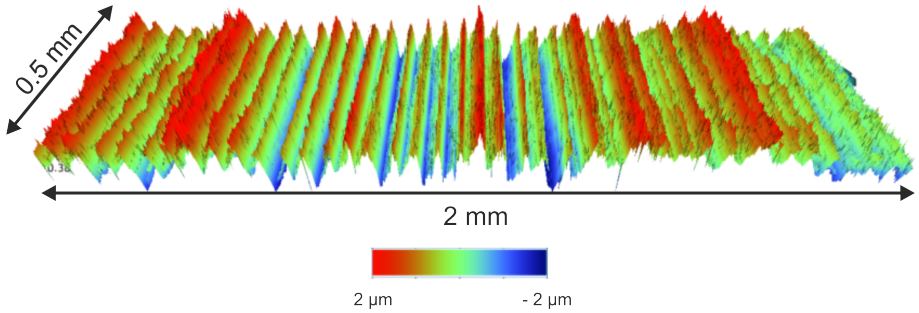

Fig. 3.18 Surface topography of a non-threaded clinically available male taper surface (MT10 in Chapter 4, see Table 3.1).

Surface topography presented a large variation, sometimes varying by whole magnitudes, as was the case with S_a, S_z and S_k (Figure 3.11). The measured values of S_a, S_z and S_k of the 'rough' (with a threaded finish) and 'smooth' (without a threaded finish) samples where in close agreement with R_a, R_z and R_k values measured by Mueller et al. [110]. In contrast, a key difference between this present study and that of Munier et al. [184], was the smaller measured S_a value of the rough samples in the Munier et al. [184] study. This could be due to possible differences in wavelength cut-off used to remove waviness from the roughness measurements. This present study used a value of 0.8 µm, in line with Mueller et al. [110], Munier et al. [184] did not specify their selection of wavelength cut-off. Table **??** summarises the quantitative comparisons of the surface topography roughness amplitude parameters measured by this study compared to those measured by previous peer reviewed studies.

Table 3.3 Roughness amplitude parameters measured by this present study and previous studies.

	Units (μm)	Rough	Smooth
Present Study	Sa	3.163 ± 0.455	0.464 ± 0.144
	Sk	7.598 ± 1.076	1.427 ± 0.241
	Sz	6.858 ± 4.338	15.616 ± 2.084
Mueller et al. [110]	Ra	3.18 0.04	0.49 ± 0.08
	Rk	7.36 ± 0.4	1.63 ± 0.24
	Rz	12.73 ± 0.22	2.63 ± 0.49
Munir et al. [184]	Sa	1.877 ± 1.017	0.407 ± 0.08
	Sk		
	Sz	14.28 ± 3.762	6.972 ± 0.619

As per Mueller [110] and Munier et al. [184], the large variation in roughness amplitude was attributed to the presence, or lack of, the aforementioned 'thread' finish, where MT8, MT9 and MT10 did not present a 'thread', whilst the rest did. Looking at the values of S_k in Figure 3.11 and profiles in Appendix A Figures A.1 and A.2, all the 'threaded' male tapers fall within the *CeramTec* tolerance. The design rationale was to allow plastic deformation upon impaction with ceramic heads, and reduce the risk of burst fracture [232]. However, they are often used with metal heads and this has been found to have implications on performance [186, 226, 164, 187, 163]. This was also highlighted in a recent court case against *Zimmer* [270], where surface finish was identified as a design parameter that can contribute to fretting and corrosion. However, as discussed in Sections 2.6.5 and 2.7.5, the effect of surface topography amplitude as a single design parameter is an unknown by currently literature with a general consensus of longer and smoother tapers presenting less susceptibility to fretting compared to shorter rougher ones corrosion [186, 187, 164]. Possible confusion in the understanding of how surface topography affects taper performance is reflected by the large variability in not just amplitude, but also shape

and distribution between those that can be grouped into ‘rough’ and ‘smooth’ categories, as identified by this present study and will be discussed in more detail below.

The parameters presented in this study (Table 3.2) were selected to parametrise the roughness amplitude and morphology which can help inform plastic deformation, contact compliance (please refer to Section 2.8.4 for further explanation) and its ability to permit fluid ingress. In view of Smith et al. [245] and with reference to Figure 2.40, larger amplitudes, predominantly comprised of peaks and sharper topography were thought to predict an increased contact compliance; these parameter in addition to a lower peak density were thought to predict a greater amount of plastic deformation. On the other hand, fluid ingress was thought to be increased by a greater peak to trough height, a topography predominately composed of valleys, a less sharp surface and a reduced peak density . Therefore, contact compliance and an interface’s ability to resist fluid ingress can sometime be in competition with one another. For example, MT8 might perform quite well in terms of contact compliance for a better engagement, but is likely to perform relatively poorly in terms of allowing fluid ingress. Additionally, contact compliance could have competing effects in terms of the portion of contact asperities within the GSR, PRS and SR i.e. if the working conditions are such that the stick fretting regime (SR) or stick-slip (PSR) are not achieved, an increased compliance could allow for increased disruption of the passive oxide layer (please refer to Section 2.8.3 for further explanation and in particular reference to Swaminathan et al. [234]). At the opposite end of the spectrum, MT7 (see Appendix A.2 for example roughness profile) tended to present a large amplitude, suggesting increased fluid ingress, and a low S_{ku}, for inferior contact compliance.

As mentioned above, a threaded finish was introduced to increase the surface roughness amplitude to that specified by CeramTec. However, this has resulted in larger variabilities in other surface topography parameters including morphology which can be at least in part parametrised in terms of pitch. The pitch differed significantly with a maximum average difference of 0.15 mm between manufacturers (Figure 3.14). This was much larger than the pitch reported by Munir et al. [184] that ranged 0.304 - 0.13 µm. However, on closer inspection of Munir et al. [184], a disparity in the reported pitch and that shown on 3D scans suggest a possible mistake in the reported units. The size of the pitch will influence the interaction and engagement of the taper junction where a pitch of around 0.2 mm only achieves a maximum engagement area of around 16 % as reported by Witt et al. [232]. The pitch present in the samples by Witt et al. [232] was similar to six out of twelve different male threaded tapers measured, where MT7 presented a greater pitch of 0.286 ± 0.005 µm.

It was hypothesised that the ovality present in the surface deviation plots from the ideal cone geometry, could be linked to variations in topography. However, the variation present between stems was greater than that on the stem and so a causal link between geometry

and topography was not found in this study. Other limitations of this study include the lack of surface topography measurements of the female tapers, however, Muller et al. [110] reported a smaller variation compared to the male tapers, with values in R_a varying between 0.23 and 1.48 μm for the female tapers.

3.5 Conclusions

The aim of this study was to assess variations in commercially available male and female THR stem and head tapers in terms of geometry and topography while also identifying key taper design parameters to take forward for further experimental investigation. According to the NJR [111], the samples in this study represent the taper design in implants present in well over half the population that have received THR surgery. As such, variations of geometry and topography captured during this study were representative and can be used to inform the manufacture of samples for further investigation. The two key parameters identified by this study that differed significantly, and around which there is confusion within the current literature, are surface topography and angular mismatch. Quantification of the range in variations of the two identified taper design parameters which were used to inform samples design are as follows:

- angular mismatch ranged from -0.04 to 0.13 ° to create either a distal or proximal engagement respectively;
- 'Smooth' tapers presented a S_a of 0.46 ± 0.14 μm
- 'Rough' tapers presented a S_a of 3.16 ± 0.45 μm

This study successfully quantified a representative group of clinically available modular head-stem taper interfaces of current THR, as such the aim of this study was met. Additional insight, new learning and thinking was also generated, and is summarised below including the relevance of the results to the manufacture of tapers in the orthopaedic industry, implications on clinical practice and implications on previous studies that investigated the modular taper interface:

- the development of new measurement and analysis methodologies to more fully characterise the taper interfaces across the length scales, these were and should be used to capture and take account of any manufacturing variations of samples used for in-vitro experimental studies;

- manufacturing tolerances achieved in the orthopaedic industry were identified as being less stringent compared to other industries, indicating that head-stem tapers can be more precisely manufactured;
- mixing of heads and stems from different manufacturers does happen, the results of this study found that there will be an increased probability of greater magnitudes of angular mismatch compared to where no mixing between manufacturers occurs, and thus the recommendation of not mixing heads and stems from different manufacturers;
- some male tapers presented 'ovality' and deviation in 'straightness' associated with differences of second moments of area, introducing manufacturing variation due to deflections of the workpiece away from the cutting tool, a problem faced by other institutes and from where solutions can be adopted into manufacturing process of orthopaedic components;
- deviations in geometry found by this study has implications on material loss calculations predominantly used by retrieval studies and recommend that pre and post surface topographies are captured for accurate estimations of material loss; and
- large variations in male taper surface topography were largely attributed to the presence of, or lack of, a 'threaded' finish and that more stringent characterisation of surface topography, not just in terms of amplitude but also spatial distribution can control this variation.

3.6 Future Work

This project aimed to help fully characterise the male and female taper interface of clinically available THR by bridging the gap across length scales. This was achieved by employing contacting CMM in conjunction with non-contacting surface profilometry. However, difficulties faced by this project included sample availability and accuracy of correlation between different data sets obtained from the two different measurement methods, please see Section 3.4 for further details.

Future work includes measurement of more samples with at least three repeats per product and measuring each sample with either a roundness measurement machine (RMM) and/or optical CMM. RMM and optical CMM techniques are capable of capturing surface topography as a function of geometry [190, 271]. RMM techniques employed previously used contacting methods with a few micron diameter diamond tipped styli whilst optical CMM techniques use non-contacting profilometry methods. Further outcomes from future

work include obtaining point clouds of data indicative of both surface topography and geometry. The point clouds can help further characterise clinically available taper interfaces and can also be imported for computational studies to supplement in-vitro studies.

Chapter 4

Representative Samples and their Engagement

4.1 Introduction

Engagement between male and female tapers is achieved by assembling the head on the stem and applying an axial force. One of the few parameters consistently identified by pre-clinical studies is that head assembly affects performance of the taper junction. In summary, greater axial assembly forces are associated with greater disassembly forces [228–231, 233], reduced motion and fretting corrosion in-vitro [211, 217, 185, 222, 218]. Additionally, studies that measure the disassembly force often use this to imply the strength and stability of a given head-stem couple. However, assembly and disassembly forces of the modular taper junction are not yet validated parameters of clinical performance. This is due to the lack of control of the assembly process currently afforded intra-operatively.

A study by Jauch-Matt et al. [229] found that shorter 'mini' tapers did not have a detrimental effect on disassembly force, in one case it was found to present a significantly higher resistance to disassembly, attributed to increased contact pressures. However, retrieval and experimental studies indicate that shorter tapers most likely contribute to a poorer taper performance [186, 187, 164, 226, 185, 213]. This indicates, that greater disassembly forces may not always be an indicator of better taper performance in terms of motion and fretting corrosion.

Higher contact stresses over a larger area are thought to be desirable for an interference fit. However, increasing the area for a given assembly force will most likely act to decrease contact pressure, indicating a possible trade-off between area and contact pressure for a given assembly force. This was seen in a study by Muller et al. [264], where an increased proximal angular mismatch lead to significantly higher torque-off values. In contrast,

a ‘rough’ threaded-type surface topography has been found to increase the interfacial pressure compared to ‘smooth’ non-threaded finishes according to computational studies [272], but have also been known to result in a lower disassembly forces compared to their ‘smooth’ non-threaded counterparts [229].

It has been found that an increased assembly force can result in a greater disassembly force [229, 228, 230**?** , 231], reduced motion [211, 212] and fretting corrosion [211, 222, 217**?** , 218], suggesting a possible link between disassembly force and performance. However, there do appear to be other interacting factors that mean disassembly force is not a parameter able to predict performance. Disassembly force can therefore be used to help understand the compressive stress achieved at the taper interface with possible implications on engagement.

This study aimed to investigate the engagement distribution and strength of the representative samples with varying angular mismatch and surface topography of that seen in the clinically available samples, to help determine the relationship, if any, between these taper deign parameters and engagement.

This aim was achieved by first characterising the representative samples in terms of geometry and surface topography in line with the methodology described in Chapter 3. This project also saw the development of a controlled assembly and disassembly methodology beyond that of ISO 7206-10 [134]. More specifically, this involved the design and precision manufacture of fixtures to control the female taper alignment with respect to the male taper. This added control helped isolate the effects of angular mismatch and surface topography on the seating mechanics and disassembly force from any affects due to asymmetrical head assembly. In order to validate this co-axial alignment of the taper junction commonly used engineers blue, used to assess the fits during manufacturing processes, was used to assess areas of contact in the samples by looking at the transferred pattern of the stain from one taper surface to the other. Utilising the precision manufactured fixtures to control the co-axial alignment between male and female taper surfaces, the force displacement response during seating and the disassembly force was then measured as per previous studies such as Ouellette et al. [228]. Greater seating displacements and disassembly forces were associated with greater engagement and a more successful, ‘stronger’ taper connection. This study also employed incremental assembly-disassembly methodology as per previous studies to maximise the amount of data collected. Previously, other studies rationalised this incremental methodology as a way of investigating the influence of in-vivo situations where a well fixed femoral stem is retained during revision surgeries; and by conducting preliminary studies which found that consecutive assembly-disassembly studies had negligible influence on the results due to the stochastic asperity–asperity nature of the contact [229, 233, 228].

4.2 Materials and Methodology

Based on NJR [11] data, head samples were all manufactured from CoCrMo (ISO 5832-6 [180]) and the male tapers were manufactured on cylindrical coupons made from high nitrogen stainless steel (ISO 5832-9 [121]) to represent the most common material couples currently implanted. Figure 4.1 shows schematics of the samples used throughout this project and Table 4.1 details the specification of the surfaces. Nominal engagement length of the male taper was such that it did not sit wholly within the female taper as this is a design variation found to influence taper performance [226], but still presented a clinically relevant nominal engagement length of between 10 and 15 mm found by Mueller et al. [110].

Three different engagement groups were created to represent the range of angular mismatch in the clinical samples, including distal, matched and proximal. The matched and proximal engagement groups were representative of those achieved by clinically available THR. The distal mismatch was exaggerated by approximately -0.05 ° to ensure a distal mismatch was able to be achieved in practice allowing for variation due to the manufacturing process.

Two different surface topographies were created, ‘smooth’ and ‘rough’. The ‘rough’ male taper surface presented a ‘threaded’ type finish to increase the roughness amplitude of the surface topography. The increased surface topography was created by turning the male tapers on a lathe creating a continuous ‘thread’. This resulted in six different test groups (Table 4.1).

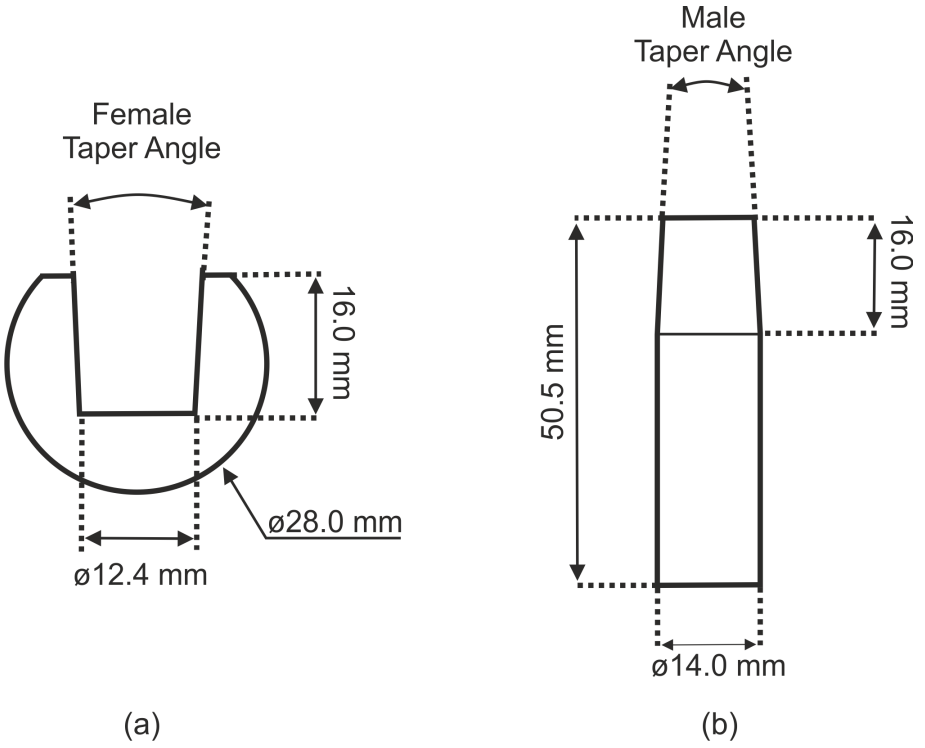

Fig. 4.1 General drawings of samples used throughout the project.

Table 4.1 Specified parameters for taper angle and surface finish for the samples used in this study

Sample Description	Taper Angle (°)	Rz (µm)	Ra (µm)	Quantity
Female Taper	5.725 - 5.805	-	2	18
Smooth Distal Male Taper	5.828 - 5.908	4	0.38	3
Smooth Matched Male Taper	5.728 - 5.808	4	0.38	3
Smooth Proximal Male Taper	5.628 - 5.708	4	0.38	3
Rough Distal Male Taper	5.828 - 5.908	6 - 14	-	3
Rough Matched Male Taper	5.728 - 5.808	6 - 14	-	3
Rough Proximal Male Taper	5.628 - 5.708	6 - 14	-	3

4.2.1 Geometry and Topography

Like clinically available taper interfaces, the samples will present variation due to the manufacturing process. These were captured by fully characterising the surfaces across the length scales using methodology developed in the previous chapter. Geometry was measured with a CMM (Legex 322, Mitutoyo, Japan) and a 1.5 mm diameter ruby to accurately capture the point cloud of data points used to map out each surface. This was then imported into Matlab (R2017a, MathWorks, USA) for calculation of cone angle and

any form deviations from the 'ideal' cone geometry. Cone angle calculations achieved by dividing the taper into quarters were omitted as this was a function of straightness which was captured by the deviations from the 'ideal' cone geometry analysis.

Surface topography was captured using VSI (NPFlex, Bruker, USA) with a 20x magnification and analysed with Vision64 (Bruker, USA). Four, equally spaced 0.25 x 15 mm scans were taken of each male taper in the 12 (θ = 90 °), 3 (θ = 0 °), 6 (θ = -90 °) and 9 ($\theta = \pm$ 180 °) o'clock positions with respect to the etched markings on the flat proximal (Figure 4.2). This differed from the methodology used in the previous chapter due to the cylindrical nature of the coupons. The same parameters detailed in Table 3.2 were used to characterise the surface topography. The female tapers were omitted from measurement with VSI due to not being able to section them.

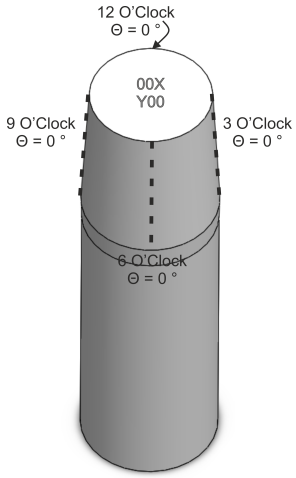

Fig. 4.2 Radial orientation of VSI scans in the 12, 3, 6 and 9 o'clock positions relative to the etched manufacture markings and the equivalent radial coordinate system for surface deviation maps using CMM data.

4.2.2 Assembly and Disassembly Mechanics

All tests were conducted with a uniaxial material testing machine (3369, Instron, US) accurate to ± 0.5 % of the measured force. Assembly and disassembly mechanics were assessed using a similar incremental assembly-disassembly method as used by Ouellette et al. [228]. This study assembled samples to loads from 0.5 to 2 kN in increments of 0.5 kN at a rate of 0.04 mms^{-1} in line with ISO 7206-10 [134]. Disassembly was not carried out at the final loading increment, i.e. when assembled to 2 kN, as the assembled samples were then used in the next chapter for dynamic simulation.

ISO 7206-10 [134] specifies a loading tolerance alignment of 0 ± 1 ° with the longitudinal axis of the neck, where the female taper is allowed to 'self-align' as shown in Figure 4.3a. During the development of this methodology, it became apparent that further control

was required due to a lack of uniform contact from the uncontrolled female taper axis. This was evident in the transferred of blue stain (Blue Micrometer Engineers Marking Paste, ICS, Wales) from the female onto the male taper of a surplus ‘smooth’ proximal sample couple shown in Figure 4.3a.

Figure 4.3b shows a schematic of the developed assembly method and the associated precision manufactured fixtures. The lower fixture held the male taper concentrically with the base of the test frame via two bosses, precision manufactured to 0.005 mm. Likewise, the female taper was held concentrically with the loading axis via the precision dimensions of the box section and a clamp at the pole of the head. Critical linear tolerances of 0.005 mm, resulted in a calculated angular tolerance of under 0.001 ° between the male and female taper with the loading axis.

Using these fixtures and blue stain, the extent of engagement between a surplus ‘smooth’ distal, matched and proximal samples was determined. This was achieved by applying an even thin layer of blue stain to the female taper, letting it dry for 60 seconds, assembling the couples to 500 N, disassembling the samples and observing the transferred pattern on the male taper.

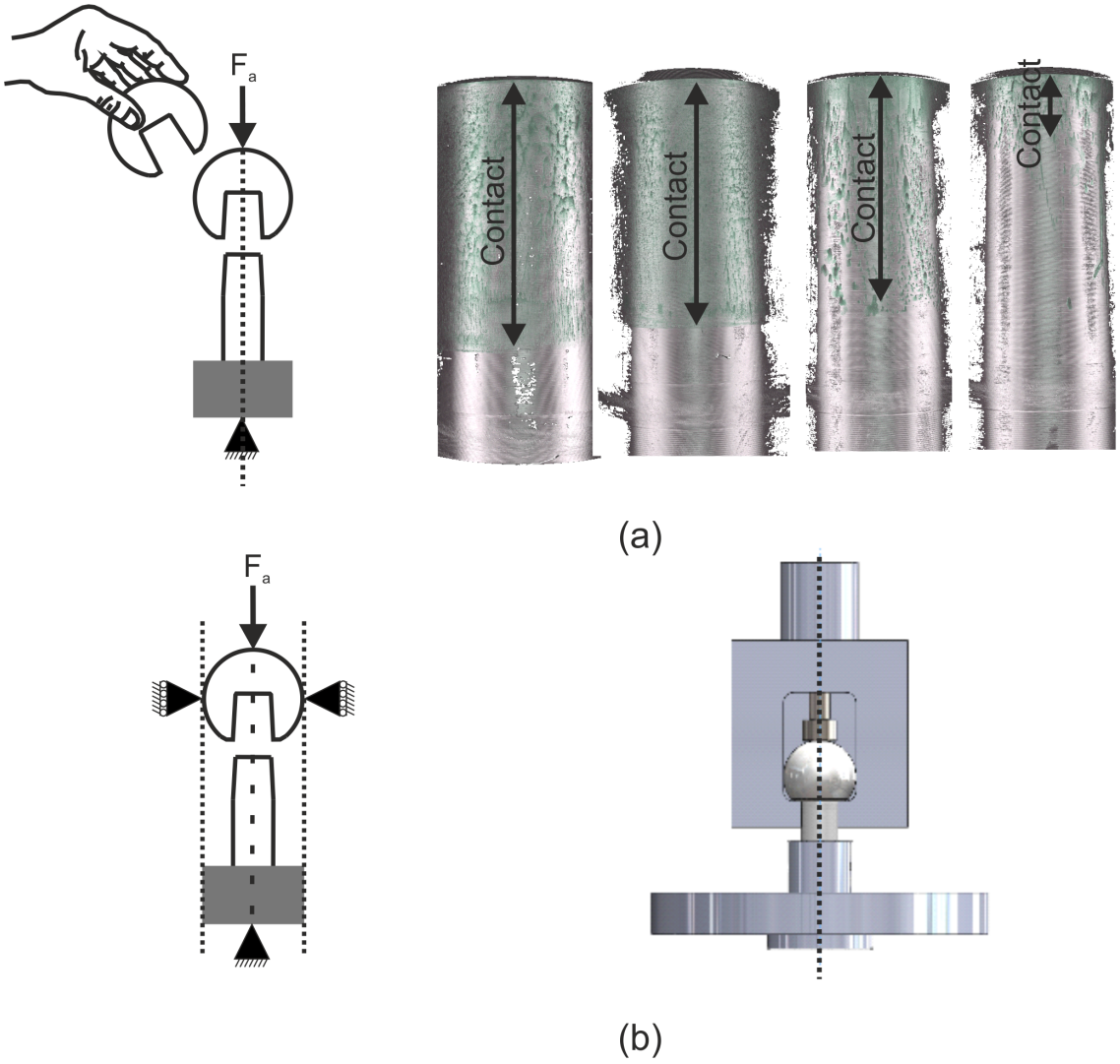

Fig. 4.3 Schematic of (a) the assembly method traditionally used by studies and (b) the resulting distribution of contact distribution from allowing the female taper to 'self-align' at an assembly force of 500 N. Images captured using an *Alicona InfiniteFocus* (InfiniteFocus G5, Bruker Alicona, UK) with x5 magnification. (b) Schematic and precision manufactured fixtures developed to ensure alignment between the male taper, female taper and loading axis.

The assemblies were disassembled at a rate of 0.008 mms^{-1}. Time, force and displacement were recorded at a rate of 10 Hz for assembly and 5 Hz for disassembly with a resolution down to 0.1 mN and 0.01 µm.

Analysis

Raw data was exported as a *.csv* file and allowed for the calculation of seating distance, seating energy and pull-off force using *Matlab* (R2020a, MathWorks, USA). Seating distance or the displacement measured during loading was taken after a small pre-load of

50 N. Seating (assembly) energy was calculated as the area under the force displacement graph (4.4 a). Disassembly force (pull off force) was taken as the peak tensile force registered, as shown in Figure 4.4b. One limitation of taking the displacement data from the test frame was that it was not a direct measure of interface stiffness and will include compliance of the whole load train. During the development stage, displacement closer to the interface was measured and found to have a very similar relationship, with the exception of a small scaling difference. Additionally, a small investigation of some unload data indicated a compressive stiffness of the load train to be around twice that of the assembly stiffness of the smooth samples, predicted to be the least compliant interface. This would indicate that although the reported 'seating displacement' will include elastic compliance from the load train, interfacial stiffness and seating mechanics can be compared within this study.

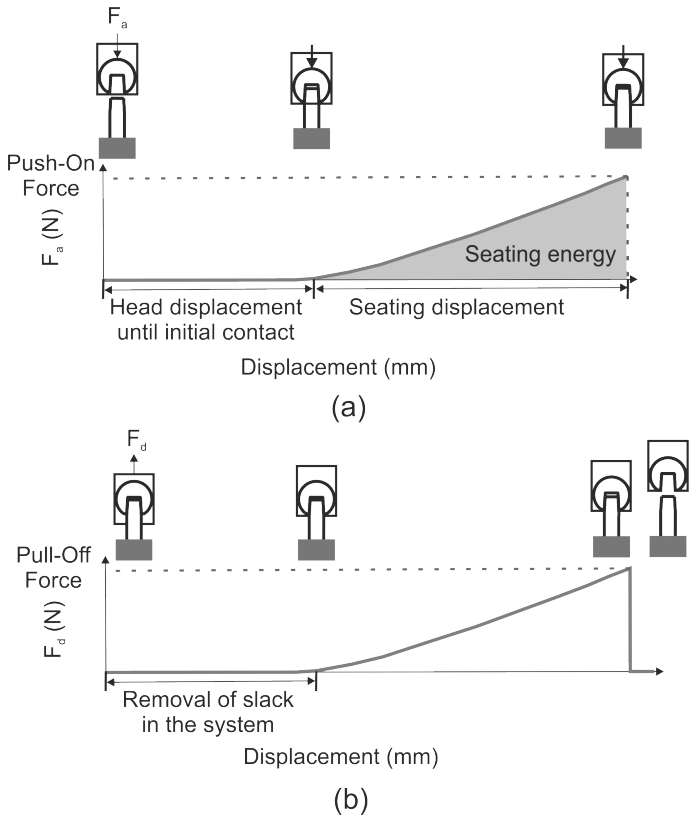

Fig. 4.4 Illustration of force-displacement raw data from (a) assembly and (b) disassembly. Where F_a corresponds to the force applied during assembly and F_d to the force applied during disassembly.

4.2.3 Statistics

Data was presented as mean ± one standard deviation. Results were compared using a two-tailed Student's t-test. Level of significance were set at p-value of 0.05 for all statistical tests and analyses was performed using Excel (Microsoft, USA).

4.3 Results

4.3.1 Geometry

The cone angles for each of the male and female tapers can be seen in Figure 4.5a and b. There was no significant difference between the male taper angles achieved in the 'smooth' samples compared to the 'rough'. The distal samples presented the largest cone angle of 5.855 ± 0.006 °. The proximal samples presented the smallest cone angle of 5.648 ± 0.012 °. The 'matched' samples presented a slightly smaller taper angle compared to the female (5.752 ± 0.002 versus 5.767 ± 0.003, p-value < 0.05). All the samples were within the manufacturing tolerance (0.08 °), only varying by a maximum range of 0.02 °.

The angular mismatch between each sample group can be seen in Figure 3.8c and d. The proximal samples presented a slightly larger mismatch than the distal (0.118 ± 0.003 ° versus -0.089 ± 0.003 °), and the matched groups a small proximal mismatch (0.016 ± 0.004 °). There was no significant difference (p-value > 0.05) between the angular mismatch achieved in the 'smooth' group of each respective groups (i.e. distal, proximal and matched) compared to the 'rough'.

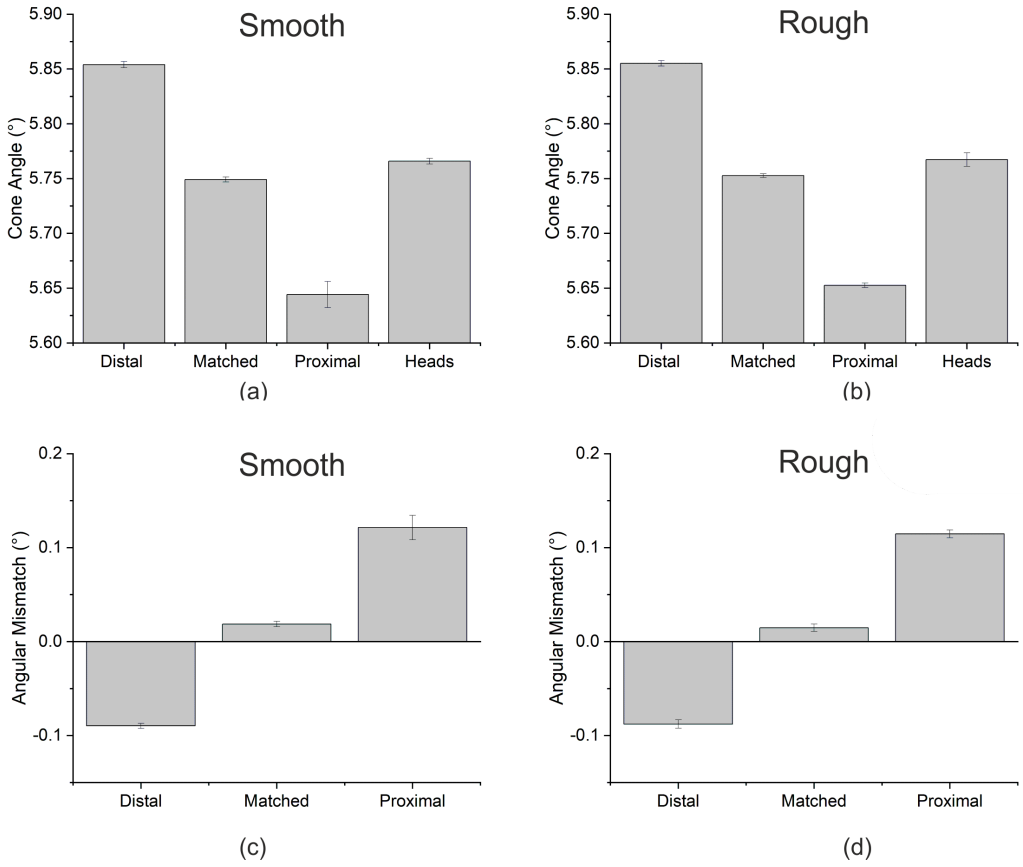

Fig. 4.5 Cone/taper angle assuming an ideal geometry of the (a) 'smooth' and (b) 'rough' threaded-type samples. Angular mismatch of the (c) 'smooth' and (d) 'rough' samples.

Deviations away from the ideal cone superimposed on differences in ideal geometry are thought to influence engagement. Figure 4.6 shows two example deviation maps for each of the female, 'smooth' male and 'rough' male taper groups, chosen to help illustrate the full range that was present. Figure 4.6a shows two female taper surfaces presenting both a triple order harmonic and ovality with an average deviation range of -2 to 2 µm. This is in contrast to the clinically available female tapers with a larger range of around -4 to 4 µm (Figure 3.10).

Figure 4.6b shows the 'smooth' male tapers that presented a slight amount of ovality with a tendency for the surface to lay slightly below the ideal cone towards the centre, and above at the proximal and distal regions, the average deviation range was -1 to 1 µm. The 'rough' male taper presented the greatest variation with two noticeably different deviation patterns seen in Figure 4.6c where the average deviation range was around 2 to -2 µm with the exception of the 'rough' proximal male tapers with a range around -3 to 3 µm. This is in comparison to the range of -4 to 4 µm (Figure 3.9g and k) seen in the 'smooth' clinically available male tapers and -5 to 5 µm in the 'rough' clinically available male tapers (Figure 3.9a, b, c, d, e, h, i, and j).

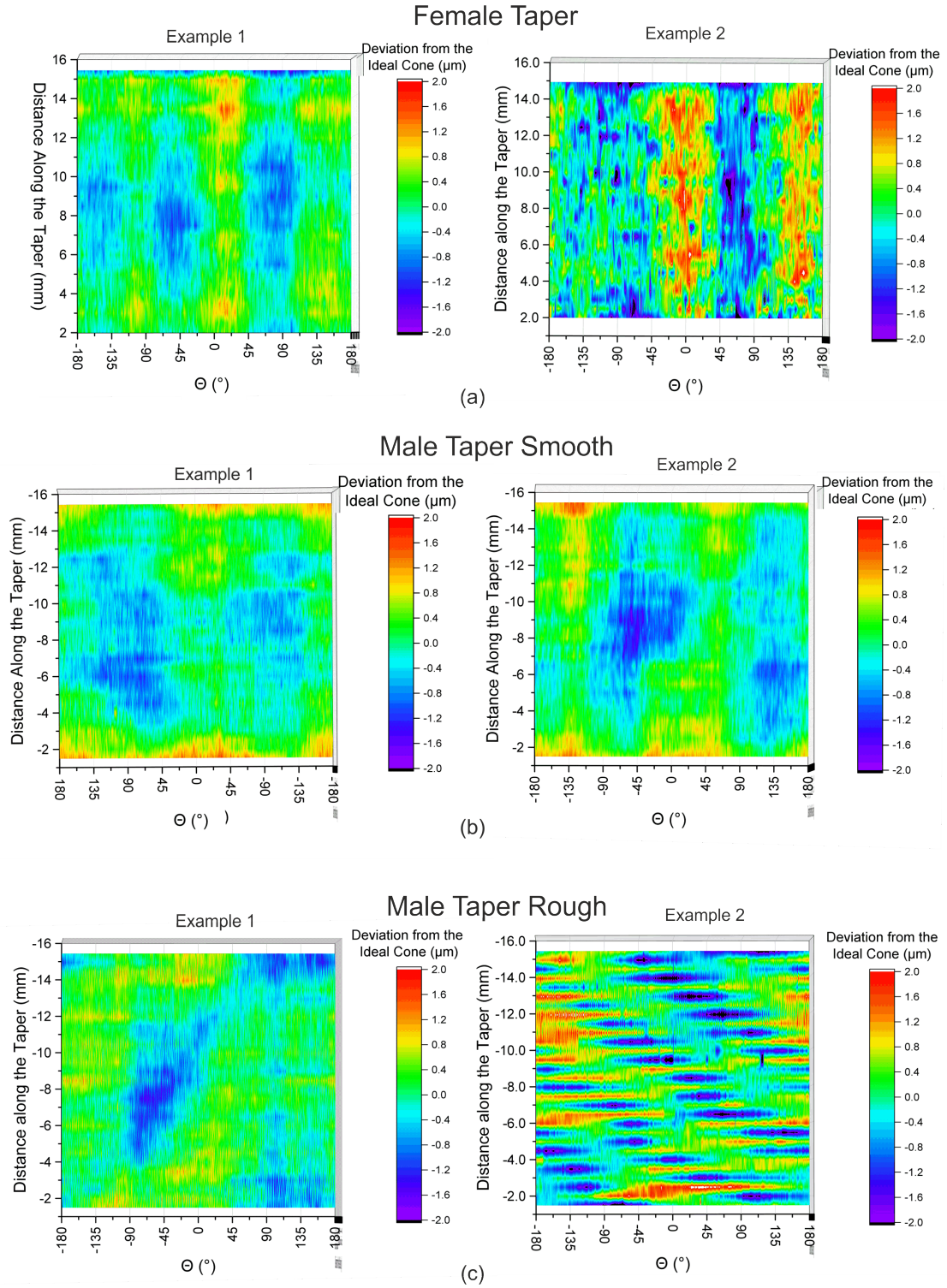

Fig. 4.6 Surface Deviation plots of the (a) female tapers, (b) ‘smooth’ male taper and (c) ‘rough’ male taper.

4.3.2 Topography

The 'rough' samples presented a greater roughness amplitude than the 'smooth' in terms of S_a, S_k and S_z (Figure 4.7a). Where the 'smooth' samples presented a S_a of 0.505 ± 0.167 µm, compared to the 'rough' with 2.474 ± 1.017 µm (p-value< 0.05). Likewise, 'smooth' presented a S_k of 1.59 ± 0.47 µm verses the 'rough' with 7.667 ± 3.796 µm.

There was a large difference in roughness amplitude between the 'rough' proximal samples (S_a of 3.888 ± 0.141 µm) and the 'rough' distal and matched (S_a 1.771 ± 0.018 µm p-value < 0.05 and 1.762 ± 0.068 µm p-value < 0.05, respectively). Example roughness profiles illustrating this are shown in Figure (Figure 4.7b). Variation in roughness amplitude was also seen between the 'smooth' distal engagement group and the matched and proximal engagement group of equivalent surface topography. The 'smooth' distal engagement group samples presented an S_a of 0.700 ±0.154 µm compared to the matched with and S_a value of 0.424 ±0.027 µm (p-value < 0.05), and the proximal with S_a value of 0.392 ±0.141 µm (p-value < 0.05). This was also reflected in values of S_k and S_z.

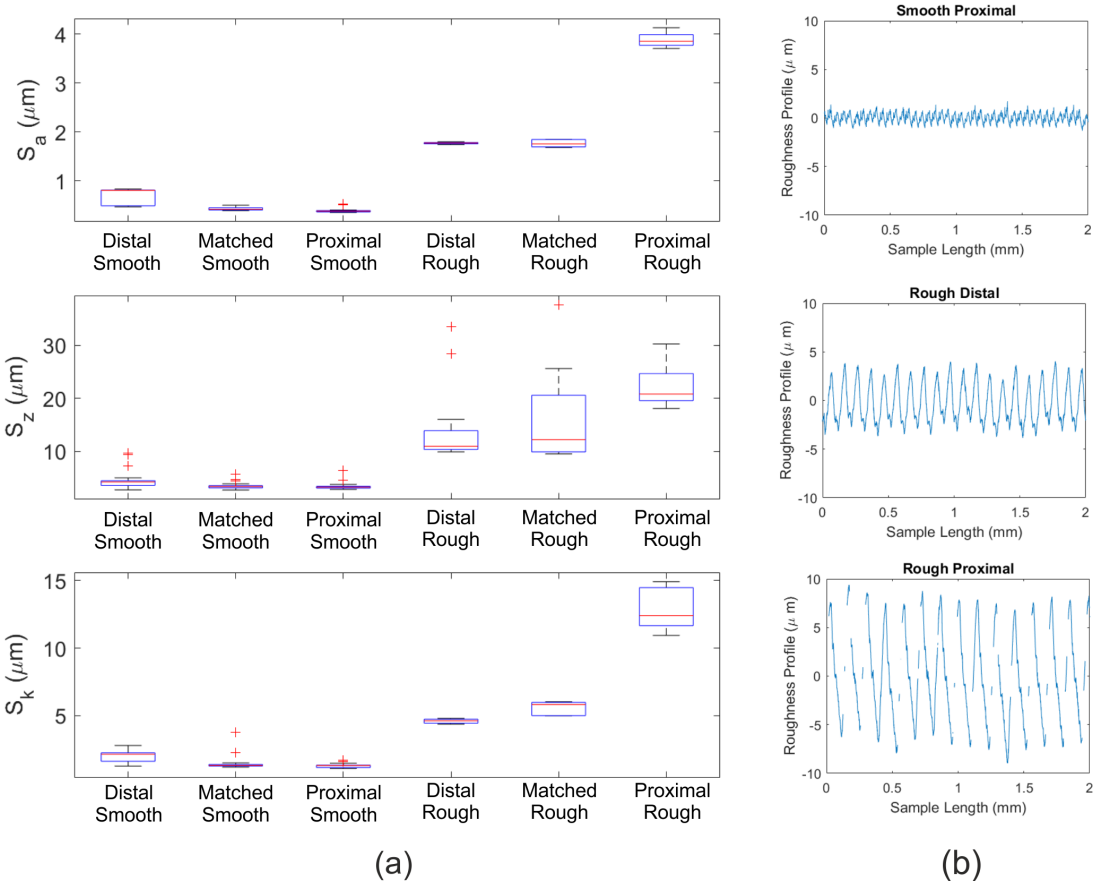

Fig. 4.7 (a) Box plots of statistical surface topography parameters of the samples used in this project to characterise amplitude, including S_a, S_z and S_k. (b) Example roughness profiles.

Figure 4.8a shows the shape and distribution parameters of the roughness profiles. The 'skew' (valleys versus peaks, S_{sk}) and sharpness (S_{ku}) of the profile did not appear to be a function of the two different surface topographies created in this study. On the other hand, the density of protruding peaks (S_{pd}) above the core roughness amplitude (S_k) was much greater in the 'smooth' samples compared the 'rough' (5387 ± 515 mm^{-2} versus 1499 ± 92 mm^{-2}, p-value < 0.05).

The majority of sample groups presented a positive S_{sk} indicating that the roughness profile tended to lay below the reference and the profile was dominated by peaks. The 'smooth' distal sample presented a negative S_{sk}, indicating a prominence of valleys. The distal 'smooth' samples also presented a smaller S_{ku} of 1.686 ± 0.186 compared to the 'smooth' matched (2.287 ± 0.112, p-value < 0.05) and 'smooth' proximal (2.273 ± 0.152, p-value < 0.05), indicating a less 'sharp' topography. Figure 4.8b shows an example roughness profile of the 'smooth' distal and 'smooth' matched to illustrate the 'spikier', valley dominated profile of the 'smooth' distal sample.

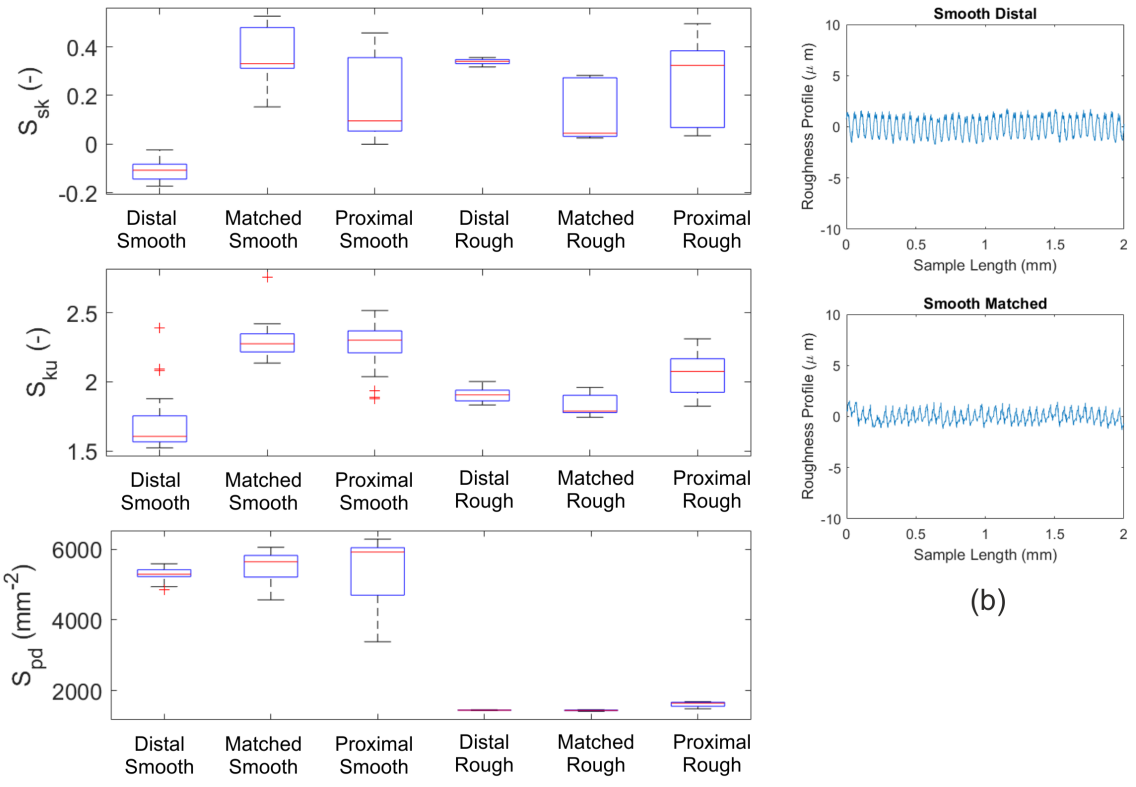

Fig. 4.8 (a) Box plots of statistical surface topography parameters of the samples used in this project to characterise the shape and distribution of the roughness profile, including S_{sk}, S_{ku} and S_{pd}. (b) Shows example roughness profiles.

4.3.3 Engagement Distribution

Engagement distribution patterns are shown in Figure 4.9. The distal group presented a strong concentration around the opening of the taper, while the proximal group presented at the inner most part of the interface. The matched samples showed a much more even distribution of engagement with evidence of a lower concentration of blue stain transferred in some regions, like that towards the middle of the interface.

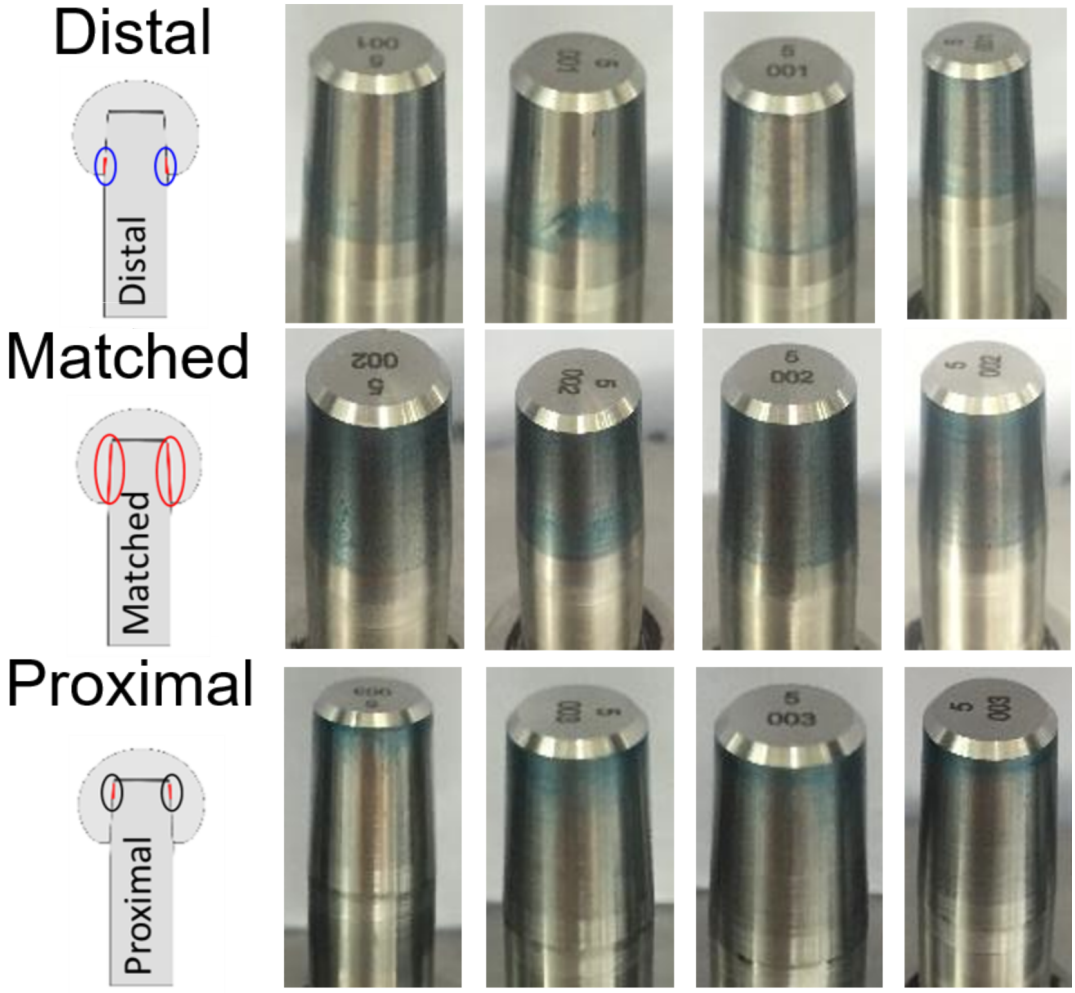

Fig. 4.9 Engagement distribution shown by the transferred pattern of the stain from the female head to the male taper for the three different 'smooth' sample groups: distal, proximal and matched.

4.3.4 Assembly Mechanics

This section presents the seating displacement and seating energy of the samples. Looking firstly to the force-displacement, Figure 4.10 shows an example force-displacement response of a 'smooth' proximal sample for each incremental assembly processes. The four loading assemblies demonstrated a very similar force-displacement response with a directly proportional linear relationship between displacement and force with the expectation of a slip event between 0.02 and 0.6 mm displacement. The slip event is identifiable by the sudden decrease in force with increase displacement.

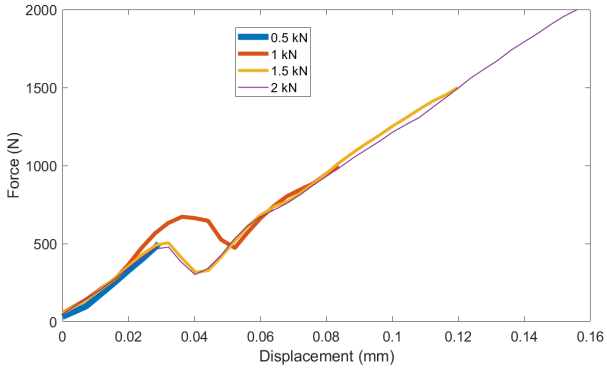

Fig. 4.10 Example force displacement response for each of the four assemblies from 0.5 to 2 kN of a proximal 'smooth' sample.

The seating displacement increased with assembly force, shown in Figure 4.11. The 'rough' samples presented a greater displacement compared to 'smooth' but this was not found to be significant for a given engagement at any given assembly increment (p-value > 0.05). In the final assembly increment of 2 kN, the 'rough' distal presented a displacement of 0.42 ± 0.12 mm compared to the 'smooth' distal with 0.14 ± 0.01 mm (p-value > 0.05), the 'rough' matched a displacement of 0.44 ± 0.08 mm compared to the 'smooth' matched with 0.16 ± 0.01 mm (p-value > 0.05), and the 'rough' proximal 0.29 ± 0.08 mm compared to the 'smooth' proximal 0.16 ± 0.01 mm (p-value > 0.05). The 'rough' samples all presented a much greater variation in displacement compared to the 'smooth' samples.

The 'rough' matched samples presented a greater seating displacement compared to the 'rough' proximal (p-value < 0.05). However in addition to the difference in angular mismatch, a difference in surface topography between the 'rough' matched and 'rough' proximal samples should also be noted. The rough' distal sample also presented a greater seating displacement compared to the 'rough' proximal but this was not found to be statistically significant (p-value > 0.05). In the 'smooth' samples, displacement did not appear to be sensitive to different engagement groups.

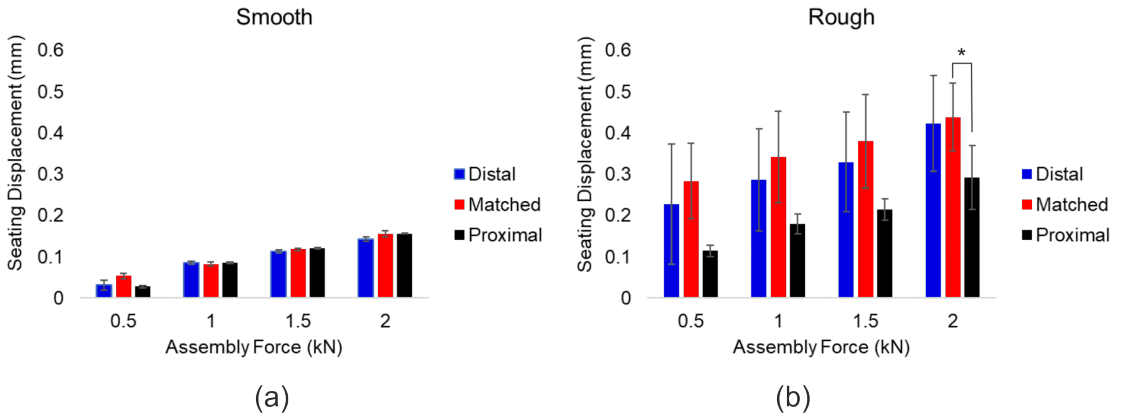

Fig. 4.11 Seating displacement at each increment for the (a) 'smooth' and (b) 'rough' taper couples. The '*' indicates a significant difference with p-value < 0.05.

The seating energy is a product of the assembly force and displacement, and is summarised for each sample group at an assembly load of 2 kN in Table 4.2. Like seating displacement, seating energy did not appear to be sensitive to angular mismatch (p-value > 0.05). The 'rough' samples presented a greater average seating energy compared to the 'smooth' of comparable angular mismatched but was not found to be statistically significant (p-value > 0.05).

Table 4.2 Average seating energy and standard deviation of each sample group when assembled to 2 kN.

	Seating Energy (N.mm)	
	Smooth	Rough
Distal	150 ± 7	601 ± 275
Matched	169 ± 7	614 ± 210
Proximal	164 ± 2	366 ± 43

4.3.5 Disassembly

Disassembly force at each assembly increment (with the exception of the 2 kN assembly force increment as these were used for dynamic simulation in the next chapter) and for each sample group can be seen in Figure 4.12a and b. Disassembly force increased with assembly force. For both the 'smooth' and 'rough' groups, disassembly force was insensitive to the level of angular mismatch present in these samples. There was no significant difference between the distal, matched and proximal groups with the exception of between the 'smooth' distal and 'smooth' proximal assembled to a force of 0.5 kN (92 ± 40 N versus 155 ± 24 N, p-value < 0.05, Figure 4.12a).

Comparing the ‘rough’ and ‘smooth’ for a given engagement, the ‘smooth’ proximal samples presented a smaller disassembly force compared to the ‘rough’ proximal when assembled to 0.5 kN (155 ± 24 N versus 398 ± 85 N, p-value < 0.05) and 1.5 kN (328 ± 92 N versus 864 ± 64 N, p-value < 0.05). The ‘smooth’ distal samples also presented a statistically smaller value of disassembly force when assembled to 500 N (92 ± 40 N versus 308 ± 38 N, p-value < 0.05).

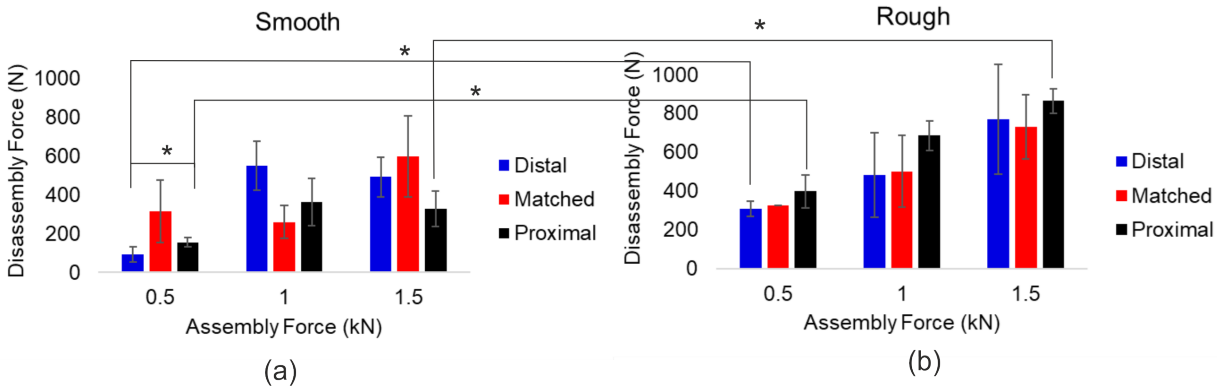

Fig. 4.12 Disassembly force vs assembly force for the (a) ‘smooth’ and (b) ‘rough’ sample groups. The ‘*’ indicates a significant difference with p-value < 0.05.

4.4 Discussion

This study aimed to investigate the engagement of head-stem modular taper junctions in THR as a function of both surface topography and angular mismatch to determine what, if any, relationship existed between these two taper design parameters and engagement. This was achieved by first manufacturing controlled test samples with varying surface topography and angular mismatch as informed by Chapter 3 and then measuring the seating mechanics and disassembly forces.

4.4.1 Characterisation of the Samples - Geometry and Surface Topography

Six different test groups were created to assess the effect of surface topography and angular mismatch on engagement. More specifically, two lots of proximal, distal and matched engagement groups, the male taper surface topography of one lot presenting a threaded-type finish to create a ‘rough’ finish, while the other did not, to create a ‘smooth’ finish. It was thought that the two different finishes might present a source of variation in the geometry due to a slightly different manufacturing process, but this was not the case with

no significant difference between the taper angles achieved in the same engagement group of different surface topographies (p-value < 0.05, Figure 4.5).

These cone angles created a distal engagement couple with a mismatch of -0.088 ±0.004 °, matched 0.015 ±0.004 ° and proximal 0.120 ±0.01 °. Although the matched and proximal engagement groups were representative of those achieved by clinically available THR (please refer to Chapter 3 for further details), the distal mismatch was more extreme on average by -0.05 °. This was due to the manufacturing tolerance allowing a window of 0.08 °, the mismatch was slightly exaggerated to be able ensure a distal mismatch could be practically achieved. However, despite the allowable manufacturing tolerance range of 0.08 °, the taper angles for each sample group where found to be precise with an average standard deviation of 0.005 °. As discussed in the previous chapter, this could place these samples within the tolerance grade of AT2 - AT3, much closer to that achieved in CNC machines capable of precision manufacture at AT3 or tighter [260], compared to those in clinically available THR at AT8 or beyond (please refer to Chapter 3 for further details). It could be argued that these samples are then no longer representative of clinical samples, however they do provide tight geometrical control for future systematic investigations. These samples were manufactured by an orthopaedic company, suggesting manufacturers may have the capacity already to manufacture samples to tighter tolerances.

The precise manufacture of the samples was also evident in the surface deviation maps in Figure 4.6 when compared to the clinically available taper interfaces in Chapter 3, Figures 3.9 and 3.10. The head samples presented a deviation range of around -2 to 2 µm, smaller than the range in clinically available female tapers with a range of around -4 to 4 µm. Likewise, the 'rough' male taper group of this present study presented a range of around -3 to 3 µm compared to -5 to 5 µm seen clinically. The 'smooth' male taper samples presented a deviation range of around -1 to 1 µm compared to -4 to 4 µm seen clinically. Figure 4.13 shows histogram plots of distributions of measured CMM points grouped into bins defined by their deviation from the ideal cone for a 'smooth' male taper sample of this present study compared to that of a clinically available 'smooth' male taper (MT10) measured in Chapter 3. The example sample manufactured for this study presented a much narrower distribution compared to that of the example clinically available taper, further demonstrating the precision manufacture of the samples manufactured for this present study compared to that achieved by tapers of femoral stems currently implanted into patients.

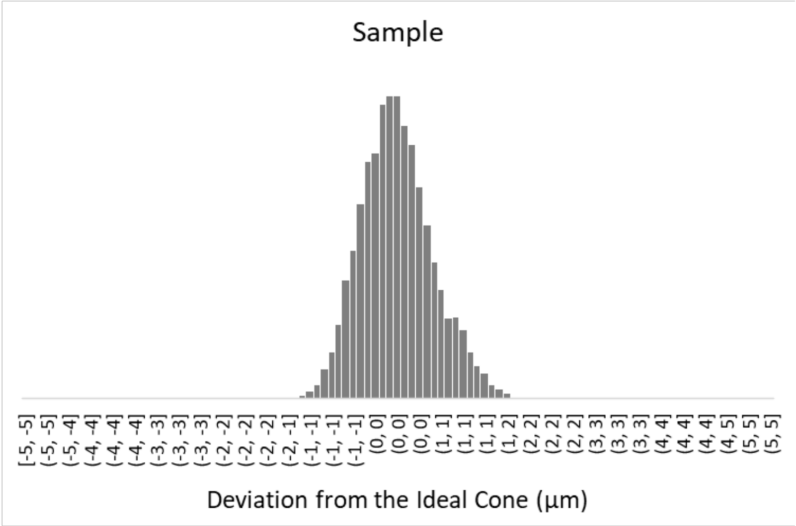

(a)

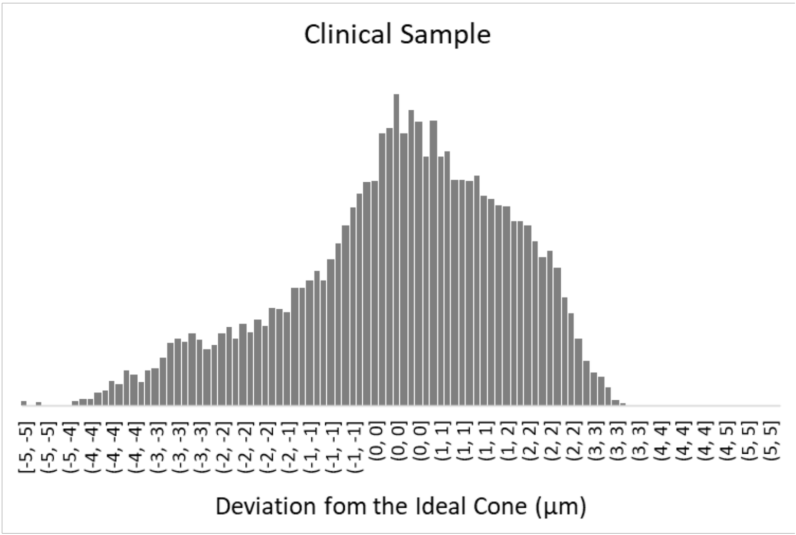

(b)

Fig. 4.13 Histogram distribution plots of deviation from the ideal cone for (a) a 'smooth' male taper surface compared to (b) a clinically available 'smooth' male tape from a femoral stem measured in Chapter 3 (MT10).

The three different distal, matched and proximal engagements were clearly seen in the transferred patten in Figure 4.9. Clear concentrated radial bands of stain were seen in the distal and proximal samples at the distal and proximal radial ends of the interface, respectively. The matched samples presented a more even distribution of transferred stain with evidence of the deviation patterns in Figure 4.6. More specifically, the picture of the 3 o'clock position (middle left of the matched row in Figure 4.9) shows evidence of the surface laying slightly below the ideal cone geometry towards the middle of the interface. In the 9 o'clock position evidence of engagement appears towards the top of the interface (middle row far right picture in Figure 4.9), indicative of the slight proximal mismatch. Comparing this now to Figure 4.6b, the deviation heat maps of the 'smooth' male taper,

blue regions indicating material below the ideal cone geometry towards to centre of the taper with a depth of between -1.3 and -0.5 µm. This material lying below the ideal cone geometry, superimposed on a slight proximal mismatch of 0.015 ±0.004 °, corroborates the finding of the transferred pattern. Looking now to a previous comparable peer-reviewed paper, Jones et al. [265] also identified material laying below the ideal cone towards the middle of the interface, along with some ovality. This was shown by regions of no contact below the apex and towards the base of the interface. This relieving of the centre of the taper interface has been reported as an intentional design feature in the tooling industry [109]. Historically, precision manufacture of the toolholder was extremely difficult to achieve, which lead to the centre of some tapers being relieved, making it easier to ensure engagement at either end for minimising motion or 'chatter' [109].

Two different surface topographies were created. The 'smooth' male tapers achieved an S_a of 0.505 ±0.167 µm and S_k 1.590 ±0.471 µm, similar to clinically available samples measured previously with S_a 0.464 ±0.144 µm and S_k 1.427 ±0.241 µm (refer to Chapter 3), and similar to the *Hipstar* stem by *Stryker* [110]. The 'rough' male taper samples achieved average amplitude parameters of S_a 2.474 ±1.0177 µm and S_k 7.667 ±3.796 µm, similar to that of the clinically available taper junctions with S**a** 3.163 ±0.455 µm and S**k** 7.598 ±1.077 µm (refer to Chapter 3), the *Corail* by *DePuy* and *SL-plus* by *Smith & Nephew* [110]. As such, the surface topographies represent a 'smooth' and 'rough' clinically available samples for further investigation.

As noted in Chapter 3, there was a large variation in surface topographies, not just in amplitude but also parameters that capture spatial distribution and shape of clinically available stem interface topographies. Findings from this study highlight the possible limitations in the degree of which surface topographies can be controlled by current manufacture processes. Hence, the variation in clinically available modular taper interfaces might not necessary be by design but rather manufacturing variation. This was shown most notably by the 'rough' proximal samples that presented a greater roughness amplitude compared to the other engagement groups with 'rough' surface topography. Additionally, this was also seen in the 'smooth' sample groups with the distal engagement group presenting a greater roughness amplitude and smaller S_{sk} and S_{ku} compared to the match and proximal samples with a 'smooth' finish.

Unlike the 'smooth' samples, the 'rough' samples did present a manufacturing tolerance of a maximum peak-to-trough height of between 6 and 14 µm. Looking at the S_z values in Figure 4.7 would place the majority of 'rough' samples out of tolerance. However, S_z is the sum of the maximum peak and valley over the whole scan independently, and were not representative of the average peak-to-trough height of the surface (see example profiles in Figure 4.7b and Appendix B Figure B.1). Therefore, looking to S_k and the example

profiles in Appendix B.1 for a more accurate understanding of average peak-to-trough height would place the 'rough' distal and matched samples, within the lower tolerance, two out of three 'rough' proximal samples just over tolerance by around 1 μm and the other within the upper tolerance. Given the above, how surface roughness amplitude parameters are calculated present limitations in accurately parameterising the average peak-to-trough height. Nevertheless, the variation in surface topography of the 'rough' samples does highlight a possible limitation in current manufacturing processes.

4.4.2 Engagement - Seating Mechanics and Disassembly Force

The samples created were representative of head-stem taper junctions of clinically available THR and characterised in terms of both geometry and surface topography and then used to investigate engagement. Previously, 'taper engagement strength' has been assessed using assembly and disassembly studies [228]. The experimental methodologies of previous studies were largely dictated by ISO 7206-10 [134] which specifies a tolerance of 0 ± 1 ° between the male taper axis and the loading axis whilst the head taper is free to self-align. However, during the development of the experimental methodology of this present study, it became apparent that further control was required due to a lack of uniform contact from the uncontrolled female taper axis. This saw the development of a more controlled assembly process by designing and developing fixtures to align the loading axis, male taper axis and female taper axis to within an angular tolerance of 0.001 °. These fixtures were then used to hold the samples to allow force and displacement measurements, permitting the investigation of how taper design influenced the seating mechanics and disassembly forces, and thus engagement. This beyond the state of the art assembly methodology also has clinical implications in view of Bormann et al. [191]. Referring back to Figure 2.26, there is shown a variation of degradation within a taper interface of a retrieved implant which was attributed to a non-uniform head assembly. Hence, results from this present study offer justification for the development of improved surgical instrumentation for intra-operatively controlling the loading axis, female and male taper axis.

Starting with the relationship between assembly force and engagement, assembly force being one of the few individual factors consistently supported by experimental studies to affect engagement, fretting corrosion and motion at the taper interface. Consistent with these previous studies, this present study found that with an increased assembly force there was an increased seating displacement and disassembly force [228–231, 233]. This was attributed to an increased compressive force as the female taper travelled down the male taper for a greater frictional interaction at the interface. More specifically and in agreement with other studies such as Ouellette et al. [228], the relationship between assembly force

and disassembly force of this present study was linear, with a disassembly force of around 30 to 67 % of the assembly force. In comparison to other comparable peer reviewed studies, Ouellette et al. [228] found a disassembly force of between 43 and 68 % of the assembly force, Rehmer et al. [230] a disassembly force of between 25 % and 50 %, and Jauch-Matt et al. [229] a disassembly force of 25 ± 10 % of the assembly force. As such the measured disassembly forces measured by this study were in agreement with that measured previously offering verification of the measurement methodology.

Comparing seating displacements, Ouellette et al. [228, 222] and Mali and Gilbert [211] used CoCrMo-CoCrMo and CoCrMo-Ti couples (with one study identifying a 'smooth' surface finish), indicated a seating displacement in the region of around 0.1 to 0.2 mm when assembled to 2 kN, as deduced from example force-displacement graphs. In comparison, this study presents a range in seating displacement of 0.13 to 0.16 mm for the 'smooth' samples and 0.2 to 0.5 mm for the 'rough' samples when assembled to 2 kN. Therefore, the 'smooth' samples fall within the range reported by other studies, but the 'rough' samples indicate a more compliant interface, with larger displacements than those reported previously. However, one limitation of this study was that displacement was taken from the test frame and was not a direct measure of interface stiffness. The measured seating displacements will therefore include compliance of the whole load train whilst other studies used displacement sensors placed at the interface to exclude any load train compliance. As such, analysis of seating displacements of this study should only be used comparatively with other seating displacements within the study.

Table 4.3 summarises the pertinent findings of the above discussed peer-review studies along with those of this present study.

Table 4.3 Seating displacement and disassembly forces of this present study compared to previous comparable peer reviewed studies. * number determined from figures within.

Study	Samples	Assembly Force (N)	Seating Displacement (μm)	Disassembly Force (N)
Present Study	Smooth distal	1500	113 ± 3	492 ± 103
	Smooth matched	1500	118 ± 3	598 ± 210
	Smooth proximal	1500	121 ± 1	328 ± 92
	Rough distal	1500	329 ± 121	769 ± 238
	Rough matched	1500	380 ± 113	731 ± 166
	Rough proximal	1500	214 ± 27	864 ± 64
Ouellette et al. [228]*	CoCrMo-Ti6AL4V, 9/10, unknown angular mismatch and 'rough' male taper finish	4000	150 ± 25	2000 ± 350
	CoCrMo-CoCrMo, 12/14 taper with an unknown angular mismatch and R_a 0.3 μm male taper finish	4000	200 ± 25	1750 ± 250
Rehmer et al. [230]*	CoCrMo-CoCrMo, 0.024 ° angular mismatch and male taper R_a value of 2.74 μm	2000		1000 ± 125
		3000		1500 ± 300
		4000		2000 ± 300
Jauch-Matt et al. [229]*	CoCrMo-Ti6AL4V, 12/14 taper, 0.10 ±0.05 ° angular mismatch and male taper R_a 2.92 ±0.44 μm	2000		600 ± 100
		4000		1050 ± 50
		6000		1490 ± 125
	CoCrMo-Ti6AL4V, 12/14 taper, 0.10 ±0.05 ° angular mismatch and male taper R_a 4.41 ± 0.54 μm	2000		500 ± 50
		4000		800 ± 60
		6000		1400 ± 200

Surface Topography

A 'rougher' surface topography on male tapers and a proximal angular mismatch in THR were design parameters introduced by *CeramTec* to allow plastic deformation of the male taper when assembled with a ceramic head to reduce the risk of burst fracture while also supporting most stress towards the equator of the femoral head [16]. However, this rougher surface topography is used with metal heads [262], and we know from the findings of Chapter 3 supported by statements by Morlock et al. [262], that this is not always in conjunction with a proximal angular mismatch. Hence, investigating the seating mechanics and disassembly force with an aim of understanding the influence on engagement is of clinical interest.

In line with *CeramTec*'s rationale of increased plastic deformation with an increased roughness, it was thought that an increased roughness amplitude would result in an increased seating displacement. On average the 'rough' samples presented a greater seating displacement (Figure 4.11) and energy (Table 4.2) compared to the 'smooth' of comparable angular mismatched, on average by 0.23 ±0.1 mm but was not found to be statistically significant (p-value > 0.05) with a large variation found in the measured seating displacements of the 'rough' samples. In comparison to a recent comparable study, Mai et al. [273] found that the smoother samples (R_z 1.76 ±0.15 µm) presented a smaller average seating displacement yet a larger variation therein of 0.25 ±0.08 mm compared to the 'rough' samples (R_z 14.74 ±0.22 µm) with 0.3 ±0.03 mm (as interpreted from Figure 7, [273]). One possible explanation for the contrasting finding of the smoother samples presenting a greater variation in measured seating displacement by Mai et al. [273], could be that Mai et al. [273] used a much greater pre-load force of 700 N and assembled to 3 kN, and so much of the force displacement response measured by this present study, namely that between 50 N and 700 N, was not measured by Mai et al. [273]. Mai et al. [273] also reports that assembly did not result in plastic deformation of the surface but engagement between the taper interfaces was supported elastically, indicating that the assembly loads used by this present study may not be large enough to sufficiently investigate engagement. Looking now to a less comparable study of Witt et al. [232] who investigated engagement by spluttering the male taper with a thin coat of gold and investigating the abraded pattern. Witt et al. [232] found that engagement at 500 N was not always achieved with the number of thread peaks found to be in contact to be 9.2 ±9.3 %, compared to 65.4 ±10.8 % at an assembly force of 2000 N. As such, findings from this study at low assembly forces 500 N should not be interpreted in isolation when drawing conclusions about engagement.

The greater average seating displacement and energy, albeit not statistically significant, seen in the 'rough' samples compared to the 'smooth' of comparable surface roughness was thought to be associated with greater engagement and thus higher disassembly forces.

This study found greater disassembly forces in the 'rough' distal and proximal samples compared to the 'smooth' distal and proximal samples respectively at a 500 N assembly force. Although as discussed above, equating greater disassembly forces to better engagement at such low assembly forces may not be an accurate reflection of better engagement. On the other hand, the 'rough' proximal samples presented a greater disassembly force compared to the 'smooth' proximal samples when assembled to 1.5 kN, however, it should be noted that the 'rough' proximal samples presented a greater roughness amplitude compared to the 'rough' distal or 'rough' matched. Furthermore, at assembly forces of 1.5 kN, the disassembly forces was on average greater in the 'rough' samples of equivalent engagement, namely the distal and matched engagement groups, but this was not found to be statistically significant. This is in agreement with Mueller et al. [233] who found that 'rough' tapers presented a larger twist-off force than the 'smooth' samples, but this was not found to be significant. A possible explanation as to why greater disassembly forces might have been seen with an increased roughness amplitude in some couples could be found in FEA studies such as Bechstedt et al. [272]. Bechstedt et al. [272] reported an increased contact pressure with roughness amplitude and more specifically, a greater contact pressure of 1112 MPa was found when a head was assembled to 2 kN with micro groove height of 2 μm compared to 515.2 MPa with a micro groove height of 11 μm. Hence, it is thought that an increased contact pressure at the interface can increased the frictional interaction for improved engagement.

There are contrasting studies, such as Yavari et al. [274] and Mai et al. [273] who found a decrease in disassembly force with an increased in roughness amplitude, attributed to a reduced area of actual contact area with 'rougher' surface topography. Another such study was that by Jauch-Matt et al. [229] who found a reduction in disassembly force by around 100 N with an increase in average peak-trough height of around 8 μm. However, one possible reason for this could be that the 'smooth' male taper used by Jauch-Matt et al. [229] still presented a R_a of around 3 μm, R_z of around 8 μm and average peak-trough height of 7.5 μm, meaning that the average roughness amplitude was closer to the 'rough' distal and matched samples used in this study. Again, another contrasting study includes that by Denkena et al. [275] who reported that disassembly force did not correlate with roughness amplitude (R_z). Looking to FEA studies to help elucidate these contrasting findings, Bechstedt et al. [272] also found a decrease in actual contact area with roughness amplitude, in addition to an increased contact pressure as discussed previously. Hence, there is a possible trade-off between contact pressure and actual contact area when understanding the influence of surface topography on engagement which might explain these contrasting findings.

As mentioned above, Denkena et al. [275] reported that disassembly force did not correlate with roughness amplitude (R_z), also reported that there was a weak correlation with contact ratio (R_k/R_z) and thus, surface topography with many plateaus would increase the disassembly force predicting a better engagement. Looking at this present study, surfaces with smaller S_{ku} values (less 'spikey') would predict a surface topography with more plateaus, and in conjugation with a more negative S_{sk} (roughness profile dominates by valleys) would describe a surface with more plateaus at peaks that are more likely to be in contact with the female taper interface. As per Denkena et al. [275]'s weak correlation between disassembly force and contact ratio, the 'smooth' distal samples of this present study would present an increased disassembly force compared to the 'rough' distal. In contrast, this present study found that the 'smooth' distal samples presented a smaller disassembly force compared to the 'rough' distal and was not found to be statistically significant.

These contrasting findings within the literature and by this present study on the influence of surface topography on engagement has a number of possible implications on assembly-disassembly studies and taper design. One implication may include that assembly-disassembly studies are not appropriate for investigating taper engagement as a function of surface topography and that more precise methods of determining engagement are required. On the other hand, it could be that variations in surface topography present in clinically available modular taper head-stem junctions in THR only plays a minor role in engagement of the two interfaces.

Angular Mismatch

It was thought that the more conforming tapers would result in greater assembly displacements and disassembly forces due to lower magnitudes of contact pressure during assembly and more uniform engagement over the interface leading to increased disassembly forces. The matched samples presented a more uniform distribution compared to the distal and proximal samples as demonstrated in Figure 4.9. However, this study did find that the 'rough' matched samples presented a greater seating displacement compared to the 'rough' distal and 'rough' proximal with statistical difference only found between the 'rough' matched and 'rough' proximal when assembled to 2 kN (Figure 4.11b). However as mentioned above, there was a notable difference between the surface topography of the 'rough' proximal samples compared to the 'rough' distal and 'rough' matched. However, the increase roughness amplitude of the 'rough' proximal samples did not result in an increased disassembly force (Figure 4.11b). Furthermore, this study did not find the disassembly force (Figure 4.12) to be sensitive to the angular mismatch present in these samples with no identifiable consistent trends across the assembly forces. In comparison, Mueller

et al. [233] found a full contact (0 °angular mismatch) to present a lower disassembly force compared to the proximal (1 °) and distal (-1 °) angular mismatched samples. This was attributed to larger contact pressure due to less conformity in the mismatched samples leading to a greater disassembly forces. A possible explanation for these contrasting findings between Mueller et al. [233] and this present study could be that this study used assembly forces of 500 and 1500 N, compared to Mueller et al. [233]'s 1000, 3000 and 6000 N assembly forces. The lower assembly forces used by this study might not have been sufficient enough to investigate these differences of angular mismatch and the result it may have on disassembly force. Additionally, another complicating factor in attempting to understand the relationship between engagement and angular mismatch could be the a trade-off between contact pressure and contact area.

This study saw the development of a beyond the state of the art assembly methodology which was used to measuring seating mechanics and disassembly force. Prior to assembly, the samples were fully characterised using the developed novel CMM and VIS measurement and analysis techniques in Chapter 3. This was the first study to the author's knowledge to characterise the taper interfaces in this way to allow for any manufacturing variations to be taken into account. However, definitive conclusions of the effect of angular mismatch and surface topography on engagement were not forthcoming in this present study, reflective of the contrasting findings reported by current literature as discussed above. This may be because of competing factors between contact pressure and contact area that render the variation in angular mismatch and surface topography in taper interfaces of head-neck THR to only play a minor role in taper engagement, and/or assembly and disassembly tests may not be appropriate for investigating taper engagement and the development of more precise methods of determining engagement are required.

4.5 Conclusion

The aim of this study was to investigate the engagement distribution and strength of the representative samples with varying angular mismatch and surface topography of that seen in the clinically available samples. This was achieved by manufacturing samples representative of the range of surface topography and angular mismatch seen clinically, characterising the samples across the length scales of geometry and topography (as per the developed methodology of Chapter 3), developing a controlled assembly and disassembly test methodology beyond that of ISO 7206-10 [134] and measuring the seating mechanics and disassembly force. However, the relationship between surface topography and angular mismatch with seating mechanics and disassembly force was not forthcoming and did not provide any definitive conclusions about engagement. This could have been a function

of competing factors of engagement between contact pressure and actual contact area. Alternatively, the seating mechanics and disassembly forces may not be the correct metrics in which to determine the 'strength' of a taper's engagement and that more precise methods are needed.

In any event, this study did reveal new learning and is summarised as follows:

- the taper angles of the samples created for this present study were manufactured by an orthopaedic company and achieved a small variation of ± 0.005 °, indicating precision manufacturing akin to that achieved in toolholders for precision CNC machines employed by the aerospace and automotive industry, is achievable within the orthopaedic industry;
- surface topography was variable between samples of intended equivalent surface topography, indicating that surface topography maybe less readily controlled using current methodology of applying a threaded-type finish and manufacturers should be looking to develop new ways of controlling the finish of the taper interfaces;
- there is a need for more controlled assembly methodology beyond that defined by ISO 7206-10 [134] to ensure alignment of the female and male taper, important for controlled experimental studies and also highlights the need for the development of surgical tools to help minimise head assembly variation intra-operatively.

4.6 Future Work

One limitation of this study includes the assembly of up to 2 kN in line with ISO 7206-10 [134] and disassembly forces when heads were assembled up to 1.5 kN, indicating that further investigations are needed. Additionally, studies that investigated the impaction forces applied by surgeons suggest a peak force of anywhere between 1-20 kN can be achieved with an average around 7 kN [34–36]. One explanation for the insensitivity of the seating mechanics with angular mismatch could be that, at assembly forces below 2 kN, with the mismatch present in these samples, the differences in local contact pressures was not extreme enough to alter the overall forced displacement response. Future work will involve measuring the seating displacements of these samples up to clinically relevant assembly forces of 7 kN.

It was acknowledged that the force-displacement response taken from the test frame was not a direct measure of interface stiffness and will include compliance of the whole load train. This resulted in assembly displacement measurements providing an overestimation of seating displacements of the taper junction and assembly energy an overestimation of

seating energy. Although, tests were performed consistently and should be comparable. Previous studies such as Ouellette et al. [228] eliminated load train compliance from their displacement measurements by mounting high resolution displacement sensors on the shaft of the male taper immediately adjacent to the taper interface on opposite sides of the head.

Another limitation of this present study included using blue stain to see where engagement occurs, due to its ability to flow. Therefore, the samples were only assessed at a low loads and investigation only of the 'smooth' samples as the stain will simply bleed into the threads of the 'rough' samples. This means that contact on the micro-scale was not achieved. Previous studies overcame this by spluttering the male tapers with a thin layer of gold and identifying where it was abraded after assembly-disassembly [232, 265]. To more fully characterise engagement distribution, the gold spluttering technique could be used in conjunction with more fully characterising the taper interfaces, as per this present study to more precisely investigate the relationship between taper design parameters and engagement distribution. Assessment of engagement could also be supplemented by an FEA studies that use the point clouds of data output from the CMM and/or VSI measurements used to characterise these samples. A more advanced method of assessing engagement in real time during the assembly process could be by way of high-energy synchrotron X-rays. Previously, LeCann et al. [276] used high-energy synchrotron X-rays to image the bone-titanium screw interface as the screw was being pulled out in order to assess fixation. Similar methodology to that of LeCann et al. [276] could be applied to the head-stem taper interface in-view of other studies such as Thomas et al. [277] who successfully imaged a welded interface between a metal coating on a metal substrate.

Chapter 5

Uniaxial Fretting Corrosion and Motion

5.1 Introduction

Modular tapers in THR can look very different from that originally intended by Morse [16]. Angular mismatch and surface topography are two such features that differentiate the taper junction in THR from those used in industrial applications, with engagement being the key factor. Despite well over 20 papers reporting on surface topography and angular mismatch, a common understanding of how they affect performance has yet to be reached (see Chapter 2, Sections 2.6.5, 2.6.6, 2.7.5 and 2.7.6).

One possible reason for why there is a lack of common understand of the effect of surface topography as a single design parameter and angular mismatch could be the lack of systematically controlled experimental studies. As such, this study aimed to first develop a short-term test protocol based on current uniaxial incremental experimental simulation methodologies within the literature [211, 217, 218], please refer to Section 2.7.1 for further details.

Like that of Mali et al. [211] and Pierre et al. [218] this study also employed the use of induction sensors and an electrochemical cell to allow the motion and fretting corrosion response to be measured. Again like the aforementioned studies, potentiostatic measurement were employed with an overpotential of + 100mV, similar to previous studies [211, 234], please refer to Section 2.8.3 for further details. The short term nature of this study meant that each simulation ran for 4,800 cycles, and according to Bergmann et al. [6], this is representative of around one and a quarter days in-situ for people considered to have a ‘normal’ activity profile.

This study sought to further develop the induction motion measurement system in line with Haschke et al. [213] who employed the use of four sensors to measure pistoning

motion, 'rocking' in two dimensions ('central' and 'lateral') and rotation ('screwing'), please refer to Section 2.7.1 for further details. Further to Haschke et al. [213] and in line with Pierre et al. [218] this study aimed to quantify each motion in terms of subsidence and micro motion, the definitions of which will be explained Section 5.2.4 below. Then using CMM and VSI protocols first utilised in Chapter 3, surface deviation maps and surface topography post simulation was compared to the as manufactured samples. Outputs from this study will be used to help understand how angular mismatch and surface topography affects the performance of taper junctions in terms of motion and fretting corrosion.

5.2 Materials and Methodology

The short term performance of taper junctions was studied in part reference to ASTM F1875-08 [196]. This included measuring the fretting corrosion and motion response of the taper interfaces subject to incremental uniaxial loading, with peak loads between 0.5 and 4 kN, to replicate the principle joint reaction forces seen in-vivo [6]. The fretting corrosion response was measured using electrochemical potentiostatic measurements. Relative motion at the taper was measured using a bespoke sensor and protocols.

5.2.1 Samples

The samples were pre assembled to 2 kN following incremental assembly-disassembly tests in Chapter 4. Table 5.1 summaries the six different test groups and their key parameters. There were three smooth samples and two rough samples, allowing for three and two repeats of each test group, respectively. The heads were manufactured from CoCrMo (ISO 5832-6 [180]) and the male tapers were manufactured from cylindrical coupons made from high nitrogen stainless steel (ISO 5832-9 [121]). The details of the samples including rationale can be found in Chapter 4 along with the details of geometry, surface topography and assembly mechanics.

Table 5.1 Sample groups used in this study and summary of key parameters determined in Chapter 5. See Table 3.2 for a description of the surface topography parameters.

Engagement Couple	Angular Mismatch (°)	Male Taper Surface Topography			
		Sa (µm)	Sz (µm)	Sk (µm)	Spd (mm^{-2})
Distal Smooth	-0.090 ± 0.003	0.700 ± 0.154	4.409 ± 1.526	2.022 ± 0.410	5305 ± 166
Matched Smooth	0.019 ± 0.003	0.424 ± 0.027	3.439 ± 0.539	1.426 ± 0.436	5485 ± 433
Proximal Smooth	0.121 ± 0.013	0.392 ± 0.048	3.362 ± 0.614	1.320 ± 0.164	5371 ± 761
Distal Rough	-0.088 ± 0.004	1.771 ± 0.018	14.582 ± 7.905	4.603 ± 0.156	1444 ± 9
Matched Rough	0.015 ± 0.004	1.762 ± 0.068	16.145 ± 8.803	5.611 ± 0.462	1439 ± 13
Proximal Rough	0.115 ± 0.004	3.888 ± 0.141	22.441 ± 3.788	12.788 ± 1.470	1615 ± 69

5.2.2 Uniaxial Dynamic Loading

Uniaxial dynamic loading was undertaken with the samples in an anatomical orientation according to ISO 7206-4 (Figure 5.1a) [278]. It describes an alpha and beta angle of 10 and 9 ° respectively along with an assumed centrum-collum-diaphyseal angle (CCD) of 135 ° to the loading axis (Figure 5.1b and c). ISO 7206-4 [278] also describes that the head offset should be reported, this study used a head offset of approximately 38 mm. This was aimed to replicate that used by clinically available THR whose head offsets tended to range from 27 to 40 mm [75]. Figure 5.1 shows an illustration of the fixtures that were made of stainless steel.

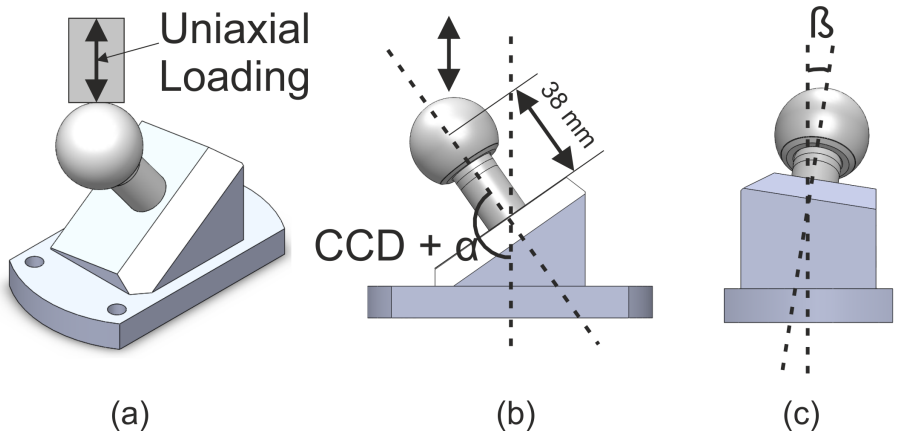

Fig. 5.1 (a) Illustration of the loading fixtures according to ISO 7206 [278] where (b) α is equal to 10 ± 1 °and (c) β to 9 ± 1 °.

The loading sequence was applied using a dynamic material testing machine (Instron E10 000, US) and consisted of a sinusoidal waveform starting with a peak-to-trough range from 5 N to 500 N. The waveform was applied at 1 Hz, for 600 cycles and followed by a 10 minute hold phase for the fretting corrosion tests and a 10 second hold phase for the motion tests. During the hold phase, the load was held at half the peak force of the preceding increment. This was repeated for a further 7 stages, increasing the peak height of the sine wave by 500 N until the final increment of 4000 N, resulting in a total of 8 increments.

5.2.3 Fretting Corrosion

The fretting corrosion test setup consisted of a three-electrode electrochemical cell, integrated into the test arrangement (Figure 5.2a) to facilitate real time measurement of corrosion in-situ. A bath was mounted on the male component, the taper junction (the only metallic interface exposed to the electrolyte) was immersed in 100 mL of phosphate buffered saline (PBS) solution. The implant sample acted as the working electrode. An Ag/AgCl reference electrode and platinum disc counter electrode completed the electrochemical cell. The electrodes were connected to a floating ground potentiostat (IVIUM Compactstat, NL). Figure 5.2a and b show the electrochemical and loading regime applied in this study.

Prior to dynamic loading, the Open Circuit Potential (OCP) of the system was allowed to equilibrise for 30 minutes under static conditions in the absence of an applied normal load. A potentiostatic technique was applied to provide a quantitative measure of the net electrochemical currents owing to corrosion. A +100 mV vs OCP under static conditions was then applied for a further 30 minutes, before starting the dynamic loading sequence.

This was to allow the measured current to settle to a sufficiently low ampere (around 500 nA), before the application of the dynamic loading sequence (Figure 5.2b). The overpotential was selected to force the anodic reaction away from the equilibrium to allow quantitative measurement of net current, without forcing it too far, as to cause changes in the oxide layer that will no longer be representative. This was shown by current measurements settling to very low values during static phases, in the region of 100 to 500 nA.

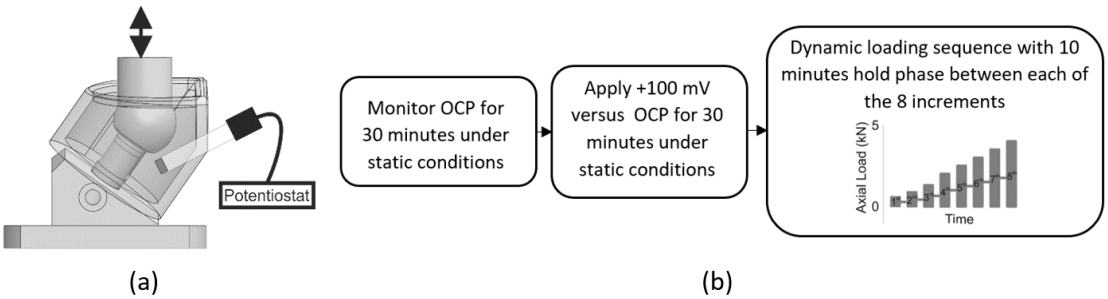

Fig. 5.2 (a) Illustration of the integrated fretting corrosion cell and (b) flow chart of the electrochemical measurements taken throughout a single test.

Current was measured at a frequency of 1 Hz which provided information on the passivation and depassivation behaviour of the tapered interface. Figure 5.3 shows a typical anodic current transient demonstrating how under dynamic loading an increase in current corresponds to the depassivation due to abrasion and subsequent repassivation of the oxide layer, causing a measurable increase in current across the working and counter electrodes. A greater increase in current would indicate a greater amount of oxide layer disruption. This study compared average and peak current measured for each increment, after removing a baseline associated with static corrosion (as shown in Figure 5.3). The baseline current was calculated using a line of best fit from the data points taken prior to loading and the last two minutes of each hold phase.

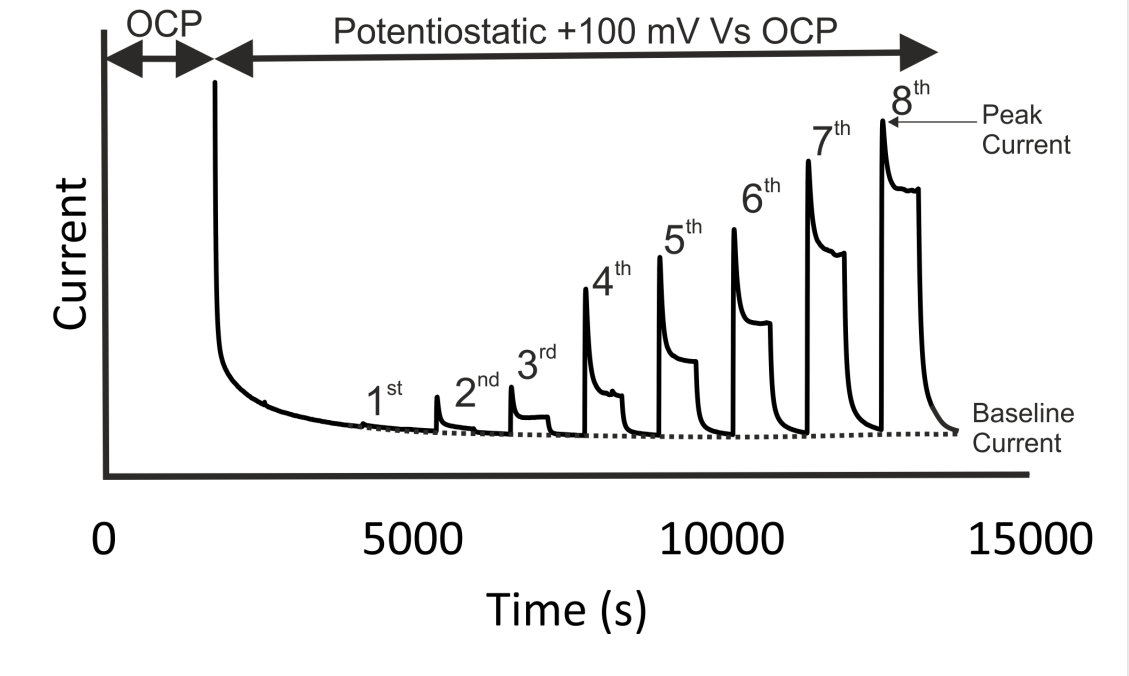

Fig. 5.3 Schematic of a typical anodic current transient where an increase in current is associated with fracture of the passive oxide film during loading. The broken line indicates current associated with static corrosion.

The same samples used for fretting corrosion tests, were used for motion assessment following the controlled disassembly-assembly process detailed in Chapter 4. Surfaces were inspected for signs of damage, sonicated cleaned in acetone, air dried and reassembled to 2 kN. Disassembly forces after motion measurements are presented.

5.2.4 Motion Measurement and Protocol

Custom motion sensors were developed using the principle of eddy-current effect as the transducer mechanism. The eddy-current effect is a form of electromagnetic induction which may be utilised to measure the distance to a conductive object. A coil is excited by and an AC current to generate an alternating magnetic field, which induces eddy currents in nearby conductive targets. These currents generate an opposing magnetic field, in accordance with Lenz's law, which cancels a part of the applied field and reduces the coil flux. This field coupling between the coil and conductive target acts to increase the coil's resistance, and reduce the observed inductance. As the target moves closer to the coil, the increased alternating field increases the eddy-current density causing a further decrease in inductance. This change in inductance may be calibrated to the distance between the coil and target, giving a displacement sensor which is highly resistant to environmental effects [279].

Unlike the simplified pin-on-disk studies discussed in Section 2.8 which only required one displacement sensor to capture uniaxial motion, simulation studies using had-stem reconstructions with CCD, α, and β angles (Figure 5.1b and c) apply bending moments around the taper junction. Motions including axial motion along the axis of the taper (pistoning), toggling primarily due to CCD and α angles (Toggling XZ), toggling which can be mainly attributed to the β angle (Toggling YZ), and rotation as a function of both CCD, α, and β angles. Figure 5.4a shows these four different motions mathematically about a Cartesian coordinate system with a z-axis aligned with the axis of the taper junction.

To capture all these aforementioned types of motion at the taper interface, this study employed four sensing coils on a single custom PCB (P& M Services ltd, UK), allowing for four degrees of freedom measurement of the motion. The coils were mounted to the male component below the taper interface and aluminium targets were mounted on the femoral head, as shown in Figure 5.4a. Three coils were used to calculate the vector of a plane which allowed pistoning and toggling in two axes to be determined (Coils 1-3, Figure 5.4b). A fourth coil perpendicular to the other three was used to measure rotation (Coil 4, Figure 5.4b).

Texas Instruments (USA) coil and LDC design tools was were used to guide sensor design [280]. Each coil comprised of two layers, each with 16 turns, 100 µm (or 4 mil) spacing between turns and 200 µm (8 mil) between layers, 100 µm trace width, an outer diameter of 10 mm and external capacitance of 330 pf. The coils were driven and monitored using a fully integrated, four-channel inductance to digital converter chip (LDC 1614, Texas Instruments, US). The digital output of the LDC 1614 was then sent to a microcontroller (myRIO, National Instruments, US) via I2C protocol and inductance was recorded at 100 Hz. Figure 5.4c shows a schematic of how each component in the sensing system was connected. Raw inductances were then calculated and stored as a .txt file using a bespoke *LabView* (2019, National Instruments, US) program for export into *Matlab* (R2020a, MathWorks, US). A bespoke, Matlab program was developed for the conversion of inductance to displacements and the different motions i.e. pistoning, toggling and rotation.

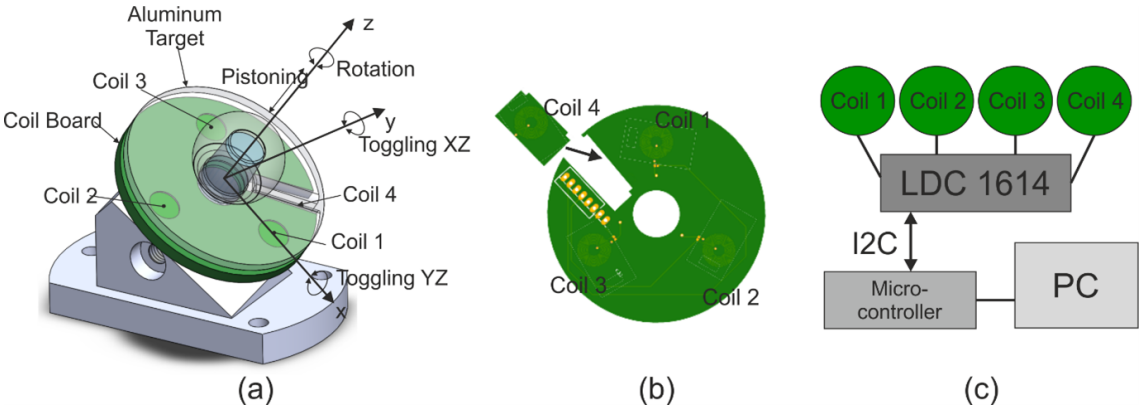

Fig. 5.4 Schematic of the motion sensing system including (a) coil board-target configuration, (b) distribution of coils on the coil board and (c) coils-linear inductance to digital converter (LDC)-PC configuration.

The sensors were calibrated using a piezo linear precision positioner stage (MikroMove, Physik Instruments, UK) accurate to 0.1 nm. Figure 5.5 shows a schematic of the setup used to calibrate Coils 1 to 3. This included fixing the aluminium target (Figure 5.5) to the precision positioner stage and moving it relative to the coil board which was fixed to a spare male component. Coil 4 was calibrated separately before soldering into position. Calibration curves were determined across the full range of target-coil distances and shown in Appendix C Figure C.1. Three separate sets of calibration data were then used to test the determined inductance-to-displacements relationships. Residuals from the three sets of data are shown in Appendix C Figure C.2, indicating that the sensing solution was found to be accurate to $\pm$ 0.5 µm. Table 5.2 summaries the coil specification.

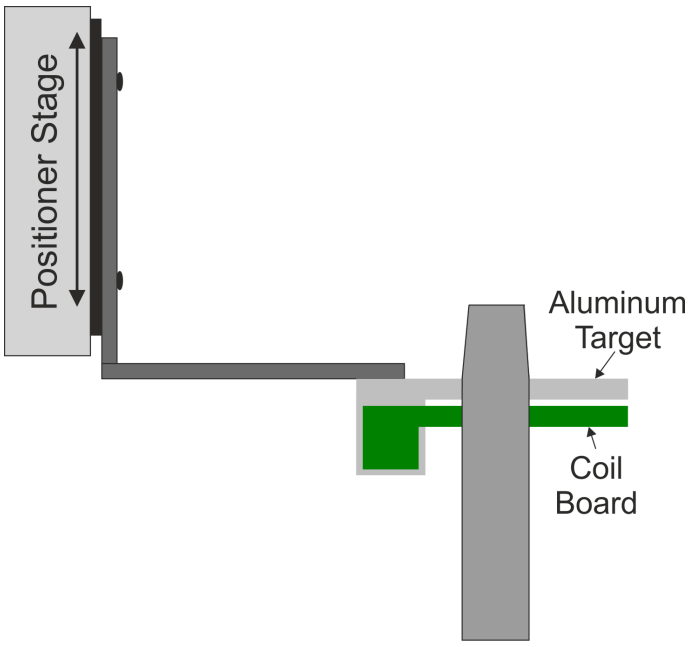

Fig. 5.5 Schematic of the set up used for calibration.

Table 5.2 Summary of sensing coil specifications. Where maximum coil-target distance corresponds to the maximum distance the sensing coil can be from the target in which a change in inductance can be measure, and measurement range, as the range over which the coils can measure to the determined accuracy.

Resolution (μm)	Accuracy (μm)	Maximum Coil-Target Distance (mm)	Measurement range (mm)
0.05	± 0.5	4	0.5

Motion data was captured subject to the loading methodology detailed in Section 5.2.2. The four coils were used to capture all the different types of motion, including: pistoning, toggling YX, toggling XZ and Rotation as shown in Figure 5.6. The x and y coordinates of the three points (A, B and C in Figure 5.2.2) were defined in the coordinate system shown in Figure 5.6 by the centre of each coil. The z coordinate was the measured target-coil distance.

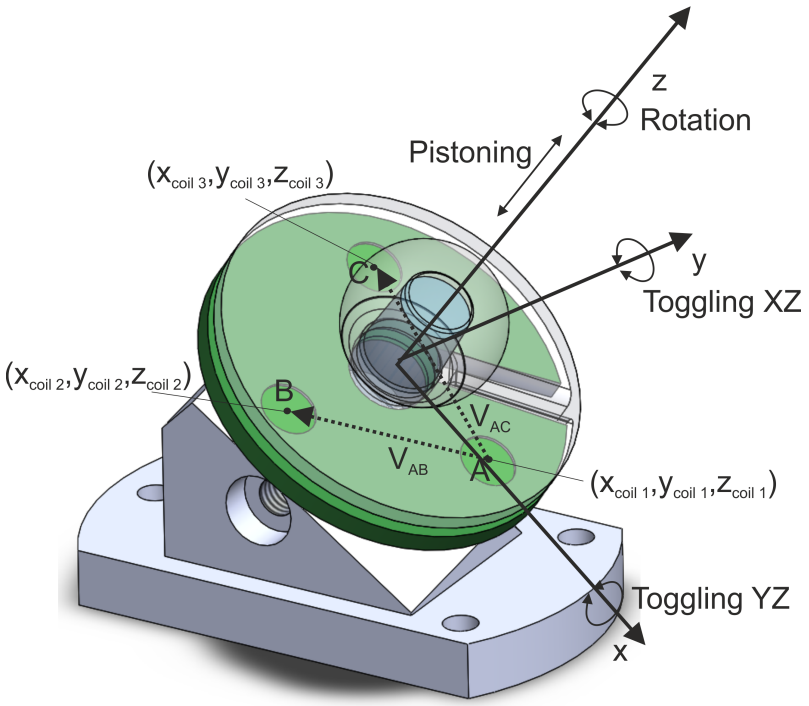

Fig. 5.6 Coordinate system for vector calculations for pistoning and toggling motions. Where point A, B and C are three points on a plane and V_{AB} and V_{AC} are two vector which lie on the plane

Pistoning was determined by first calculating two vectors in the plane (V_{AB} and V_{AC} using three points (A, B and C), Figure 5.6). The second step was to determine the normal (n) to the plane by taking the cross product of these two vectors (Equation 5.1). Thirdly,

the perpendicular distance (d) from the origin to the plane was determined by taking the dot product of the normal and a point on the plane (Equation 5.2). This was done for each measurement i.e. 100 planes per second due to a sampling rate of 100 Hz. Finally, pistoning was then determined by subtracting each subsequent value of 'd' from the first.

$$n = V_{AB} \times V_{AC} \tag{5.1}$$

$$d = A.n \tag{5.2}$$

Toggling YZ was found by first determining the angle the plane, at each sampling point, made with Y axis in the YZ plane i.e. rotation about the x-axis (σ_x, Equation 5.3). Likewise, Toggling XZ was found by determining the angle the plane, at each sampling point, made with X axis in the XZ plane i.e. rotation about the y-axis (σ_y, Equation 5.4). Each rotation was converted to an equivalent displacement at the taper surface assuming a radius (r) of 7 mm using Equations 5.5 and 5.6.

$$\sigma_x = 90 - cos^{-1}(\frac{n.\hat{j}}{|n||\hat{j}|}) \tag{5.3}$$

$$\sigma_y = 90 - cos^{-1}(\frac{n.\hat{i}}{|n||\hat{i}|}) \tag{5.4}$$

$$TogglingYZ = rtan(\beta_x) \tag{5.5}$$

$$TogglingXZ = rtan(\beta_y) \tag{5.6}$$

Rotation was calculated by use of a fourth coil perpendicular to coils 1 to 3. Once the inductance was converted to a displacement, this was then used to calculate a rotation angle using a radius distance from the centre of coil 4 to the z-axis. The displacement at

the taper interface was then calculated as the arc length assuming a radius of 7 mm and the rotation angle derived from the coil. Each subsequent rotation displacement was subtracted from the first calculated value of rotation for relative position with respect to the start of the experiment.

In addition to separating motion out into pistoning, toggling YZ, toggling XZ and rotation, motion was further divided into subsidence and micro motion. Subsidence attributed to how the heads moved further down into the taper over the course of the experiment, while micro motion was attributed to those small displacements about subsidence. Figure 5.7 shows a schematic of pistoning motion where subsidence is shown by the green line following the overall form of the motion measurements, while micro motion is the higher frequency (1 Hz) motion about subsidence.

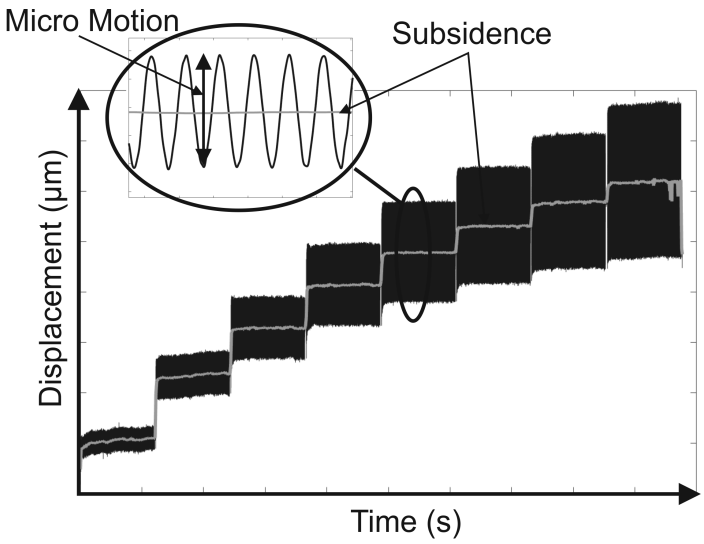

Fig. 5.7 Schematics of subsidence (green line) and micro motion (blue line).

The average subsidence and micro motion measured at each increment contained both elastic deformation of the components and rigid body motion at the taper junction. To isolate the amount of relative motion occurring at the tapered junction, motion measurements were performed on an equivalent monobloc sample manufactured by MatOrtho Ltd (Leatherhead, UK). The monobloc was a sample that was a surplus 'smooth' matched sample that was assembled to a high force of 8 kN and welded at the taper opening. Subsidence and micro motion measured from the monobloc were then subtracted from that measured on each sample. Measurements of the equivalent monobloc can be found in Appendix C, Figure C.3.

5.2.5 Surface Analysis

Geometry and surface topography post dynamic testing was captured using the same methodology detailed in Chapter 4, Section 4.2.1. In terms of geometry, this included comparing ideal cone angle and surface deviation maps pre and post testing. In terms of surface topography, this included comparing S_a, S_k and S_{pd}, see Table 3.2 for definitions.

5.2.6 Statistics

All data was presented as mean ± one standard deviation. There were three samples of 'smooth' -distal, matched and proximal samples, and two samples of 'rough' - distal, matched and proximal samples, allowing for three and two repeats respectively. Statistical comparison of results between the different engagement groups with the 'smooth' male taper topography was achieved using a two tailed paired students t-test. The level of significance was set at a p-value of 0.05. Analysis was performed using Excel (Microsoft, USA).

5.3 Results

5.3.1 Fretting Corrosion

The anodic current transient response for modular taper components is shown in Figure 5.8. After stabilisation of the OCP and application of the applied electrochemical overpotential, a decay in the net anodic current to a stable baseline value was observed. Upon the application of cyclic loading, all samples presented evidence of passive oxide layer disruption indicated by a sudden and sustained increase in current. The magnitude of current increased with increasing loading increment and recovered to the baseline during hold phases. The current signal differed between the six samples groups.

Comparing between the 'smooth' and 'rough' samples of equivalent engagements, the 'rough' samples presented greater currents compared to the 'smooth'. The 'rough' samples also presented a more consistent spike in current upon the onset of a loading increment (Figure 5.8b) compared to the 'smooth' (Figure 5.8a), which was less consistent. For example, the 'smooth' matched sample in Figure 5.8a presented increasing current trends in the 4th to 6th increment followed by a spike and reduction in current in the 7th increment.

Comparing between the different engagement groups of equivalent surface topographies, the distal samples presented the smallest currents, while the matched presented the greatest. Within the 'smooth' samples, a variation in the recorded current signal was also noted. The 'smooth' distal samples presented a noisier signal compared to the proximal.

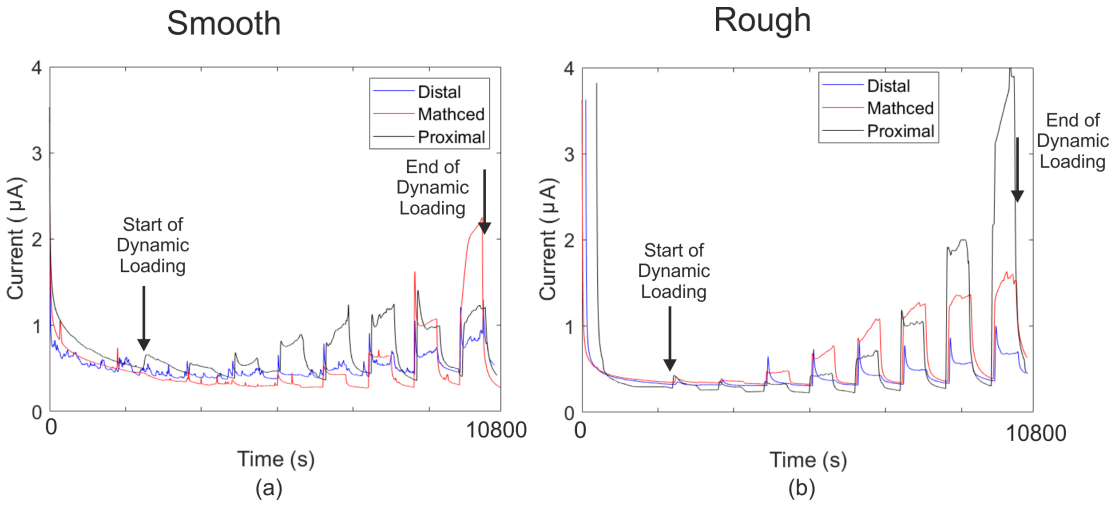

Fig. 5.8 Example of typical current transients of the (a) smooth and (b) rough samples.

The average current for each loading increment is shown in Figure 5.9 a and b and the peak current can be seen in Figure 5.9 c and d. Comparing between the 'rough' and 'smooth' samples, the 'rough' presented a greater average current (Figure 5.9a versus b) and peak current (Figure 5.9c versus d) compared to the 'smooth' for a given engagement. This was most evident at higher loading increments and less so as the loading increments with peak force less than 2000 N. The greatest difference between the 'rough' and 'smooth' samples was seen in the matched engagement group. In the final increment, the 'rough' matched sample presented a 12.6 ± 5 μA greater average current compared to the 'smooth' matched (5-fold increase). The distal engagement group presented the smallest difference between 'rough' and 'smooth'. In the final loading increment, the 'rough' distal sample presented a greater average current of 3.6 ± 2.1 μA compared to the 'smooth' distal (6-fold increase). Likewise, the 'rough' proximal presented a greater average current of 8.0 ± 0.5 μA compared to the 'smooth' proximal in the final loading increment (10-fold increase).

Within the 'smooth' group, the matched group tended to present greater average current (Figure 5.9a) per increment than the proximal or distal groups, most evident at higher loading increments with peak force greater than 2000 N. Statistically greater average current was found between the matched and proximal groups in the final increment (2.0 ± 0.6 μA versus 0.8 ± 0.2 μA, p-value < 0.05). The matched also presented a greater current compared to the distal but this was not found to be statistically significant (2.0 ± 0.6 μA versus 0.5 ± 0.4 μA, p-value of 0.07). The distal samples presented the lowest

average current compared to the matched or proximal. This was not the case for peak current (Figure 5.9c). The proximal samples presented the lowest peak current in the final increment, compared to the matched (1.3 ± 0.3 µA versus 3.1 ± 0.8 µA, p-value < 0.05) or distal (1.3 ± 0.3 µA versus 3.6 ± 0.5 µA).

When comparing between the different engagement groups in the 'rough' samples, similar patterns can be seen as was with the 'smooth'. More specifically, the distal samples presented the smallest average current and matched the greatest (Figure 5.9b). In this case, however, the distal samples also presented the smallest peak current (Figure 5.9d) compared to the matched or proximal. In the final increment, the distal presented an average current of 4.1 ± 3.0 µA, matched 14.7 ± 5.1 µA and proximal 8.7 ± 0.6 µA. The peak current (Figure 5.9d) found in the 'rough' samples presented similar trends to the average current.

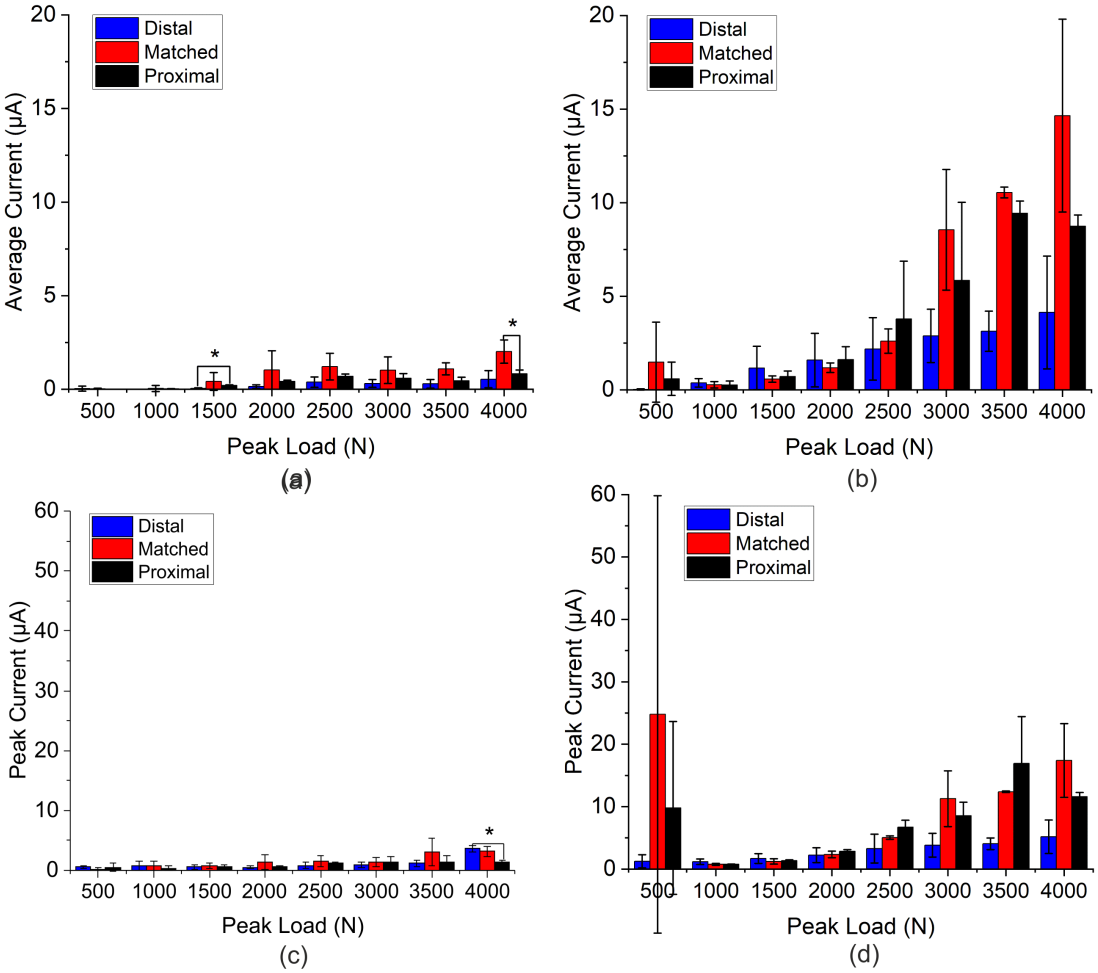

Fig. 5.9 Fretting corrosion results showing: average current per increment for the (a) smooth samples and (b) rough samples, and peak current per loading increment for the (c) smooth samples and (d) rough samples.

5.3.2 Motion

Subsidence

Figure 5.10a and b show the pistoning subsidence displacement as a function of time and loading increment (i.e. the head migrating axially down the male taper) of the six different sample groups for 'rough' and 'smooth' samples, respectively. Example raw data from coils 1, 2 and 3 used to calculate the 'smooth' match pistoning motion data presented in Figure 5.10a can be found in Appendix C Figure C.4. Subsidence tended to increase with increasing loading increments, indicating that the heads were still seating. Subsidence was seen at the start of each increment and tended remained constant for the duration of an increment. The 'smooth' matched and proximal samples, as shown in Figure 5.10a, presented evidence of sudden subsidence upon the onset of the 7^{th} loading increment. The 'smooth' proximal and matched samples also presented evidence of the heads moving back up the male taper before the sudden seating event. In the 'smooth' matched case, evidence of migration back up the taper was evident before the subsidence event upon the onset of the 7^{th} increment. In the 'smooth' proximal case, head migration back up the taper was evident before the subsidence event upon the onset of the 5^{th} increment. This was not shown by the 'smooth' distal sample that presented minimal pistoning subsidence compared to the 'smooth' matched or proximal. The 'rough' samples (Figure 5.10b) tended to migrate down the taper axis more gradually than the 'smooth' shown by the more step-wise increase with each increment.

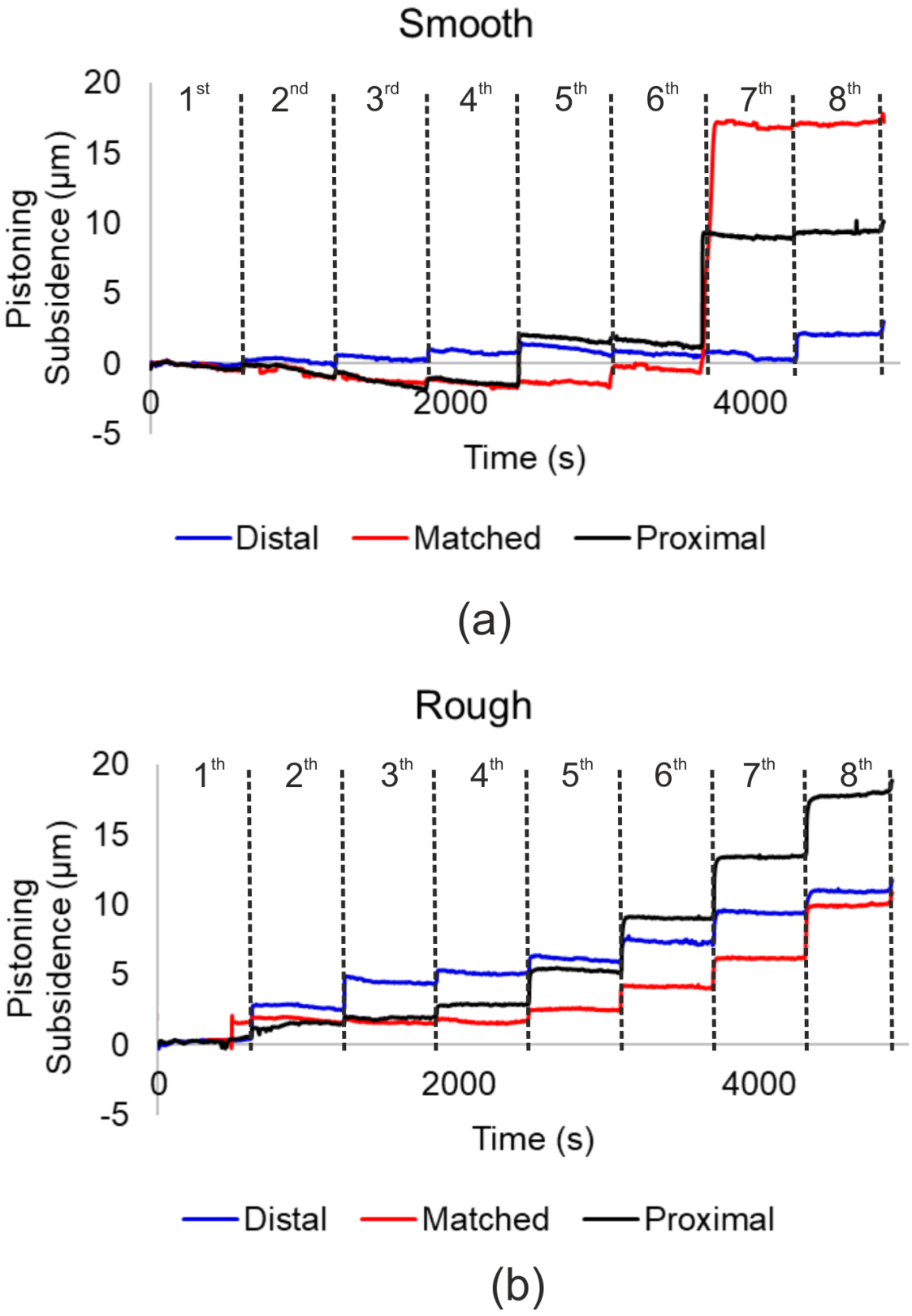

Fig. 5.10 Example of pistoning subsidence for the (a) 'smooth' and (b) 'rough' samples with annotations indicating the boundary of each increment.

Figure 5.11 shows the average subsidence of the femoral head relative to the male taper in the pistoning (axial), YZ, XZ and rotational directions during cyclic loading. In line with the greater loading vectors acting along the taper axis and bending moments in the XZ plane due to sample orientation (Figure 5.1a), the greatest magnitude of subsidence tended to be in the pistoning direction (Figure 5.11a and b). Subsidence in the XZ (Figure 5.11g and h) direction presented the second largest values of subsidence followed by rotation (Figure 5.11j and k) and YZ subsidence (Figure 5.11d and e).

Comparing between the 'smooth' and 'rough' samples of equivalent engagement, the 'smooth' matched and proximal samples present larger magnitudes of pistoning subsidence (Figure 5.11a) in the final load increments. Additionally, the 'rough' matched and proximal samples (Figure 5.11b) presented a more gradual increase with each loading increment. The sudden subsidence events in the 'smooth' matched samples resulted in a greater magnitude of pistoning subsidence in the final increment at peak force of 4 kN compared to the 'rough' matched (17.4 ± 0.7 µm versus 12.0 ± 3.2 µm). This was not the case for the distal or proximal engagements, where the 'rough' samples presented a greater magnitude of subsidence compared to the 'smooth' (8.9 ± 3.9 µm versus 2.1 ± 0.9 µm distal engagement and 17.2 ± 1.6 µm versus 9.5 ± 5.6 µm proximal engagement).

Differences between the 'smooth' and 'rough' samples were also seen in the XZ (Figure 5.11d and e) and rotational directions (Figure 5.11j and k). The 'rough' distal samples presented a greater amount of XZ subsidence compared to the 'smooth' distal, presenting subsidence of 8.2 ± 1.0 µm versus 5.3 ± 0.6 µm in the final loading increment. In the rotational direction, the 'smooth' matched and proximal samples presented a greater amount of subsidence compared to the 'rough' matched and proximal. In the final increment, the 'smooth' matched and proximal samples presented subsidence of 1.5 ± 0.5 µm and 2.8 ± 1.0 µm compared to the 'rough' proximal and matched samples with 0.7 ± 0.3 µm and 0.7 ± 0.2 µm, respectively. Unlike pistoning, subsidence in the XZ, YZ and rotational direction tended to increase proportionally with each increment as opposed to discrete subsidence events at particular loading increments.

Within the 'smooth' samples there was a difference in subsidence behaviour between the different engagement groups. The distal samples tended to present the smallest magnitudes of pistoning subsidence compared to the matched or proximal (Figure 5.11a) but larger values in the remaining three motions i.e. YZ (Figure 5.11d), XZ (Figure 5.11g) and rotation (Figure 5.11j). In the final loading increment (Figure 5.11a), the distal sample presented a pistoning subsidence of 2.1 ± 1.0 µm compared to the matched with 17.4 ± 0.7 µm (p-value < 0.05) and proximal 9.5 ± 5.6 µm (p-value > 0.05). In contrast, when comparing rotational subsidence in the final increment, distal presented a subsidence of 4.1 ± 0.4 µm compared to matched with 1.5 ± 0.5 µm (p-value < 0.05) and proximal with 2.8 ±

1.0 μm (p-value > 0.05). Likewise, in the YZ direction in the final loading increment, distal presented a subsidence of 2.0 ± 0.6 μm compared to matched with 0.0 ± 0.4 μm (p-value < 0.05) and proximal with 1.3 ± 2.0 μm (p-value > 0.05).

Comparing the different engagement groups in the 'rough' samples, similar trends were seen as with the 'smooth'. That being the distal samples presented the smallest pistoning subsidence but greater off-axis and rotational subsidence. In the final loading increment, the distal samples presented an XZ subsidence of 8.2 ± 1.0 μm compared to the matched with 1.7 ± 1.2 μm and proximal with 2.6 ± 0.4 μm. Likewise, in the rotational direction, the distal presented subsidence of 4.4 ± 1.4 μm in the final increment compared to the matched with 0.7 ± 0.3 μm and distal 0.7 ± 0.2 μm.

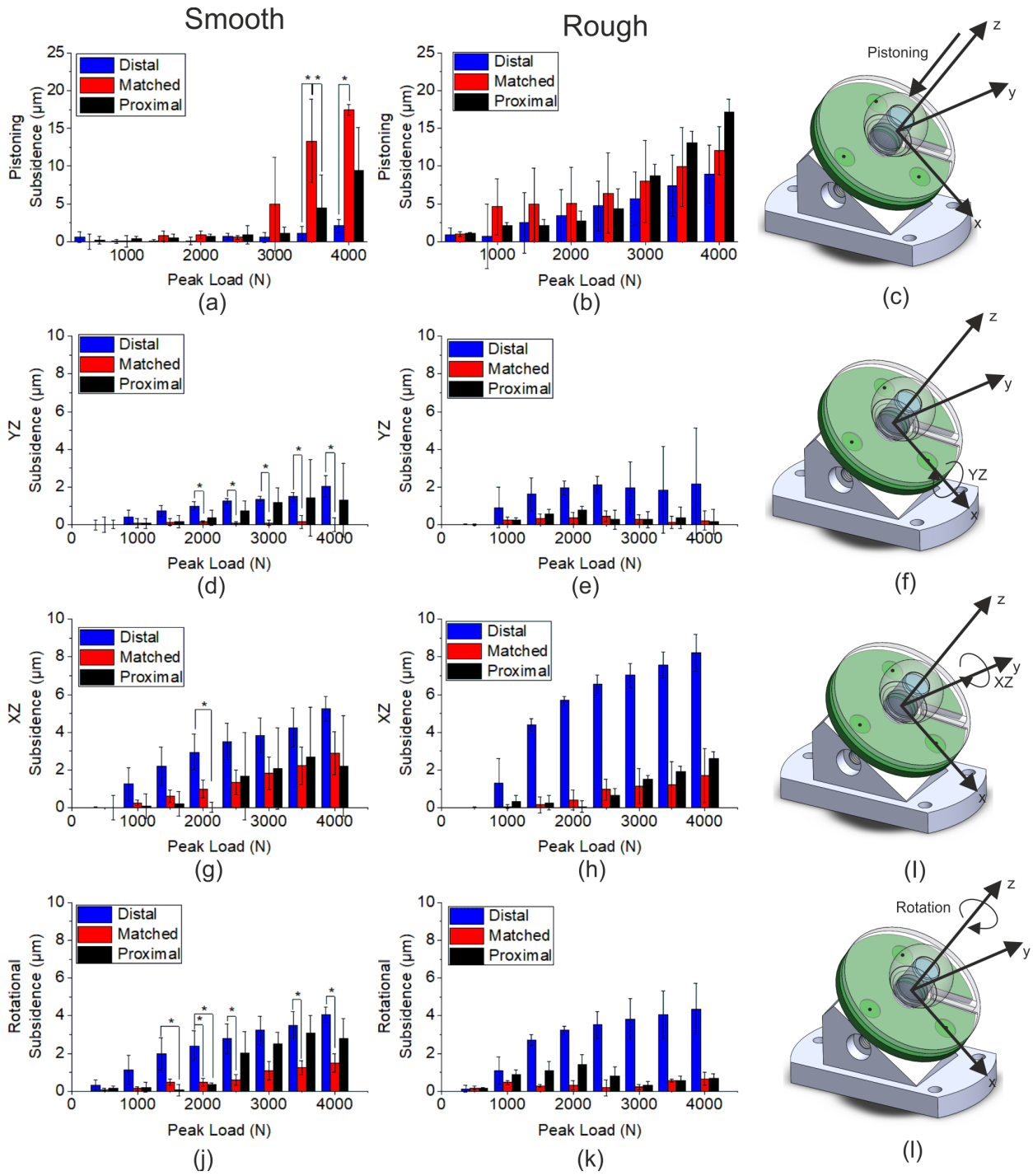

Fig. 5.11 Magnitude of subsidence at each loading increment for the (a, d, g and j) 'smooth' and (b, e, h and k) 'rough' samples, in each of the different directions: (a and b) pistoning, (d and e) YZ, (g and h) XZ and (j and k) rotation shown schematically in adjacent subfigures (c, f, i and l). Significant difference between the different engagement groups of the 'smooth' samples is indicated by '*'.

Micro Motion

Like subsidence, the magnitude of micro motion increased with increasing loading increment. This is shown in Figure 5.12a and b which presents area plots of pistoning micro motion on a cycle-by-cycle basis for a typical example of each of the six sample groups. Almost all samples at each increment presented a tendency for micro motion to peak upon the onset of loading and then settle, more evident in some cases than others, such as the 'smooth' distal sample in the 8th increment (peak force of 4000 N) (Figure 5.12a). Comparison between Figure 5.12a and b also suggests differences between the different samples groups. The 'smooth' proximal samples (Figure 5.12a) demonstrated a greater magnitude compared to the 'smooth' distal and matched. The 'rough' samples tended to present less of a difference between the different engagement groups (Figure 5.12b).

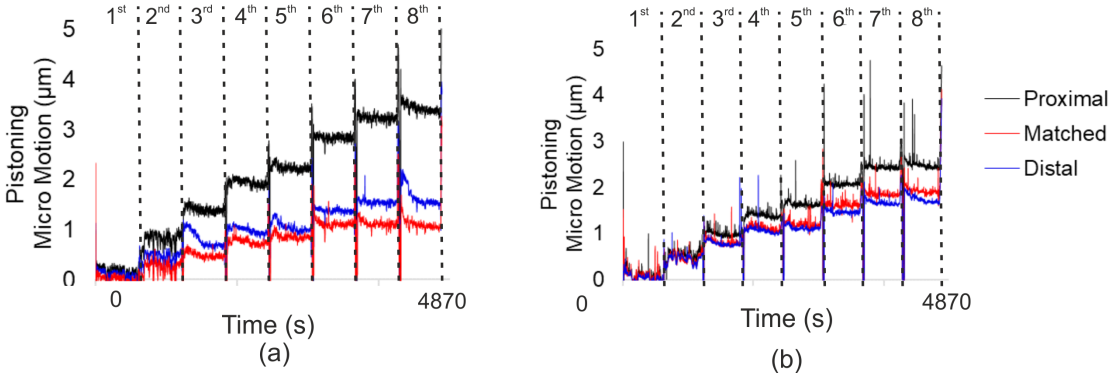

Fig. 5.12 Example plot of pistoning micro motion of the (a) 'smooth' and (b) 'rough' samples on a cycle-by-cycle basis with annotated increment boundaries.

Micro motion presented an increasing trend with loading increment in each of the different directions as shown in Figure 5.13. The greatest magnitude of micro motion was shown in the pistoning and toggling XZ direction, whereas toggling YZ and rotational micro motion presented the smallest magnitudes.

Comparing the 'smooth' and 'rough' samples for a given engagement, similar magnitudes of micro motion were observed for a given engagement. In the pistoning direction (Figure 5.13a and b), the matched engagement group presented the greatest difference, with the 'rough' matched presenting a greater magnitude of 0.8 ± 0.2 µm in the final increment. Smaller differences were found between the distal (1.6 ± 0.9 µm 'smooth' versus 1.6 ± 0.2 µm rough, in the final increment) and proximal (2.9 ± 0.5 µm versus 2.3 ± 0.3 µm in the final increment) engagement groups. Like pistoning, toggling XZ presented small differences between the 'smooth' and 'rough' samples of equivalent engagement (Figure 5.13g and h). The greatest differences were seen in the proximal group, where the 'smooth' proximal presented a greater average micro motion (3.3 ± 0.7 µm) in the final loading

increment compared to the 'rough' proximal (2.5 ± 0.3 µm). Only small magnitudes of micro motion were recorded in the toggling YZ and rotational direction. One difference noted in toggling YZ direction was that the 'rough' distal engagement group presented a much greater variability compared to the 'smooth' distal. The 'smooth' samples appeared to present a greater amount of rotational micro motion compared to the 'rough', more evident in the distal (by 0.8 ± 0.3 µm in the 8th increment) and proximal engagement groups (by 1.1 ± 0.3 µm in the 8th increment) (Figure 5.13j and k).

Comparing the different engagements in the 'smooth' samples, the proximal samples tended to present a greater magnitude of pistoning micro motion compared to the distal and matched with significant differences in the 6th (2.5 kN peak axial force) and 7th (3 kN peak axial force) loading increments (Figure 5.13a). In the 7th loading increment, the proximal samples presented a magnitude of 2.8 ± 0.5 µm compared to the distal with 1.5 ± 0.6 µm (p-value < 0.05) and matched with 1.0 ± 0.2 µm (p-value < 0.05). In the rotational direction, the matched presented the smallest level of micro motion compared to the distal and proximal. A significant difference was found between the distal and matched samples in 6th and 7th loading increments, wherein only a marginal difference of 0.5 ± 0.2 µm in the 6th increment was found. Little difference was seen between the different engagement groups in the toggling directions.

Comparing within the 'rough' samples, in the pistoning direction (Figure 5.13b), the proximal samples presented the greatest average micro motion compared to the distal or matched. In the final increment, the proximal samples presented a magnitude of 2.3 ± 0.3 µm compared to the distal with 1.6 ± 0.2 µm and matched with 1.8 ± 0.2 µm. In contrast, the proximal samples on average presented less toggling XZ micro motion compared to the distal or matched samples (2.5 ± 0.3 µm versus 3.5 ± 2.0 µm and 3.3 ± 1.1 µm, Figure 5.13h).

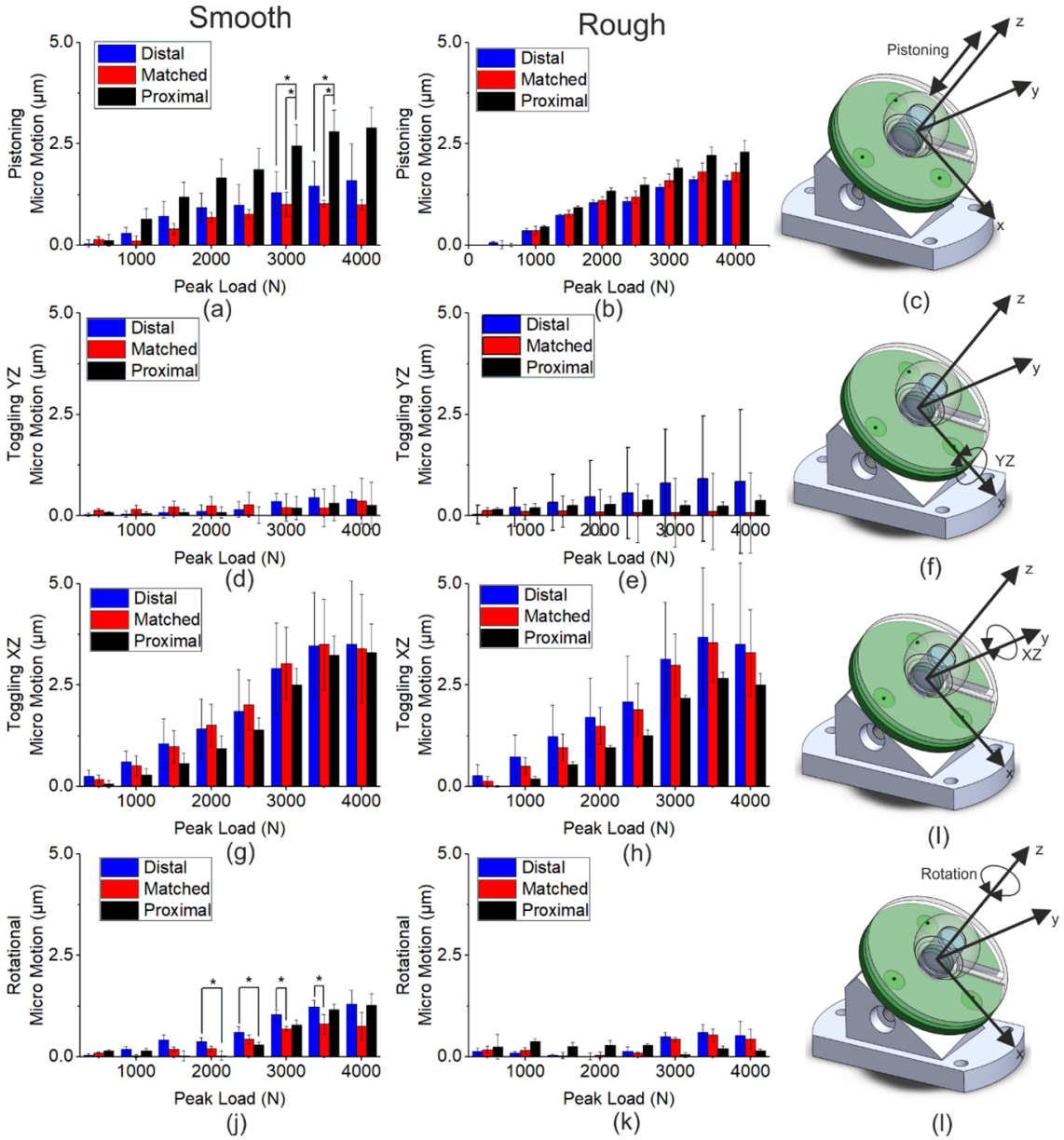

Fig. 5.13 Micro motion at each loading increment for the (a) smooth samples and (b) rough samples.

5.3.3 Disassembly Force

The force required to separate the heads from the male taper after 2 kN assembly and dynamic uniaxial loading are shown in Figure 5.14. The smooth distal group presented a disassembly force of 794 ± 409 N, the smooth matched an average force of 1660 ± 572 N and smooth proximal of 1255 ± 215 N. This compares to the rough distal presenting a disassembly force of 936 ± 145 N, the rough matched 1360 ± 172 N and the rough proximal with 1341 ± 137 N. There was no statistical difference found between the different engagement groups within the 'smooth' samples (p-value > 0.05). However, it

was noted that the rough samples tended to present a smaller variation in disassembly force than the smooth samples.

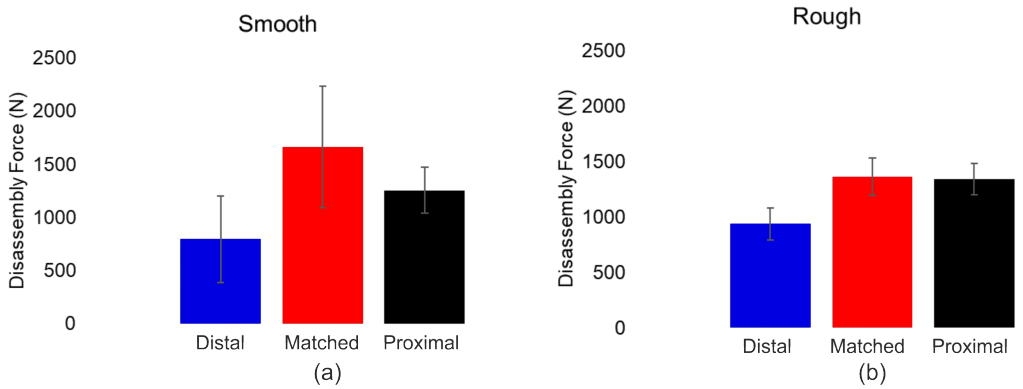

Fig. 5.14 Disassembly force post 2 kN assembly and dynamic uniaxial loading for fretting corrosion and motion measurements for the (a) 'smooth' samples and (b) 'rough'.

5.3.4 Surface Analysis

CMM and VSI measurements were taken post testing (i.e. post 2 kN assembly, uniaxial dynamic loading for fretting corrosion and motion measurements and disassembly) and compared to the same measurements pre testing to assess if there were any changes to both the geometry and topography of the taper interfaces.

Geometry - Comparison Pre versus Post Testing

Figure 5.15 shows the angular mismatch of each couple of the as manufactured taper interface (pre testing) compared to post uniaxial dynamic loading tests. Cone angle did not change due to assembly, dynamic loading and disassembly described in this chapter. Overall, the angular mismatch changed by a magnitude of 0.003 ± 0.002 ° pre testing compared to post testing.

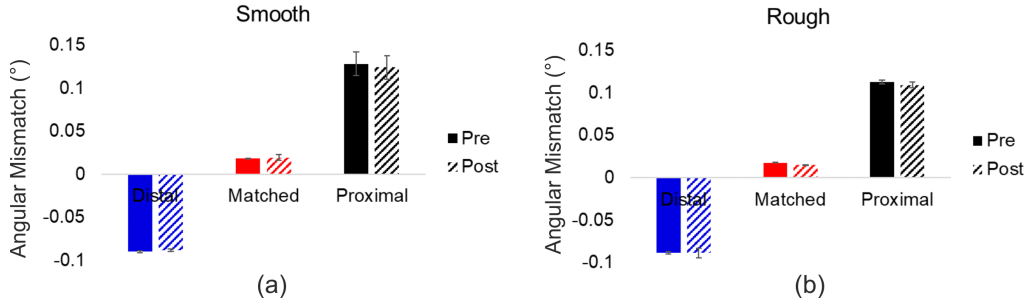

Fig. 5.15 Angular mismatch of the as manufactured couples (pre) verses post assembly to 2 kN and dynamic uniaxial loading for fretting corrosion and micro motion measurement of the (a) smooth and (b) rough samples.

The surface deviation maps of the taper interfaces did not present an observable difference post testing, compared to pre testing in any of the sample groups. Figure 5.16a and b shows an example of a rough distal male taper, and the associated head Figure 5.16c and d. This sample presented a reduction in angular mismatch by 0.002 ° after testing but an observable engagement pattern was not evident in the deviation pattern. An example of a smooth male taper surface deviation maps pre and post testing can be found in Appendix C Figure C.5, where again no observable engagement was seen.

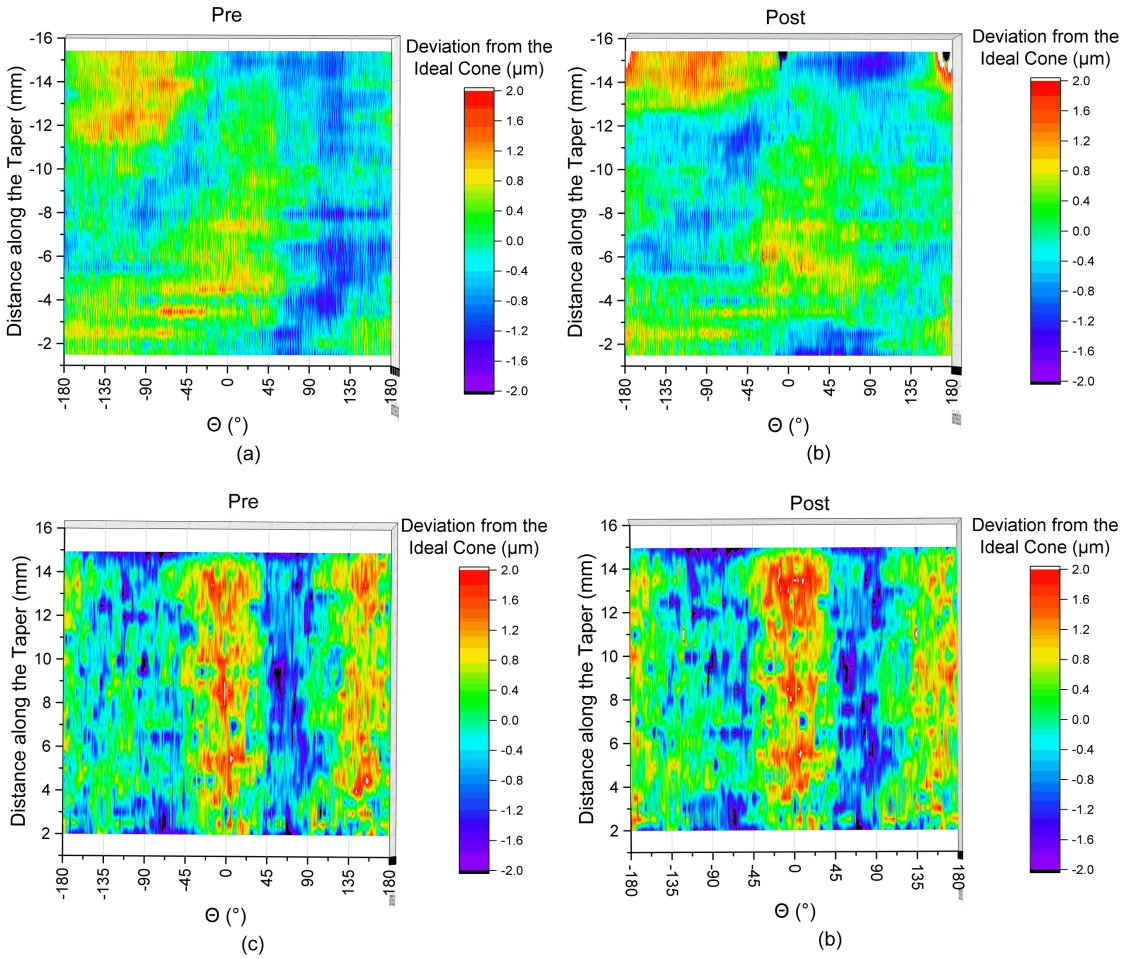

Fig. 5.16 Example surface deviation maps of a rough distal couple, (a) male taper prior to testing i.e. as manufactured, (b) post uniaxial dynamic testing and (c) female taper pre testing and (d) male taper post testing.

Surface Topography - Comparison Pre verses Post Testing

Figure 5.17 shows surface topography parameters pre compared to post testing, describing roughness amplitude and peak distribution. Comparison of all the surface topography parameters used in Chapter 4 of the as manufactured samples and the same surfaces post testing can be found in Appendix C Figures C.6 and C.7.

It was thought that the roughness amplitude may have presented a reduction after testing compared to the as manufactured surfaces. This was not the case, on average the samples presented a reduction in S_a by 0.02 ± 0.03 µm (Figures 5.17a and b). The greatest difference was found in the 'rough' proximal samples by a small margin of 0.08 ± 0.17 µm. In contrast, S_k demonstrated an average increase of 0.03 ± 0.06 µm (Figure 5.17c and d). Unlike, S_k, the peak density (S_{pd}) decreased in all test groups shown in Figure 5.17e and f. The 'smooth' samples decreased on average by 231 ± 114 mm^{-2} and the 'rough' by 30 ± 23 mm^{-2}. Although the reduction in S_{pd} in the 'smooth' proximal samples was found to be statistically significant, the average magnitude of reduction was found to be comparable to the variation seen in the as manufactured surfaces.

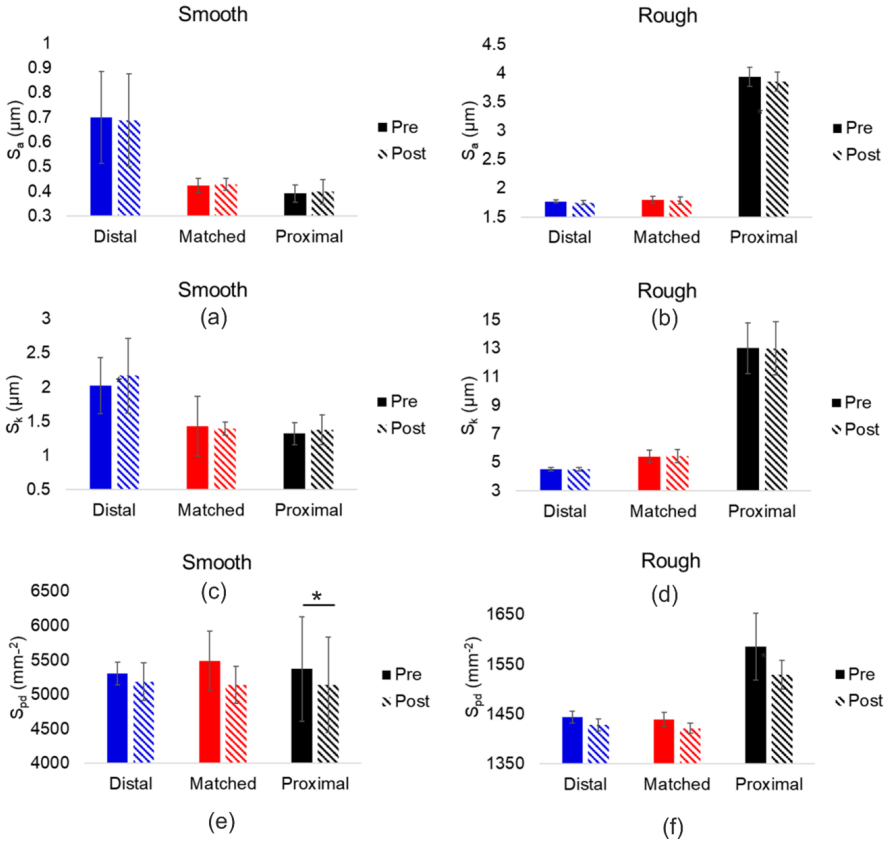

Fig. 5.17 Surface topography of the as manufactured surface (pre) compared to post testing: (a) S_a of the 'smooth' samples, (b) S_a of the 'rough' samples, (c) S_k of the 'smooth' samples, (d)S_k of the 'rough' samples, (e) S_{pd} of the 'smooth' samples and (f) S_{pd} of the 'rough' samples. Statistical difference between pre and post testing was indicated by an asterisks, p-value <0.05.

5.4 Discussion

The aim of this study was to assess the relative performance of the clinically representative samples with varying surface topography and angular mismatch in terms of fretting corrosion and motion. This was achieved by developing a short-term test protocol based on current incremental uniaxial simulation methodology and including the development of electrochemical and motion measurement apparatus, methodologies and analysis.

5.4.1 Experimental Design Rationale

The loading methodology, fixtures and samples for fretting corrosion and motion measurement were designed to replicate the modular tapered junction between the head and stem in a THR. A head offset, β angle, combined CCD and α angle (as defined by ISO 7206-4 [278], Figure 5.1b) of 38 mm, 145 ° and 9 ° was used to reflect a typical implantation orientation and a high offset. High offsets are associated with an increased susceptibility to fretting corrosion in-vivo due to an increased bending moment [164, 168, 169, 172, 171]. Simple beam bending theory predicts that deflection is related to the perpendicular distance between the effective cantilever, cubed i.e. sensitive to the head offset. Although this study subtracted the motion experienced by an equivalent monobloc to account for elastic deflection as per previous studies [211, 213], it is nevertheless thought to be important in clinical performance in terms of fretting corrosion at the taper interface. This was shown by the positive correlation between flexural rigidity and clinical performance [1, 213, 165, 172, 178, 179, 170, 177].

The fretting corrosion response was measured by applying an overpotential of 100 mV Vs OCP. Although applying a voltage away from equilibrium is a step away from that occurring in-vivo, it served to provide a greater anodic current that could be assessed quantitatively. An electrochemical study of 316L Stainless Steel by Xu et al. [281] (similar to the less noble metal of the two), indicates that the overpotential used in this study falls within the passive range (overpotential of around 0.15 V to 0.29 V for 316L Stainless Steel), well below the breakdown potential, only marginally driving the growth of the passive film i.e. without changing the surface to something that could be considered unrepresentative. Furthermore, the overpotential used by this present study is comparable to that utilised by Swaminathan et al. [234] as discussed in Section 2.8.3 to be equivalent to an overpotential of around 156 mV.

Although the rough samples presented measured currents that were around five times larger than that of the smooth samples, currents measured in this study were not dissimilar to that measured by a comparable study that employed incremental fretting corrosion

techniques. Pierre et al. [218] found an average current around 3.5 to 6 µA when a 12/14 Ti-CoCrMo couple with an unknown surface finished was assembled to 2 kN and dynamically loaded to 4 kN, reaching currents up to 9 µA when assembled to 1 kN. Pierre et al. [218] also used potentiostatic electrochemistry methodology with a fixed potential of -50 mV versus Ag/AgCl and an electrolyte of PBS. In comparison, this present study measured average currents in the region of 13 µA in the rough and 3 µA in the smooth. PBS was also used in this study and was considered a justified simplification for the purposes of comparing different taper designs.

The use of PBS as an electrolyte, as discussed in Section 2.7 and with reference to Table 2.5, lacks the simulation of proteins and other organic molecules like lubricin and hyaluronic acid present in synovial fluid. Previous studies have used bovine derived solutions to investigate the effect that the presence of proteins have on corrosion, tribocorrosion and wear mechanisms. Yan et al. [282, 283] investigated static corrosion and tribocorrosion, using a simplified pin-on-disk arrangement, of CoCrMo and 316l-stainless steel alloys using electrochemical and gravimetric methods. Yan et al. [282, 283] found that the presence of bovine serum increases the metal ion release in static environments (i.e. less able to resist desegregation by pure corrosion mechanisms), a finding supported by other studies such as Karimi et al. [203] who observed a lower OCP with a proteinaceous solution compared to that without, but decreases the degradation process in sliding systems. Overall, the tribocorrosion mechanisms in this sliding contact were found to dominate degradation with the total material loss being less in proteinaceous NaCl solutions compared to NaCl solutions without bovine serum [282, 283]. This reduction of material degradation in the presence of proteinous NaCl solution was attributed to the formation of a film containing metal oxides and organometallic species (metal ion-protein complexes), forming a barrier layer reducing friction, wear and tribocorrosion. This reduction in tribocorrosion due to the formation of a film was also seen on CoCrMo surfaces submerged in proteinaceous PBS when compared to PBS alone [284]. With that said, it follows that the currents measured in this present study, and thus tribocorrosive desegregation, would be an over estimation compared to if a more biologically relevant electrolyte was used. It should also be noted that Yan et al. [282, 283] and Bryant et al. [284] investigated reciprocating sliding contacts with an amplitude of 10 mm i.e., not a fretting contact which may affect the translation of their findings to this present study.

Looking now to a fretting contact, Baxmann et al. [285] investigated the effect of different solutions on the long-term fretting corrosion and fatigue response of modular neck tapers. Baxmann et al. [285] found a reduced cobalt ion concentration released into the solution in the instance where bovine serum was present in the solution compared to simulated solutions without bovine serum. However, a reduced fatigue life was also noted

in the instance where of bovine serum was used. Nevertheless, the findings of Baxmann et al. [285] further support that the currents measured by this present study (a short-term experimental study) are likely to be an under estimate. An aspect failed to be considered by Yan et al. [282, 283], Bryant et al. [284] and Baxmann et al. [285] was the effect of other organic molecules present in synovial fluid including hyaluronic acid and lubricin which are thought to be key components important for joint lubrication, including playing roles in boundary lubrication, boundary lubrication being pertinent to fretting contacts [286].

Motion measurement at the taper junction was achieved by the development of a non-contacting displacement measurement solution based on the principle of eddy current formation. Using four sensing coils, all the different types of motion were captured around the interface. Each coil was found to be accurate to ± 0.5 μm, which should result in an accuracy of ± 0.2 μm in the reported values of motion at the taper interface. Previous studies that used a similar methodology, tended to use two non-contacting displacement sensors with specifications of 'sub-micro' resolution (Lord Microstrain, US) and one reporting a 2 μm resolution (Micro-Epsilon,UK) [211, 218]. Direct comparison of motion measurement with these previous studies that also measured the electrochemical response was difficult due to using four sensing coils and calculating the equivalent motion at the taper interface. However, similar magnitudes of subsidence and motion were observed by a comparable study by Pierre et al. [218], reporting subsidence in the range of 0 to 50 μm and micro motion in the range of 5 to 20 μm at dynamic loading to a peak force of 4 kN, depending on the location of the sensor and assembly force. This present study, with a subsidence range of around 0 to 20 μm and micro motion 0 to 5 μm at the interface, depending on direction and test group. A different study that used six motion sensors to measure motion in three dimensions in dry conditions and without electrochemical measurements was that of Haschke et al. [213]. Comparable pistoning micro motion measurements were reported in the range of 2 and 3 μm and 'lateral rocking' micro motion in the range of 0.5 to 2 μm when assembled to 2 kN and uniaxially dynamically loaded between 230 and 2300 N. This compared to this present study with pistoning micro motion measured at 0.7 ±0.5 μm averaged across the different samples and toggling XZ micro motion measured at 1.2 ±0.7 μm. Haschke et al. [213] also measured rotational motion in the range of 0.002 and 0.02 °, converting the present study's rational micro motions back into degrees, comparable rotational motion of was measured between 0.002 ±0.001 °averaged across the samples of this present study.

Although this measurement system developed in this present study is verifiable in view of Pierre et al. [218] and Haschke et al. [213], a key advantage of Pierre et al. [218]'s measuring motion at the interface, was the ability to take concurrent motion and electrochemical measurements. The motion sensing solution in this study does present the

capacity to be adapted to allow for it to be submerged. One limitation in the development process in this project, was the ability to calibrate the coils within an aqueous environment. Other areas for development of this motion sensing solution include considering how the target and coils were fixed to the samples. Any motion between the aluminium target and head and coil board and spigots could introduce error into the measurements. This effect was minimised by calibrating the solution in an arrangement as close to that used in the test as possible and also use of an acrylic adhesive (Loctite, US) to fix the target to the head, like that in a previous studies [211, 218].

5.4.2 The Role of Surface Roughness

This present study found that the samples with an increased surface roughness resulted in an increased susceptibility to fretting corrosion demonstrated by the rough samples presenting higher current measurements (9.2 ±5.4 μA, average across the different engagement groups for the final loading increment) compared to the smooth samples (1.5 ±0.9 μA, average across the different engagement groups for the final loading increment). Assuming that increases in current from the baseline was due to the depassivation-repassivation of the passive oxide layer as in Gilbert and Zhu [240], the rough samples presented a greater proportion of abrasion and subsequent repassivation. This is in agreement with the study by Panagiotidou et al. [226] who reported that rough threaded-type surface topography presented evidence of oxide layer disruption with measurable peak current in the region of 2.5 μA when sinusoidally loaded between 100 and 1500 N, whilst the smooth non-threaded did not for tapers of the same length [226].

Comparing the average peak currents across the different engagement groups for the rough and smooth samples at the third loading increment with a peak load of 1500N of this present study with Panagiotidou et al. [226], comparable magnitudes of current were reported. More specifically, the smooth samples presented a small measurable current of 0.6 ±0.3 μA whilst the 'rough' samples presented an average greater measured peak current of 1.4 ±0.5. Further comparisons with the more recent study by Mueller et al. [4] who used ZRA methods to measure the resulting current of 12/14, CoCrMo-on-Ti6Al4V head-stem modular tapers, measured a lower average current of 1.8 ±1.3 μA for comparable smooth proximal samples (group 4) compared to 3.5 ±1.3 μA for a comparable rough proximal sample (group 1) when dynamically loaded between 300 and 2500 N. In comparison with this present study, the rough proximal samples at the fifth loading increment, with peak load of 2500 N, presented a greater average current of 3.8 ±3.0 μA, whilst the smooth proximal sample presented a lower average current of 0.7 ±0.1 μA. Despite Mueller et a. [4] also reporting that taper roughness did not reveal any significant difference on metal

ion release (unlike contact ratio that did) and retrieval studies supporting the finding of increased taper roughness increasing taper degradation in-vivo but only in conjunction with shorter tapers lengths [186, 187, 164, 163], the findings of this present study, those of Panagiotidou et al. [226] and the results highlighted in Mueller et al. [4], indicate that surface topography roughness as a single design parameter does play a role in taper degradation when considered in isolation, and thus, may be secondary to other parameters.

A key finding of this present study not reported previously, was that the 5 to 10 fold increase in current of the rough samples in the final loading increment compared to the smooth samples of equivalent engagement, was not due to a corresponding 5 to 10 fold increase in motion, in either subsidence (Figure 5.11), nor micro motion (Figure 5.13). Two key properties, important to the electrochemical response that topography will influence, include contact stress at sites of interaction and surface area, both exposed to the solution and also that experiencing abrasion. Again, assuming that increases in current from the baseline was due to the depassivation-repassivation of the passive oxide layer as in Gilbert and Zhu [240], the rough samples presented a greater proportion of abrasion and subsequent repassivation. The most probable explanation for this was due to differences in the contact mechanics at thread peaks. Looking to simplified pin-on-disk studies for a possible explanation, Royhman et al. [248] investigated the effect of a machined rough surface compared to a polished surface of a flat-on-flat fretting contact in the gross fretting regime using potentiostatic methods. Royhman et al. [248] determined a greater charge density of 2.0 ±0.25 mC cm^{-2} in the rough machined samples, 4-fold greater than the polished samples with 0.5 ±0.1 mC cm^{-2} with a constant fretting amplitude of 25 µm. The normal force of 200 N on the other hand was reported to result in a 25-fold greater contact pressure in the rough machined surface of 1200 ±700 MPa compared to the polished with 52 ±10 MPa, and although not discussed by Royhman et al. [248], it could be that the greater contact pressure results in an increased contact area and thus, oxide disruption. This explanation is supported by Swaminathan et al. [234] who found that if the increase in contact pressure did not alter the prevailing fretting regime (i.e. GSR to PSR), as was the case in Royhman et al. [248], this resulted in an increase in oxide abrasion due to increased contact area that overcame the yield point of the surface (i.e., hardness).

It was thought that the increased contact pressure at the thread peaks, which was thought to be responsible for the increased susceptibility to fretting corrosion as discussed above, would result in an increased disassembly forces of the rough samples compared to the smooth. However, this was not the case with the smooth samples presenting similar disassembly forces compared to the rough samples (please refer to Figure 5.14). This further supports that suggested in Chapter 4 in that disassembly force may not be a suitable parameter to determine the ‘strength’ a taper’s engagement.

In addition to differences in the magnitude of the measured current between the rough and smooth groups, the signal also differed. The rough samples presented a more consistent spike upon the onset of loading compared to the smooth (Figure 5.8a versus Figure 5.8b). This 'spike' in current upon the onset of dynamic loading has been reported previously and found to correspond to subsidence events at the start of a new loading increment [211]. This study found that the rough samples presented a more gradual, step-wise increase in subsidence which was thought to contribute to the consistent spike in current upon the onset of each loading increment (Figure 5.8b and Figure 5.10b). The smooth samples on the other hand, presented evidence of discrete subsidence events, which were thought to be reflected in the less consistent spike in current (Figure 5.8b and Figure 5.10b). This was particularly poignant in the subsidence event shown in the smooth matched sample in Figure 5.10a, and a corresponding spike and rapid decay in current upon the onset of the 7th increment shown in Figure 5.8a. The more gradual seating of tapers with an increased roughness has also been reported previously by Ouellette et al. [228] which found 'ridged' 9/10 tapers presented a smooth seating plot whilst the smooth 12/14 tapers presented a chattering/ratcheting (possible stick-slip) behaviour. It was thought the rougher samples were less suitable to stick-slip behaviour compared to smoother surface which could present a greater disparity between static and kinetic friction. Additionally, the more step-wise increase seen in the rough samples could be due to a more material response of the asperities deforming with seating compared to that of the smooth samples with a smaller roughness amplitude.

Prior to the discrete subsidence events shown in the subsidence versus time plots of the smooth matched and proximal samples (Figure 5.10a), there was evidence of the heads moving back up the taper. This has been documented before by Mali et al. [211], however this was attributed to toggling subsidence likely due to the lack of three dimensional characterisation of motion due to the use of only two sensing coils. However, this present study fully characterised motion in three-dimensional space, confirming movement of the head back up the taper. One possible explanation for this is air being trapped and compressed, forcing the heads off the taper until it could escape. This was not evident in the rough samples (Figure 5.10b), one possible explanation for this could be the thread-type finish, where the continuous thread could have allowed an unobstructed pathway for air to escape the taper junction.

5.4.3 The Role of Angular Mismatch

It was thought that an increased conformity through reduced angular mismatch would increase engagement of the modular taper junction, reduce the amount of motion experienced

at the taper interface and thus, reduce the taper junctions susceptibility to fretting corrosion. However, in both the 'smooth' and 'rough' samples, the matched engagement groups did not present the lowest levels of motion (Figure 5.11) and presented the greatest average current compared to the distal and matched samples of equivalent surface topography (Figure 5.9a and b) indicating an increased susceptibility to fretting corrosion. This finding is in contrast to Mueller et al. [4] who found that the matched samples, with both 'rough' and 'smooth' topography presented the lowest measurable currents and metal ion release (please refer to Table 5.3 for quantitative comparisons between this present study and that so Mueller et al. [4]). That said, Mueller et al. [4] found that the matched samples presented a similar current response and metal ion release compared to the distally engaged sample which presented a 'rough' surface topography, yet a lower compared to the proximally engaged samples. This was attributed to an increased resistance to fluid flow in and out of the taper junction, primarily in the distally engaged sample but also in the matched samples, at least compared to that of the proximally engaged samples. Focusing on the comparison of the fifth loading increment with peak load of 2500 N, the same as that used by Mueller et al. [4], the smooth matched presented an average greater current compared to smooth distal and smooth matched, whilst the rough proximal presented on average a greater current compared to the rough distal and rough matched (not the case in the sixth to eighth loading increments where the rough matched presented the greatest current). A possible explanation for this difference in findings could be that this present study only assembled the heads to 2 kN (a lower force than they were dynamically loaded to) whilst Mueller et al. [4] used a 3 kN assembly force (a greater force than they were dynamically loaded to). As such, the heads of this present study were still seating, supported by the measurements of subsidence (Figure 5.11). This possible instability of the taper junction due to a lower assembly force compared to the dynamic loading force could negatively affect this compromise between contact area and contact pressure (as discussed in Chapter 3), particularly in the matched samples whose interfacial contact pressure will be lower compared to the less conforming distal and matched samples i.e., the matched samples may present a greater proportion of contacting asperities experiencing the GSR over a greater area compared to the distal and proximal. Further explanation of the possible effects of contact pressure in a fretting contact is provided below.

Table 5.3 Average current measured by this present study at the fifth loading increment, with peak load of 2500 N compared to the average current and total ion release measured by Mueller et al. [4]. NB all values stated from the Mueller et al. [4] study are interpreted from graphical representations therein.

Present Study Sample	Average Current Measurement (μA)	Mueller et al. [4]'s Equivalent Sample	Average Current Measurement (μA)	Total Ion Concentration (mg/mL)
Smooth Distal	0.4 ±0.3			
Smooth Matched	1.2 ±0.7	Group 6	0.7 ±0.5	3.0 ±0.5
Smooth Proximal	0.7 ±0.1	Group 4	1.8 ±1.3	6.0 ±2.0
Rough Distal	2.2 ±1.7	Group 3	1.2 ±0.2	3.0 ±0.5
Rough Matched	2.6 ±0.6	Group 2	0.8 ±0.3	4.0 ±0.3
Rough Proximal	3.8 ±3.0	Group 1	3.5 ±1.3	8.0 ±1.3

Another contributory reason for the disparity between this present study and that of Mueller et al. [4] could be that the matched samples of this present study had a slight proximal mismatch of 0.017 ± 0.004 °. This reduced proximal mismatch would result in lower contact pressures (as mentioned above), approximately a pressure decrease of 85 MPa for every 0.1 °reduction in angular mismatch as determined by Donaldson et al. [136]'s FEA study, whilst also facilitating mass transport of corrosion reactants and products (Figure 5.18). Lower contact pressures resulting in more abrasion might seem counter-intuitive. However, within a fretting contact, higher pressures can sometimes be advantageous in terms of minimising sliding between the two surfaces by allowing motion to be accommodated by the contact stiffness (i.e. the PSR) [142]. Increased contact pressure has been shown to help minimise oxide layer disruption, resulting in lower measured currents using electrochemical techniques if the increase is sufficient enough to alter the prevailing fretting regime [234]. Within the matched samples, there was a higher probability of a greater portion of these asperities to experience gross slip for a greater proportion of oxide abrasion. Additionally, the matched samples' slight proximal mismatch would predicted a reduction in contact pressure towards the opening of the taper (Figure 5.18b). Therefore, asperities junctions with a higher probability of experiencing sliding

occur closer to the taper opening, exposed to the electrolyte. However, when comparing to the Mueller et al. [4] study, they reported angular mismatch to one decimal place and so the angular tolerance in their samples is unknown.

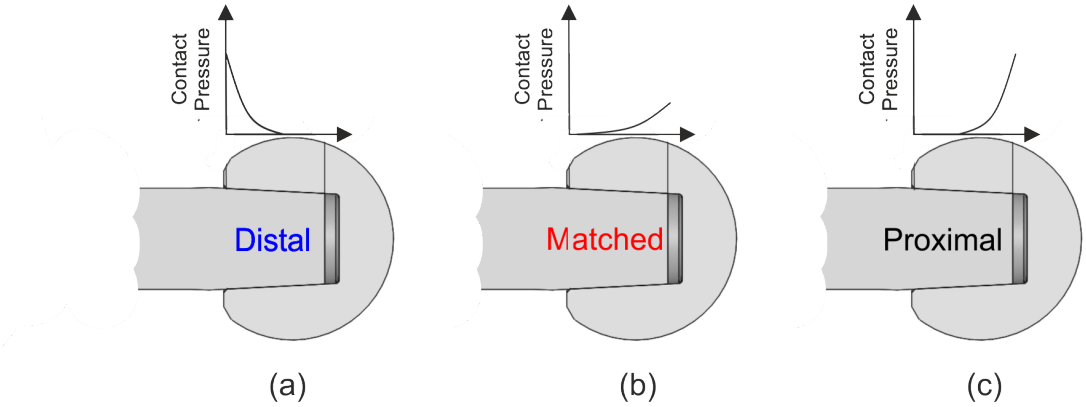

Fig. 5.18 Schematic of contact pressure as a function of axial position within the interface for the (a) distal, (b) matched and (c) proximal angular mismatch groups.

In both this present study and that of Mueller et al. [4], it was the distal engagement samples that presented the lowest average current compared to the matched or proximal of equivalent surface topography (Figure 5.9a and b). Other previous studies have also suggested that a distal mismatch could help provide an effective seal [232, 139]. However, the distal samples presented an increase in current above the baseline, suggesting that a complete seal was not achieved. In this study, i.e. when heads were assembled to 2 kN and subject to uniaxial loading up to peak forces of 4 kN, subsidence motions indicate that the heads were still seating. It remains to be seen if the distal samples are able to support an effective seal. Nevertheless, if an effective seal cannot be created crevice corrosion theory would predict that a narrower crevice opening would result in a more aggressive crevice geometry [160].

Nevertheless, the distal samples tended to present the least pistoning subsidence but the greatest off-axis and rotational subsidence motions (Figure 5.11). Additionally, micro motion results indicate that they were able to resist pistoning micro motion to a similar degree as the matched, possibly helping the distally engaged samples ability to resist fretting corrosion (Figure 5.13a and b). The distal samples' aforementioned greatest off-axis and rotational subsidence motions could help explain their ability to resist pistoning micro motion compared to the proximal samples which presented a similar magnitude of angular mismatch but in opposite direction (-0.090 ± 0.004 ° versus 0.120 ± 0.004 °). With reference to (Figure 5.19a and b), the distal engagement at the taper opening, away from the centre of the head and loading axis would provide a more stable contact (two points of contact as opposed to one) better able to support pistoning micro motion after sufficient off-axis subsidence.

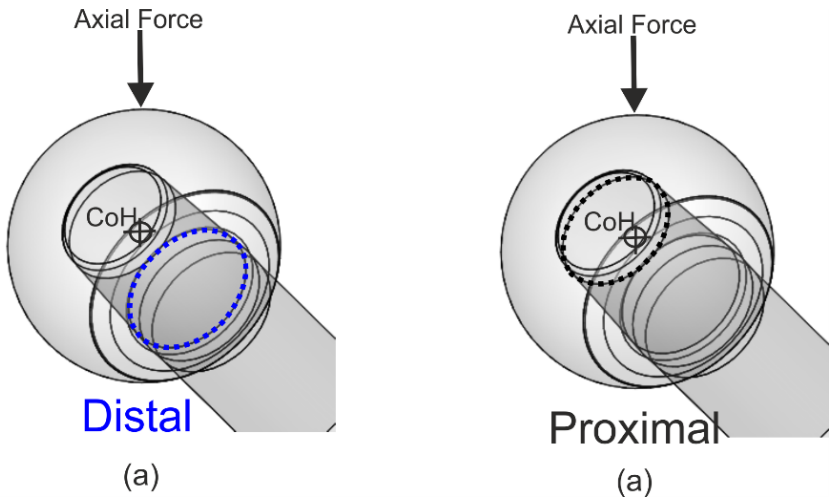

Fig. 5.19 Schematic of engagement location with respect to the centre of rotation (CoF) for the (a) distal and (b) proximal samples.

The proximally engaged samples represent the most severe and common engagements seen within the clinically available THR systems, as seen in Chapter 3 and reported previously by Mueller et al. [110]. Interestingly, this study found that the proximally engaged samples presented a greater current response than the distal samples but smaller than the matched samples of equivalent surface topography (Figure 5.9). However, the proximal samples presented the greatest pistoning micro motion compared to the distal or match. It was also thought that this may have been reflected in the XZ direction, but the proximal samples presented the smallest average toggling XZ micro motion (Figure 5.13g and h). One explanation for this unexpected result was due to the use of a uniaxial loading profile. One hypothesis is that subject to more complex loading with a higher degree of dynamic off-axis loading, may have further implications on a proximally engaged taper junction.

Looking at the comparable currents between this present study and that of Mueller et al. [4], it can be assumed that the metal ion release is also comparable, however, it should be appreciated that Mueller et al. [4] employed a CoCrMo-on-Ti6Al4V material couple compared to this study that employed a CoCrMo-on-stainless steel material couple. With that said, Mueller et al. [4] used 80 mL of test fluid compared to this present study that used 100mL and thus a metal ion concentration in the region of 3 to 8 mg/mL is predicted. Looking now to in-vivo studies, Forsthoefel et al. [287] measured the blood metal ion concentrations of patients that underwent a hip resurfacing and patients that underwent a THR with identical bearing interfaces. Subtracting the median total metal ion concentrations measured in the blood of patients that underwent THR (sum of Co and Cr metal ions, 4 µg/L over a median of 3.12 years) from those that underwent a resurfacing (sum of Co and Cr metal ions, 2.3 µg/L over a median of 4.36 years), 0.75 µg/mL per year

metal ion concentration (Co and Cr) can be attributed to the fretting interfaces present in THR that are not present in a resurfacing, despite Forsthoefel et al. [287] specifically attributing this to metal ion relates at the 'trunnion'. Referring back to the assumed metal ion concentration of between 3 to 8 mg/mL released by the taper junction of this present study in 100 mL of test fluid and further assuming a total fluid concentration in the body of 42 L [288], metal ion concentration released by the taper interface of this present study would equate to between 7 and 20 x 10^{-3} µg/L if dissolved in 42 L of fluid. As discussed above, this present study is thought to be comparable to one and a quarter days in-situ according to Bergmann et al. [6], extrapolating this estimated ion concentration to one year, this present study would predict a metal ion concentration release of between 2 and 6 µg/L per year from the head-stem taper interface, no too dissimilar to Forsthoefel et al. [287] 0.75 µg/mL per year Co and Cr metal ion concentration released from the fretting interface of a THR. Although the above quantitative comparisons makes some assumptions, such as 42 L of fluid in the human body being equivalent to fluid in the blood stream, the secretion some metal ions by the body and reduction of the measured metal ion concentration the further the measurement site is from the source [289], somewhat reducing the accuracy of this estimation, this nevertheless offers some validation to the developed test methodology.

5.5 Conclusion

The aim of this study was to assess the relative performance of clinically representative samples with varying surface topography and angular mismatch in terms of both fretting corrosion and motion. This was achieved by first manufacturing test fixtures to allow the samples to by uniaxially dynamically loaded in an orientation according to ISO 7206 [278]. Next saw the development of an electrochemical cell and motion measurement system. Whilst the electrochemical cell and measurement methodology was similar as that used by previous studies that investigated both the electrochemical response and the motion response [211, 218], the motion measurement system was further developed beyond these studies, more akin to that developed by Haschke et al. [213]. This was the first study to the author's knowledge to fully characterise the motion response of the taper junction in three dimensions whilst also measuring the electrochemical response. Next saw the development of a short term test methodology to allow for a high throughput of samples. This permitted the efficient determination of the relative performance of samples, representative of the variation in surface topography and angular mismatch seen in clinically available samples. Again, to the author's knowledge, this is the first study to systematically determine the fretting corrosion and motion response of tapers with varying surface topography and angular mismatch. The aforementioned short term test methodology was determined to be

representative of one and a quarter days in-situ in view of Bergmann et al. [6], validated to some degree against metal ion release measured in the blood stream of patients. Key findings from this study on the relative performance of the clinically representative samples include:

- all the samples in this study presented some level of susceptibility to fretting corrosion, including the distally engaged samples, indicating that optimisations in terms of angular mismatch and surface topography may not completely remove the issue of taper degradation in THR;
- samples were still seating, subsidence during short term tests has been shown to have a correlation with fretting corrosion measurements presenting limitations on the medium to long term insight afforded by this test methodology;
- the rough samples were more susceptible to fretting corrosion the smooth male taper interface, not attributed to an increase in motion at the interface and most likely attributed to increased contact pressures without altering the prevailing fretting regime at contacting asperities, the rough surface topography design parameter introduced for use with ceramic heads should not be implanted into patients in conjunction with metallic heads;
- the distally engaged head-stem couples i.e. engagement around the opening of the taper interfaces presented the lowest probable susceptibility to fretting corrosion compared to proximally engaged (i.e. engagements concentrated further within the interface) samples attributed to an increase in contact pressure at the taper opening, could inform a different design specification for modular metal head-stem systems; and
- the most conforming tapers, the matched engagement samples (0.017 ± 0.004 °), presented the highest currents suggesting a higher susceptibility to fretting corrosion compared to tapers that present more severe angular mismatch, attributed to a lower contact pressure altering the prevailing fretting regime of contacting asperities, however, the matched samples also presented the least off-axis subsidence and some of the lowest levels of micro motion which may indicate better longer term performance subject to more complex biomechanical loading.

5.6 Future Work

A challenge faced by this study in assessing the relative performance of clinically representative samples of surface topography and angular mismatch, was the lack of concurrent

electrochemical and motion measurements. Future work will involve further development of the motion sensing solution to allow measurements to be taken in an aqueous environment, allowing motions to be captured in three dimensions simultaneously with electrochemical measurements with sub-cycle resolution. However, high resolution measurements introduce the problem of data management with increased duration of simulation. This present study was thought to be representative of one and quarter days in-situ and would therefore be suitable for such high resolution measurements. Future work will involve the development of studies to assess the medium to long term performance of representative samples, balancing simulation duration and measurement resolution.

The ultimate assessment of relative performance of representative samples is the assessment of a patients biological response to corrosion and wear products. Quantifying and characterising the degradation products is key to gaining an understanding of the possible biological response [290]. Additionally, being able to demonstrate the risk posed by degradation products produced by medical devices is as small as possible is a requirement for approval on the EU market [98]. Future work will therefore involve quantifying and characterising degradation products, previous comparable studies have achieved by ICP-MS [197, 4] to identifying the ionic species and their respective concentrations in the test solution. Looking to how this is achieved in other joints replacements, characterising wear particles via more traditional SEM and TEM techniques and low angle laser light scattering which is able to capture and characterise a greater number of particles, biologic assays to assess the biological activity in response to corrosion and wear products [291].

Another aspect of this project that limited the capacity to assess the relative performance of the representative samples in terms of fretting corrosion and motion was the use of PBS as a test solution. Other studies have introduced bovine serum to introduce organic molecules into the test solution, as discussed above. However, a study by Brandt et al. [292] compare osteoarthritic human synovial fluid to four different bovine derived serum solutions frequently used by in-vitro studies and found significant differences. They suggested the use of alpha-calf serum, phosphate-buffered saline solution and hyaluronic acid to be essential components for in-vitro simulations.

Chapter 6

Fretting Corrosion and Motion Subject to ISO Walking Gait Profile

6.1 Introduction

Tapers in other industries are capable of operating in extreme conditions. CNC machines are able to resist over hundreds of newton-meters at tens of thousands of revolutions per minute, with the aid of a constant compressive axial force [293]. Modular tapers in THR on the other hand, tend to experience more complex dynamic torques on the tens of newton-meters scale, at a much lower frequency but a greater proportion of off-taper axis to on-taper axis loading [6, 294]. In other words, a key difference between tapers for industrial use and those used in THR is the complex biomechanical loading profile, an aspect not currently fully incorporated into preclinical experimental methodology.

As such, this study aimed to further develop the short-term test protocol from the previous chapter, Chapter 5, by incorporating a more complex simulation loading profile. More specifically, a simulation of a walking gait loading profile, akin to that stipulated in ISO 14242-1 [8] and similar to that used by Wight et al.[7]. Like Wight et al.[7], this study also employed an incremental loading methodology. Wight et al.[7]'s incremental loading profile was achieved by increasing axial force from 100 N to 1,100 N in steps of 100 N and from 1,100 N to 3,300 in steps of 200 N. Unlike Wight et al.[7], and as detailed in Section 2.7.1, this study built on that of Wight et al.[7]'s by incorporating motion measurement methodologies and excluded the bearing interface from the electrochemical measurements.

This study also investigated the effect of surface topography and angular mismatch present in clinically available THR systems on the fretting corrosion and motion response when subject to a simulated walking gait profile. This was done first when the heads were assembled to 2 kN, and then when the heads were assembled to 7 kN. Outcomes from this

chapter will be used to help understand the effect of introducing a more complex loading profile compared to that used by preclinical studies used to date, how surface topography and angular mismatch affect taper performance and the interaction with different head assembly forces.

6.2 Materials and Methodology

The short term performance of taper junctions was studied in part reference to a test methodology detailed in Chapter 5. This included measuring the fretting corrosion and motion response of the taper interfaces subject to incremental loading, with peak loads scaled from 0.5 to 4 kN in increments of 0.5 kN, to replicate the principle joint reaction forces seen in-vivo [6].

6.2.1 Samples

This chapter used three samples per test group to allow for three repeats, with the surface properties detailed in Table 6.1. The ‘smooth’ samples from the previous test were cleaned using an ultrasonic bath with acetone and reused for this study. New ‘rough’ samples were used for this study. Although, the surface post potentiostatic testing will affect the thickness of the passive layer, it was thought that the small overpotential and the short-term nature of the test would allow for comparison.

Table 6.1 Sample groups used in this study and summary of key parameters. See Table 3.2 for a description of surface topography parameters.

Engagement Couple	Angular Mismatch (°)	Male Taper Surface Topography			
		Sa (µm)	Sz (µm)	Sk (µm)	Spd (mm)
Distal Smooth	-0.088 ± 0.001	0.688 ± 0.157	5.006 ± 1.613	2.167 ± 0.551	5189 ± 166
Matched Smooth	0.019 ± 0.003	0.429 ± 0.032	5.150 ± 3.387	1.394 ± 0.093	5140 ± 271
Proximal Smooth	0.124 ± 0.014	0.399 ± 0.056	5.856 ± 5.729	1.327 ±0.218	5141 ± 693
Distal Rough	-0.091 ± 0.002	1.795 ± 0.043	14.795 ± 8.916	4.792 ± 0.043	1440 ± 12
Matched Rough	0.014 ± 0.011	1.755 ± 0.057	14.149 ± 7.795	5.694 ± 0.259	1435 ± 9
Proximal Rough	0.119 ± 0.008	3.917 ± 0.112	30.951 ± 3.764	12.570 ± 0.783	1625 ± 53

6.2.2 Dynamic Loading using a Simulated Walking Gait

Dynamic loading was applied using a six-axis single station universal joint simulator (Prosim, Simsol, UK). This allowed the application of a scaled simulated walking gait profile detailed in ISO 14242-1 [8] at a frequency of 1 Hz (Figure 6.1). In the same manner as the methodology detailed in Chapter 5, eight loading increments were scaled from a peak force of 500 N to 4000 N in increments of 500 N. Ten minute and ten second hold phases at 10 % of the peak force of the preceding increment were employed between each increment for the fretting corrosion and motion measurement tests respectively.

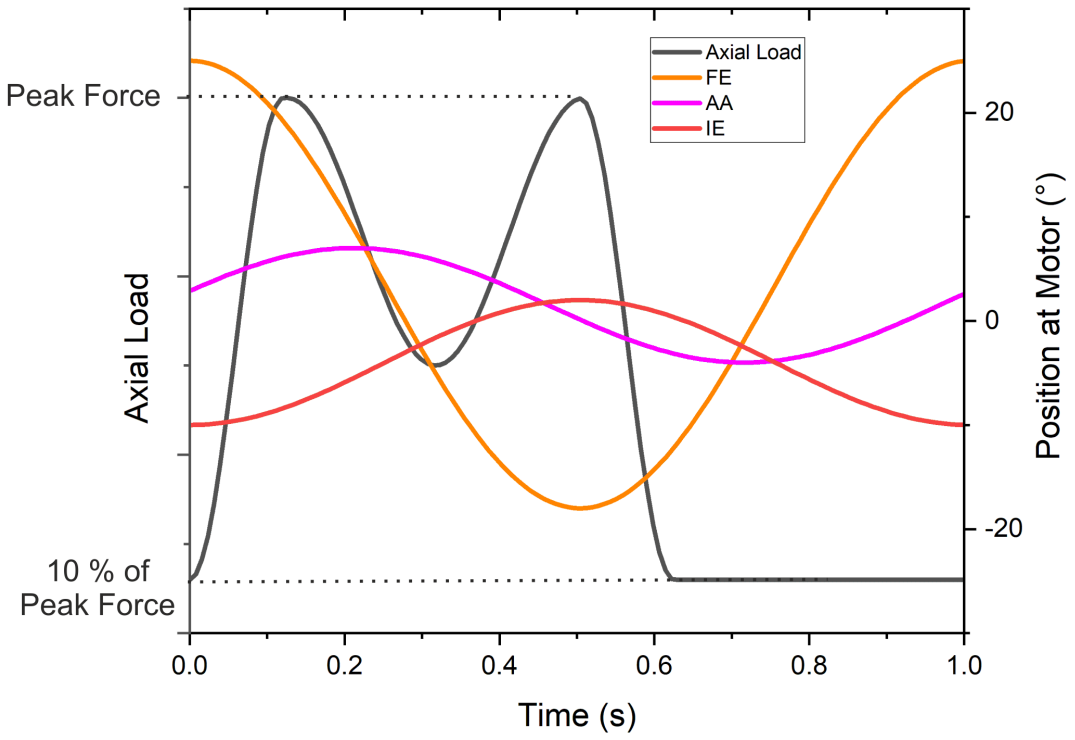

Fig. 6.1 Graphical representation of one cycle in a loading increment. Where FE stands for Flexion-Extension, AA Adduction-Abduction and IE Internal-External Rotation. Data for image adapted from ISO 14242-1 [8].

To measure the fretting corrosion and motion response of the taper samples with heads assembled to 2 and 7 kN, tests were conducted in series. Figure 6.2 shows a flow chart of tests carried out on each sample. This included first assembling the heads quasistatically to 2 kN in dry conditions using bespoke precision manufactured fixtures to control the loading axis, female and male taper axis concentrically to a tolerance of ± 0.001 °. Further details of the assembly protocol can be found in Chapter 4. The fretting corrosion test was conducted, followed by the motion measurement tests after disassembly and reassembly to 2 kN. The same fretting corrosion and motion measurements were then undertaken following disassembly and reassembly to 7 kN. Before and after each test the samples were cleaned in an ultrasonic bath immersed in acetone for 10 minutes, rinsed in deionised water and air dried. Disassembly forces after motion measurements after 2 kN and 7 kN assembly are presented.

Despite cleaning the samples between each test, it was acknowledged that there would be changes to the surfaces after dynamic loading which could have implications on subsequent tests. However, surface analysis presented in Chapter 5 Section 5.3.4 indicate

marginal changes to the surfaces. Therefore, conducting tests with heads assembled to 7 kN was predicted to have little influence on the results due to the stochastic asperity-asperity contacting nature of the surfaces.

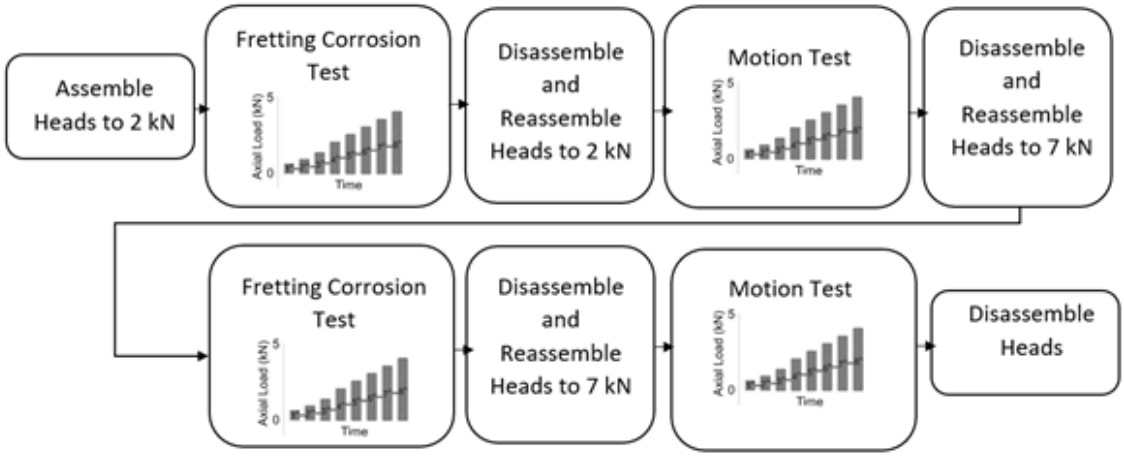

Fig. 6.2 Flow chart of the fretting corrosion and motion tests with head components assembled to 2 and 7kN.

Dynamic loading was applied to the samples held in anatomical orientation according to ISO 7206-4 [278] with a centrum-collum-diaohyseal angle (CCD) of 135 ° and head offset of 38 mm. To avoid electrolyte entrainment into the bearing interface or collisions with the motion sensing solution, modifications were made to a full 'cup-head' bearing interface. A loading pin (Figure 6.3) made of ultra high molecular weight polyethene, with a dome of radius 14.005 mm was designed to replicate half the nominal area of a full acetabular cup (590 mm^2 versus approximately 1200 mm^2). Full cup and head configurations have been found to present initial contact patches in the region of 17 to 24 % of the nominal cup area [295], meaning that the loading pin used in this study was able to support a realistic initial contact.

To isolate the electrochemical response to that of the taper junction, ASTM 1875-98 [196] uses seals to separate the point contact for uniaxial loading from the electrolyte. Separating the bearing interface from the electrolyte is of more importance in the present study due to this contact now being a sliding contact. This was achieved by not immersing the head in the solution. However, in-vivo this interface is fully immersed providing lubrication. Lubrication in this present study was achieved by introducing grease (Molykote, US). Grease was selected as it did not run into the electrolyte, affecting the electrochemical measurements. However, it is recognised that this is a step away from what happens in-vivo and a limitation of this study.

Upon the application of the scaled walking gait, load was applied to the taper junction via a frictional interaction between the loading pin and head. Figure 6.3a and b shows

schematics of all the different forces and moments acting about the head including axial force (F_{AF}), anterior-posterior (F_{AP}), medial-lateral (F_{ML}), flexion-extension (M_{FE}), adduction-abduction (M_{AA}) and internal-external rotation (M_{IE}). These were measured by a six-axis load cell integrated into the universal joint simulator (Prosim, Simsol, UK).

In order to see how the frictional response between the articulating surfaces changed with loading increment, the resultant torque ($\tau_{Resultant}$) and frictional factor were calculated. The vector components of resultant torque (τ_{FE}, τ_{AA} and τ_{IE}) were calculated by resolving the moments about the head. Using Figure 6.3a and b to help resolve the moments, the following equations for the three dimensions are as follows.

$$M_{FE} + \tau_{FE} - F_{AP} \times 0.1 = 0 \tag{6.1}$$

$$M_{AA} + \tau_{AA} - F_{ML} \times 0.1 = 0 \tag{6.2}$$

$$M_{IE} + \tau_{IE} = 0 \tag{6.3}$$

Rearranging Equations 6.1, 6.2 and 6.3 to calculate the frictional torques on the heads to give Equations 6.4, 6.5 and 6.6.

$$\tau_{FE} = F_{AP} \times 0.1 - M_{FE} \tag{6.4}$$

$$\tau_{AA} = F_{ML} \times 0.1 - M_{AA} \tag{6.5}$$

$$\tau_{IE} = -M_{IE} \tag{6.6}$$

The resultant torque on the heads and friction factor was then calculated using Pythagoras and the definition of friction factor by Scholes and Unsworth [296], Equation 6.7 and 6.8.

$$\tau_{Resultant} = \sqrt{\tau_{FE}^2 + \tau_{AA}^2 + \tau_{IE}^2} \tag{6.7}$$

$$FrictionFactor = \frac{\tau_{Resultant}}{HeadRadius \times F_{AF}} \tag{6.8}$$

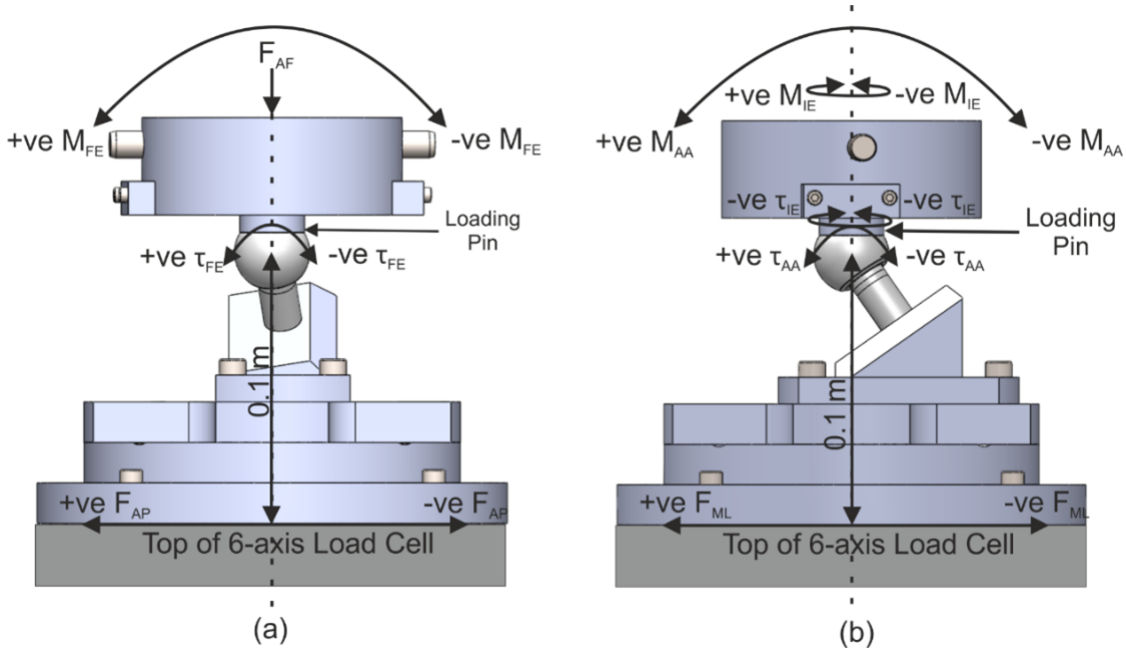

Fig. 6.3 Experimental configuration with annotations of moments acting around the head in the (a) sagittal and (b) coronal plane. Where M stands for moments, F for force and τ for frictional torque. AF denotes axial force, FE flexion-extension, AA adduction-abduction, AP anterior-posterior, ML medial-lateral and IE internal-external rotation.

6.2.3 Fretting Corrosion

The fretting corrosion test setup consisted of a three electrode electrochemical cell, integrated into the test arrangement (Figure 6.4) to facilitate real time measurement of corrosion in-situ. Two baths connected by a 600 mm long tube with a 10 mm diameter were filled with 300 mL of phosphate buffered saline (PBS) solution. One bath surrounded the sample (working electrode). The other allowed a Ag/AgCl reference electrode and

platinum counter electrode to sit within the electrolyte without colliding with the fixtures during dynamic loading. The solution level was such that the taper interface was immersed and just below the articulating surface. The distance between the two baths was made as small as possible to reduce any possible effects of solution resistance and a resulting IR drop. Due to the high solution conductivity and small currents, on a scale of μA, this was assumed to be low.

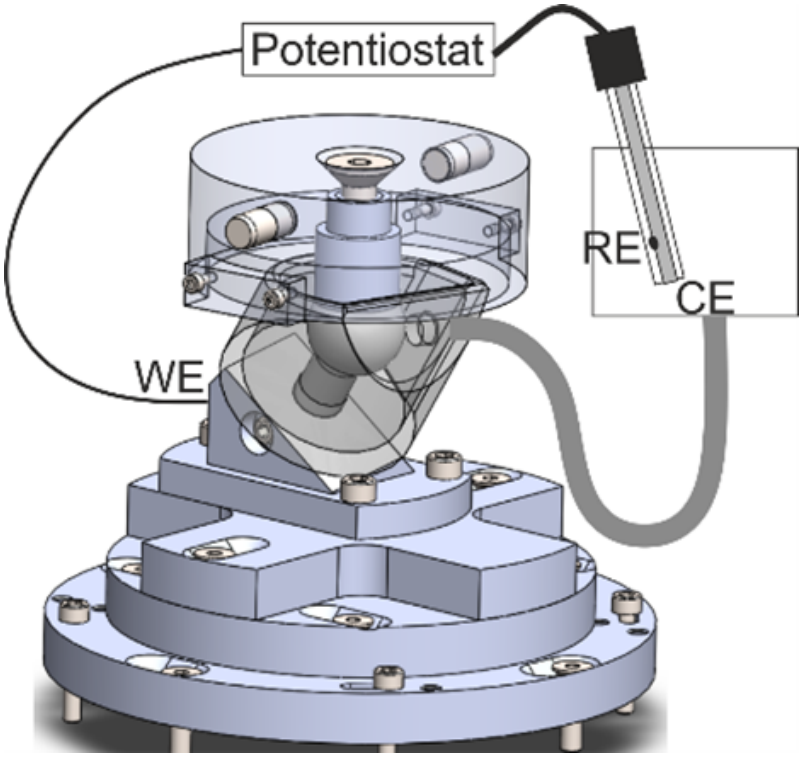

Fig. 6.4 Schematic of the (a) fretting corrosion and (b) motion set up for measurement subject to more complex loading profiles. Where WE indicated the working electrode connection, RE reference electrode and CE counter electrode.

The same electrochemical methodology detailed in Chapter 5 Section 5.2.3 was adopted in this study. This included connecting the electrodes to a floating ground potentiostat (IVIUM Compactstat, NL), measuring the Open Circuit Potential (OCP) for 30 minutes and applying a +100 mV vs OCP and measuring current at a rate of 1 Hz for a further 30 minutes under static conditions before applying the dynamic loading sequence. This allowed the measured current to settle to a sufficiently low ampere (around 500 nA), before the application of the dynamic loading sequence. Applying a positive, anodic potential, current can be measured as a function of time and provide information on the passivation and depassivation behaviour of the tapered interface. A sudden increase in current upon the onset of a loading increment was attributed to the depassivation and subsequent repassivation of the oxide layer. A greater increase in current would indicate a greater amount of oxide layer disruption. This study compared the average current in each

increment after subtracting the baseline current associated with static corrosion as per the same methodology detailed in Chapter 5.

6.2.4 Motion

The same motion measurement protocol developed detailed in Chapter 5 Section 5.2.4 and was used in this study. This involved the use of custom motion sensors, accurate to 0.5 µm, based on the principle of eddy-current formation as the transducer mechanism between sensing coil and conductive target (Figure 6.5a). Four sensing coils were used to capture motion at the taper interface in three dimensions, this included the axial direction along the taper axis (pistoning), off-axis motions in two dimensions (toggling YX and toggling XZ) and rotation about the taper axis (rotation), see Figure 6.5b.

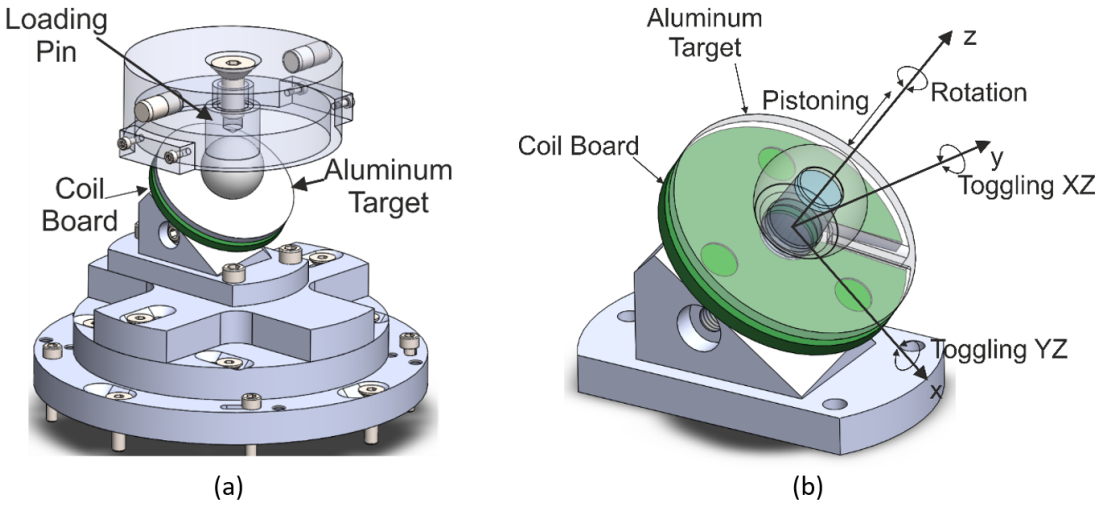

Fig. 6.5 (a) Schematic of the motion measurement configuration and (b) the four different motions captured to fully characterise relative movement at the taper interface in three dimensions.

In addition to separating motion out into pistoning, toggling YZ, toggling XZ and rotation, motion was further divided into subsidence and micro motion. Subsidence was attributed to movement of the heads down onto the taper over the course of the experiment, while micro motion was attributed to the small displacements about subsidence. Figure 6.6 shows a schematic of pistoning motion over the eight loading increments, where subsidence is shown by the light grey line following the overall form of the motion measurements and micro motion is the peak-to-trough height of the higher frequency (1 Hz) motion about subsidence. Subsidence and micro motion at each increment was calculated as an average and subtracted from an equivalent monobloc in order to isolate relative movement at the taper interface. Details of how the different motions were calculated from the four sensing

coils and subtraction from the equivalent monobloc can be found in Chapter 5 Section 5.2.4.

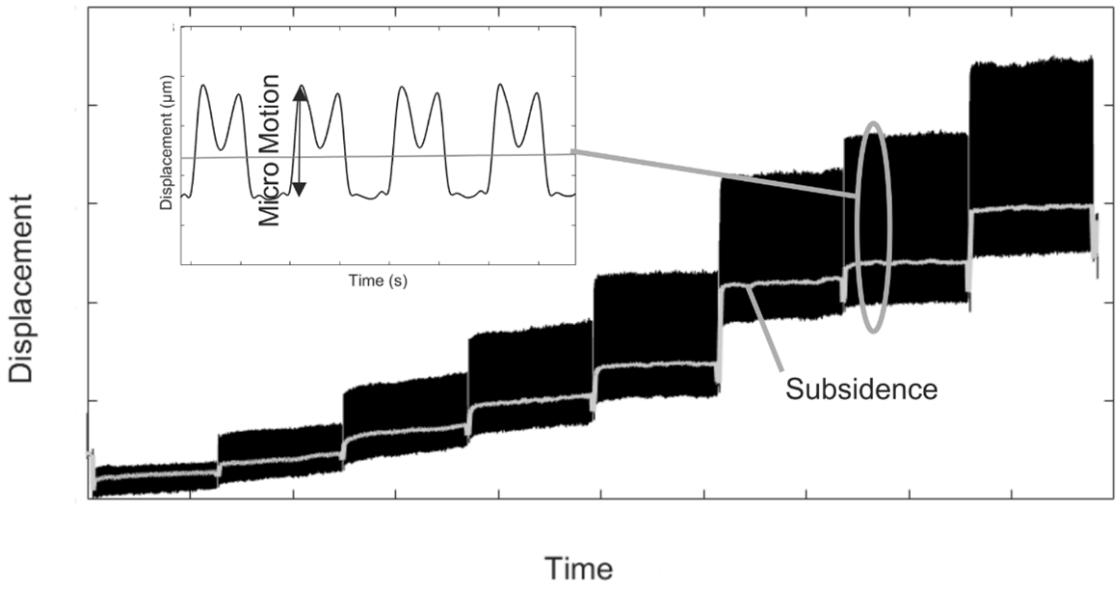

Fig. 6.6 Schematic of subsidence (light grey line) and micro motion (dark grey line), including evidence of the 8 loading increments can be seen with a short 10 second hold phase between each.

6.2.5 Surface Topography

Geometry and surface topography post dynamic testing was captured using the same methodology detailed in Chapter 4, Section 4.2.1. In terms of geometry, this included comparing ideal cone angle and surface deviation maps pre and post testing. In terms of surface topography, this included comparing S_a, S_k and S_{pd}, see Table 3.2 for definitions. Example roughness profiles traces, pre and post, were shown for each samples to illustrate any engagement.

6.2.6 Statistics

All data was presented as mean ± one standard deviation from the three repeat samples of each of the six test groups. Results were compared using a two tailed paired students t-test. Level of significance was set at p-value of 0.05 for all statistical tests. Analysis was performed using Excel (Microsoft, US).

6.3 Results

6.3.1 Forces Experienced by the Samples

Scaling the axial force component of the ISO walking gait profile detailed in ISO 14242-1 [8] resulted in an incremental increase in forces and torques experienced by the taper junction as a result of a frictional interaction between the head and articulating plug. Figure 6.7a to h shows the typical forces and torques measured by the six-axis load cell at each loading increment.

The axial force was the largest but did not reach that demanded from the simulator. On average, the measured axial force was 10 % lower than demanded at each force increment. The anterior-posterior force was the next largest, scaling from 0 to 140 N in the first increment to -80 and 410 N in the final. The smallest force was that of the medial-lateral direction scaling from ranges of -62 to 20 N, to -200 to 175 N. The largest turning moment was that in the flexion-extension direction reaching ranges from 0 to 20 Nm in the first increment, to -10 to 57 Nm in the final. The adduction-abduction presented the next largest torques scaling from -1.1 to 11 Nm, to -20 to 38 Nm. The smallest torque was that in the internal-external rotation direction where in the final increment a range from -4 to -0.5 Nm was achieved.

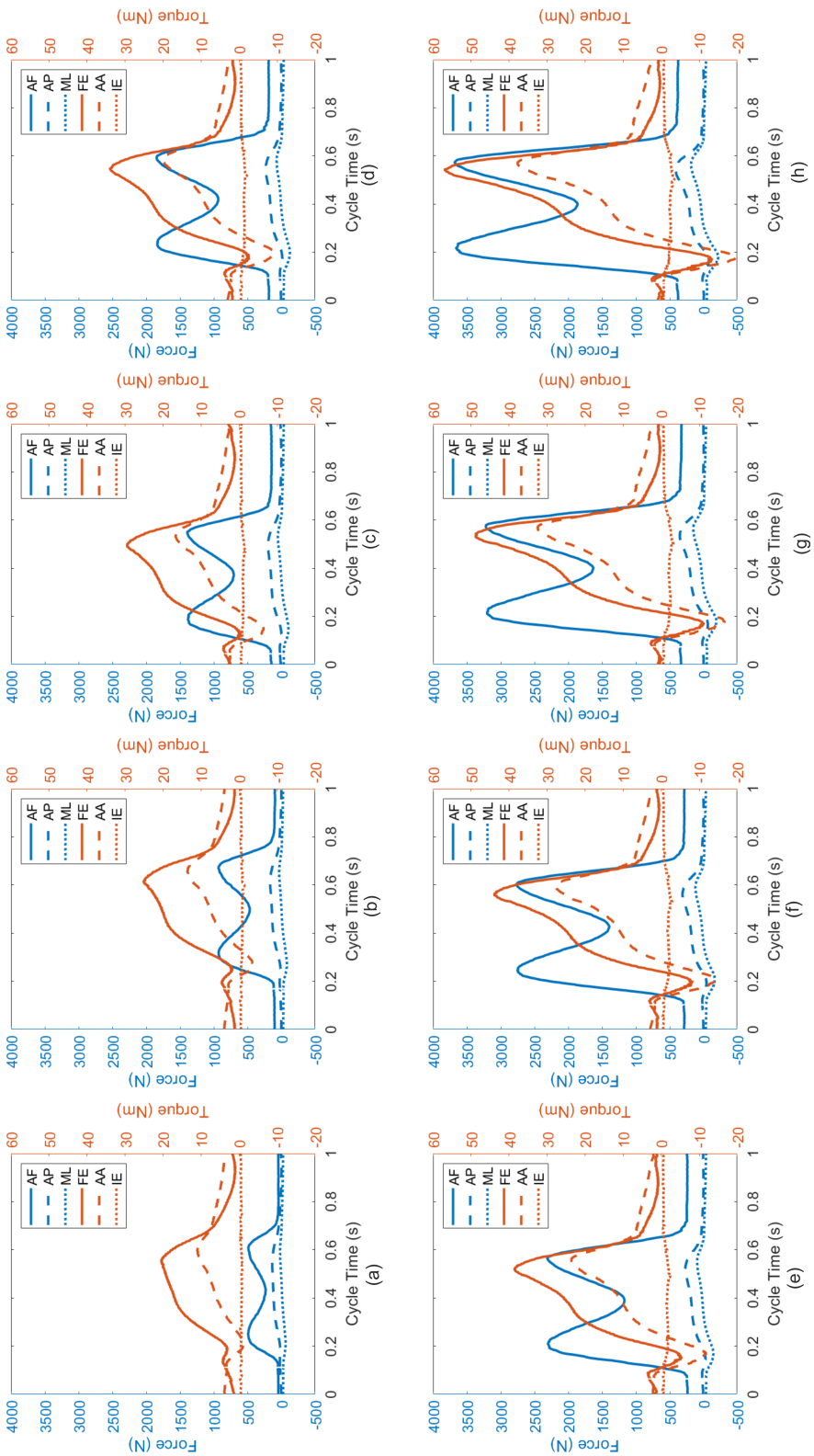

Fig. 6.7 Typical example of forces and torques measured by the six-axis load cell of the joint simulator at the (a) 0.5 kN, (b) 1 kN, (c) 1.5 kN, (d) 2 kN, (e) 2.5 kN, (f) 3 kN, (g) 3.5 kN and (f) 4 kN loading increment.

Table 6.2 summarises the axial force and resultant torques experienced at each loading increment. The resultant torque scaled with axial force in an approximately linear relationship demonstrated a ratio of 0.006 Nm per one newton of axial force. The force measurements from the single station indicate that the forces and torques transferred through the universal joint simulator were repeatable. At the smaller loading increments, high frictional factors were calculated in the region of between 1 and 1.5 attributed to a high proportion of toque in the flexion-extension direction. At greater loading increments, scaled from 2 to 4 kN peak force, peak frictional factors of between 0.5 and 0.6 were determined, comparable to a dry hard-on-hard articulation [176].

Table 6.2 Axial force and resultant torque from 6-axis load cell, calculated using Equations 6.7 to 6.7.

Increment No.	Axial Force (N)	Peak Resultant Torque (Nm)
1	495 ± 4	10 ± 2
2	936 ± 6	12 ± 1
3	1392 ± 7	14 ± 1
4	1847 ± 6	17 ± 1
5	2311 ± 6	19 ± 1
6	2766 ± 6	22 ± 1
7	3225 ± 6	26 ± 2
8	3682 ± 9	31 ± 4

6.3.2 Fretting Corrosion

Current increase above the baseline, correlating with the onset of a loading increment, increased with loading increment. This is shown in Figure 6.8a, b, c and d which presents example current transients. The onset of a loading increment current tended to present a sudden increase in the majority of cases which continued to climb throughout the increment. This was shown most clearly in the 'rough' proximal sample assembled to 7 kN (Figure 6.8d). In some cases, such as the 'rough' distal samples assembled to 2 kN, current presented a spike upon the onset of loading (Figure 6.8b). All samples assembled to 2 kN and 7 kN presented evidence of oxide layer disruption except for the 'smooth' distal samples assembled to 7 kN. This was shown in Figure 6.8c where an increase in current above the baseline was not seen. Differences in the measured current also appeared to exist between samples when assembled to different forces, between the 'rough' and 'smooth' samples of equivalent engagements and the different engagements of equivalent topographies.

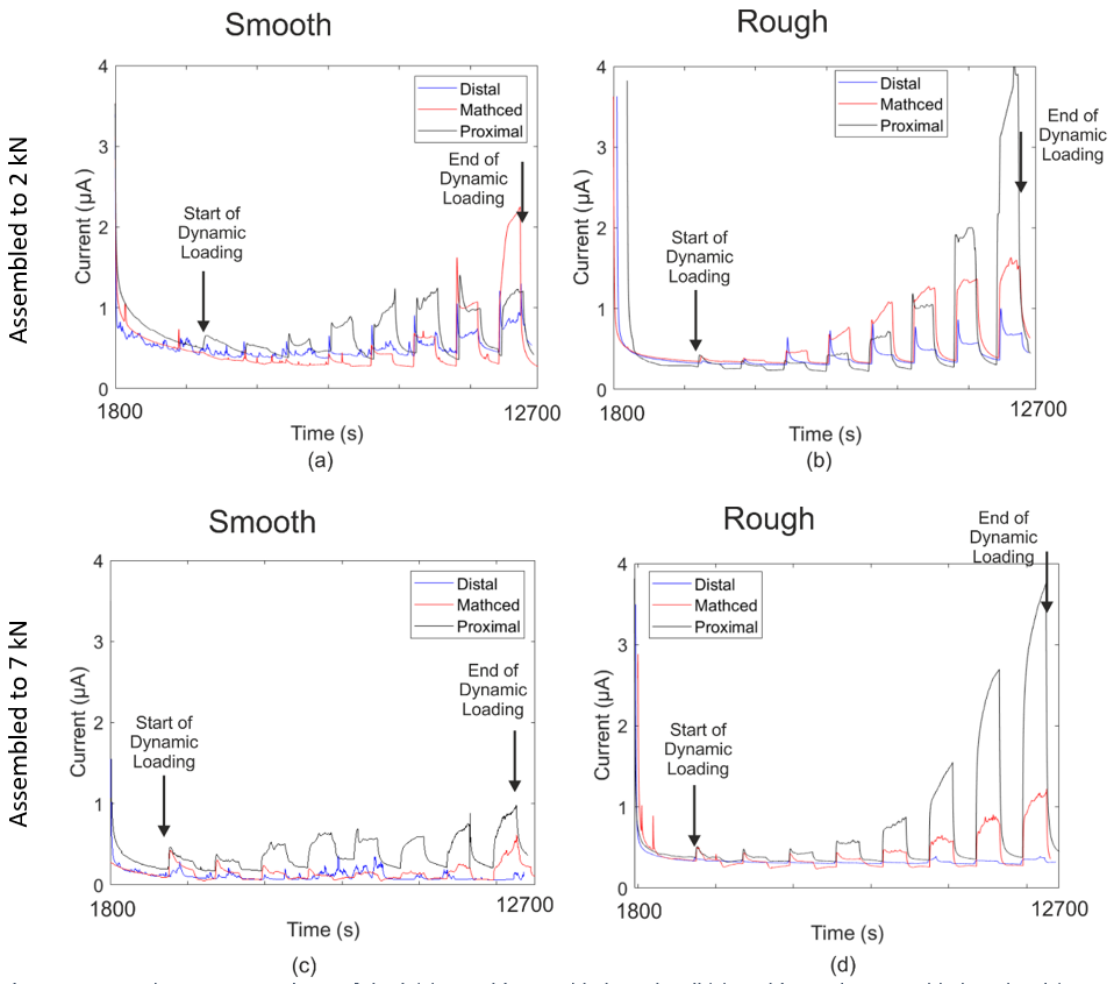

Fig. 6.8 Example current transients of the (a) 'smooth' samples assembled to 2 kN, (b) 'rough' samples assembled to 2kN, (c) 'smooth' samples assembled to 7 kN and (d) 'rough' samples assembled to 7 kN.

Figures 6.9a to d shows the average current above the baseline at each increment for each of the different samples assembled to 2 and 7 kN. On average most samples presented a reduction in current when assembled to 7 kN compared to 2 kN (Figure 6.9a and b versus Figure 6.9c and d). This was most evident in the distally engaged samples. The 'smooth' distal samples assembled to 7 kN did not present an increase in current above the baseline in any three of the repeats, presenting an average current of 0.02 ± 0.01 μA in the final increment attributed to 'noise' in the measured signal. This compared to the 'smooth' distal samples assembled to 2 kN which presented an average current of 0.10 ± 0.14 μA, not found to be significantly greater than when assembled to 7 kN (p-value > 0.05) due to only two out of the three repeats presenting an increase in current upon the onset of loading. The 'rough' distal samples assembled to 7kN did present significantly smaller currents then when assembled to 7 kN from the 4th loading increment with peak forced scaled to 2 kN onwards (p-value < 0.05). In the final loading increment the 'smooth' distal samples

presented an average current of 0.49 ± 0.22 µA when assembled to 2 kN compared to 0.07 ± 0.04 µA when assembled to 7 kN. On average the matched samples also presented an average reduction in current when assembled to 7 kN compared to 2 kN with significant difference in the 'rough' matched in the 6th loading increment (0.66 ± 0.14 µA compared to 0.16 ± 0.10 µA, p-value < 0.05, Figure 6.9b and d). Likewise in the 'smooth' matched samples in the final loading increment, an average reduction current was also seen (1.85 ± 0.87 µA compared to 0.18 ± 0.09 µA, p-value of 0.08, Figure 6.9a and c). The lowest probability of a statistical reduction in current due to greater assembly force was found in the proximal samples (p-value > 0.2). Where in the final loading increment the 'smooth' proximal samples presents an average current of 0.67 ± 0.26 µA when assembled to 2 kN compared to 0.33 ± 0.19 µA when assembled 7 kN (p-value >0.05, Figure 6.9a and c). This was also reflected in the rough proximal samples with an average current of 2.31 ± 0.44 µA versus 1.39 ± 1.14 µA (p-value > 0.05, Figure 6.9b and d).

The 'rough' samples tended to present a greater average current compared to the 'smooth' of equivalent engagement. This was reflected in all samples except for the matched engagement when assembled to 2 kN (Figure 6.9a and b). In the final loading increment, the 'rough' matched presented an average current of 0.66 ± 0.14 µA compared to the 'smooth' matched with 1.85 ± 0.87 µA (p-value > 0.05). When assembled to 7 kN, the 'rough' matched did present a greater average current with significant difference found in the final increment (0.18 ± 0.09 µA versus 0.52 ± 0.15 µA, p-value < 0.05, Figure 6.9c and d). Significant difference was also found in the proximally engaged samples when assembled to 2 kN in the final loading increment and in the distal in the 6th loading increment (Figure 6.9a and b). The 'smooth' distal samples assembled to 7 kN did not present evidence of oxide layer disruption, whereas the 'rough' distal samples did, although significant difference was not found between the two.

The distally engaged samples presented the lowest average current increase above the baseline in all cases. The proximal samples of equivalent engagement presented the greatest average current above the baseline with the exception of the 'smooth' samples assembled to 2 kN. In this case (Figure 6.9a), the matched group tended to present a greater average current than the proximal or distal at higher loading increments. Where, in the final loading increment, the matched group presents an average current of 1.85 ± 0.87 µA compared to the distal 0.10 ± 0.14 µA (p-value of 0.09) and proximal 0.67 ± 0.26 µA (p-value of 0.08).

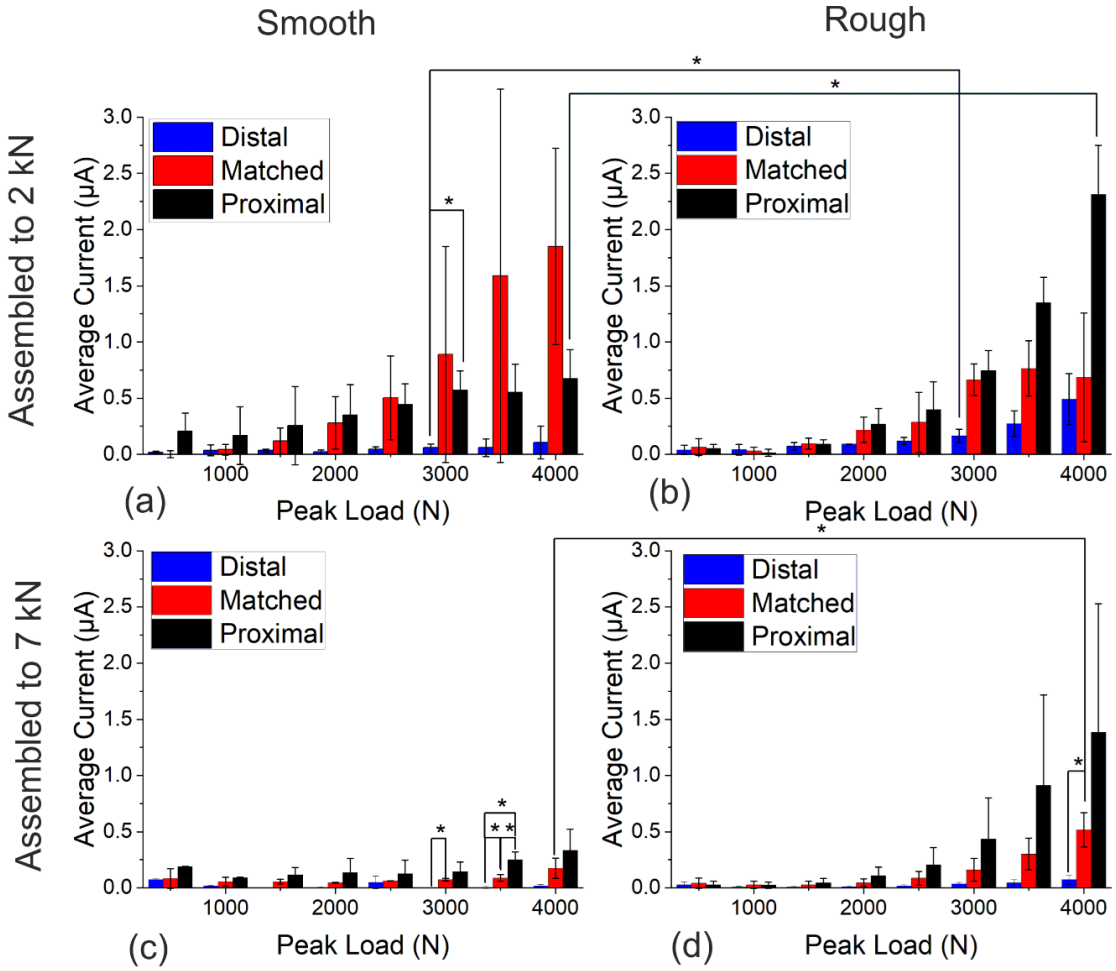

Fig. 6.9 Average current per increment of the (a) 'smooth' samples assembled to 2 kN, (b) 'rough' samples assembled to 2 kN, (c) 'smooth' samples assembled to 7 kN and (d) 'rough' samples assembled to 7 kN. Significant difference between 'rough' and 'smooth' samples of equivalent engagement and the different engagements of equivalent surface topography was denoted by '*'.

6.3.3 Motion

Subsidence

Example pistoning subsidence transients are shown in Figure 6.10 and describe how heads moved axially down the male taper. The 'smooth' samples assembled to 2 kN presented the greatest magnitude of seating due to sudden 'seating' events which tended to occur in the 7th or 8th increment (Figure 6.10a). Further seating during dynamic loading was not seen when the heads were assembled to 7 kN (Figure 6.10c). The 'rough' samples presented minimal pistoning subsidence compared to the 'smooth' samples (Figure 6.10b). Evidence of small more step-wise movement can be seen in the rough proximal sample

(Figure 6.10b). However, when the 'rough' samples were assembled to 7 kN, there was no evidence of 'seating' upon the onset of a new loading increment.

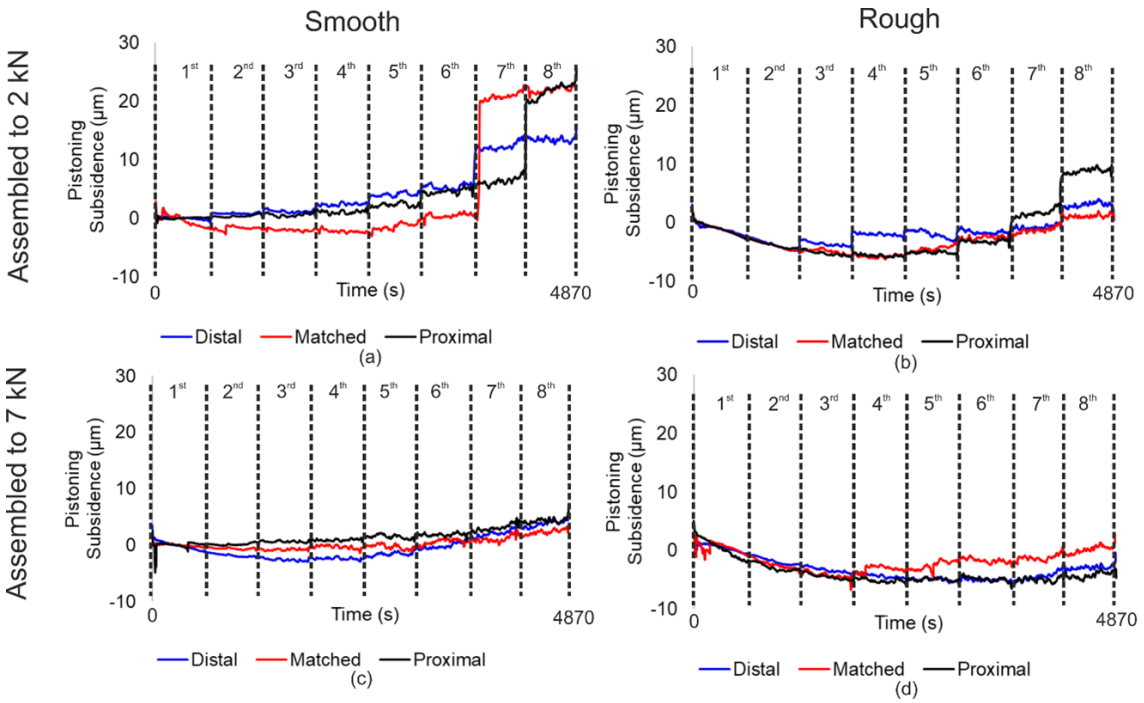

Fig. 6.10 Example pistoning subsidence for the (a) 'smooth' samples assembled to 2 kN, (b) 'rough' samples assembled to 2 kN, (c) 'smooth' samples assembled to 7 kN and (d) 'rough' samples assembled to 7 kN.

Subsidence transients in the XZ direction are shown in Figure 6.11. When the 'smooth' samples were assembled to 2 kN, the distal engagement group presented evidence of a step-wise increase with each increment, not presented in the matched or proximal (Figure 6.11a). Likewise, in the 'rough' samples, the distal engagement group presented evidence of a step-wise increase with each increment, again, not evident in the matched or proximally engaged samples. When the samples were assembled to 7 kN, the was no evidence in a step-wise increase with loading increment (Figure 6.11c). The rough distal samples also presented this step-wise increase when assembled to 2 kN (Figure 6.11d). When the 'rough' samples were assembled to 7 kN, evidence of XZ subsidence was still present in the distal engagement group.

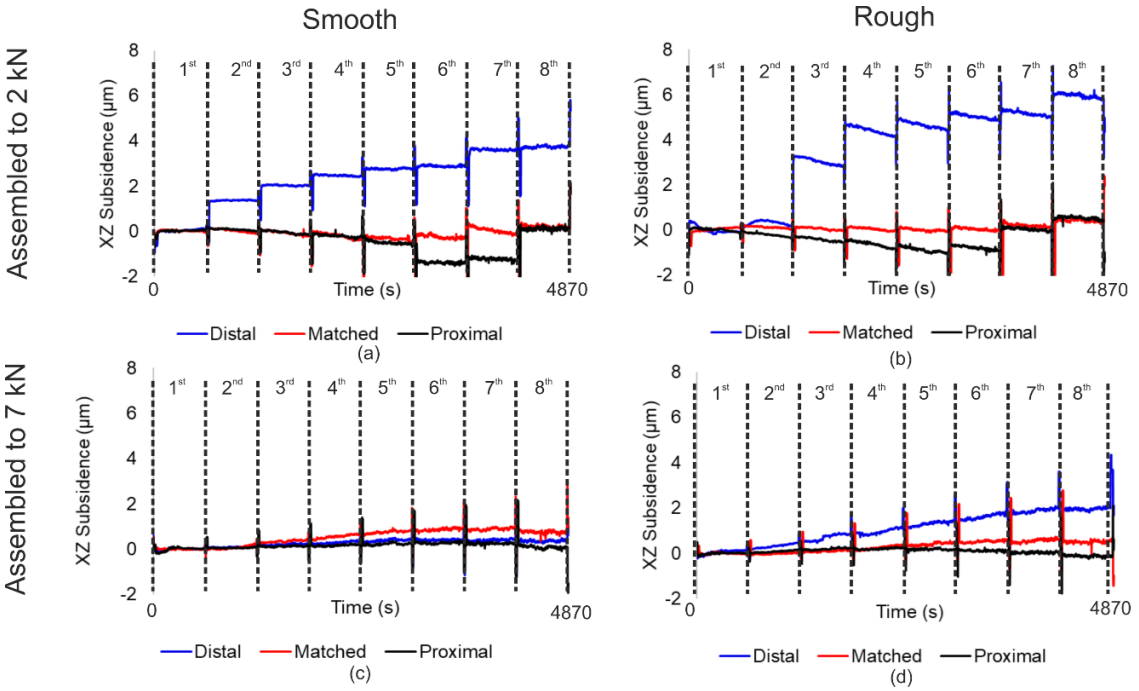

Fig. 6.11 Example XZ subsidence for the (a) 'smooth' samples assembled to 2 kN, (b) 'rough' samples assembled to 2 kN, (c) 'smooth' samples assembled to 7 kN and (d) 'rough' samples assembled to 7 kN.

Figure 6.12 shows the magnitude of subsidence in the pistoning (axial) and XZ directions for the final increment. The 'smooth' samples assembled to 2 kN presented some of the largest magnitudes of pistoning subsidence (distal 23.5 ± 18.0 µm, matched 17.9 ± 9.1 µm and proximal 23.7 ± 14.6 µm). However, large variability in the magnitude of subsidence between samples meant that there was no statistical significance between when the samples were assembled to 2 kN compared to 7 kN (p-value > 0.05, Figure 6.12a and c). Likewise, comparing the 'smooth' and 'rough' samples, no significant difference was found between the two groups with equivalent engagement and assembly force.

Within the 'smooth' samples in the XZ direction, the distally engaged present the largest magnitude of 3.3 ± 2.6 µm in the final increment. When assembled to 7 kN, the 'smooth' distal samples presented minimal subsidence of 0.4 ± 0.6 µm. However, like pistoning, large variability between samples meant that there was no statistical significance between the 'smooth' distal samples when assembled 2 kN compared to 7 kN in XZ subsidence.

The 'rough' samples when assembled to both 2 kN and 7 kN presented minimal pistoning subsidence with no significant difference between the two (Figure 6.12b and d). When assembled to 2 kN (Figure 6.12b), the 'rough' distal samples presented the largest XZ subsidence (4.6 ± 1.2 µm) compared to the matched (0.9 ± 0.5 µm, p-value < 0.05) or proximal (1.1 ± 3.1 µm, p-value > 0.05). When assembled to 7 kN, the 'rough' distal

samples presented a smaller XZ subsidence of 3.4 ± 1.5 µm compared to when assembled to 2 kN (p-value > 0.05).

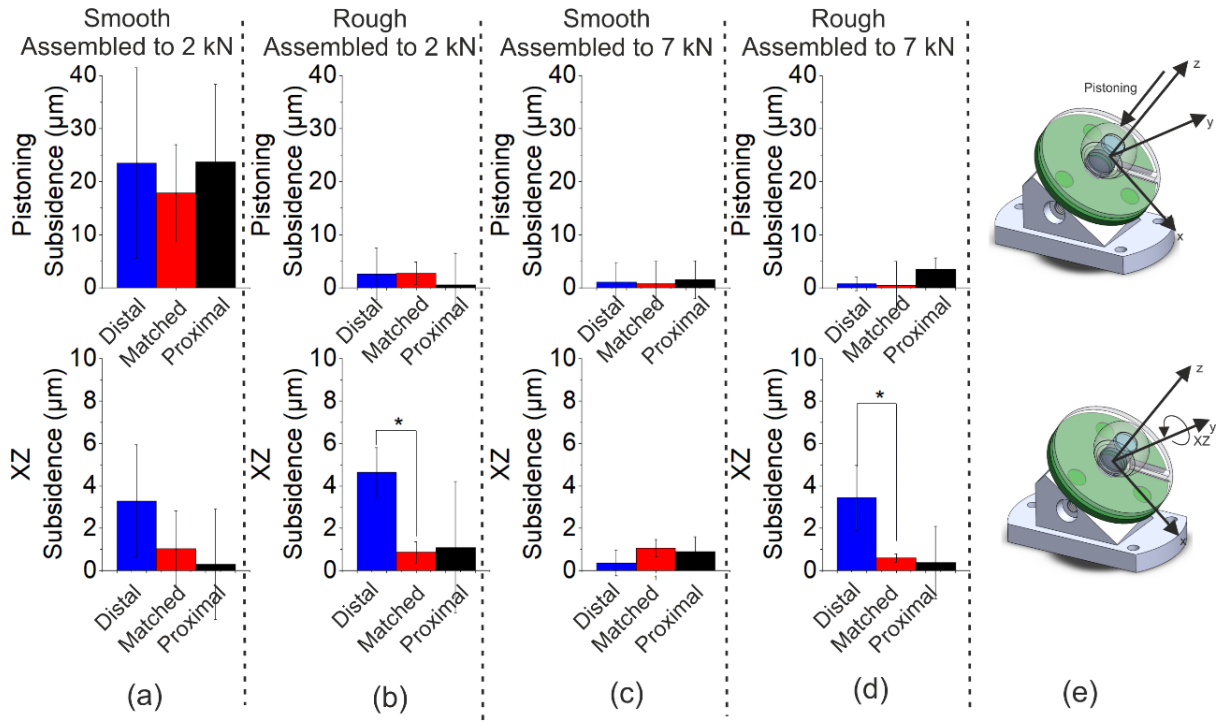

Fig. 6.12 Magnitude of subsidence for the (a) 'smooth' samples assembled to 2 kN, (b) 'rough' samples assembled to 2 kN, (c) 'smooth' samples assembled to 7 kN and (d) 'rough' samples assembled to 7 kN, in the (e) axial (pistoning) direction and XZ. Significant difference between 'rough' and 'smooth' samples of equivalent engagement and the different engagements of equivalent surface topography was denoted by '*'.

Micro Motion

Micro motion scaled with loading increment. This is shown in Figure 6.13 which shows three seconds of motion data for a 'smooth' distal, matched and proximal sample in the 2nd, 4th, 6th and 8th loading increment. The greatest magnitude of micro motion was that in the toggling XZ direction, followed by pistoning. Figure 6.13 indicates possible differences between the engagement groups. The distal and matched samples (Figure 6.13a and b respectively) demonstrate similar magnitudes of micro motion. The smooth proximal sample (Figure 6.13c) presented a greater magnitude of micro motion compared to the distal and matched. It should be noted that micro motion shown in Figure 6.13 had not been subtracted from the equivalent monoblock due to the complexity of undertaking this on a sub-cycle basis.

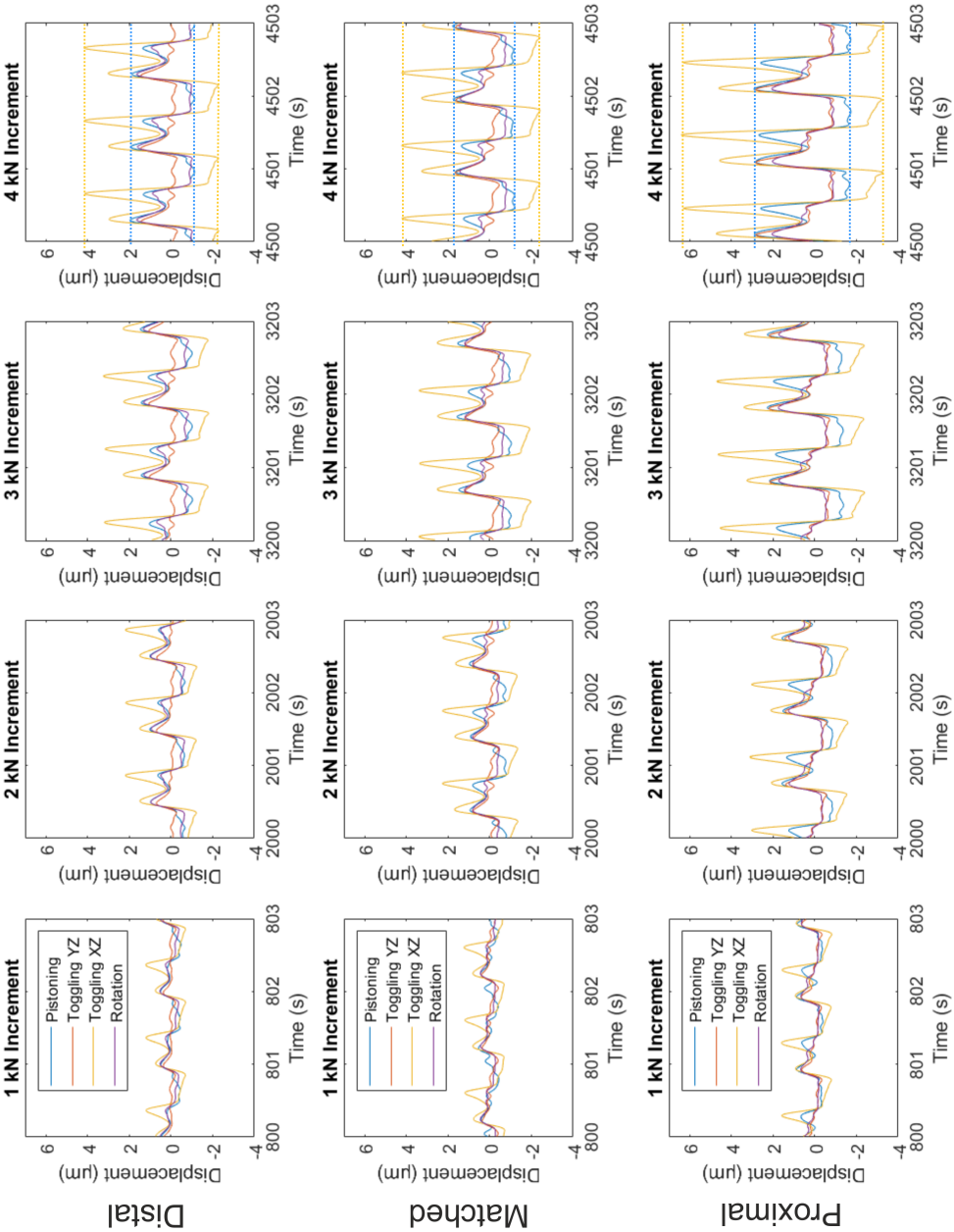

Fig. 6.13 Three seconds of micro motion data captured for a 'smooth' (a) distal, (b) matched and (c) proximal. NB these will include any elastic deflection.

All the samples presented evidence in Figure 6.14 show how toggling XZ micro motion changes with time by plotting magnitude on a cycle-by-cycle basis. Upon the onset of a new loading increment, micro motion presented a corresponding step increase. Some samples presented an initial 'spike' in micro motion upon the onset of a new loading increment, like that in the 'smooth' matched samples in the 7th loading increment (Figure 6.14a) and the 'rough' distal samples assembled to 2kN in the 5^{th} to 8^{th} loading increment (Figure 6.14b). In all sample groups, a lower average toggling XZ micro motion was seen when the heads were assembled to 7 kN compared to 2 kN. Irrespective of assembled force and surface topography, the proximally engaged samples presented the greatest magnitude of toggling XZ micro motion compared to matched or distally engaged.

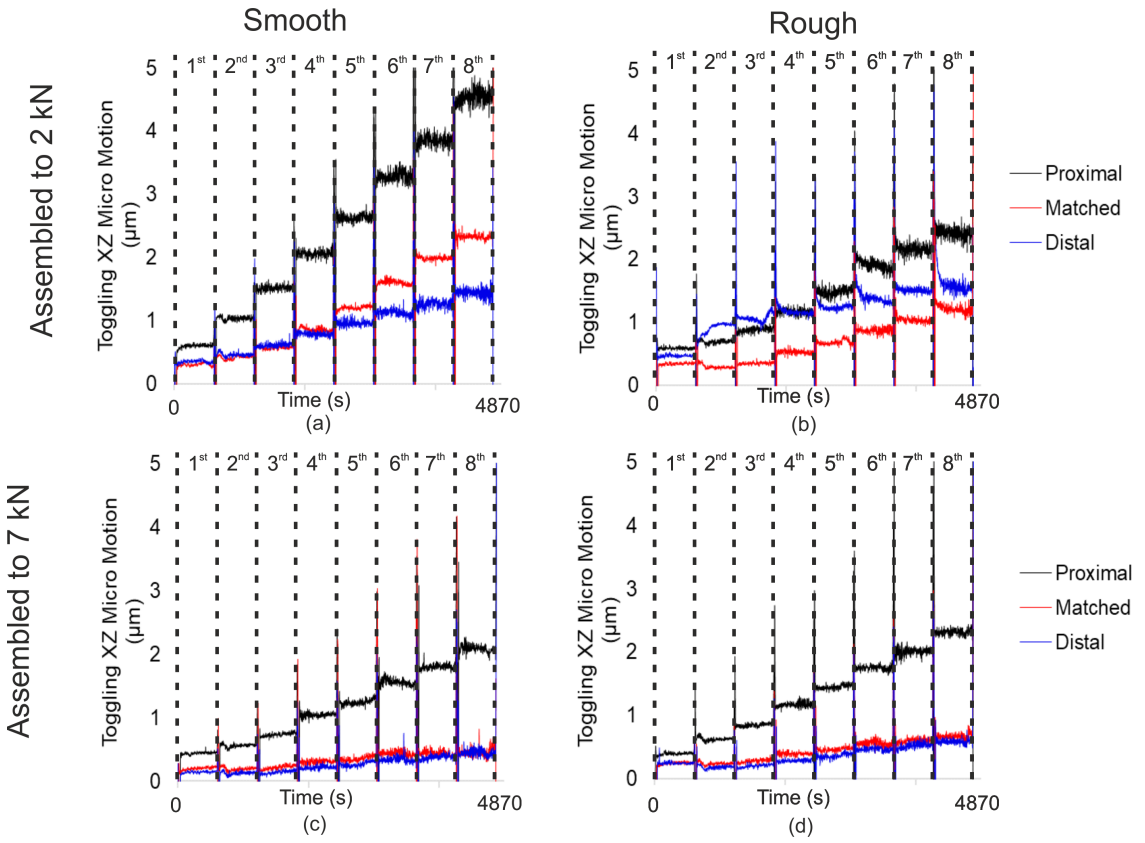

Fig. 6.14 Example toggling XZ micro motion of the (a) 'smooth' samples assembled to 2 kN, (b) 'rough' samples assembled to 2 kN, (c) 'smooth' samples assembled to 7 kN and (d) 'rough' samples assembled to 7 kN, on a cycle-by-cycle resolution with annotated increment boundaries.

The average micro motion in the final increment in each direction can be seen in Figure 6.15. Smaller magnitudes of micro motion were presented when the heads were assembled to 7 kN compared to 2 kN. In the pistoning direction, the greatest reduction in micro motion of 1.2 ± 0.4 µm was seen in the 'smooth' proximal samples (2.1 ± 0.3 µm versus 0.8 ± 0.4 µm, p-value < 0.05 , Figure 6.15a and c respectively). The 'rough' proximal

samples presented the second largest difference in pistoning micro motion between the two assembly forces of 0.9 ± 0.3 µm (1.9 ± 0.3 versus 1.0 ± 0.2 µm, p-value < 0.05, Figure 6.15b and d). The smallest difference in pistoning micro motion between 2 kN and 7 kN head assembled was that seen in the 'rough' matched samples with a 0.4 ± 0.6 µm reduction (0.7 ± 0.4 µm versus 0.3 ± 0.6 µm, p-value > 0.05), followed by the 'smooth' matched with a 0.6 ± 0.4 µm reduction (0.9 ± 0.4 versus 0.3 ± 0.2 µm, p-value of 0.06). The 'smooth' and 'rough' distal samples also presented a significant reduction (p-value < 0.05) in pistoning micro motion when the heads were assembled to 7 kN compared to 2 kN. No significant reduction in toggling YZ micro motion was seen in the samples due to assembled force (p-value > 0.05). In the toggling XZ direction, a significant reduction in micro motion in the 'smooth' and 'rough' distally engaged samples was seen by 1.3 ± 0.8 µm (1.7 ± 0.8 µm versus 0.4 ± 0.2 µm, p-value < 0.05) and 1.2 ± 0.5 µm (1.7 ± 0.5 µm versus 0.5 ± 0.3 µm, p-value < 0.05), respectively. The 'smooth' and 'rough' matched samples of also presented a reduction in toggling XZ micro motion of 1.3 ± 0.6 µm and 1.2 ± 0.7 µm, respectively, not found to be statistically significant with p-values within the range of 0.07 and 0.08. The proximally engaged samples also presented an average reduction with greater assembled force in toggling XZ but was not found to be statistically significant with p-values within the range of 0.4 and 0.6. In the rotational direction, a reduction in micro motion when assembled to 7 kN compared to 2 kN was seen in all samples. The largest reduction in rotational micro motion was seen in the 'smooth' distal sample of 0.5 ± 0.2 µm (p-value > 0.05, Figure 6.15a and c) and the smallest in the 'rough' matched of 0.2 ± 0.2 µm (p-value > 0.05, Figure 19b and d).

Micro motion between the 'smooth' and 'rough' samples of equivalent engagements presented very similar magnitudes with no statistical difference (p-value > 0.05). Comparing the different engagements groups of equivalent surface topography, the proximally engaged samples presented the largest magnitude of micro motion in all directions, whilst the distal and matched samples presented similar magnitudes of micro motion. In the pistoning direction (axial), 'smooth' and 'rough' assembled to 2 kN, the proximally engaged samples presented significantly greater micro motion of 2.1 ± 0.3 µm and 1.9 ± 0.3 µm ('smooth' and 'rough' respectively) compared to the distal 0.7 ± 0.2 µm (both 'smooth' and matched) and matched with 0.9 ± 0.4 µm and 0.7 ± 0.4 µm, in the final loading increment (Figure 6.15a and b). However, when the heads were assembled to 7 kN, significant difference in pistoning was only found between the 'smooth' and 'rough' proximal and distally engaged samples (Figure 6.15c and d). Significantly greater micro motions found in the proximally engaged samples was also seen in the rotational direction. For example, in the 'smooth' samples assembled to 7 kN, the distal and matched engagement groups presented negligible rotational micro motion (0.0 ± 0.2 µm) compared to the proximally engaged sample (0.8 ± 0.3 µm).

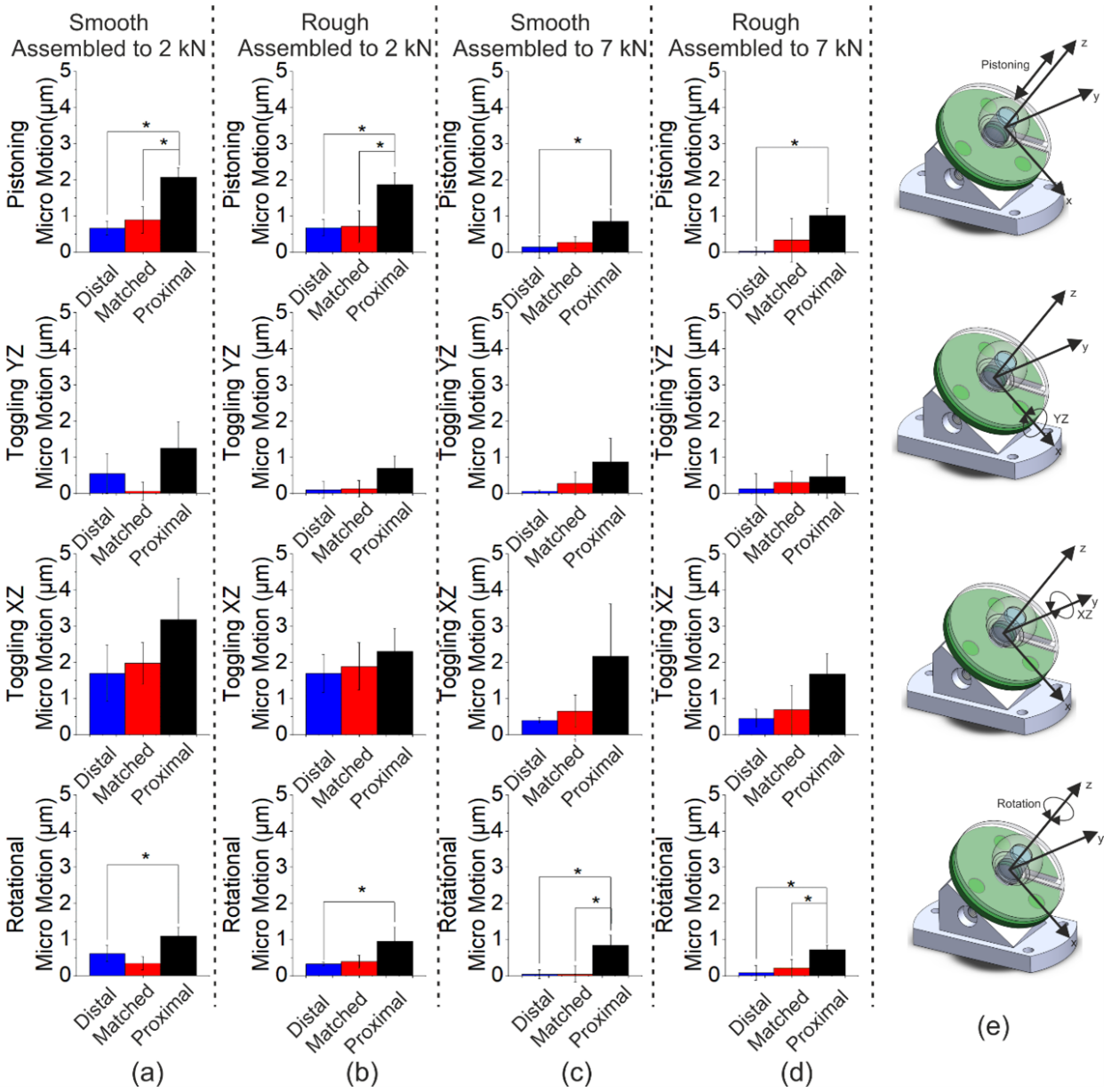

Fig. 6.15 Micro motion at the final loading increment (a) 'smooth' samples assembled to 2 kN, (b) 'rough' samples assembled to 2 kN, (c) 'smooth' samples assembled to 7 kN and (d) 'rough' samples assembled to 7 kN, in the directions shown by the adjacent schematics (e). Significant difference between 'rough' and 'smooth' samples of equivalent engagement and the different engagements of equivalent surface topography was denoted by '*'..

6.3.4 Disassembly Force

The forces required to separate the heads are shown in Figure 6.16. The disassembly force was greater when the heads were first assembled to 7 kN compared to when the heads were assembled to 2 kN. The greatest difference between disassembly force when assembled to 7 kN compared to 2 kN was that seen in the 'smooth' distal samples (1324 $\pm$ 889 N versus

4207 $\pm$ 1562 N, p-value < 0.05). Significant difference was also seen in the 'smooth' matched and 'rough' matched samples (p-values < 0.05). The smallest difference was seen in the 'rough' distal samples with a disassembly force of 1772 $\pm$ 1386 N when assembled to 2 kN compared to 2914 $\pm$ 389 N when assembled to 7 kN (p-value > 0.05).

Comparing the 'smooth' and 'rough' samples, significant difference was found in the proximally engaged samples when the heads were assembled to 2 kN, with the 'smooth' proximal samples presenting a greater disassembly force compared to the 'rough' proximal samples (1953 $\pm$ 370 N verses 776 $\pm$ 130 N, p-value < 0.05). No significant difference was found in the other samples groups when assembled to 2 kN or 7 kN. When the heads were assembled to 7 kN, the disassembly force for the 'smooth' samples was 55.36 $\pm$ 0.14 % of the assembly force (7 kN) and 40.00 $\pm$ 0.06 % for the 'rough'.

Comparing the different engagements of equivalent surface topography, the 'rough' matched samples presented a greater disassembly force (1084 $\pm$ 143 N) than the 'rough' proximal samples (p-value < 0.05). No statistical difference was found between the other engagement groups of equivalent surface topography and assembly force.

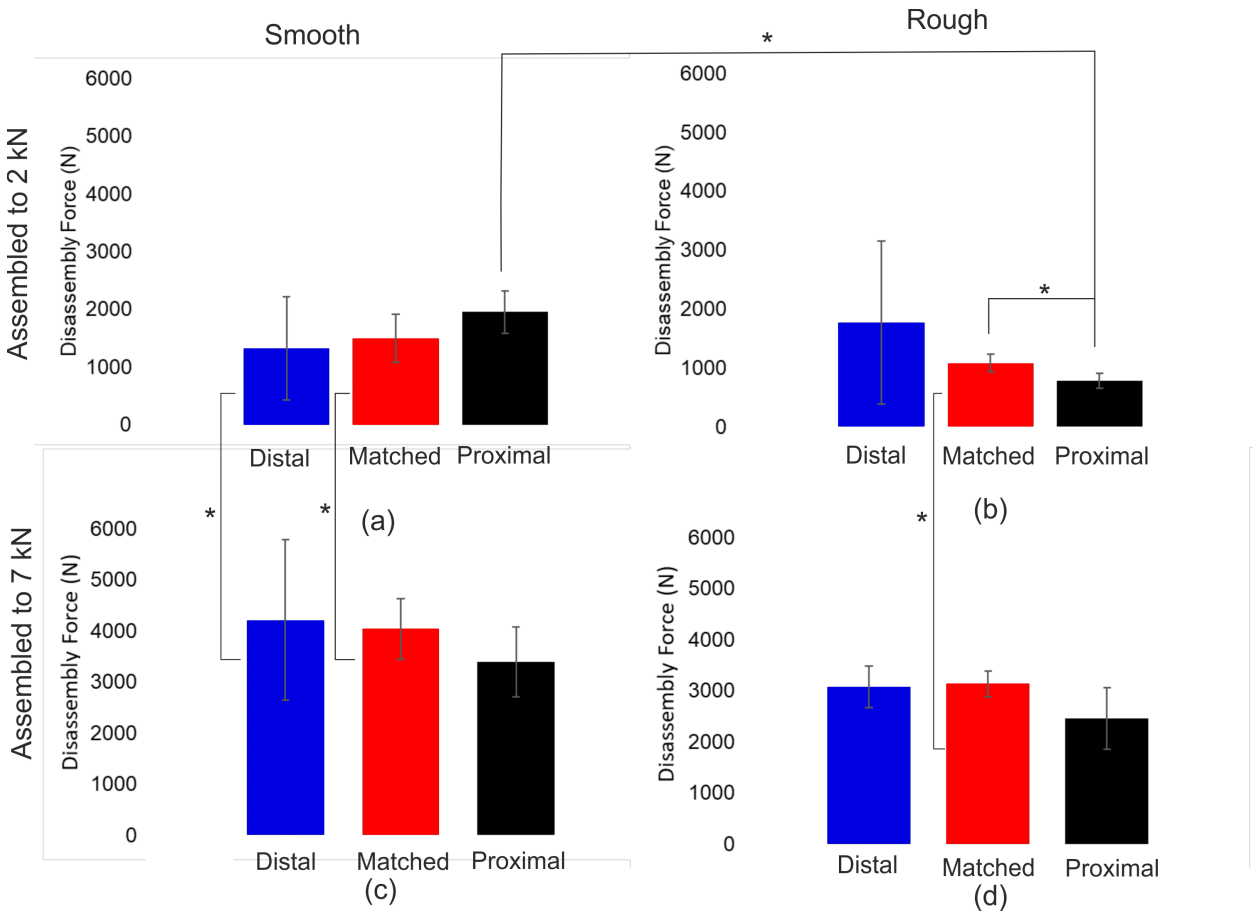

Fig. 6.16 Disassembly force post 2 kN assembly and dynamic loading for fretting corrosion and motion measurements for the (a) 'smooth' samples and (b) 'rough samples', and disassembly force post 7 kN assembly and dynamic loading for fretting corrosion and motion measurements. Significant difference between 'rough' and 'smooth' samples of equivalent engagement, the different engagements of equivalent surface topography and samples of equivalent engagement and surface topography when assembled to 2 kN and 7 kN was denoted by '*'.

6.3.5 Surface Analysis

Geometry - Comparison Pre versus Post Testing

Evidence of engagement was seen when comparing surface deviation maps taken of the 'as manufactured' surfaces and the same surfaces after testing. Figure 6.17 shows example surface deviation maps of the 'smooth' samples. The 'smooth' distal samples presented material below the ideal cone geometry, either due to loss or deformation, around the whole circumference at around -13 to -12 mm below the flat proximal of the male taper sample after testing (Figure 6.17b), not seen in the 'as manufactured' surface deviation map (Figure 6.17a). Compared to the 'smooth' distal samples, less localised changes to the deviation maps due to testing were seen in the 'smooth' matched samples, with subtle

material loss at the proximal end of the interface (distance of around -3 to -1.5 mm along the taper, Figure 6.17c and d). The as manufactured 'smooth' proximal sample presented material protruding around above the ideal cone geometry at the proximal region of the taper interface (distance along the taper between -3 and -1.5 mm, Figure 6.17e), this was diminished after testing (Figure 6.17f).

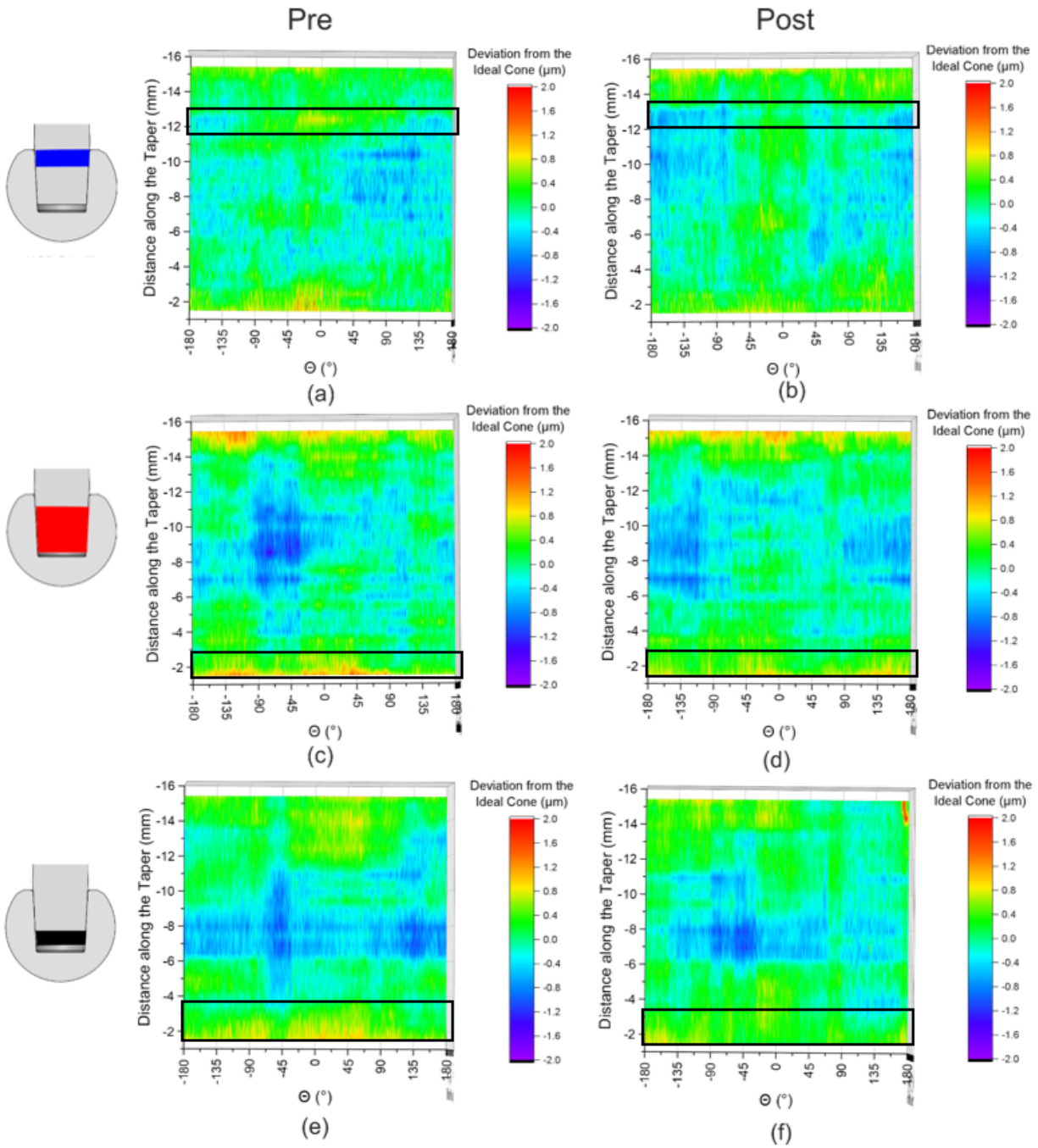

Fig. 6.17 Surface deviation maps from the ideal cone geometry of the 'smooth' samples including the (a) as-manufactured distal samples and (b) after testing described in this chapter, the (c) as-manufactured matched samples and (d) after testing, the (e) as-manufactured proximal and (f) after testing. Rectangles indicate changes to the deviation maps seen in the surface after testing compared to the as manufactured surfaces.

Like the ‘smooth’ distal samples, the ‘rough’ distal samples presented more material below the ideal cone geometry around the circumference at around -13 to -11 mm distance below the proximal flat of the male taper (‘Distance along the Taper’) post testing compared to the ‘as manufactured’ surface (Figure 6.18a and b). The ‘rough’ matched samples did not appear to present any observable changes to the surface deviation map due to testing (Figure 6.18c and d). The ‘rough’ proximal sample (Figure 6.18e and f) presented material around 2 mm below the ideal cone between 0 and 180 ° at -3 to -1.5 mm along the taper and -90 and 0 ° at -15 to -13 mm along the taper axis after testing, not seen in the ‘as manufactured’ surface.

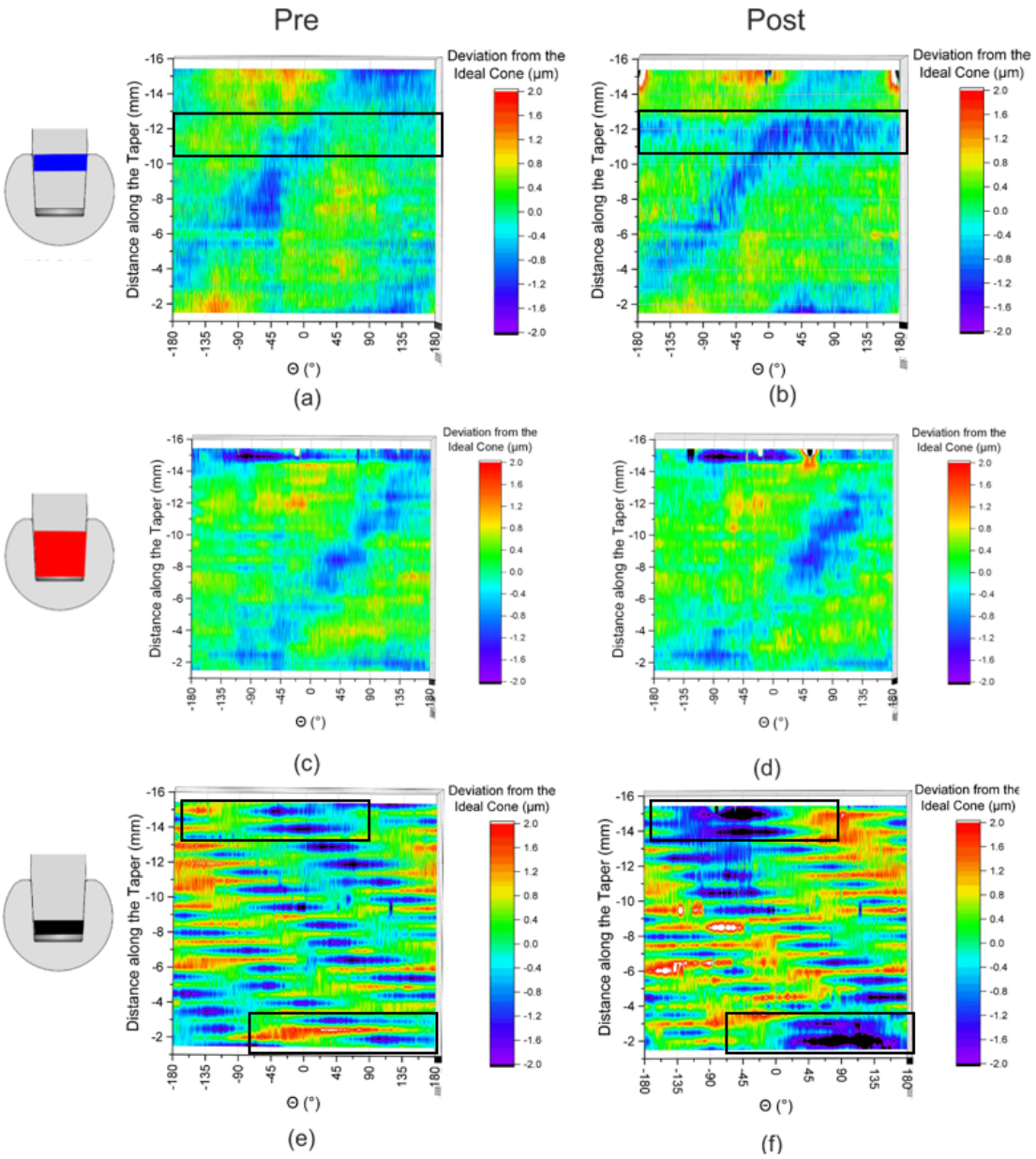

Fig. 6.18 Surface deviation maps from the ideal cone geometry of the 'rough' samples. The (a) as-manufactured distal samples and (b) after testing described in this chapter, the (c) as-manufactured matched samples and (d) after testing, the (e) as-manufactured proximal and (f) after testing. Rectangles indicate changes to the deviation maps seen in the surface after testing compared to the as manufactured surfaces.

Surface Topography - Comparison Pre versus Post Testing

Evidence of engagement around the opening of the taper in the 'smooth' distal sample was seen in the deviation map (Figure 6.19b). This was also reflected in the VSI data where Figure 6.19 shows how roughness profiles can reflect measurements taken using the CMM. The deviation map (Figure 6.19a) demonstrated a 1 µm step-like feature at 13 mm below

the proximal end of the male taper (Distance of -13 mm along the taper). A corresponding 1 µm 'step' was also seen in the roughness profile at around -13 (Distance along the Taper, Figure 6.19b). Towards the proximal end of the taper (between -7 and 0 distance along the taper, Figure 6.19b) the roughness profile matched that which would sit outside the interface (-15 to -13 mm distance along the taper, Figure 6.19b and Figure 6.19c).

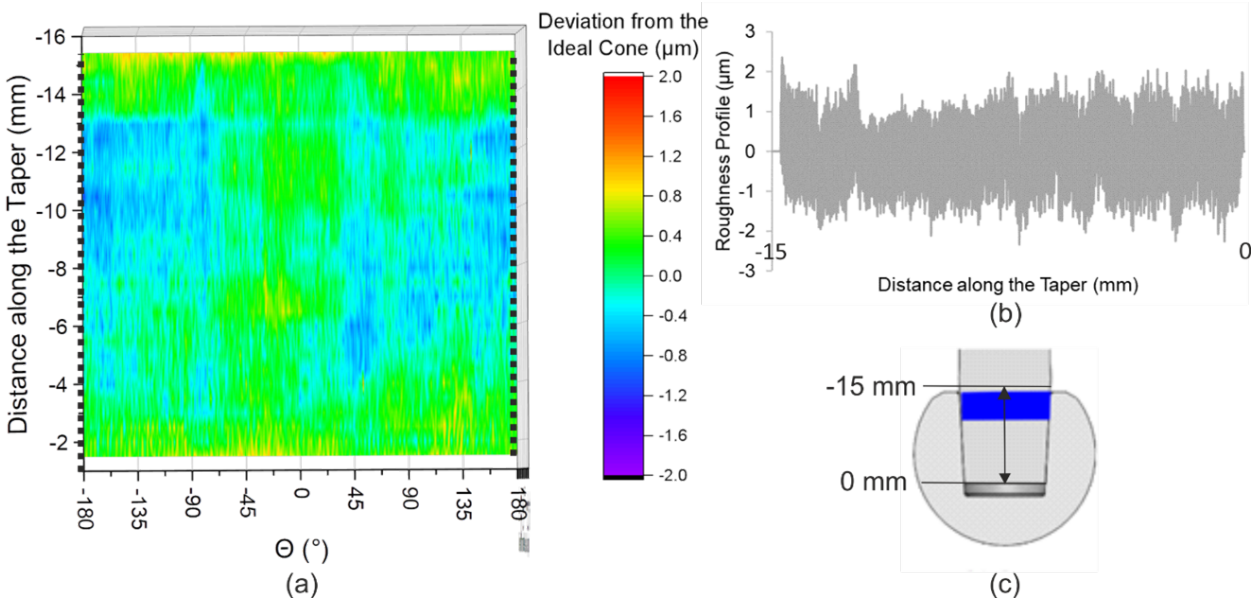

Fig. 6.19 (a) Surface deviation map of an example 'smooth' distal samples after testing, (b) a roughness profile trace taken in the location indicated by the broken black line in (a) and (c) where the scan correlated to with respect to the taper geometry.

Figure 6.20 shows the key surface topography parameters including S_a, S_k and S_{pd}, of the as manufactured surfaces ('Pre') and after testing described in this chapter ('Post'). All samples demonstrated an average decrease in roughness amplitude (S_a) compared to the 'as manufactured' surface. Looking at the 'smooth' samples, there was no statistically significant reduction in the roughness amplitude (see Figure 6.20a and c). However, there was a significant reduction in the peak density (S_{pd}, Figure 6.20e) in the distal, matched and proximal engagements on average by 3859 ± 136 m^{-2}.

Looking at the 'rough' samples, the greatest decrease in average roughness amplitude was that seen in the 'rough' proximal samples, demonstrating an average decrease that was less than variability in the as manufactured surfaces (average decease in S_a of 0.12 ± 0.15 µm, p-value < 0.05, Figure 6.20b). It should be noted that the roughness amplitude achieved in the 'rough' proximal samples (S_a of 3.94 ± 0.15 µm) was greater than the 'rough' distal (1.77 ± 0.02 µm) and matched (1.80 ± 0.05 µm). The rough distal samples presented a very slight reduction in Sa by 0.05 ± 0.02 µm (p-value < 0.05). This reduction in S_a was not reflected in the core roughness depth (S_k), demonstrating an average reduction in S_k by 0.18 ± 0.29 µm. Like the 'smooth' samples, the 'rough' presented a reduction in S_{pd}.

However, unlike the 'smooth' that presented a reduction of around 71 % of that measured on the as manufactured surface, the 'rough' only presented a 3 % reduction. The 'rough' matched samples was the only engagement group which presented a statistically significant reduction in S_{pd} of 30 ± 20 m^{-2} (p-value < 0.05). Again, it should be noted that the average reduction was small in comparison to the variation in the samples.

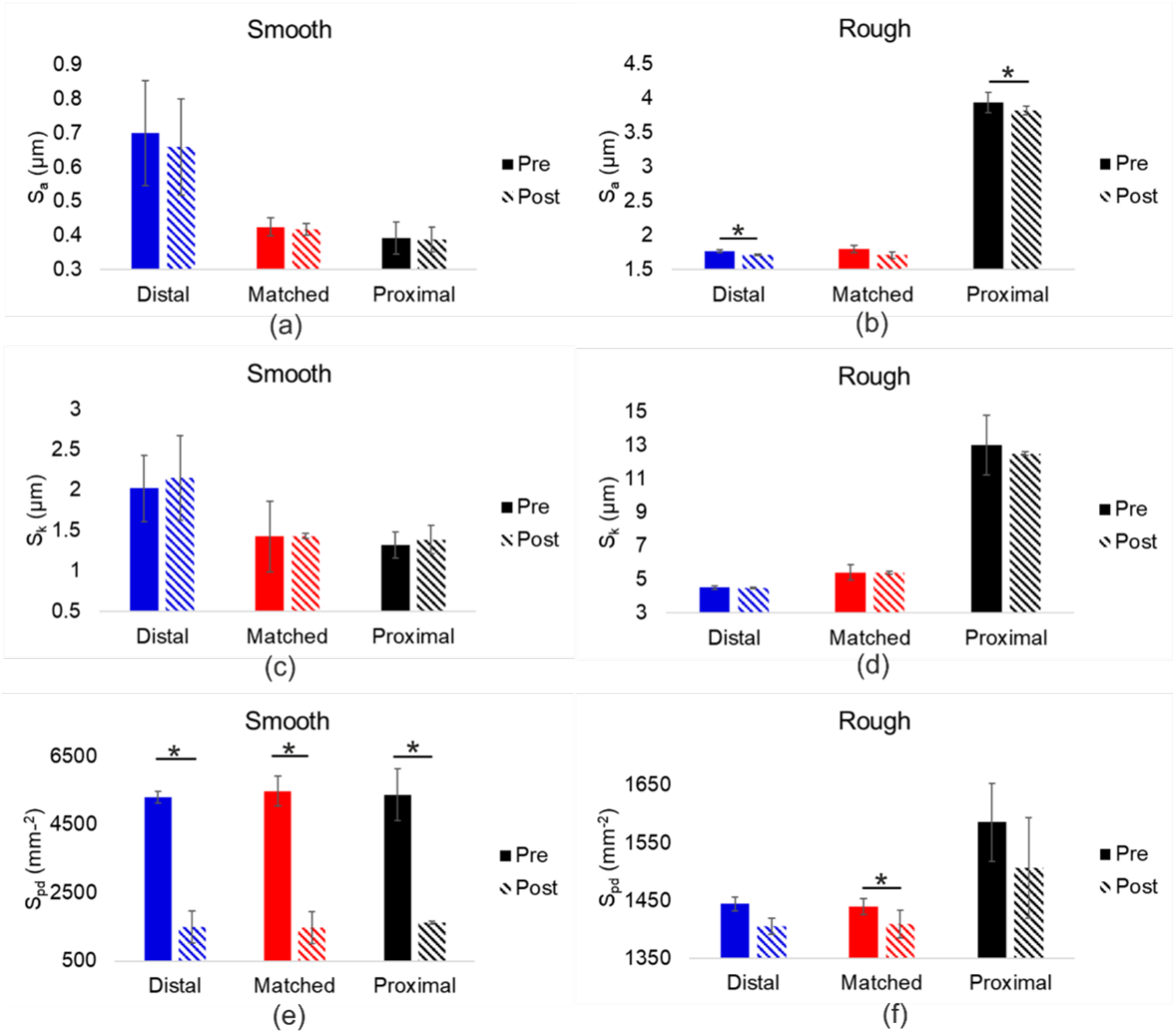

Fig. 6.20 Surface topography of the 'as manufactured' surface (pre) compared to post testing: (a) S_a of the 'smooth' samples, (b) S_a of the 'rough' samples, (c) S_k of the 'smooth' samples, (d) S_k of the 'rough' samples, (e) S_{pd} of the 'smooth' samples and (f) S_{pd} of the 'rough' samples. Statistical difference between pre and post testing was indicated by an asterisks, p-value <0.05.

6.4 Discussion

To date, pre-clinical test protocols had been largely based on the ASTM standard practice for fretting corrosion tests of modular tapered interfaces, originally approved in 1998 [196]. ASTM F1875-98 [196] describes a dynamic uniaxial loading profile facilitated by a point load on the femoral head. This differs quite significantly from realistic biomechanical loading profiles which are much more complex, with greater off-axis force vectors [6] (please refer to Section 2.2.2 for further details). The aim of this study was to further develop the short-term test protocol developed in the previous Chapter to include a more realistic dynamic simulation profile to that experienced in-vivo. This was then used to assess the pre-clinical relative performance in terms of motion and fretting corrosion of the representative samples with varying surface topography and angular mismatch. This was achieved by first designing and manufacturing fixtures to accommodate motion and electrochemical measurement apparatus while applying a dynamic articulating bearing load to the femoral head using the six-axis single station universal joint simulator (Prosim, Simsol, UK). The relative performance of the samples with varying surface topography and angular mismatch was then assessed at two different head assembly forces to simulate the variation seen in the surgical assembly process.

6.4.1 Simulated Walking Gait Test Protocol

In this present study, a simulated walking gait loading profile was applied to the taper junction via a domed plug-femoral head articulating bearing interface. The plug was used in lieu of a full acetabular cup to accommodate the electrochemical cell and motion measurement systems during simulation. The articulating surface of the plug was domed with a radius of 14.005 mm and replicates half the area of a full acetabular cup (590 mm^2 versus approximately 1200 mm^2). It could be considered that the plug may not be representative, however, full cup and head configurations have been found to present initial contact patches in the region of 17 to 24 % of the nominal cup area [295]. As such, the articulating surface of the plug of 590 mm^2 is larger than 24 % of a full acetabular cup with radius 14.005 (288 mm^2) and therefore does have the capacity to support a representative initial contact patch of a full acetabular cup-femoral head bearing interface.

Considering now the location of contact compared to where it is positioned clinically, Figure 6.21 shows the position of wear scars of the acetabular component from a retrieved MoM bearing [297]. Contact is not concentrated at the pole of acetabular component, but at the periphery. On the other hand, this present study used a plug orientated as if it was a full acetabular hemisphere. As such, compensating by off-setting the plug to take into

account this peripheral contact appearing in clinical samples could be made in future to more accurately model in-vivo loading conditions.

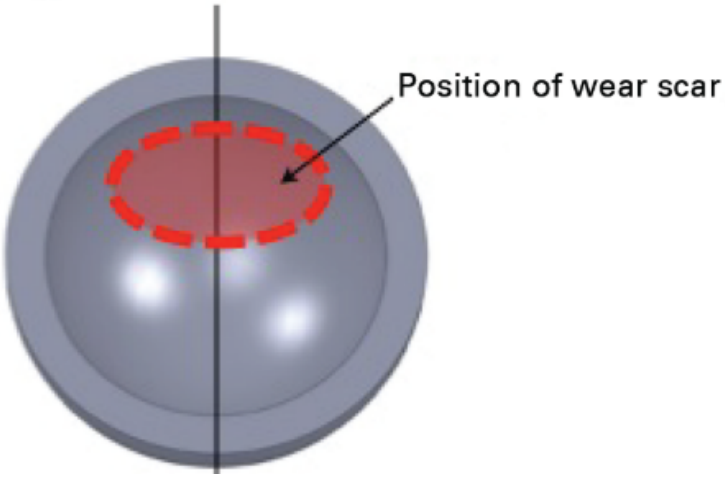

Fig. 6.21 Diagram showing the position of wear scars of the acetabular component from a retrieved MoM bearing. Image taken from Matthies et al. [297].

Considering now the forces and torques measured during this study compared to those measured at the hip joint by literature, a summary of which can be found in Table 6.3. Whilst axial loads in-vitro have been informed by in-vivo studies, the in-vivo moments acting about the hip are reported to be higher than that presented by in-vitro studies. This discrepancy can be explained by differences in the defined coordinate systems where Crowninshield et al. [5] defines the moments acting relative to a reference frame located at the centre of the pelvis, Bergmann et al. [6] defines the moments acting about a point in the shaft of the femoral stem ('NS' in Figure 2.3) and in the in-vitro studies presented in Table 6.3, including that of the present study, defines the torsional moments relative to the centre femoral head. The Bergmann research group did go on to publish a study on the moments acting about a ceramic-on-polymer (CoP) 32 mm head in-vivo and reported moments as being 0.25 % of that of body weight, and thus a 2.1 Nm moment for an average body weight of 820 kg, in line with that measured in vitro [298].

With the comparability between in-vivo and in-vitro moments acting about the head, the resultant torques measured by this study are therefore higher than expected. A key difference between the in-vitro studies and this present study was that the bearing interface was not immersed in the test solution in order to isolate the electrochemical response of the taper interface. Although a thin layer of grease was added to the bearing interface to help lubrication, grease was displaced from the interface during simulation. With that said, the resultant torque was comparable to that of a dry metal-on-metal (MoM) and ceramic-on-ceramic (CoC) bearing interface found by Bishop et al. [176], with the present study measuring resulting torques of 17 ±1 Nm at an axial force of 1847 ±6 N. Furthermore,

a recent retrieval study by McCarty et al. [299] measured the resultant torques that act around the head of 85 large-diameter metal-on-metal retrieved THR in bovine calf serum, subject to the walking gait simulated specified by ISO 14242-1 [8] with peak axial force of 3000 N, and found that resultant torques to range from 9.1 to 26.3 Nm with peak axial load of 3000 N, with the highest of that range being comparable to this present study of 22 ±1 Nm and 26 ±2 Nm at peak axial forces of 2766 ±6 N and 3225 ±6 N, respectively.

Table 6.3 Forces and moments acting on the hip determined by literature compared with this present study. Naming convention of the moments were translated into those relative to anatomical movement, the resultant moments of Crowninshield et al. [5] and Bergmann et al. [6] were calculated as the Pythagorean result of M_{FE}, M_{AA} and M_{IE}.

Study	Measurement methodology		Parameter	Value
Crowninshield et al. [5] (in-vivo)	Inverse dynamics analysis with typical body weight of 69 kg during walking		Peak axial force	4x body weight
			M_{FE}	0.05 kNm
			M_{AA}	0.06 kNm
			M_{IE}	-0.01 kNm
			$M_{Resultant}$	79 Nm
Bergmann et al. [6] (in-vivo)	Sensorised hip prosthesis of patient with 75 kg during walking		Peak axial force	1736 N
			M_{FE}	6 Nm
			M_{AA}	33.3 Nm
			M_{IE}	-11.5 Nm
			$M_{Resultant}$	35 Nm
Haider et al. [219] (in-vitro)	Measurement using a 6-axis load cell of hip simulator with 40 mm diameter MoP immersed in bovine calf serum, subject ISO walking gait and held in anatomical orientation		Peak axial force	3000 N
			Resultant Torque (calculated from 0.06 frictional factor, head diameter and axial force)	3.6 Nm
Bishop et al. [176] (in-vitro)	Measurement using 6-axis load cell of hip simulator subject to simplified flexion-extension simulation of:		Peak axial force	2000 N
		50 mm MoM in bovine calf serum	M_{FE}	7 Nm
		50 mm MoM dry	M_{FE}	11.8 Nm
		48 mm CoC bovine calf serum	M_{FE}	2.4 Nm
		48 mm CoC dry	M_{FE}	24.2 Nm
Present Study			Peak axial force	3225 ±6 N
			Peak resultant torque	26 ±2 Nm

Comparing this study to the uniaxial study (Chapter 5), some key differences and similarities in terms of fretting corrosion, subsidence and micro motion were noted. Similar magnitudes of average current were seen in the smooth samples, please refer to Table 6.4 summarising the average current in the penultimate loading increment for the uniaxial study with peak load of 3500 N and the final load of the simulated walking gait study with peak axial load of 3682 ±9 N. This is in agreement with that found by Wight et al. [7] who found that the inclusion of flexion-extension, abduction-adduction and internal-external rotation as per ISO 14242-1 [8] did not affect the measured current response compared to when only the twin-peak axial force component was applied (twin-peak axial force as opposed to the sinusoidal waveform employed by this present study).

Table 6.4 details the currents measured by Wight et al. [7] using ZRA electrochemical methods with 28 mm diameter heads. Although Wight et al. [7] did not report the details of the taper design save for the manufacturer (Smith & Nephew, UK) and material (CoCrMo head and Titanium alloy stem), Mueller et al. [110] found that Smith & Nephew tapers to present a proximal angular mismatch in the region of 0.06-0.08 °, with either a smooth roughness with an R_a of 0.59 ±0.04 µm or a rough roughness with R_a of 3.66 ±0.05 µm, such that Wight et al. [7]'s samples can be assimilated to smooth or rough matched and proximal samples of this present study. With that said, in the uniaxial loading scenario, Wight et al. [7] measured a similar current to that of the smooth proximal samples. In the simulated walking gait scenario, Wight et al. [7] current measurements were most comparable to the smooth proximal and rough matched samples. The close agreement between the measured currents and this present study and that of Wight et al. [7]'s offers verification of the electrochemical cell arrangement of this preset study. A possible explanation for this above mentioned similarity in measurable currents could be that the axial force was the largest changing component of the loading scenario compared to that of torques about the femoral head.

Whilst this present study did not find the inclusion of the more complex walking gait to affect the measured current in the smooth samples, the rough samples presented a much smaller current when subject to the more complex loading profile compared to the uniaxial study. This was an unexpected finding, as the introduction of more off-axis loading was thought to increase off-axis motion and therefore fretting corrosion. Although this finding requires further work to understand the underlying mechanisms, below are some possible explanations as to why smaller currents may be measured in the simulated walking gait scenario compared to that of the uniaxial.

Table 6.4 Average current of each sample group in the penultimate loading increment subject to uniaxial loading with peak axial force of 3500 N and the average current subject to a simulated walking gait with peak axial force of 3682 ±9 N compared to the currents measured by Wight et al. [7] when subject to only the axial component of ISO 14242-1 [8] with peak axial force of 3300 N (uniaxial) and the full simulated walking gait cycle defined in ISO 14242-1 [8] with peak axial force of 3300 N.

	Average Current (μA)					
	Uniaxial			Simulated Walking Gait		
	Distal	Matched	Proximal	Distal	Matched	Proximal
'Smooth'	0.30 ± 0.44	0.23 ± 0.62	1.09 ± 0.32	0.45 ± 0.20	0.185 ± 0.87	0.67 ± 0.26
'Rough'	3.13 ± 1.08	10.54 ± 0.29	9.43 ± 0.65	0.49 ± 0.22	0.66 ± 0.14	2.31 ± 0.44
Wight et al. [7]	0.933 ±0.185			1.253 ±0.386		

Oxide layer disruption has been shown to occur upon loading and unloading, current starts to drop immediately at full load or unload i.e. when static [23]. Therefore, the rate of change of axial force with respect to time is important to the current response. As such, another contributory reason as to why greater currents were not seen in the more complex case could have been due to the twin peak loading profile versus the sinusoidal uniaxial loading profile. Figure 6.22a and b shows a 3-second example of the micro motion data of a proximal sample for the two loading scenarios. The uniaxial sinusoidal (Figure 6.22a) profile indicates continuous motion important for oxide abrasion, whereas the simulated walking gait (Figure 6.22b) demonstrates a greater proportion of time in an effectively static state between cycles.

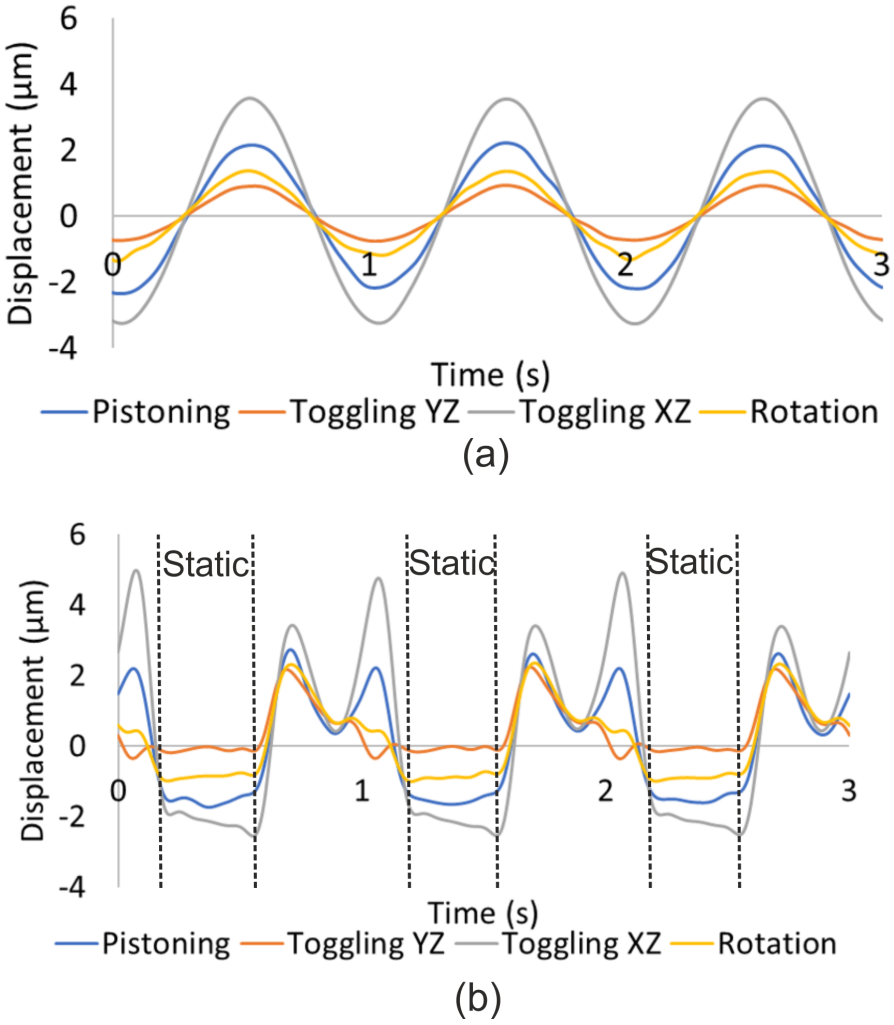

Fig. 6.22 Example three seconds of the motion data in the final increment of a smooth proximal sample assembled to 2 kN subject to (a) the uniaxial loading profile and (b) the more complex loading profile according to ISO 14242-1 [8] with scale axial loading component to peak force of 4 kN. NB these motions are not subtracted from the equivalent monobloc.

Another possible reason contributing to why a greater current may be found in the uniaxial case compared to the simulated walking gait includes a possible IR drop due to the increased distance of the reference and counter electrode from the taper junction (working electrode). The electrochemical cell had to be adapted from the uniaxial arrangement to avoid collision between the plug and electrode. The counter and reference electrode sat within a secondary bath, away from the taper junction. This would result in a potential drop, commonly referred to an IR drop, across the solution between the working and reference electrode [300]. Effects of solution resistance were thought to be minimal due to the high conductively of the solution, small currents and a distance of 60 cm via a 10 mm diameter tube.

The magnitude of micro motion found by this study compared to the uniaxial study was similar, demonstrating some consistency in the measurement system. This is also in line with that reported by Wight et al. [7] finding that the inclusion of frictional torque as per ISO 14242-1 [8] did not have a significant effect on the fretting corrosion response of the taper junction. However, it was noted that this study did not measure the frictional torque nor micro motion at the taper interface. This present study did, and found some differences in the toggling YZ micro motion response, where the simulated walking gait loading scenario presented a greater magnitude compared to the uniaxial case. Figure 6.23 shows the magnitude of micro motion for the smooth proximal samples as a function of the peak-to-trough axial force for the uniaxial and walking gait loading scenarios. Additionally, Figure 6.23b also shows the resultant torque acting about the head. The peak-to-trough axial force was greater for the uniaxial loading scenario, which was thought to largely dictate the magnitude of micro motion in the toggling YZ and pistoning directions. The resultant torque acting about the head did appear to have some effect on toggling YZ, in-line with the large contribution in the flexion-extension direction. Where in the final loading increment the smooth proximal samples presented toggling YZ micro motion of 1.3 ± 0.7 µm subject to the simulated walking gait profile compared to the uniaxial loading scenario with 0.3 ± 0.6 µm (p-value of 0.10).

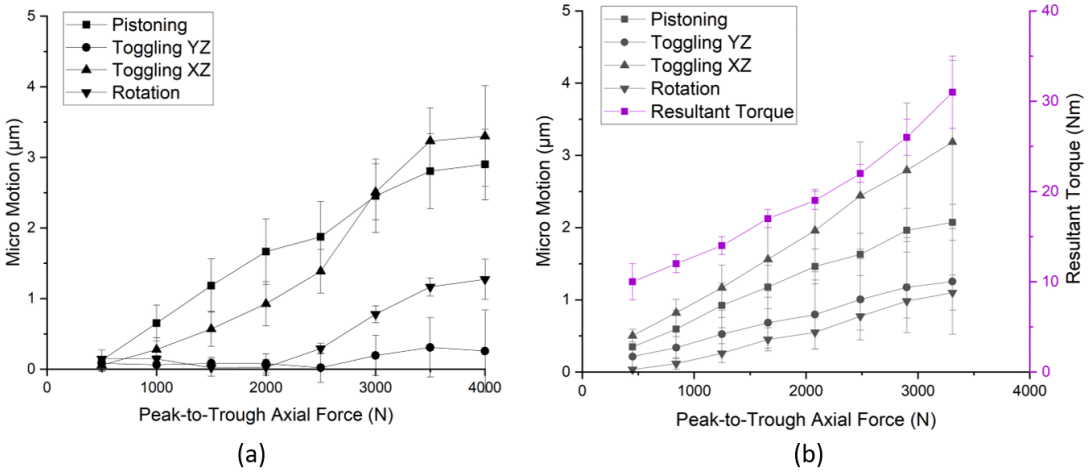

Fig. 6.23 Micro Motion of the smooth proximal sample group versus peak-to-trough axial force with heads assembled to 2 kN for (a) uniaxial dynamic loading and (b) subject to the simulated walking gait profile with resultant torque acting about the head.

Nevertheless, this study did not find that the introduction of more complex loading to increase the fretting corrosion response. As mentioned above this is in line with the comparable in-vitro study by Wight et al. [7] that found the measured current, and thus fretting corrosion, not to be affected by the introduction of joint movement. McCarty et al. [299] offers some validation to this finding after measuring the implant wear prior

to the measurement of resultant torques (discussed above) and found that taper interface material loss not to be correlated with higher frictional moments. This is in contradiction to other retrieval studies such as Witt et al. [301] and Dyrkacz et al. [175]. These studies found increased bearing articulation wear and serum metal ion concentrations in cases with taper interface corrosion and increased visible evidence of fretting corrosion at the taper interface with larger diameter heads, respectively, with both studies highlighting increased torque acting about the head as a reason for increase taper degradation. Additionally another contradictory retrieval study was that of Meyer et al. [302] who reported friction of metal-on-metal articulations to be a possible cause of taper interface failure, despite finding no correlation between head size with metal release from the taper interface. With the above said, Witt et al. [301], Dyrkacz et al. [175] and Meyer et al. [302] failed to establish a causal link between torques acting about the head and head-stem modular taper degradation whilst this present study, Wight et al. [7] and McCarty et al. [299] offer more robust evidence of bending moments having a greater influence on the modular taper junction compared to that of frictional torques acting about the femoral head. The lack of significant effect on the introduction of the more complex loading was also reported in-silico by Farhoudi et al. [303]. Farhoudi et al. [303] determined the contact pressures and micro motions at the taper interface when the head was subject to a simulated walking gait's axial force only, moments acting about the head only, and combined gait forces and moments acting about the head. Farhoudi et al. [303] attempted to present the narrative that the combined gait forces and moments acting about the head would increase relative micro motion at the taper interface compared to that of the gait forces only, however, it was clear from the presented results that the gait forces dominated the mechanical environment of the taper interface.

In both studies, a 'spike' in current at the onset of a loading increment 6.24 was attributed to subsidence events whilst the constant depassivation-repassivation thereafter was attributed to micro motions. This explanation was in line with that provided by Mali and Gilbert [211] who took concurrent motion and corrosion measurements subject to incremental uniaxial dynamic loading. Although this present study did not take concurrent motion and fretting corrosion measurements, it was thought that micro motions largely governed the average current at a given increment. Figures 6.24a and b show the average fretting corrosion current against pistoning micro motion when assembled to 2 kN and subject to the uniaxial loading profile and simulated walking gait profile, respectively. There was a positive relationship between pistoning micro motion and current in both cases. However, R^2 values of around 0.6 and 0.4 were found for the uniaxial and simulated walking gait loading scenarios respectively, indicate that approximately 60 and 40 % of this data follows the model that fretting corrosion current linearly increased with micro motion. Possible explanations as to why greater R^2 were not found could be due to the stochastic

nature of the contact and the fact that fretting corrosion and motion measurements were not taken concurrently, meaning that slight differences in the behaviours of the interface could explain, at least in part, this deviation from the linear model. Other sources of possible variation could also arise from the measurement methods. The smaller R^2 value found in the simulated walking gait loading scenario compared to the uniaxial could have arisen from increased error in the motion measurements. More specifically, the introduction of internal-external rotation causing movement of the measurement apparatus.

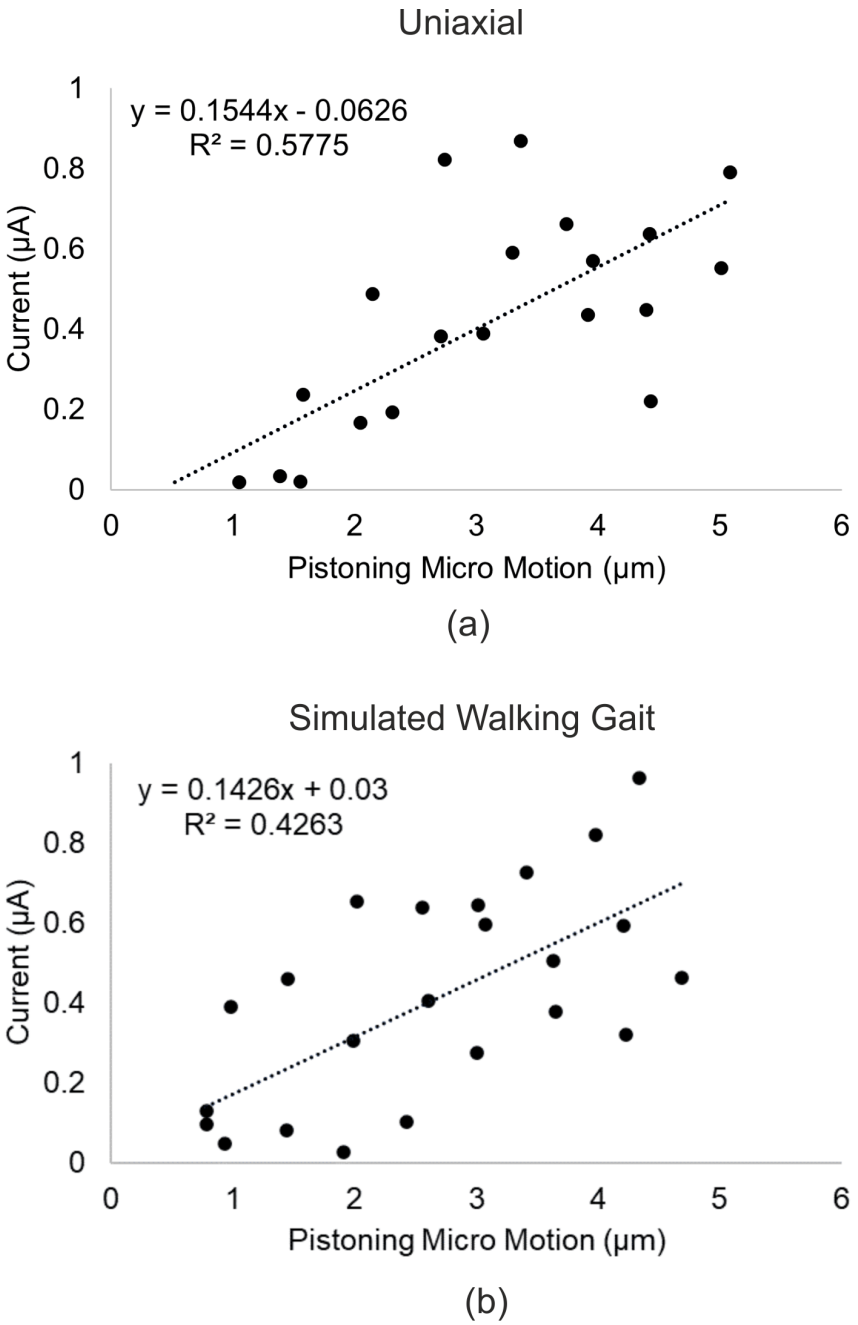

Fig. 6.24 Linear regression analysis of the 'smooth' proximal samples assembled to 2 kN and subject to incremental (a) uniaxial and (b) simulated walking gait loading scenarios.

The current response of some sample groups measured in this study, employing the simulated walking gait profile had a tendency to present a sudden increase upon the onset of a loading increment and then continued to climb throughout the increment. This was mostly seen in the proximal and matched engagement groups with both rough and smooth surface topography (Figure 6.8). Compared to the comparable uniaxial study, a sudden spike in current was registered upon the initiation of a loading increment followed, in most cases, by a decay. Spikes before a decay in current upon the onset of uniaxial dynamic loading has been reported by other research groups, and found to correspond to subsidence events at the start of a new loading increment [211]. Subsidence motions subject to the more complex loading scenario and when the heads were assembled to 2 kN, presented greater variability (Figure 6.12a and b) compared to the uniaxial study (Figure 5.11a, b, g and h in the final loading increment with peak load of 4 kN). For example, the smooth matched samples in this study presented an axial subsidence magnitude of 17.9 ± 9.1 µm in the final loading increment (Figure 6.12a), compared to 17.4 ± 0.7 µm in the uniaxial case (Figure 5.11a). The lower prevalence of a spike followed by decay behaviour in the current response could be due to the less consistent seating mechanics when subject to a more realistic simulated walking gait profile compared to that when loaded uniaxially. However, to develop a clearer understanding of this interplay between current, subsidence and motion, concurrent fretting corrosion and motion measurements are required.

6.4.2 The Role of Assembly Force

One of the few individual factors that has been found to consistently affect taper performance in pre-clinical studies was assembly force [211, 217, 222, 218, 212, 185]. This is a parameter that is not controlled during surgical assembly and has been shown to range from anywhere between 1 to 20 kN [34–36]. Therefore, this study assessed the fretting corrosion and motion response of the samples subject to two assembly forces of 2 kN, in line with ISO 7206-10 [134], and 7 kN, in line with the average surgical assembly force achieved by surgeons.

Previously, greater assembly forces have been associated with increased engagement, contact pressure, plastic deformation at the interface, reduced motion and thus, a reduced susceptibility to fretting corrosion [232, 138, 218]. In agreement with that found previously, this project found lower average currents, increased disassembly force, reduced subsidence motion and reduced micro motions when the samples were assembled to a greater assembly force [211, 217, 222, 218]. A comparable in-vitro study of Pierre et al. [218] measured average currents of 5.0 ±1.0 µA and 1.2 ±1.0 µA when assembled to 2000 N and 8000 N respectively and uniaxially dynamically loaded to peak forces of 4 kN, this was most

comparable to the smooth matched samples that presented an average current of 1.8 ±0.9 µA when assembled to 2 kN and 0.2 ±0.1 µA when assembled to 7 kN and dynamically loaded to 3682 ±9 N.

Comparing subsidence, Pierre et al. [218] reported subsidence in the region of 20 ±25 µm when assembled to 2 kN and 5 ±8 µm when assembled to 7 kN, comparable when compared to the smooth matched samples that presented a pistoning subsidence of 17.9 ±9.1 µm when assembled to 2 kN and 1.1 ±0.4 µm when assembled to 7 kN in the final loading increment. Comparing micro motion, Pierre et al. [218] reported micro motions in the region of 12 ±4 µm when assembled to 2 kN and 13 ±6 µm when assembled to 8 kN, greater then that found in the smooth proximal samples of this present study with pistoning micro motion of 1.0 ±0.4 µm and 0.3 ±0.2 µm, when assembled to 2 kN and 7 kN respectively. An explanation as to the smaller magnitudes of micro motion measured by this preset study compared to that of Pierre et al. [218] was the way in which Pierre et al. [218] accounted for motion due to elastic stains and the greater peak axial force of 4 kN. Pierre et al. [218] acknowledged that micro motion measurements my still include elastic strain due to inaccuracies of the estimated spring constant of the less rigid Ti6Al4V male taper material compared to that of the stiffer stainless steel samples of this present study. Nevertheless, increased assembly forces for increased contact pressure and reduced motion at the taper interface would predict a greater proportion of contacting asperities in the SR and PSR as opposed to the GSR and thus help explain the reduced currents measured by this study in line with the mechanism discussed with respect to angular mismatch in Section 5.4.3.

A key finding from this study in agreement that of Pierre et al. [218] and Panagiotidou et al. [185] was that when the heads were assembled to higher forces that exceeded the axial force of the dynamic simulation, most sample groups still presented some level of micro motion and fretting corrosion. This indicates that, even after sufficient seating, modular junctions were still susceptible to degradation via fretting corrosion. This finding suggests that optimising the taper interface is of clinical interest despite the large variations in surgical assembly force which have been found to heavily influence pre-clinical performance. Furthermore, a longer term in-vitro study suggested that the increased susceptibility to fretting corrosion of femoral heads subject to a low surgical assembly forces, decreased with time in-situ attributed to secondary seating [185], further highlighting the importance of optimising taper design.

6.4.3 The Role of Surface Topography

Like that seen previously using uniaxial dynamic loading, the rough samples presented a greater average current response compared to the smooth samples of equivalent angular mismatch and assembly force (Figure 6.9), with the exception of the matched engagement samples with heads assembled to 2 kN. This occurred without a corresponding increase in micro motion (Figure 6.15). This suggests a greater susceptibility to fretting corrosion, with the most probable explanation that of a greater amount of passive oxide disruption at threaded peaks (please refer to Section 5.4.2 for further explanation of the proposed mechanism on the effect of contact pressure). In the case of the matched samples assembled to 2 kN, the rough matched samples did not present a greater current response than the smooth matched samples. On average, the smooth matched samples presented a greater current response that was not found to be statistically significant, indicating that this difference could be due to other reasons such as experimental variation. Alternatively, the increased roughness amplitude could increase the contact pressure sufficiently in this particular instance to alter the prevailing fretting regime to reduce the number of contacting asperities experiencing the GSR [142].

The greatest difference in the fretting corrosion response between the rough and smooth samples was that seen in the proximally engaged samples when assembled to both 2 and 7 kN, compared to the distal or matched engagements. It was noted that the rough proximal samples presented a greater roughness amplitude compared to the rough distal or matched. Additionally, the rough proximal samples presented the greatest average decrease in roughness amplitude after testing, compared to the as manufactured surface (Figure 6.20). This supports the theory that increased contact pressure at thread peaks can increase the proportion of oxide abrasion compared to surfaces that do not present this threaded-type finish (please refer to Section 5.4.2 for the explanation as to the effect of surface topography and contact pressure). However, the rough proximal samples presented the lowest average disassembly force (see Figure 6.16b and d), with the rough proximal samples presenting statistically significant lower disassembly forces compared to the smooth proximal samples when assembled to 2 kN after dynamic loading, suggesting a weaker compressive fit and lower compressive contact pressures in contrast with the above proposed explanation of the effect of increased roughness of rough proximal samples on the measured current. However, as indicated in Chapters 4 and 5, disassembly force is not the best parameter to define taper performance.

6.4.4 The Role of Angular Mismatch

There are limited pre-clinical studies investigating the effect of angular mismatch on motion and fretting corrosion, and no experimental studies to the author's knowledge that have employed a simulated walking gait loading scenario. Computational studies on the other hand, unanimously report a reduction in relative motion with a reduced angular mismatch and a reduced contact pressure [141, 136, 227]. This is generally attributed to a lower mechanical contribution to fretting corrosion occurring at the interface. One computational study by Raji and Shelton [139] also reports on the sensitivity of a taper gap opening to angular mismatch, inferring possible fluid sealing capacities desirable for corrosion. They found that taper gap opening of distally mismatched taper junctions were much less sensitive compared to proximally mismatched taper junctions. This study found that the distal engagement samples presented the lowest average current compared to the matched or proximal samples of equivalent surface topography and head assembly force (Figure 6.9), in line with that seen in the uniaxial study (Chapter 5) and the study presented by Mueller et al. [4]. Another possible explanation for this, in addition to that proposed by Mueller et al. [4] on an effective seal limiting mass transport in and out of the junction for reduced corrosion, was the increasing trend in contact pressure towards to opening of the taper (Figure 5.18a) affecting the contact mechanics. More specifically, contacting asperity junctions exposed to the electrolyte present a higher probability of being able to accommodate motion by a material response (please refer to Section 5.4.3 for further explanation). This study also found that the smooth distal samples assembled to 7 kN did not present an observable increase in current above the baseline (Figure 6.8c), indicating the presence of an effective seal as suggested by Raji and Shelton [139]. This was also evident in the surface analysis post testing (Figure 6.20) and in line with that suggested by Mueller et al. [4].

The distally engaged samples also tended to present the lowest levels of micro motion, similar to the matched samples with a smaller magnitude of angular mismatch (Figure 6.15). One possible explanation for this was the location of engagement with respect to the centre of the head, where the distal engagement at the taper opening and contact along one length or point within the taper being better able to support micro motion. Interestingly, when the rough distal samples were assembled to 7 kN, there was still evidence of XZ subsidence (Figure 6.12d). This was in-line with a hypothesis previously introduced by the author in Chapter 3, specifically why distally engaged samples presented smaller micro motion compared to a similar magnitude of angular mismatch but proximal; that is, contact within the taper interface was achieved after sufficient subsidence. This was also supported when the heads were assembled to 2 kN, in both the rough and smooth samples, where the

distally engaged samples presented the greatest XZ subsidence (see Figures 6.11a and b, and Figures 6.12 a and b).

The proximal samples allowed the greatest amount of micro motion compared to the distal or matched (Figure 6.15). It was thought that the more extreme proximal engagement, with larger gap at the opening of the taper and an effective clamping point much closer to the centre of rotation would allow a greater amount of rigid body motion compared to the distal and matched (Figure 5.19c). The proximally engaged samples presented the greatest average fretting corrosion response compared to the distal or matched samples when: the heads were assembled to 2 kN and the male taper presented a rough surface topography, and when the heads were assembled to 7 kN in both the rough and smooth sample groups. This suggests that increased micro motion would result in increased fretting corrosion.

Looking to studies that have investigated the motion at other taper junctions, namely that of the stem-neck modular taper junction, Heschke et al. [212] found that an increased angular mismatch ranging from 0.076° to 0.130° reduced the magnitude of micro motion attributed to increased contact pressure. At the neck-stem modular taper junction a proximal mismatch defines contact concentrated towards the taper opening, and that only proximal angular mismatches were investigated, such that Heschke et al. [212]'s findings more accurately reads that an increased proximal angular mismatches were associated with reduced micro motion. This offers some verification to the finding of by this present study of lower micro motion of the distal samples compared to the proximal, and similar to the matched. Hence, the employment of an angular mismatch for contact to be concentrated around the taper opening has applicability across other taper junctions.

The smooth matched samples assembled to 2 kN presented the greatest average fretting corrosion response, despite not being statistically significant, compared to the matched or distal (Figure 6.9a). This was unexpected as it was originally thought that increased conformity would reduce micro motion and therefore fretting corrosion. In comparison to the study where the samples were subject to 2 kN assembly and loaded uniaxially, the matched samples presented the greatest current response in both the rough and smooth samples group. This was thought to be at least in part explained by a reduced interfacial contact pressure compared to the distal or proximal engagements. This study found the rough proximal samples assembled to 2 kN presented a greater current response compared to the rough distal and matched samples.

6.5 Conclusion

Previously, the fretting corrosion and motion response of the modular taper junction with varying surface topography and angular mismatch has only been investigated under uniaxial loading. The aim of this study was to further develop the short-term test protocol developed in the Chapter 3 to include more realistic simulation of the working conditions in-vivo and assess the pre-clinical relative performance in terms of motion and fretting corrosion of the representative samples with varying surface topography and angular mismatch. This was achieved by developing fixtures to hold the samples in the universal hip simulator (Prosim, Simsol, UK) for incremental dynamic simulation to the loading profile detailed in ISO 14242-1 [8] while accommodating the motion measurement system developed in Chapter 5 and a newly developed electrochemical cell for potentiostatic measurements to be taken without collision with the hip simulator. A key difference of this simulation compared to other in-vitro simulations that have employed the ISO 14242-1 [8] walking gait articulation scenario and to that in-vivo, was the use of a domed polyethylene plug with a domed area of half a hemisphere articulated against the CoCrMo femoral head in dry conditions. The reasons for this was two fold, to allow the accommodation of the motion measurement system and electrochemical cell while isolating the electrochemical response to one interface, the head-stem modular taper interface. Nevertheless, the articulating bearing loadings were found to be representative of extreme torsional loading conditions acting about the head and applied axial loads and moments of a 100 kg person while walking. A key finding of this present study was that the modular taper junction response in terms of fretting corrosion and motion was dominated by the applied gait's axial force and not torques acting about the head. This was in line with a recent study that investigated the electrochemical response of the taper junction subject to the ISO 14242-1 [8] walking gait scenario and a recent retrieval study that measured the torques experienced of the femoral head upon explanation and correlated this with taper degradation [7, 299].

This study also saw the measurement of motion and fretting corrosion of the taper junction when the heads were assembled to 2 kN and 7kN. The head assembly force is one of the few individual factors that has been found to consistently affect taper performance in pre-clinical studies and not a parameter controlled in-vivo with large variation in-vivo with peak forces thought to be between 1 to 20 kN [34–36]. Consistent with previous studies, this present study found lower average currents, increased disassembly force, reduced subsidence motion and reduced micro motions when the samples were assembled to a greater assembly force, predicting a lower susceptibility to fretting corrosion in-vivo. However, in most scenarios assembly of the heads to 7 kN, exceeding the simulated axial force, did not eliminate fretting corrosion, highlighting the clinical importance of taper

design optimisation despite the large variation in surgical assembly force which has been found to have a large effect on fretting corrosion by pre-clinical studies.

With gait forces being the predominant agitator of the taper junction, the similar comparable performances between the representative samples with that of the uniaxial study, were found to be:

- the rough samples were more susceptible to fretting corrosion than the smooth male taper interface, not attributed to an increase in motion at the interface and most likely attributed to increased contact pressures without altering the prevailing fretting regime at contacting asperities, the rough surface topography design parameter introduced for use with ceramic heads should not be implanted into patients in conjunction with metallic heads; and
- the distally engaged head stem couples i.e. engagement around the opening of the taper interfaces presented the lowest probable susceptibility to fretting corrosion compared to proximally engaged samples i.e. engagements concentrated further within the interface, attributed to an increase in contact pressure at the taper opening which could inform a different design specification for modular metal head-stem systems.

Different comparable performances between this present study and that of the uniaxial study were found to be:

- the proximally engaged samples with a rough threaded-type finish assembled to 2 kN and the rough and smooth proximally engaged samples assembled to 7 kN, presented the greatest fretting corrosion and micro motion compared to the matched or distal samples of equivalent surface topography, this was attributed to increased micro motion and a greater taper opening compared to that of the matched and distal samples; and
- the smooth distal samples assembled to 7 kN did not present an increase in current above the baseline suggesting the presence of an effective seal and thus a possible design optimisation in modular metal head-stem systems.

6.6 Future Work

The relative performance of the samples with varying surface topography and angular mismatch was assessed in terms of motion and fretting corrosion using a simulated walking

gait loading scenario, a development on from the uniaxial loading scenario used previously, and thus the aim of this study was satisfied. Nevertheless, this study did present limitations and further developments can be made to more fully understand the underlying modular taper degradation mechanisms. For example, a full explanation as to why greater currents were seen in the rough samples subject to uniaxial loadings in the previous Chapter 5 compared to the simulated walking gait loading scenario of this present study. In order to establish a fuller understanding, a multi-scale FEA study of each particular sample capable of modelling the asperity scale interactions superimposed on their macro-scale geometries to understand the mechanical interaction, validated against a like-for-like experimental study starting with a sinusoidal uniaxial dynamic loading profile, followed by a twin-peak uniaxial profile (as per Wight et al. [7]) before introducing flexion-extension, adduction-abduction and finally internal-external rotation systematically. Development of the motion measurement solution to take concurrent electrochemical and motion measurements can then be used to link the mechanical response, elucidated by the FEA study, with that of the fretting corrosion response. Furthermore, an extra layer of data can be enhanced by sampling the force measurements from the 6-axis load cell of the universal joint simulator. This proposed methodology could also be used to systematically investigate the surface topography parameters. Although the results of Chapter 3 would indicate certain limitations of controlling surface topography, systematic investigation of surface topography parameters in terms of both amplitude and morphology could be achieved by manufacturing many samples, measuring them and then grouping them based on their surface topography parameters.

To facilitate fretting corrosion and motion measurements subject to a simulated walking gait profile without collision with the motion sensing solution or electrochemical cell, a plug representing 50 % of a full acetabular cup was loaded against the head sample mediated by a layer of grease. Whilst the layer of grease helped fluidly isolate the bearing interface from the electrolyte, it was easily displaced leading to non-ideal lubrication. Future work is aimed at developing an electrochemical cell that can measure the simultaneous fretting corrosion response at both the taper and bearing interface where the electrolytes of the femoral head and taper interface are separated [304]. This can be facilitated by the use of smaller electrodes that can be integrated into the electrolyte bath around the working electrode, negating any possible IR drop introduced by a distance of 60 cm via a 10 mm diameter tube of this present study.

Although this study, in line with that found previously, found the axial gait force to primarily dictate the taper junction's fretting corrosion and motion response, the ISO 14242 Part 1 [8] walking gait profile can still be considered to be on the conservative side. A finite element study by Raji and Shelton [139] report a much greater maximum taper opening

when subject to a simulated stair climb, approximately a magnitude larger than a simulated walking gait. Further developments in this area include employing patient derived gaits which can be determined from studies like Bergmann et al. [6] that used sensorised total hip replacements, the open access data from such studies can be readily found in the *Orthoload* database [305], and Lunn et al. [67] that used a motion capture laboratory with the aid of load plates and The *AnyBody* Modelling System software. Further development in the measurement parameters could also be made, for example, the use of onset loads (the loading increment at which an increase in current above the baseline was determined) used by previous studies [7, 218, 306, 224, 211] might help differentiate between the fretting corrosion response subject to more complex loading scenarios compared to that of the uniaxial, despite this not being the case found by Wight et al. [7]. In order to facilitate the determination of onset load, finer incremental loading increments than 500 N, as used by this study are needed and a robust mathematical method of consistently and objectively determining fretting corrosion onset load. Previously, onset load has been determined subjectively, most probably from current-time plots [7, 306], with some studies employing more robust mathematical methods such as Rowan et al. [224] who employed an established 'kneedle' algorithm [307] and the frequency domain of the data after applying a Fast Fourier Transform of the time domain data to determine the load at which the measured current demonstrated a frequency that matched the loading frequency.

Chapter 7

Discussion, Conclusions and Future Work

7.1 Overall Discussion

Modularity is ubiquitous in THR, and orthopaedic devices in general, and is considered important for a successful surgical outcome [86, 111]. Fretting corrosion related failures at these junctions has been identified as an issue since the mid-1990s [28]. With a general year-on-year increase of joint replacements and a growing and ageing population, the clinical importance of fretting corrosion at taper junctions is only set to increase. In 2014, the European Commission published a report on the risk of metal-on-metal joint replacements, identifying the taper junction as an important particle and ion generation site [97]. This report also highlighted a gap in knowledge and pre-clinical research aimed at investigating the influence of relevant taper parameters on wear and corrosion.

7.1.1 Contribution of Findings with Respect to the Head-Stem Modular Taper Junctions in THR

Contribution to the Understanding of the Role of Surface Topography and Angular Mismatch in Head-Stem Modular Taper Junctions

This thesis presents an investigation into the effect of surface topography and angular mismatch seen in clinically available head-stem modular taper junctions of THR on performance, and primarily on the fretting corrosion response. The motivation for this investigation was the uncertainty within current literature on the effect of surface topography as a single design parameter and the lack of pre-clinical investigations into the

effect of angular mismatch. Some studies attributed a rougher surface topography to increased fretting corrosion [186] due to increased contact pressure, micro motion and fluid ingress [163, 226], however, there is a lack of experimental investigation within the literature to conclusively support these suggested mechanisms. There are fewer retrieval and experimental studies that have investigated the effect of angular mismatch, however, FEA studies unanimously support the likelihood of reduced fretting corrosion with reduced angular mismatch due to findings of reduced motion and contact pressure suggesting less oxide disruption [141, 136, 227].

This investigation helped to elucidate how surface topography and angular mismatch affect the fretting corrosion response by measuring the electrochemical and motion response, which has not been done before with respect to both surface topography and angular mismatch. Key findings beyond the state of the art include:

- the rough samples were found to be more susceptible to fretting corrosion than the smooth samples, not attributed to an increase in motion at the interface and most likely attributed to increased contact pressures without altering the prevailing fretting regime at contacting asperities, as such findings from this study suggest that the rough surface topography design parameter introduced for use with ceramic heads should not be implanted into patients in conjunction with metallic heads;

- the distally engaged head stem couples i.e. engagement around the opening of the taper interfaces, presented the lowest probable susceptibility to fretting corrosion and magnitudes of micro motion, magnitudes of micro motion of the distally engaged samples were similar to that of taper junctions that presented a smaller level of angular mismatch compared to proximally engaged (i.e. engagements concentrated further within the interface) samples, attributed to an increase in contact pressure at the taper opening which could inform a different design specification for modular metal head-stem systems;

- the most conforming tapers, the matched engagement samples (0.017 ± 0.004 °), did not present the lowest susceptibility to fretting corrosion, attributed to a lower contact pressure altering the prevailing fretting regime of contacting asperities, additionally, the most conforming taper still presented a slight proximal angular mismatch predicting a reduction in contact pressure towards the opening of the taper, and thus, asperities junctions with a higher probability of experiencing sliding occur closer to the taper opening being more exposed to the electrolyte; on the other hand, the matched samples also presented the least off-axis subsidence and some of the lowest levels of micro motion which may indicate better longer term performance subject to more complex biomechanical loading; and

- in most scenarios, most samples did presented some level of susceptibility to fretting corrosion, there was one exception of the distally engaged samples with smooth surface topography that did present evidence of a successful seal, and although this has been suggested as a possibility by previous studies, this was the first study to experimentally demonstrate this through optimisation of the taper interface using surface topography and angular mismatch seen in current clinically available head-stem modular taper junctions of THR.

Some of the above findings were unexpected, particularly, the samples that presented the lowest level of angular mismatch not presenting the lowest susceptibility to fretting corrosion, and in some scenarios presenting the highest susceptibility to fretting corrosion. This was in contradiction to the hypothesis of increased engagement would result in a reduction in motion and therefore fretting corrosion. However, the FEA study by Donaldson at al. [136] found that although micro motion was found to increase with angular mismatch, micro motion was only weakly correlated with angular mismatch and more strongly correlated with contact pressure. The effects of contact pressure were hypothesised to play a significant role in the fretting corrosion response in the simulation studies presented in Chapters 5 and 6, altering the proportion of contacting asperities experiencing different fretting regimes. The different fretting regimes having been shown to be unequivocally linked to the fretting corrosion response using simplified pin-on-disk studies [234, 308, 238].

A less unexpected finding was that of the distal samples presenting the lowest measurable currents, indicating that the distally engaged samples were the least susceptible to fretting corrosion. Previous studies have speculated at the possible sealing effect of a distal angular mismatch limiting the transport of electrolyte in and out of the taper interface, and thus, limiting the rate of corrosion reactions and possibly even inhibiting corrosion [232, 136, 4]. This is in agreement with the recent study by Mueller et al. [4], who found reduced current measurements using zero resistance ammeter electrochemical methods and reduced metal ion release using mass spectroscopy methods subject to uniaxial dynamic loading of the taper junction in the distally engaged samples with a threaded-type finish compared to the proximally mismatched samples with smooth or rough male taper surface topography. This study further advanced on the findings of Mueller et al. [4] with respect to the possible advantages of distally engaged head-stem taper interfaces, by presenting evidence that a taper interface experiencing fretting can be sealed from the electrolyte with a smooth surface topography, a distal angular mismatch in the region of -0.090 ±0.003 µm and sufficient assembly force.

In addition to the effects of contact pressure distribution concentrations towards the opening of the taper interface reported by previous studies thought to reduce corrosion by

limiting the ingress and egress of fluids, this present study highlighted another mechanism that may help distally engaged taper junctions to limit fretting corrosion. Engagement around the taper opening being offset from the centre of the head may provide a more stable interface. This hypothesis was supported by the distal samples presenting the greatest off-axis subsidence, as the female taper moved to rest on the male taper with the application of the axial loading vector This was reported in conjunction with smaller magnitudes of micro motion compared to the proximally engaged tapers with a similar magnitude of angular mismatch, and similar levels of micro motion compared to the matched samples.

Looking now to overall relative performance of the samples, taking into account both surface topography and angular mismatch. In the uniaxial scenario, surface topography presented a greater influence on the fretting corrosion response compared to angular mismatch. This was shown by the rough distal samples presenting a greater average current measurement compared to any of the smooth samples, irrespective of engagement. The greater influence of surface roughness amplitude than angular mismatch is in contrast with a previous study by Mueller et al. [4] that found surface roughness amplitude not to have a significant influence on the fretting corrosion (p-value > 0.05) response unlike angular mismatch (p-value < 0.001), but was in agreement with Panagiotidou et al. [226] that found evidence of fretting corrosion in the rough samples but not in the smooth samples. In the simulated walking gait loading scenario of this present investigation, the relative influence of surface topography and an angular mismatch on the fretting corrosion response was more comparable. This was demonstrated by the rough distal samples presenting a similar average current to the smooth proximal samples (0.49 ±0.23 μA vs 0.67 ±0.30 μA, p-value of 0.42) and a smaller average current compared to the smooth matched samples (0.49 ±0.23 μA vs 1.85 ±0.87 μA, p-value of 0.06) when assembled to 2 kN. This was also seen when the heads were assembled to 7 kN, the rough distal samples presented a lower average current compared to the smooth matched (0.07 ±0.04 μA vs 0.18 ±0.09, p-value 0.15) and smooth proximal samples (0.07 ±0.04 μA vs 0.33 ±0.19, p-value 0.08). Hence, the results from the uniaxial studies suggest that greater emphasis on optimising the surface topography in head-stem modular taper junctions in metal head should be made whilst the simulated walking gait loading scenario suggest that more equal emphasis on optimising surface topography and angular mismatch should be made. Further studies are required to understand this discrepancy between the uniaxial and simulated walking gait loading scenario.

The state of the art on the understanding of how surface topography and angular mismatch affect the fretting corrosion response of head-stem modular taper junctions in THR is that:

- long smooth tapers perform better than short rough ones [186, 187, 164, 185];

- there is no common understanding on how surface topography as a single design parameter influences degradation; and
- there is a lack of studies that have investigated the effect of angular mismatch both in-vivo and in-vitro in order to establish a common understanding across the literature [190, 4].

This investigation provides evidence that reducing the surface topography roughness amplitude and having a distal angular mismatch of less than -0.1 ° both as single design parameters and together, can reduce degradation via fretting corrosion in CoCrMo femoral heads coupled with stainless steel male stems.

Contribution to Experimental Testing of Head-Stem Modular Taper Junctions

The primary aim of this study was to assess the relative performance of surface topography and angular mismatch present in head-stem modular taper junctions. It was thought that the simplified uniaxial loading scenario primarily used to date, did not fully capture the complex dynamic off-axis loads experienced in-vivo and could be a reason as to why there was a lack of common understanding of how surface topography and angular mismatch affect degradation. Therefore, this study saw the development of a motion measurement system, electrochemical cell and fixtures to allow motion and the electrochemical response to be captured whilst the taper junction was loaded to a simulated walking gait loading scenario detailed in ISO 14242-1 [8].

Although there was no increase in current measured with the inclusion of the more complex walking gait loading scenario compared to the uniaxial loading scenario, in line with a recent study by Wight et al. [7], nor obvious increase in the magnitude of micro motion, there was a suitable differentiation in the toggling YZ micro motion. The inclusion of the ISO walking gait [8] saw torques acting about the head with the largest being in the flexion-extension (see Figure 7.1 for a schematic showing the direction of applied torque in the flexion-extension direction), this also saw a differentiation in toggling YZ micro motion in the proximal samples (see Figure 7.1 for a schematic showing the direction of toggling XZ micro motion), as shown and discussed with respect to Figure 6.23. This observation is in line with the hypothesis that proximal samples with engagement closer to the centre of rotation may be less stable than the distal samples with engagement offset from the centre of rotation, and therefore better able to resist fretting corrosion, particularly when subject to more complex loading scenarios. However, the ISO walking gait [8] can be thought to be conservative with other daily living activities such as jogging, running and contact sports exceeding peak forces by around 50 % compared to that of a walking gait [41]. Although many hip replacement patients may not be partaking in sports and

contact sports, accidental events which may be common after surgery such as stumbling can achieve peak resultant forces that exceed that of the ISO walking gait by a around a factor of four during stumbling [6]. There are no studies to the author's knowledge of any experimental studies having investigated the motion and fretting corrosion response of the head-stem modular taper junction subject to other daily living activities with some studies highlighting the need to go beyond that of more standard testing protocol [220]. FEA studies on the other hand present findings that more extreme daily living activities can significantly alter stresses, forces and motions experienced at the taper interface [139, 309]. Looking to experimental studies of other taper junctions, Jauch et al. [310] measured the motion response of the neck-stem modular taper junction subject to uniaxial loading simulating the peak axial forces of different daily living activities. Jauch et al. [310] found micro motion increased by 2 µm in CoCrMo neck adaptors and 5 µm in Ti6Al4V adapters when subject to a stumbling peak force compared to a walking gait peak force (as determined from Figure 9 therein), this suggested an increased fretting corrosion response which is could be translated to the head-stem modular taper junction.

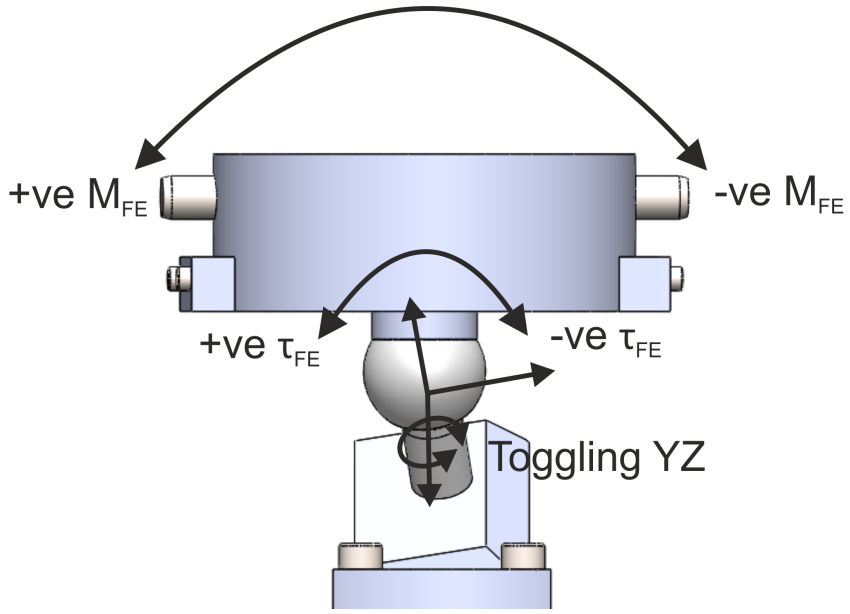

Fig. 7.1 Schematic showing how the inclusion of flexion-extension moments about the head can increase YZ toggling.

The PBS test solution used in this investigation was a simplified model of synovial fluid and has been used by many studies that have investigated the fretting corrosion response of the head-stem taper junction [226, 218, 222, 7]. As discussed in more detail in Chapters 5 and 6, the use of PBS isolated from the bearing interface could affect the fretting corrosion response of the taper junction by virtue of the differences in the chemical and biochemical composition of PBS compared to that of synovial fluid, and the lack of fluid mediating the contact between the bearing interface of the femoral head. The inclusion of

more complex loading when investigating the fretting corrosion response of the head-stem taper junction can more accurately simulate biomechanical loading experienced in-vivo. However, isolating the corrosion response of the taper junction and bearing interface while submerging both interfaces can introduce experimental difficulty. Previously, uniaxial studies often fluidly isolate the point load interface between the femoral head and the loading applicator, in ASTM 1875 [196] this is suggested by way of a seal. A recent study by Wight et al. [7] that also employed the ISO walking gait [8] loading scenario did not isolate the bearing interface from the test solution and justified this by way of it being a polymer-on-metal bearing interface, as opposed to a metal-on-metal interface. A key advantage of Wight et al. [7]'s experimental methodology was the more accurate simulation of the fluid environment, however may have introduced experimental error by including the corrosion response of the bearing interface. With that said, similar magnitudes of current were measured by Wight et al. [7] when compared to this present investigation, as detailed in Table 6.4 suggesting that the corrosion response of the bearing interface may have been minimal.

The resultant torque applied by this present study was found to be similar to that of a dry hard-on-hard bearing interface. Future work will include submerging the bearing interface in the test solution while fluidly isolating it from that of the taper interface. Advancements in the test solution in the first instance can include the use of synovial fluid constituents such as hyaluronate, albumin, globulins and phospholipids which have the effect of reducing friction at the sliding interface [311], and thus likely reduce the frictional torque transmitted through the femoral head which could have the effect of reducing fretting corrosion of the taper interface. However, in terms of short term testing, the enhanced lubrication is likely to play a minor role in fretting corrosion of the taper interface compared to that of the axial load due to body weight as per Wight et al. [7] and this present investigation. In terms of the corrosion response, current literature would indicate that the inclusion of albumin can have competing effects, whereby corrosion resistance is likely to be decreased in anodic passive potentials [282, 283, 202] used by this present investigation, whilst decreasing tribocorrosion attributed to a protective adsorbed biofilm [282**?** , 284, 285]. Taking the simulation of the fluid environment further, a recent study by Radice et al. [312] reports a possible interacting effect of albumin and hylauronate, highlighting the importance of more accurately simulating synovial fluid when assessing corrosive degradation of medical implants in-vitro.

This present investigation also saw the development of a more controlled assembly process, beyond that specified by ISO 7206-10 [134]. The methodology of the assembly process detailed in ISO 7206-10 [134] has been adopted by the vast majority of in-vitro studies and specifies that a tolerance of 0 ± 1 ° between the male taper axis and the loading

axis whilst the head taper is free to self-align. However, during the development of the experimental methodology of this present study, it became apparent that further control was required due a lack of uniform contact from the uncontrolled female taper axis as shown in Figure 2.26. The more controlled assembly process developed involved the design and manufacture of precision manufactured fixtures to align the loading axis, male taper axis and female taper axis to within an angular tolerance of 0.001 °. With early 1900s literature detailing how tapers used in industry should be pressed together and not impacted to ensure a uniform distribution of stress over the whole interface [108] and a more recent modular head-stem engagement study highlighting the non-uniformity of engagement between the two surfaces [232], suggest that a more controlled concentric assembly methodology could provide a more repeatable sample assembly method for more controlled in-vitro testing.

Contribution to Manufacturers of Total Hip Replacements and Clinical Practice

With manufactures so far rejecting an industry standard, there is large variation in taper designs as shown in Chapter 3 along with those of previous studies [110, 184]. This rejection of the so called 'euro-taper' was due to potential difficulties in establishment within the industry, the lack of a complete description, the lack of common understanding of what the standard taper should look like and the risk posed to patients if not done so correctly [86, 250]. Nevertheless, some design parameters such as a proximal angular mismatch and a male taper surface topography with roughness amplitude of between 6 and 20 µm [185], have been enforced on total hip replacement stem manufacturers by the ceramic head manufacturer *CeramTec*. These design parameters have been translated over to metal heads with little to no rationale. This investigation suggests that head-stem taper junctions with a threaded finish and roughness amplitude (S_a) of between 1.8 and 4 µm may be more susceptible to fretting corrosion than those with a non-threaded finish with roughness amplitude (S_a) of between 0.4 and 1.0 µm. These findings of the relative surface topography are in agreement with previous clinical studies that found short rough tapers to suffer greater degradation than long smooth tapers [186, 187, 164, 163] and pre-clinical studies [226, 185]. Considering angular mismatch, taper junctions with a proximal angular mismatch between 0.01 and 0.12 °may be more susceptible to fretting corrosion that those with a distal angular mismatch of between -0.09 and -0.08 °. Findings of the better relative performance of the distal angular mismatched samples are in agreement with a recent study by Mueller at al. [4] and theories put forward by Witt et al. [232] and Raji and Shelton. [139], yet contrary to a retrieval study [190] and an experimental study [222] that found little to no effect of angular mismatch present in total hip replacements on degradation and also contrary to most computational studies [141, 136, 227] that found increased contact stress, motion and predicted wear with an increase in angular mismatch.

Considering roughness and angular mismatch together, the best resistivity to fretting corrosion found by this study was the smooth distal samples, a newly supported experimental finding of this present investigation. These findings suggest that a one-size fits all taper standard is not appropriate, and different design parameters such as head material should have different taper designs. Additionally, that is not to say that smooth distally engaged tapers should be used in all metal head-stem couples, other design parameters such as taper length need to be considered and how they might interact with these design parameters on the overall taper performance. This design combination of a smooth distally engaged CoCrMo head-stainless steel stem modular taper junction with a male taper length that extends beyond that of the female taper when engaged, can be selected by surgeons from the current clinically available THR as determined by Chapter 3 and that of previous studies such as Mueller et al. [110]. Additionally, this design combination can be one that manufacturers consider upon designing of new THR solutions. Future work will need to consider the interaction of each individual design parameters present in clinically available THR systems.

One of the few individual factors that has been found to consistently affect taper performance in-vitro is head assembly, with studies showing that an increased head assembly force increased: seating displacement [228, 211, 212, 218], disassembly force [229, 228, 230, 231, 233], engagement [232, 138], deformation at the interface [232, 138], and in the short to medium term, a reduction in the amount of motion [211, 212] and fretting corrosion [211, 222, 217, 185, 218]. In agreement with these aforementioned studies, this present investigation also found a reduced susceptibility to fretting corrosion, a reduction in subsidence motion and a slight reduction in micro motion in some scenarios. Unlike that of previous experimental studies, this study went beyond that specified by ISO 7206-10 [134] and controlled the concentric assembly between the male taper axis, the loading axis and the head taper axis. This controlled assembly methodology was developed after findings of the non-concentric nature of the engagement process in cases where the head tapers was free to self-align, as discussed in the preceding Section in more detail. Further control of the surgical head assembly process also has clinical applications in view of Bormann et al. [191] who found evidence of non-concentric assembly to affect taper degradation in-vivo. The concentric assembly method developed by this investigation can be used by surgeons to inform current head assembly processes intra-operatively and orthopaedic manufactures in the development of a new surgical tool to help surgeons achieve concentric head assembly intra-operatively.

This investigation found that head-stem modular taper junctions can be manufactured with tighter angular tolerances than is currently achieved by clinically available THR. This was shown by a maximum difference of around 0.05 ° in cone angle and 20 µm

in diameter for a given taper design from the same manufacturer, found by this study, that of Mueller et al. [110] and also in agreement with an early study by Cales and Stefani [250]. This would place clinical tapers closer to the tolerance grade of AT8 (AT_α = 0.057 °, L = 10-16 µm), if not beyond [107]. With tapered interfaces in CNC machines routinely being manufactured to AT3 tolerance grades or tighter [260] and the samples created for this present investigation by an orthopaedic company being manufactured to between AT5 - AT6; current manufactures of THR using current tools and techniques can manufacture tighter tolerances of head-stem modular tapers. The same cannot be said for surface topography, as shown in Figures 4.7 and 4.8. This tells us that unlike geometrical tolerances, further developments in manufacturing tools and techniques are required to achieve tighter control over surface finish on the micro-scale.

With the above said, a key contribution of the study presented in Chapter 3 was the identification of patterns in 'roundness' and 'straightness' which appeared to be linked to differences in the second moments of area during the lathing process, please refer to Section 3.4.3. A future possible standard for the head-stem tapers in orthopaedic applications should therefore include description of 'roundness' and 'straightness'. Control over such form deviations in the orthopaedic industry can be found in other industries that have seen the development of adaptive clamping forces. This is where clamping forces can be adjusted to compensate for variability in component stiffness during machining for geometrical accuracy of the finished component [267].

7.1.2 Contribution of Findings with to Modular Junctions in other Orthopaedic Implants

Applicability of the findings of this present study may also extend to other modular interfaces. Figure 7.2 shows a schematic of other implants and their typical component parts with modular interfaces there between. Starting with modular dental implants, dental implants are surgically fixed into the maxilla (upper jaw) or mandible (lower jaw) and are used to restore normal function and appearance of teeth. Unlike alternatives treatments such as bridges and dentures which do not employ implants as a means of fixation, implants help retain the natural bone stock by transmitting force to the jaw that would otherwise be transmitted by the natural tooth. However, early implant failure, and more specifically marginal bone loss, has been associated with movement caused by mastication between interfaces releasing microbials and their harmful by-products, metal corrosion and wear products [313–316]. One interface that is commonly cited as a site for biological matter, wear and corrosion release is that of the metal-on-metal implant-abutment interface (please refer to Figure 7.2 for an annotated diagram of these aforementioned component parts). The

implant-abutment interface can have different designs, including a tapered and hexagonal interfaces, with tapered interfaces presenting a lower risk of marginal bone loss attributed to their superior sealing capacity [314, 317]. In view of the desirable sealing of interfaces within the oral cavity, a key finding of this present investigation which is pertinent to that of the abutment-implant interface is the ability to seal tapered interfaces with a designed angular mismatch coupled with a high compressive force.

Total shoulder replacements (as shown in Figure 7.2) and reverse shoulder replacements (the humeral bearing component being the cap and the glenoidal bearing component being a head), like THR are replacements of a synovial ball-and-socket joints. A key difference between THR and shoulder replacements is the biomechanical loading. The loads achieved at shoulder replacements is around one third of that achieved at the hip or knee replacements [318]. Shoulder replacements between the humeral head and humeral stem present a Morse-type taper like that of the head-stem taper in THR, reverse shoulder replacements present a Morse-taper taper between the glenoidal head and a base plate which in turn fixes onto the patient's bone, both of these can be metal-on-metal tapered junctions and have been reported to be susceptible to fretting corrosion [319, 320]. Like that of THR, male tapers can show different surface topographies and angular mismatches with large variation between manufacturers [321]. In terms of male surface topography, R_a has been reported to vary between 1.59 and 3.27 µm and R_z between 8.15 and 20.01 µm with the surface profile presenting either a random finish from being blasted or a periodic finish from being turned [321]. This range in surface topography is similar to that seen in Chapter 3 due to the presence of both turned and threaded male tapers. In terms of taper angle, male taper angle has been reported to vary between 5.670 and 5.958 °and female tapers between -0.293 to 0.334 °[321]. Assuming the worst case scenario of mixing components from different manufacturers, angular mismatch could achieve a range of -0.293 to 0.334 °which is larger than that found in head-stem taper junctions of THR as presented in Chapter 3. Learning from this present investigation could be pertinent to that of shoulder replacements, more specifically a reduced surface topography amplitude and a slight angular mismatch to create compression round the taper opening to reduce the effects of fretting corrosion. The effect of a blasted surface topography, not a feature present in THR, could be investigated further to assess its relative performance compared to turned male taper finishes and its applicability to other modular taper junctions in the body.

THR systems also present other tapered modular interface beyond that of the head-stem junctions, including between the acetabular shell and liner (see Figure 7.2), and in fewer cases, modularity between the femoral neck and femoral stem due to a lower 10-year survival rate compared to just head-stem modularity in the femoral component

[322]. Fretting corrosion has been associated with both of these modular tapers leading to early failure of the implant [323–325]. Earlier in this discussion and in the Chapter 6, agreement between findings of this present study and earlier studies of the neck-stem taper interface were drawn. More specifically, the parallels between these the head-stem and neck-stem modular interfaces, including similar magnitudes of micro motion measured by this present study and that reported by Jauch et al. [214] and the reduced level of micro motion with a slight increase in angular mismatch for engagement round the opening of the taper [212]. By extension, learning from this present investigation to that of neck-stem tapers could be the reduction in susceptibility to fretting corrosion with a slight angular mismatch to create pressure round the taper opening. In terms of surface topography, to the author's knowledge, neck-stem tapers do not present a threaded finish and the exact nature of their surface topography is not common knowledge, and so learning from this investigation with respect to surface topography is unlikely to be applicable. Unlike the head-stem and neck-stem tapers, where dominant degradation mechanisms are reported by literature to be tribocorrosive mechanisms, a recent study reports that the leading mechanism of the acetabular component is corrosion dominated [326] corroborated by earlier studies that focus on corrosion mechanisms in their explanations as opposed to tribocorrosion mechanisms [327]. Assuming that corrosion mechanisms are in fact dominant over tribocorrosion mechanisms at the acetabular modular interface, learning from this present investigation on how motions can be minimised may not be as pertinent as other taper junctions, rather the potential sealing of this interface to reduce the effect of corrosion may be more applicable.

Total knee replacements also present modularity by way of tapered junctions, however, unlike THR, the option of whether or not to use modular designs with tapered junctions is still a choice of the surgeon, possibly due to the more comparable clinical outcomes of non-modular compared to modular designs [328]. With that said, modular taper junctions are susceptible to fretting corrosion in total knee replacements [329–331] but like other taper junctions in the body, is not as heavily researched as the head-stem modular taper junction of THR. Like THR, total knee replacements experience the greatest load acting vertically down [332]. Unlike THR, in total knee replacements, this vertical load due to body weight is aligned with the long axis of the femur and tibia, and thus, presents a larger component force acting along any modular tapered junctions compared to that of the head-stem junction of THR. Morse's original design was for the purpose of resisting rotational torque about the taper axis in direct compression, and hence modular tapered tibial components of total knee replacements are more akin to Morse's original design intentions. According to Newton's third law, any modularity by way of a tapered junction in the femoral component will be in tension when unloading, the opposite to Morse's original intentions. This could help explain a finding by Arnholt et al. [329] who found

that male tapers of the femoral components had a statistically higher visual corrosion score than that of the tibial components, not an explanation explicitly put forward by Arnholt et al. [329]. Although, learning from this investigation suggests that disassembly force may not be a good pre-clinical parameter for assessing taper performance, it may be more pertinent to clinical outcomes in modular femoral components of total knee replacements due to their more on-axis loading compared to THR. Like THR, Arnholt et al. [329] also associated more flexible, lower elastic modulus metal stems to be more susceptible to fretting corrosion at the taper junction due to increased micro motion, hence learning of a slightly increased angular mismatch to create compression round the taper opening may be applicable total knee replacements in order to reduce their susceptibility to fretting corrosion. In agreement with this present study, an FEA study by Snethen et al. [333] suggests that angular mismatch in modular tapers in total knee replacement should also be limited to within ±0.1 °.

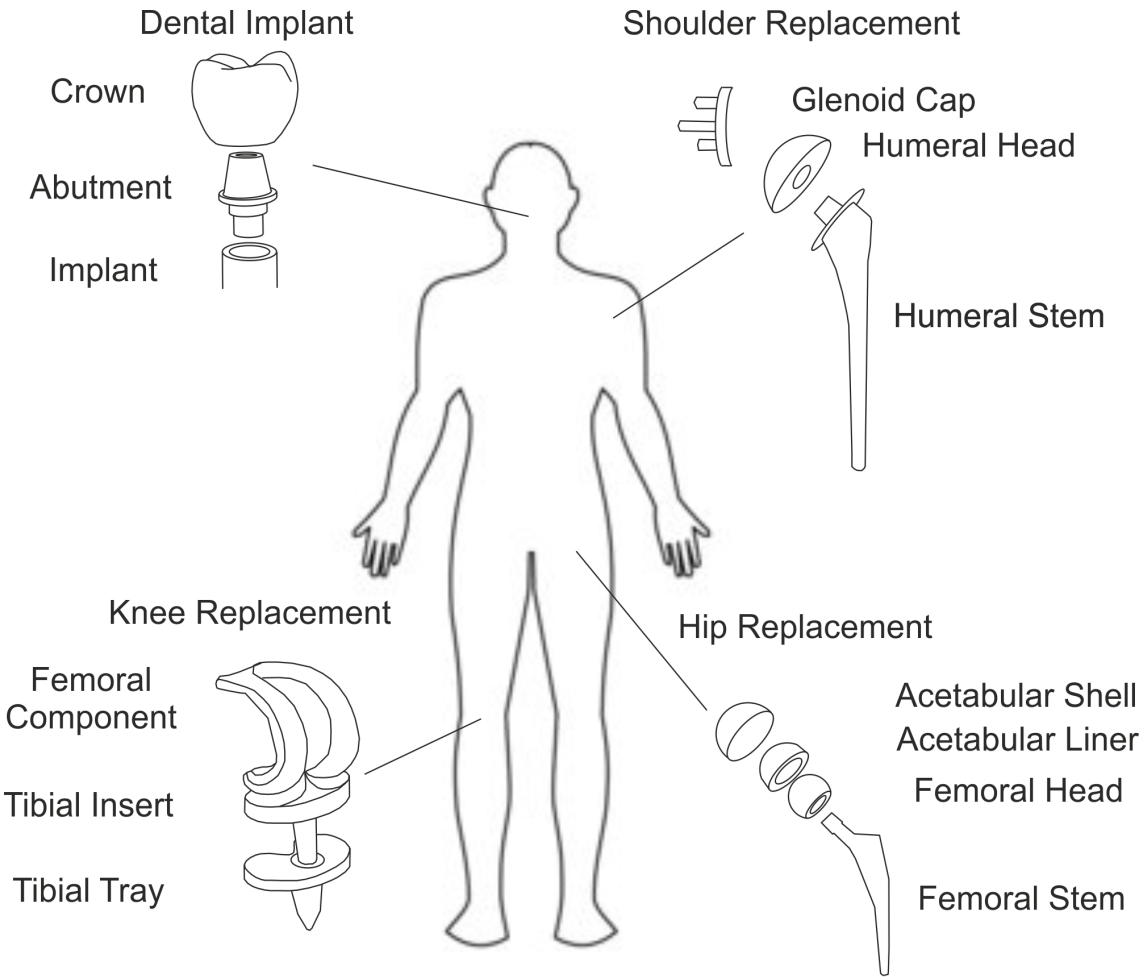

Fig. 7.2 Schematic showing other joint replacements in the body with modular junctions.

7.2 Conclusions

Following higher than acceptable failure rates due to the release of metal particles and ions, the European Commission published a report on the risk of metal-on-metal joint replacements [97]. This report also identified the taper junction as an important particle and ion generation site. A gap in knowledge and pre-clinical research was also highlighted in this report, aimed at investigating the influence of relevant taper parameters on wear and corrosion.

This project aimed to develop a clearer understanding of how variations in modular taper junction design parameters present in clinically available THR affected performance in terms of fretting corrosion. This was achieved by first measuring a variety of clinically available head-stem modular tapers in terms of geometry and surface topography, before conducting assembly-disassembly studies on representative samples followed by fretting corrosion simulation studies, this allowed the following conclusions to be reached:

- clinically available male tapers presented a large variation in the surface topography, largely attributed to the presence, or lack thereof, of a micro thread, introduced for use with ceramic heads but also being used with conjunction metal head couples; dynamic simulation studies found that samples with male tapers that presented a micro-threaded finish were more susceptible to fretting corrosion compared to couples with male tapers that did not present the micro-threaded finish, this was shown by lower current measurements using potentiostatic methods, indicating that taper design specifications for use with ceramic heads may not be directly applicable to metallic head couples;

- the increase in susceptibility to fretting corrosion of taper junctions with male tapers that presented a threaded finish was not found to be attributed to an increase in micro motion at the interface, indicating that the increased susceptibility to fretting corrosion was most likely associated with the contact situation;

- the range of angular mismatch present in clinically available THR, either by design or manufacturing tolerance was from -0.047 ° to 0.160 ° creating a distal and proximal mismatch respectively, with a mean proximal mismatch of 0.043 ° this was attributed to the proximal angular mismatch design specification for ceramic head couples which has been translated over the metal head couples;

- distally angular mismatched taper junctions of this present investigation (-0.089 ± 0.004 °) were found to be more resistant to fretting corrosion compared to proximally mismatched groups (0.017 ± 0.004 °and 0.118 ± 0.013 °), attributed primarily to

the contact situation, this indicated that the proximal angular mismatch design specification for use with ceramic head couples may not be directly applicable to metal head couples; and

- the inclusion of a more complex simulated walking gait loading scenario over the uniaxial simulated loading scenario did not cause an increase in susceptibility to fretting corrosion, suggesting that complex loading according to ISO 14242-1 [8] may not be a valuable addition to short term simulation studies.

7.3 Future Work

Modularity in orthopaedic devices is important for a successful surgical outcome and is present in almost all devices implanted today. One key advantage offered by modularity is the flexibility it offers the surgeon intra-operatively. Flexibility that does not extend to mixing components from different manufacturers which goes against manufacturer recommendations and is considered 'off-label' by the Medicines and Healthcare Products Regulatory Agency [334]. The key reason being that their compatibility, in terms of design and manufacturing tolerance, is unknown [16, 250]. However, mixing of components does occur and is associated with an increased risk of early revision [263]. Standardisation is one solution that can provide other additional benefits, including reducing inventory. Manufacturers have so far rejected an industry standard due to difficulties in establishing one and the potential risk if it is not done correctly [86, 250]. One reason for the failed attempt at drafting a suitable ISO and ASTM standard was the lack of a complete description, most possibly due to the lack of common consensus on what makes a 'good' taper junction available in the literature. A possible reason for the confusing and often conflicting outcomes from literature is the variation in pre-clinical testing, often very different from the environment in-vivo which is extremely complex and multi-factorial [38]; resulting in an incomplete understanding of how different design parameters can interact. Although the ability to fully replicate the in-vivo environment is not yet viable, further development of simulation methods and use of multiple approaches that are viable, can help paint a more vivid picture of their performance.

This project attempted to understand how different taper design parameters might affect performance by taking a systematic approach to understand engagement, motion and fretting corrosion. To achieve this, two key tools were developed including methods of describing the taper interface more fully and a method of measuring the motion and fretting corrosion response subject to more complex

loading than that currently used in pre-clinical studies. However, this project presents limitations and further work is required to address them. In summary:

- **Fully describing the taper interface.** Actual contact at conforming interfaces is complex and very difficult to predict as it is a function of geometries, form, waviness, roughness and so on down the length scales. This project aimed to help bridge this gap by employing contacting CMM in conjunction with non-contacting surface profilometry but presented difficulties when trying to correlate between the two. Compromise between measurement resolution and the area of measurement is common across all sensing technology but optical CMM methods could provide the next step in spanning multiple length scales [271].
- **Concurrent measurements.** One limitation of this study was the ability to take concurrent electrochemical and motion measurements. Developments in the data capture procedure and the motion sensing solution would allow concurrent load, motion and electrochemical measurements for sub-cycle correlation.
- **The Loading scenario.** Despite this project employing a more physiologically relevant profile then that used to date, the ISO 14242 Part 1 [8] walking gait profile can still considered to be on the conservative side, especially when considering the taper response [139]. Further developments in this area include employing other physiologically relevant profiles that are considered to be more extreme such as stumbling and stop-dwell-start protocol [6, 335].
- **The electrolyte.** This project employed PBS as an electrolyte, which was deemed sufficient for this comparative study by ASTM 1875 [196]. Use of a solution that more accurately represents that in-vivo is often achieved by the inclusion of proteins via use of Bovine serum. However, a more basic corrosion rate determining factor, and by extension fretting corrosion, is the availability and concentration of reactants such as oxygen, which are very different to that in the atmosphere than in-vivo [192].
- **Within the interface measurements.** One limitation in the more complex loading scenario was the position of the reference and counter electrodes relative to the working electrode. A recent study by Bermudez-Castaneda et al. [336] positioned electrodes at different locations within the taper interface. Significant insight into how different taper designs affect the motion and fretting corrosion response could be gained from interface measurements and visualisation. Visualisation of tapered interfaces has been achieved previously with synchrotron-based radiography [337].

- **Dual computational and experimental approach.** Accurate in-vitro simulation and high resolution measurement can be expensive. Computational models are a cost-effective way assessing the mechanics of the taper, but complex surface interactions are often simplified to a coefficient of friction [272]. A multi-scale model that is able to simulate the asperity level interaction within a conforming contact could help provide a valuable piece of the picture to help compliment the understanding of the complex fretting corrosion problem at the interface.
- **The long-term performance assessment with real-time measurements.** THR are often in-situ for over 15 years [111]. In comparison, long-term testing in-vitro normally takes somewhere in the region of two months [8]. There is a drive for the development of short in-vitro tests that are capable of comparing the performance of a large number of taper design parameters over the length of their service life. One way of accelerating tests is by creating a more aggressive simulation environment. A recent study by Hornus et al. [338] was able to recreate the morphology and extent of degradation of that seen in-vivo. This was achieved by incrementing the anodic over potential, accelerating the occurrence of a critical crevice solution. However, accelerated test methodologies can be difficult to validate.
- **Biological interactions.** Quantifying and characterising the degradation products, including debris composition and morphology, is key to gaining an understanding of the possible biological response [290**?**]. Additionally, being able to demonstrate the risk posed by degradation products produced by medical devices is as small as possible is a requirement for approval on the EU market [98]. Consequently, there are big clinical drivers for quantifying and characterising degradation products released in pre-clinical studies.
- **Innovations to the modular junction.** Results from this project indicate that the taper junction can be optimised. One possible optimisation to the taper junction could include relieving the centre of the interface. This could offer an increased contact pressure to form a seal at the interface, like that in the distal samples in this study, whilst minimising micro motion due to engagement also occurring at the proximal end of the interface. Traditionally, this was common practice as a way of more easily achieving a good fit free of chatter in cutting tools [109].

References

[1] Jay R. Goldberg, Jeremy L. Gilbert, Joshua J. Jacobs, Thomas W. Bauer, Wayne Paprosky, and Sue Leurgans. A Multicenter Retrieval Study of the Taper Interfaces of Modular Hip Prostheses. *Clinical Orthopaedics and Related Research*, 401:149–161, aug 2002.

[2] David A. Porter, Robert M. Urban, Joshua J. Jacobs, Jeremy L. Gilbert, José A. Rodriguez, and H. John Cooper. Modern Trunnions Are More Flexible: A Mechanical Analysis of THA Taper Designs. *Clinical Orthopaedics and Related Research*, 472(12):3963–3970, 2014.

[3] Murat Songür, Hüseyin Çelikkan, Faruk Gökmeşe, S. Aykin Şimşek, N. Şükrü Altun, and M. Levent Aksu. Electrochemical corrosion properties of metal alloys used in orthopaedic implants. *Journal of Applied Electrochemistry*, 39(8):1259–1265, 2009.

[4] Ulrike Mueller, Therese Bormann, Stefan Schroeder, Tobias Renkawitz, and J. Philippe Kretzer. Taper corrosion in total hip arthroplasty – How to assess and which design features are crucial? *Journal of the Mechanical Behavior of Biomedical Materials*, 133(June):105307, 2022.

[5] R. D. Crowninshield, R. C. Johnston, J. G. Andrews, and R. A. Brand. A biomechanical investigation of the human hip. *Journal of Biomechanics*, 11(1-2):75–85, 1978.

[6] G. Bergmann, F. Graichen, A. Rohlmann, A. Bender, B. Heinlein, G. N. Duda, M. O. Heller, and M. M. Morlock. Realistic loads for testing hip implants - Copyright (2010), with permission from IOS Press. *Bio-Medical Materials and Engineering*, 20:65–75, 2010.

[7] Christian M. Wight, C. M. Whyne, E. R. Bogoch, R. Zdero, R. M. Chapman, D. W. van Citters, W. R. Walsh, and E. Schemitsch. Effect of head size and rotation on tapecorrosion in a hip simulator. *Bone and Joint Open*, 2(11):1004–1016, 2021.

[8] ISO(14242-1:2002). Implants for surgery — Wear of total hip-joint prostheses —. *ISO*, 2002.

[9] Alarcos Cieza, Kate Causey, Kaloyan Kamenov, Sarah Wulf Hanson, Somnath Chatterji, and Theo Vos. Global estimates of the need for rehabilitation based on the Global Burden of Disease study 2019: a systematic analysis for the Global Burden of Disease Study 2019. *The Lancet*, 396(10267):2006–2017, 2020.

[10] WHO Scientific Group. The Burden of Musculoskeletal at the Start if the New Millenium ii WHO Library Cataloguing-in-Publication Data. *World Health Organization*, 2003.

[11] Mike Reed Chairman, Editorial Board, Robin Brittain, Sebastian Dawson-bowling, Andy Goldberg, Andrew Toms, Elaine Young, Victoria Mccormack, and Mike Swanson. 18th Annual Report 2021. *NJR Uk*, (December 2020), 2021.

[12] John Charnley. Arthroplasty of the Hip: A New Operation. *Clinical Orthopaedics & Related Research*, (95):4–8, 1961.

[13] Ian D Learmonth, Claire Young, and Cecil Rorabeck. The operation of the century: total hip replacement. *Lancet*, 370(9597):1508–1519, 2007.

[14] NJR. Metal-on-metal hip implants - NJR Statement regarding metal-on metal implants.

[15] Robert L. Barrack. Modularity of Prosthetic Implants. *Journal of the American Academy of Orthopaedic Surgeons*, 2(1):16–25, 1994.

[16] Philippe Hernigou, Steffen Queinnec, and Charles Henri Flouzat Lachaniette. One hundred and fifty years of history of the Morse taper: From Stephen A. Morse in 1864 to complications related to modularity in hip arthroplasty. *International Orthopaedics*, 37(10):2081–2088, 2013.

[17] Francesco Traina, Marcello De Fine, Federico Biondi, Enrico Tassinari, Andrea Galvani, and Aldo Toni. The influence of the centre of rotation on implant survival using a modular stem hip prosthesis. *International Orthopaedics*, 33(6):1513–1518, 2009.

[18] William J Hozack, Joseph J Mesa, and Richard H Rothman. Head-neck modularity for total hip arthroplasty: Is it necessary? *Journal of Arthroplasty*, 11(4):397–399, 1996.

[19] Nitin Goyal, Henry Ho, Kevin B Fricka, and Charles A Engh. Do You Have to Remove a Corroded Femoral Stem? *The Journal of Arthroplasty*, 29(9):139–142, sep 2014.

[20] Goran Garellick, J Kärrholm, Cecilia Rogmark, Peter Herberts, and Ola Rolfson. *Swedish Hip Arthroplasty Register - Annual Report 2017*. 2017.

[21] H. Krishnan, S. P. Krishnan, G. Blunn, J. A. Skinner, and A. J. Hart. Modular neck femoral stems. *Bone and Joint Journal*, 95 B(8):1011–1021, 2013.

[22] Jeremy L Gilbert, Christine A Buckley, and Joshua J Jacobs. In vivo corrosion of modular hip prosthesis components in mixed and similar metal combinations. The effect of crevice, stress, motion, and alloy coupling. *Journal of Biomedical Materials Research*, 27(12):1533–1544, 1993.

[23] S. A. Brown, C. A. C. Flemming, J. S. Kawalec, H. E. Placko, C. Vassaux, K. Merritt, J. H. Payer, and M. J. Kraay. Fretting corrosion accelerates crevice corrosion of modular hip tapers. *Journal of Applied Biomaterials*, 6(1):19–26, 1995.

[24] H. John Cooper, Craig J. Della Valle, Richard A. Berger, Matthew Tetreault, Wayne G. Paprosky, Scott M. Sporer, and Joshua J. Jacobs. Corrosion at the head-neck taper as a cause for adverse local tissue reactions after total hip arthroplasty. *Journal of Bone and Joint Surgery - Series A*, 74-A(18):1655–1661, 2012.

[25] Deborah J. Hall, Robin Pourzal, Craig J. Della Valle, Jorge O. Galante, Joshua J. Jacobs, and Robert M. Urban. Corrosion of Modular Junctions in Femoral and Acetabular Components for Hip Arthroplasty and Its Local and Systemic Effects. In *Modularity and Tapers in Total Joint Replacement Devices*, pages 410–427. ASTM International, 100 Barr Harbor Drive, PO Box C700, West Conshohocken, PA 19428-2959, dec 2015.

[26] Jason M Jennings, Douglas A Dennis, and Charlie C Yang. Corrosion of the Head-neck Junction After Total Hip. *J Am Acad Orthop Surg*, 24(6):349–356, 2016.

[27] J U Lindgren, B H Brismar, A C Wikstrom, and Associate Professor. Adverse reaction to metal release from a modular metal-on-polyethylene hip prosthesis. *J Bone Joint Surg Br*, 9393(10):1427–30, 2011.

[28] Michael M. Morlock. The Taper Disaster - How Could it Happen? *HIP International*, 25(4):339–346, jul 2015.

[29] Pierre Emmanuel Ridon, Sophie Putman, Henri Migaud, Charles Berton, Gilles Pasquier, and Julien Girard. Long-term comparative study of large-diameter metal-on-metal bearings: Resurfacing versus total arthroplasty with large-diameter Durom™ bearing. *Orthopaedics and Traumatology: Surgery and Research*, 2019.

[30] Rohan M. Bhalekar, Simon L. Smith, and Thomas J. Joyce. Hip simulator testing of the taper-trunnion junction and bearing surfaces of contemporary metal-on-cross-linked-polyethylene hip prostheses. *Journal of Biomedical Materials Research - Part B Applied Biomaterials*, 108(1):156–166, 2020.

[31] Ashley K. Matthies, Radu Racasan, Paul Bills, Liam Blunt, Suzie Cro, Anna Panagiotidou, Gordon Blunn, John Skinner, and Alister J. Hart. Material loss at the taper junction of retrieved large head metal-on-metal total hip replacements. *Journal of Orthopaedic Research*, 31(11):1677–1685, nov 2013.

[32] R. P. Sidaginamale, T. J. Joyce, J. G. Bowsher, J. K. Lord, P. J. Avery, S. Natu, A. V.F. Nargol, and D. J. Langton. The clinical implications of metal debris release from the taper junctions and bearing surfaces of metal-on-metal hip arthroplasty. *Bone and Joint Journal*, 98B(7):925–933, 2016.

[33] Nargol A. Langton D, Sidaginamale R, Lord J, Joyce T, Natu S. Metal debris release from taper junctions appears to have a greater clinical impact than debris released from metal on metal bearing surfaces. *Orthop Procs*, 95-B:28–28, 2013.

[34] Laura Scholl, Gregg Schmidig, Ahmad Faizan, Kevor Tenhuisen, and Jim Nevelos. Evaluation of surgical impaction technique and how it affects locking strength of the head-stem taper junction. *Proceedings of the Institution of Mechanical Engineers, Part H: Journal of Engineering in Medicine*, 230(7):661–667, 2016.

[35] Jake P. Heiney, Suneel Battula, Gregory A. Vrabec, Anand Parikh, Rebecca Blice, Andrew J. Schoenfeld, and Glenn O. Njus. Impact magnitudes applied by surgeons and their importance when applying the femoral head onto the Morse taper for total hip arthroplasty. *Archives of Orthopaedic and Trauma Surgery*, 129(6):793–796, jun 2009.

[36] Toni Wendler, Robert Möbius, and Andreas Roth. Investigation of Assembly Forces During Creation of Head-Neck Taper Junction Following Total Hip Arthroplasty : A Biomechanical Study. *BMC Musculoskeletal Disorders*, pages 1–16, 2020.

[37] Robin Pourzal, Hannah J. Lundberg, Deborah J. Hall, and Joshua J. Jacobs. What Factors Drive Taper Corrosion? *Journal of Arthroplasty*, 33(9):2707–2711, 2018.

[38] Jeremy L. Gilbert, Sachin A. Mali, and Shiril Sivan. Corrosion of Modular Tapers in Total Joint Replacements: A Critical Assessment of Design, Materials, Surface Structure, Mechanics, Electrochemistry, and Biology. In *Modularity and Tapers in Total Joint Replacement Devices*, pages 192–223. ASTM International, 100 Barr Harbor Drive, PO Box C700, West Conshohocken, PA 19428-2959, dec 2015.

[39] D. Dowson, B. Seedhom, G. Johnson, and T English. *Introduction to the Biomechanics of Joints and Joint Replacements*. Mechanical Engineering Publications Ltd, London, 1 edition, 1981.

[40] By Timothy Mctighe. Design considerations for cementless total hip arthroplasty. *Journal of Joint Implant Surgery and Research Foundation*, pages 1–9, 1999.

[41] Damien P. Byrne, Kevin J. Mulhall, and Joseph F. Baker. Anatomy & Biomechanics of the Hip. *The Open Sports Medicine Journal*, 4(1):51–57, jan 2010.

[42] V Wright and D Dowson. Lubrication and cartilage. *Journal of anatomy*, 121(Pt 1):107–18, 1976.

[43] K.C. Geoffrey Ng, Jonathan R.T. Jeffers, and Paul E. Beaulé. Hip Joint Capsular Anatomy, Mechanics, and Surgical Management. *The Journal of Bone and Joint Surgery*, 101(23):2141–2151, dec 2019.

[44] Mark Grabowski and Charles C. Roseman. Complex and changing patterns of natural selection explain the evolution of the human hip. *Journal of Human Evolution*, 85:94–110, 2015.

[45] Christopher B. Ruff. Biomechanics of the hip and birth in early Homo. *American Journal of Physical Anthropology*, 98(4):527–574, 1995.

[46] Comprehensive Orthopaedics. Anatomy of a Joint, 2016.

[47] Alexander Y. Hui, William J. McCarty, Koichi Masuda, Gary S. Firestein, and Robert L. Sah. A systems biology approach to synovial joint lubrication in health, injury, and disease. *Wiley Interdisciplinary Reviews: Systems Biology and Medicine*, 4(1):15–37, jan 2012.

[48] S. Shanfield, P. Campbell, M. Baumgarten, R. Bloebaum, and A. Sarmiento. Synovial fluid osmolality in osteoarthritis and rheumatoid arthritis. *Clinical Orthopaedics and Related Research*, (235):289–295, 1988.

[49] Piotr Bełdowski, Maciej Przybyłek, Przemysław Raczyński, Andra Dedinaite, Krzysztof Górny, Florian Wieland, Zbigniew Dendzik, Alina Sionkowska, and Per M. Claesson. Albumin–hyaluronan interactions: Influence of ionic composition probed by molecular dynamics. *International Journal of Molecular Sciences*, 22(22):1–17, 2021.

[50] Norman A. Cummings and Gordon L. Nordby. Measurement of synovial fluid pH in normal and arthritic knees. *Arthritis & Rheumatism*, 9(1):47–56, 1966.

[51] Ingrid Milošev, Vesna Levašič, Janja Vidmar, Simon Kovač, and Rihard Trebše. pH and metal concentration of synovial fluid of osteoarthritic joints and joints with metal replacements. *Journal of Biomedical Materials Research - Part B Applied Biomaterials*, 105(8):2507–2515, 2017.

[52] Taryn E. Ludwig, Jenelle R. McAllister, Victor Lun, J. Preston Wiley, and Tannin A. Schmidt. Diminished cartilage-lubricating ability of human osteoarthritic synovial fluid deficient in proteoglycan 4: Restoration through proteoglycan 4 supplementation. *Arthritis and Rheumatism*, 64(12):3963–3971, 2012.

[53] A. P. Harsha and T. J. Joyce. Challenges associated with using bovine serum in wear testing orthopaedic biopolymers. *Proceedings of the Institution of Mechanical Engineers, Part H: Journal of Engineering in Medicine*, 225(10):948–958, 2011.

[54] Keith WJ Wright. Friction and wear of materials and joint replacement prostheses. *Biocompatibility of orthopedic implants*, 1:141–195, 1982.

[55] Tamer Mahmoud Tamer. Hyaluronan and synovial joint: Function, distribution and healing. *Interdisciplinary Toxicology*, 6(3):111–125, 2013.

[56] A.P. Briggs. A Study of the Inorganic Elements of Blood Plasma. *Journal of Biological Chemistry*, 57(2):351–357, 1923.

[57] Bansal VK. Serum Inorganic Phosphorus. In *Clinical Methods: The History, Physical, and Laboratory Examinations*, chapter 198. Butterworths, Boston, 3rd edition, 1990.

[58] J. Rodney Levick. Permeability of Rheumatoid and Normal Human Synovium to Specific Plasma Proteins. *Arthritis & Rheumatism*, 24(12):1550–1560, 1981.

[59] J. R. Levick and J. N. McDonald. Fluid movement across synovium in healthy joints: Role of synovial fluid macromolecules. *Annals of the Rheumatic Diseases*, 54(5):417–423, 1995.

[60] Dan Mazzucco, Richard Scott, and Myron Spector. Composition of joint fluid in patients undergoing total knee replacement and revision arthroplasty: Correlation with flow properties. *Biomaterials*, 25(18):4433–4445, 2004.

[61] Scott R. Brannan and David A. Jerrard. Synovial fluid analysis. *Journal of Emergency Medicine*, 30(3):331–339, 2006.

[62] K. A. Elsaid, B. C. Fleming, H. L. Oksendahl, J. T. Machan, P. D. Fadale, M. J. Hulstyn, R. Shalvoy, and G. D. Jay. Decreased lubricin concentrations and markers of joint inflammation in the synovial fluid of patients with anterior cruciate ligament injury. *Arthritis and Rheumatism*, 58(6):1707–1715, 2008.

[63] A. S. Greenwald and J. J. O'Connor. The transmission of load through the human hip joint. *Journal of Biomechanics*, 4(6):507–528, 1971.

[64] Wright V Dowson D, Unsworth A. The Frictional Behavior of Human Synovial Joints-Part I: Natural Joints. (July):369–376, 1975.

[65] J.P. Paul. Force actions transmitted by joints in the human body. *Society*, 192(1107):163–172, 1967.

[66] G Bergmann, G Bergmann, G Deuretzabacher, G Deuretzabacher, M Heller, M Heller, F Graichen, F Graichen, A Rohlmann, A Rohlmann, J Strauss, J Strauss, G N Duda, and G N Duda. Hip forces and gait patterns from rountine activities. *Journal of Biomechanics*, 34:859–871, 2001.

[67] David E. Lunn, Enrico De Pieri, Graham J. Chapman, Morten E. Lund, Anthony C. Redmond, and Stephen J. Ferguson. Current Preclinical Testing of New Hip Arthroplasty Technologies Does Not Reflect Real-World Loadings: Capturing Patient-Specific and Activity-Related Variation in Hip Contact Forces. *The Journal of Arthroplasty*, 35(3):877–885, mar 2020.

[68] Georg Bergmann, Alwina Bender, Jörn Dymke, Georg Duda, and Philipp Damm. Standardized loads acting in hip implants. *PLoS ONE*, 11(5):1–23, 2016.

[69] Adeel Aqil, Anatole Wiik, Michela Zanotto, Victoria Manning, Milad Masjedi, and Justin P. Cobb. The Effect of Hip Arthroplasty on Osteoarthritic Gait: A Blinded, Prospective and Controlled Gait Study at Fast Walking Speeds. *Journal of Arthroplasty*, 31(10):2337–2341, 2016.

[70] Junyan Li, Anthony C. Redmond, Zhongmin Jin, John Fisher, Martin H. Stone, and Todd D. Stewart. Hip contact forces in asymptomatic total hip replacement patients differ from normal healthy individuals: Implications for preclinical testing. *Clinical Biomechanics*, 29(7):747–751, 2014.

[71] A. UNSWORTH, D. DOWSON, V. WRIGHT, and D. KOSHAL. the Frictional Behaviour of Human Synovial Joints-Part Ii. Artificial Joints. *Trans. a.S.M.E. Series F, Journal of Lubrication Technology*, 97(3 (JULY, 1975)):377–382, 1975.

[72] NJR. 14th Annual Report National Joint Registry for England, Wales, Northern Ireland and the Isle of Man. *National Joint Registry*, 2017.

[73] NHS. Hip replacement, 2019.

[74] James L Howard and Brent L Lanting. Surgical approach in primary total hip arthroplasty: anatomy, technique and clinical outcomes. *Canadian Journal of Surgery*, 58:128–139, 2015.

[75] Stryker. ACCOLADE® II Femoral Hip Stem - Surgical Technique.

[76] Aaron J Tande and Robin Patel. Prosthetic Joint Infection Copyright © 2014, American Society for Microbiology. 27(2):302–345, 2014.

[77] Stephen Richard Knight, Randeep Aujla, and Satya Prasad Biswas. 100 Years of Operative History. *Orthopedic Reviews*, 3(16):72–74, 2011.

[78] G K MCKEE and J WATSON-FARRAR. REPLACEMENT OF ARTHRITIC BY THE McKEE-FARRAR PROSTHESIS HIPS. *The Bone & Joint Journal*, 48B(2):245–259, 1966.

[79] Mark N. Charles, Robert B. Bourne, J. Roderick Davey, A. Seth Greenwald, Bernard F. Morrey, and Cecil H. Rorabeck. Soft-Tissue Balancing of the Hip. *THE JOURNAL OF BONE & JOINT SURGERY*, 86-A(5):1078–1088, 2004.

[80] NJR. National Joint Registry 19th Annual Report. *NJR*, 2022.

[81] Johnson DePuy Synthes and Johnson Med Tech. CORAIL® Total Hip System.

[82] Stryker. Exeter® Cementing our place in history.

[83] Johnson DePuy Synthes and Johnson Med Tech. C-STEM™ AMT.

[84] Patrice Mertl and Massinissa Dehl. Femoral stem modularity. *Orthopaedics and Traumatology: Surgery and Research*, 106(1):S35–S42, 2020.

[85] Chan-Woo Park, Seung-Jae Lim, and Youn-Soo Park. Modular Stems: Advantages and Current Role in Primary Total Hip Arthroplasty. *Hip & Pelvis*, 30(3):147, 2018.

[86] John P Collier, Michael B Mayor, Ian R Williams, Victor A Surprenant, Helene P Surprenant, and Barbara H Currier. The Tradeoffs Associated With Modular Hip Prostheses. *CLINICAL ORTHOPAEDICS AND RELATED RESEARCH Number*, 311:91–101, 1995.

[87] Jonathan T. Evans, Jonathan P. Evans, Robert W. Walker, Ashley W. Blom, Michael R. Whitehouse, and Adrian Sayers. How long does a hip replacement last? A systematic review and meta-analysis of case series and national registry reports with more than 15 years of follow-up. *Lancet (London, England)*, 393(10172):647–654, 2019.

[88] Adam C. Marsh, Natalia Pajares Chamorro, and Xanthippi Chatzistavrou. Long-term performance and failure of orthopedic devices. In *Bone Repair Biomaterials*, pages 379–410. Elsevier, 2019.

[89] Mikael Sundfeldt, Lars V. Carlsson, Carina B. Johansson, Peter Thomsen, and Christina Gretzer. Aseptic loosening, not only a question of wear: A review of different theories. *Acta Orthopaedica*, 77(2):177–197, 2006.

[90] Yousef Abu-Amer, Isra Darwech, and John C. Clohisy. Aseptic loosening of total joint replacements: Mechanisms underlying osteolysis and potential therapies. *Arthritis Research and Therapy*, 9(SUPPL.1):1–7, 2007.

[91] Yunpeng Jiang, Tanghong Jia, Paul H. Wooley, and Shang You Yang. Current research in the pathogenesis of aseptic implant loosening associated with particulate wear debris. *Acta Orthopaedica Belgica*, 79(1):1–9, 2013.

[92] R. Dattani. Femoral osteolysis following total hip replacement. *Postgraduate Medical Journal*, 83(979):312–316, 2007.

[93] Brian P. Chalmers, Kevin I. Perry, Michael J. Taunton, Tad M. Mabry, and Matthew P. Abdel. Diagnosis of adverse local tissue reactions following metal-on-metal hip arthroplasty. *Current Reviews in Musculoskeletal Medicine*, 9(1):67–74, 2016.

[94] Wadih Y. Matar, S. Mehdi Jafari, Camilo Restrepo, Matthew Austin, James J. Purtill, and Javad Parvizi. Preventing infection in total joint arthroplasty. *Journal of Bone and Joint Surgery*, 92(SUPPL. 2):36–46, 2010.

[95] H B Waterson, M R Whitehouse, N V Greidanus, D S Garbuz, B A Masri, and C P Duncan. Revision for adverse local tissue reaction following metal-on-polyethylene total hip arthroplasty is associated with a high risk of early major complications. *The Bone & Joint Journal*, 100-B(6):720–724, jun 2018.

[96] M. Bryant, M. Ward, R. Farrar, R. Freeman, K. Brummitt, J. Nolan, and A. Neville. Characterisation of the surface topography, tomography and chemistry of fretting corrosion product found on retrieved polished femoral stems. *Journal of the Mechanical Behavior of Biomedical Materials*, 32:321–334, apr 2014.

[97] SCENIHR (Scientific Committee on Emerging and Newly Identified Health Risks). *Scientific opinion on the Safety of Poly Implant Prothèse (PIP) Silicone Breast Implants (2013 update)*. Number September. 2013.

[98] European Parliament and of the Council. Regulations (EU) 2017/745 on medical devices. *Official Journal of the European Union*, L 117:1–228, 2017.

[99] ECHA. Committee for Risk Assessment RAC Opinion proposing harmonised classification and labelling at EU level of Cobalt. *EU Scinetific Commettees*, (September), 2017.

[100] David Fitz, Christian Klemt, Wenhao Chen, Liang Xiong, Ingwon Yeo, and Young Min Kwon. Head-Neck Taper Corrosion in Metal-on-Polyethylene Total Hip Arthroplasty: Risk Factors, Clinical Evaluation, and Treatment of Adverse Local Tissue Reactions. *Journal of the American Academy of Orthopaedic Surgeons*, 28(22):907–913, 2020.

[101] M. R. Whitehouse, M. Endo, S. Zachara, T. O. Nielsen, N. V. Greidanus, B. A. Masri, D. S. Garbuz, and C. P. Duncan. Adverse local tissue reactions in metal-onpolyethylene total hip arthroplasty due to trunnion corrosion: The risk of misdiagnosis. *Bone and Joint Journal*, 97-B(8):1024–1030, 2015.

[102] Zhidao Xia, Benjamin F. Ricciardi, Zhao Liu, Christopher von Ruhland, Mike Ward, Alex Lord, Louise Hughes, Steven R. Goldring, Edward Purdue, David Murray, and Giorgio Perino. Nano-analyses of wear particles from metal-on-metal and non-metal-on-metal dual modular neck hip arthroplasty. *Nanomedicine: Nanotechnology, Biology, and Medicine*, 13(3):1205–1217, 2017.

[103] R. Chana, C. Esposito, P. A. Campbell, W. K. Walter, and W. L. Walter. Mixing and matching causing taper wear: Corrosion associated with pseudotumour formation. *The Bone & Joint Journal*, 94-B(2):281–286, 2012.

[104] Pepijn Bisseling, Timothy Tan, Zhen Lu, Pat A. Campbell, and Job L.C. Van Susante. The absence of a metal-on-metal bearing does not preclude the formation of a destructive pseudotumor in the hip - A case report. *Acta Orthopaedica*, 84(4):437–441, 2013.

[105] David M. Freccero, Kenneth J. McAlpine, and Eric L. Smith. Taper fretting corrosion with Stryker Anato stem after hip replacement. *Arthroplasty Today*, 6(2):210–213, 2020.

[106] NJR. National Joint Registry 20th Annual Report. *NJR*, 2023.

[107] ISO1947-1973. BS 4500 Limits and Fits: Part 5. Specification for system of cone tolerances for conical work pieces from C=1:3 to 1:500 and lengths from 6mm to 630mm, 1988.

[108] Oscar E Perrigo. *Modern American Lathe Practice*. The Norman W. Henley Publishing Co., New York, 1907.

[109] Fred H Colvin. *Turning and Boring Tapers*. Practical Papers. The Derry-Collard Company, New York, 1903.

[110] Ulrike Mueller, Steffen Braun, Stefan Schroeder, Robert Sonntag, and J. Philippe Kretzer. Same Same but Different? 12/14 Stem and Head Tapers in Total Hip Arthroplasty. *Journal of Arthroplasty*, 32:3191–3199, 2017.

[111] Robin Brittain, Elaine Young, Victoria Mccormack, and Mike Swanson. 16th Annual Report National Joint Registry for England, Wales, Northern Ireland and the Isle of Man. *NJR*, (December 2018), 2019.

[112] Stryker MedEd. Exeter-Using-Modular-Broach-Surgical-Technique.

[113] CeramTec. BIOLOX - First Class Material.

[114] Jean Pierre Vidalain. Twenty-year results of the cementless Corail stem. *International Orthopaedics*, 35(2):189–194, 2011.

[115] R.E. Smallman and A.H.W. Ngan. Case examination of biomaterials, sports materials and nanomaterials. *Physical Metallurgy and Advanced Materials Engineering*, pages 583–621, 2007.

[116] T. Hanawa. *Metals for Biomedical Devices - Part 1 General Introduction*. Duxford, United Kingdom : Woodhead Publishing, 2nd edition, 2005.

[117] Lorenzo Vaiani, Antonio Boccaccio, Antonio Emmanuele Uva, Gianfranco Palumbo, Antonio Piccininni, Pasquale Guglielmi, Stefania Cantore, Luigi Santacroce, Ioannis Alexandros Charitos, and Andrea Ballini. Ceramic Materials for Biomedical Applications: An Overview on Properties and Fabrication Processes. *Journal of Functional Biomaterials*, 14(3):146, mar 2023.

[118] R. O. Adams. A review of the stainless steel surface. *Journal of Vacuum Science & Technology A: Vacuum, Surfaces, and Films*, 1(1):12–18, 1983.

[119] ASTM Standards. ASTM F138-00 Standard Specification for Wrought 18 Chromium-14 Nickel-2.5 Molybdenum Stainless Steel Bar and Wire for Surgical Implants. *ASTM Standards*, 2017.

[120] Ke Yang and Yibin Ren. Nickel-free austenitic stainless steels for medical applications. *Science and Technology of Advanced Materials*, 11(1):014105, feb 2010.

[121] BSI Standards. Implants for surgery — Metallic materials Part 9: Wrought high nitrogen stainless steel. *ISO5832-9*, 2019.

[122] G. K. McKee. Total hip replacement - past, present and future. *Biomaterials*, 3(3):130–135, 1982.

[123] Philip Wiles. The surgery of the osteo-arthritic hip. *British Journal of Surgery*, 45(193):488–497, dec 2005.

[124] M. N. Smith-Petersen. THE CLASSIC: Evolution of Mould Arthroplasty of the Hip Joint. *Clinical Orthopaedics & Related Research*, 453(August):17–21, dec 2006.

[125] ASTM. ASTM F75-18 Standard Specification for Cobalt-28 Chromium-6 Molybdenum Alloy Castings and Casting Alloy for Surgical Implants (UNS R30075). *ASTM Standards*, Book of St:5 pages.

[126] BSI. BS EN ISO 5832-6:2022 Implants for surgery. Metallic materials. Wrought cobalt-nickel-chromium-molybdenum alloy. *BSI*, 2019.

[127] BSI. BS ISO 5832-4:2014 Implants for surgery. Metallic materials. Cobalt-chromium-molybdenum casting alloy. *BSI*, 2014.

[128] H G Willert, L G Brobäck, G H Buchhorn, P H Jensen, G Köster, I Lang, P Ochsner, and R Schenk. Crevice corrosion of cemented titanium alloy stems in total hip replacements. *Clinical orthopaedics and related research*, 333(333):51–75, dec 1996.

[129] BSI. BS EN ISO 5832-3:2021 Implants for surgery. Metallic materials. Wrought titanium 6-aluminium 4-vanadium alloy. *BSI*, 2021.

[130] Massimiliano Merola and Saverio Affatato. Materials for Hip Prostheses: A Review of Wear and Loading Considerations. *Materials*, 12(3):495, feb 2019.

[131] M. Hamadouche and L. Sedel. Ceramics in orthopaedics. *Journal of Bone and Joint Surgery - Series B*, 82(8):1095–1099, 2000.

[132] B. Weisse, Ch Affolter, G. P. Terrasi, G. Piskoty, and S. Köbel. Failure analysis of in vivo fractured ceramic femoral heads. *Engineering Failure Analysis*, 16(4):1188–1194, 2009.

[133] Toni Wendler, Torsten Prietzel, Robert Möbius, Jean Pierre Fischer, Andreas Roth, and Dirk Zajonz. Quantification of assembly forces during creation of head-neck taper junction considering soft tissue bearing: a biomechanical study. *Arthroplasty*, 3(1), 2021.

[134] ISO 7206-10:2003. Implants for surgery - Partial and total hip joint prostheses-Part 10: Determination of resistance to static load of modular femoral heads. *International Standard Organization*, ISO 7206-1, 2003.

[135] Nicholas Bishop, Florian Witt, Robin Pourzal, Alfons Fischer, Marcel Rütschi, Markus Michel, and Michael Morlock. Wear patterns of taper connections in retrieved large diameter metal-on-metal bearings. *Journal of Orthopaedic Research*, 31(7):1116–1122, jul 2013.

[136] Finn E. Donaldson, James C. Coburn, and Karen Lohmann Siegel. Total hip arthroplasty head-neck contact mechanics: A stochastic investigation of key parameters. *Journal of Biomechanics*, 47:1634–16–41, 2014.

[137] Thom Bitter, Imran Khan, Tim Marriott, Elaine Lovelady, Nico Verdonschot, and Dennis Janssen. A combined experimental and finite element approach to analyse the fretting mechanism of the head – stem taper junction in total hip replacement. 231(9):862–870, 2017.

[138] J. A. Gustafson, R. Pourzal, B. R. Levine, J. J. Jacobs, and H. J. Lundberg. Modelling changes in modular taper micromechanics due to surgeon assembly technique in total hip arthroplasty. *Bone and Joint Journal*, 102(7):33–40, 2020.

[139] Halimat Y. Raji and Julia C. Shelton. Prediction of taper performance using quasi static FE models: The influence of loading, taper clearance and trunnion length. *Journal of Biomedical Materials Research - Part B Applied Biomaterials*, 107(1):138–148, 2019.

[140] Jonathan A. Gustafson, Steven P. Mell, Brett R. Levine, Robin Pourzal, and Hannah J. Lundberg. Interaction of surface topography and taper mismatch on head-stem modular junction contact mechanics during assembly in modern total hip replacement. *Journal of Orthopaedic Research*, 41(2):418–425, 2023.

[141] Thom Bitter, Imran Khan, Tim Marriott, Elaine Lovelady, Nico Verdonschot, and Dennis Janssen. The effects of manufacturing tolerances and assembly force on the volumetric wear at the taper junction in modular total hip arthroplasty. *Computer Methods in Biomechanics and Biomedical Engineering*, 22(13):1061–1072, 2019.

[142] Olof Vingsbo and Staffan Söderberg. On fretting maps. *Wear*, 126(2):131–147, sep 1988.

[143] Z.R. Zhou, K. Nakazawa, M.H. Zhu, N. Maruyama, Ph Kapsa, and L. Vincent. Progress in fretting maps. *Tribology International*, 39(10):1068–1073, oct 2006.

[144] R.D. Mindlin and H. Deresiewicz. Elastic spheres in contact under varying oblique forces. *ASME Tram J. Appl. Mech.*, 20:327–344, 1953.

[145] Batchelor Andrew W Stachowiak Gwidon W. 10.4 Friction and Wear, 2014.

[146] D Tabor and J. S. McFarlane. Relation between friction and adhesion. *F.R.S*, 202(1069):244–253, 1950.

[147] F. P. BOWDEN and J. E. YOUNG. The adhesion of clean metals. *Proceedings of the Royal Society of London. Series A. Mathematical and Physical Sciences*, 233(1195):429–442, 1956.

[148] J T Terwey, S Berninger, G Burghardt, G Jacobs, and G Poll. Numerical Calculation of Local Adhesive Wear in Machine Elements Under Boundary Lubrication Considering the Surface Roughness. In *Fracture, Fatigue and Wear*, pages 796–807. Springer, 2018.

[149] Donald H. Buckley and Kazuhisa Miyoshi. Friction and wear of ceramics. *Wear*, 100(1-3):333–353, 1984.

[150] E. Rabinowicz, L. A. Dunn, and P. G. Russell. A study of abrasive wear under three-body conditions. *Wear*, 4(5):345–355, 1961.

[151] Renato Altobelli, Mara Cristina, and Lopes De Oliveira. Acta Biomaterialia Corrosion fatigue of biomedical metallic alloys : Mechanisms and mitigation. *Acta Biomaterialia journal*, 8:937–962, 2011.

[152] Danieli C. Rodrigues, Robert M. Urban, Joshua J. Jacobs, and Jeremy L. Gilbert. In vivo severe corrosion and hydrogen embrittlement of retrieved modular body titanium alloy hip-implants. *Journal of Biomedical Materials Research - Part B Applied Biomaterials*, 88(1):206–219, 2009.

[153] Volkan Cicek. 1. Corrosion of Materials, 2014.

[154] Ahmad Zaki. *Principles of corrosion engineering and corrosion control*. Elsevier/BH, Boston, MA, first edit edition, 2006.

[155] William Stephen Tait. *An Introduction to Electrochemical Corrosion Testing for Practicing Engineers and Scientists*. PairODocs Publications, 1994.

[156] A. R. Beadling. Biotribocorrosion of Hard-on-Hard Bearing Surfaces in Orthopaedic Hip Replacements. *PhD Thesis University of Leeds*, 2016.

[157] IRENA GOTMAN. Characteristics of Metals Used in Implants. *Journal of Endourology*, 11(6):383–389, 1997.

[158] G. S. Frankel. Pitting Corrosion of Metals. *Journal of The Electrochemical Society*, 145(6):2186, 1998.

[159] P Marcus, V Maurice, and H H Strehblow. Localized corrosion (pitting): A model of passivity breakdown including the role of the oxide layer nanostructure. *Corrosion Science*, 50(9):2698–2704, 2008.

[160] J.W. Oldfield and W.H. Sutton. Crevice Corrosion of Stainless Steels I. A Mathematical Model. *Corrosion*, 13(1):13 – 22, 1978.

[161] R B Waterhouse. Fretting Corrosion. *Proceedings of the Institution of Mechanical Engineers*, 169(1):1157–1172, jun 1955.

[162] Jeremy L. Gilbert, Sachin Mali, Robert M. Urban, Craig D. Silverton, and Joshua J. Jacobs. In vivo oxide-induced stress corrosion cracking of Ti-6Al-4V in a neck-stem modular taper: Emergent behavior in a new mechanism of in vivo corrosion. *Journal of Biomedical Materials Research - Part B Applied Biomaterials*, 100 B(2):584–594, 2012.

[163] Robert K. Whittaker, Harry S. Hothi, Antti Eskelinen, Gordon W. Blunn, John A. Skinner, and Alister J. Hart. Variation in taper surface roughness for a single design effects the wear rate in total hip arthroplasty. *Journal of Orthopaedic Research*, 35:1784–1792, 2017.

[164] Timothy M. Brock, Raghavendra Sidaginamale, Steven Rushton, Antoni V. F. Nargol, John G. Bowsher, Christina Savisaar, Tom J. Joyce, David J. Deehan, James K. Lord, and David J. Langton. Shorter, rough trunnion surfaces are associated with higher taper wear rates than longer, smooth trunnion surfaces in a contemporary large head metal-on-metal total hip arthroplasty system. *Journal of Orthopaedic Research*, 33(12):1868–1874, dec 2015.

[165] Michael M. Morlock, Emilie C. Dickinson, Klaus Peter Günther, Dennis Bünte, and Valerie Polster. Head Taper Corrosion Causing Head Bottoming Out and Consecutive Gross Stem Taper Failure in Total Hip Arthroplasty. *Journal of Arthroplasty*, 33(11):3581–3590, 2018.

[166] Harry S. Hothi, Ashley K. Matthies, Reshid Berber, Robert K. Whittaker, John A. Skinner, and Alister J. Hart. The Reliability of a Scoring System for Corrosion and Fretting, and Its Relationship to Material Loss of Tapered, Modular Junctions of Retrieved Hip Implants. *The Journal of Arthroplasty*, 29(6):1313–1317, jun 2014.

[167] C. P. McCarty, M. A. Nazif, S. N. Sangiorgio, E. Ebramzadeh, and S. H. Park. Can severity of trunnion damage be estimated by visual inspection alone? INTRODUCTION OF AN ENHANCED VISUAL GRADING SYSTEM AND VALIDATION USING METROLOGY. *Bone and Joint Research*, 12(3):155–164, 2023.

[168] D. J. Langton, R. Sidaginamale, J. K. Lord, A. V. F. Nargol, and T. J. Joyce. Taper junction failure in large-diameter metal-on-metal bearings. *Bone & Joint Research*, 1(4):56–63, apr 2012.

[169] Christopher Del Balso, Matthew G Teeter, Sok Chuen Tan, James L Howard, and Brent A Lanting. Trunnionosis: Does Head Size Affect Fretting and Corrosion in Total Hip Arthroplasty? *The Journal of Arthroplasty*, 31(10):2332–2336, oct 2016.

[170] Christina Arnholt, Richard Underwood, Daniel W. MacDonald, Genymphas B. Higgs, Antonia F. Chen, Gregg Klein, Brian Hamlin, Gwo-Chin Lee, Michael Mont, Harold Cates, Arthur Malkani, Matthew Kraay, Clare Rimnac, and Steven M. Kurtz. Microgrooved Surface Topography Does Not Influence Fretting Corrosion of Tapers in Total Hip Arthroplasty: Classification and Retrieval Analysis. In *Modularity and Tapers in Total Joint Replacement Devices*, pages 99–112. ASTM International, 100 Barr Harbor Drive, PO Box C700, West Conshohocken, PA 19428-2959, dec 2015.

[171] Genymphas B. Higgs, Josa A. Hanzlik, Daniel W. MacDonald, Jeremy L. Gilbert, Clare M. Rimnac, and Steven M. Kurtz. Is Increased Modularity Associated With Increased Fretting and Corrosion Damage in Metal-On-Metal Total Hip Arthroplasty Devices? *The Journal of Arthroplasty*, 28(8):2–6, sep 2013.

[172] Genymphas B. Higgs, Daniel W. MacDonald, Jeremy L. Gilbert, Clare M. Rimnac, Steven M. Kurtz, Antonia F. Chen, Gregg R. Klein, Brian R. Hamlin, Gwo Chin Lee, Michael A. Mont, Harold E. Cates, Arthur L. Malkani, and Matthew J. Kraay. Does Taper Size Have an Effect on Taper Damage in Retrieved Metal-on-Polyethylene Total Hip Devices? *Journal of Arthroplasty*, 31(9):277–281, 2016.

[173] C. Del Balso, M. G. Teeter, S. C. Tan, B. A. Lanting, and J. L. Howard. Taper-erosis - DOES HEAD LENGTH AFFECT FRETTING AND CORROSION IN TOTAL HIP ARTHROPLASTY? *The Bone & Joint Journal*, 97-B(7):911–916, jul 2015.

[174] Nader A. Nassif, Danyal H. Nawabi, Kirsten Stoner, Marcella Elpers, Timothy Wright, and Douglas E. Padgett. Taper Design Affects Failure of Large-head Metal-on-metal Total Hip Replacements. *Clinical Orthopaedics and Related Research®*, 472(2):564–571, feb 2014.

[175] Richard M.R. Dyrkacz, Jan M. Brandt, Olanrewaju A. Ojo, Thomas R. Turgeon, and Urs P. Wyss. The influence of head size on corrosion and fretting behaviour at the head-neck interface of artificial hip joints. *Journal of Arthroplasty*, 28(6):1036–1040, 2013.

[176] Nicholas E Bishop, Arne Hothan, and Michael M Morlock. High friction moments in large hard-on-hard hip replacement bearings in conditions of poor lubrication. *Journal of Orthopaedic Research*, 31(5):807–813, 2013.

[177] Ying Ying J. Kao, Chelsea N. Koch, Timothy M. Wright, and Douglas E. Padgett. Flexural Rigidity, Taper Angle, and Contact Length Affect Fretting of the Femoral Stem Trunnion in Total Hip Arthroplasty. *Journal of Arthroplasty*, 31(9):254–258, 2016.

[178] Zein El-Zein, Corinn K. Gehrke, J. Sawyer Croley, Matthew P. Siljander, Murphy A. Mallow, Michael A. Flierl, James J. Verner, and Erin A. Baker. Assessing Taper Geometry, Head Size, Head Material, and Their Interactions in Taper Fretting Corrosion of Retrieved Total Hip Arthroplasty Implants. *The Journal of Arthroplasty*, 2021.

[179] Thomas M. Grupp, Thomas Weik, Wilhelm Bloemer, and Hanns-Peter Knaebel. Modular titanium alloy neck adapter failures in hip replacement - failure mode analysis and influence of implant material. *BMC Musculoskeletal Disorders*, 11(1):3, dec 2010.

[180] BSI Standards. Implants for surgery – Metallic materials Implants for surgery – Metallic materials Part 6: Wrought cobalt-nickel-chromium-molybdenum alloy (ISO. *ISO5832-6*, 2019.

[181] BSI. BS EN ISO 5832-3:2012 Implants for surgery. Metallic materials. Wrought titanium 6-aluminium 4-vanadium. 2012.

[182] Steven M. Kurtz, Sevi B. Kocagöz, Josa A. Hanzlik, Richard J. Underwood, Jeremy L. Gilbert, Daniel W. MacDonald, Gwo Chin Lee, Michael A. Mont, Matthew J. Kraay, Gregg R. Klein, Javad Parvizi, and Clare M. Rimnac. Do ceramic femoral heads reduce taper fretting corrosion in hip arthroplasty? A retrieval study. *Clinical Orthopaedics and Related Research*, 2013.

[183] Sok Chuen Tan, Adrian C.K. Lau, Christopher Del Balso, James L. Howard, Brent A. Lanting, and Matthew G. Teeter. Tribocorrosion: Ceramic and Oxidized Zirconium vs Cobalt-Chromium Heads in Total Hip Arthroplasty. *The Journal of Arthroplasty*, 31(9):2064–2071, sep 2016.

[184] Selin Munir, William L. Walter, and William Robert Walsh. Variations in the trunnion surface topography between different commercially available

hip replacement stems. *Journal of Orthopaedic Research*, 33(1):98–105, jan 2015.

[185] Anna Panagiotidou, Timothy Cobb, Jay Meswania, John Skinner, Alister Hart, Fares Haddad, and Gordon Blunn. Effect of impact assembly on the interface deformation and fretting corrosion of modular hip tapers: An in vitro study. *Journal of Orthopaedic Research*, 36(1):405–416, jun 2017.

[186] Harry S. Hothi, Antti P. Eskelinen, Reshid Berber, Olli S. Lainiala, Teemu P.S. Moilanen, John A. Skinner, and Alister J. Hart. Factors Associated With Trunnionosis in the Metal-on-Metal Pinnacle Hip. *The Journal of Arthroplasty*, 32(1):286–290, jan 2017.

[187] Harry S. Hothi, Robert K. Whittaker, Jay M. Meswania, Gordon W. Blunn, John A. Skinner, and Alister J. Hart. Influence of stem type on material loss at the metal-on-metal pinnacle taper junction. *Proceedings of the Institution of Mechanical Engineers, Part H: Journal of Engineering in Medicine*, 229(1):91–97, jan 2015.

[188] Christina M. Arnholt, Daniel W. MacDonald, Richard J. Underwood, Eric P. Guyer, Clare M. Rimnac, Steven M. Kurtz, Michael A. Mont, Gregg R. Klein, Gwo-Chin Lee, Antonia F. Chen, Brian R. Hamlin, Harold E. Cates, Arthur L. Malkani, and Matthew J. Kraay. Do Stem Taper Microgrooves Influence Taper Corrosion in Total Hip Arthroplasty? A Matched Cohort Retrieval Study. *The Journal of Arthroplasty*, 32(4):1363–1373, apr 2017.

[189] A. M. Kop, C. Keogh, and E. Swarts. Proximal Component Modularity in THA—At What Cost?: An Implant Retrieval Study. *Clinical Orthopaedics & Related Research*, 470(7):1885–1894, jul 2012.

[190] Sevi B. Kocagöz, Richard J. Underwood, Shiril Sivan, Jeremy L. Gilbert, Daniel W. MacDonald, Judd S. Day, and Steven M. Kurtz. Does taper angle clearance influence fretting and corrosion damage at the head-stem interface? A matched cohort retrieval study. *Seminars in Arthroplasty*, 24(4):246–254, 2013.

[191] Therese Bormann, Ulrike Müller, Jens Gibmeier, Phuong Thao Mai, Tobias Renkawitz, and Jan Philippe Kretzer. Insights into Imprinting: How Is the Phenomenon of Tribocorrosion at Head-Neck Taper Interfaces Related to Corrosion, Fretting, and Implant Design Parameters? *Clinical Orthopaedics & Related Research*, Publish Ah:1–16, 2022.

[192] Masafumi Morita, Tadashi Sasada, Hitoshi Hayashi, and Yukio Tsukamoto. The corrosion fatigue properties of surgical implants in a living body. 22:529–540, 1988.

[193] Yangping Liu and Jeremy L. Gilbert. The effect of simulated inflammatory conditions and pH on fretting corrosion of CoCrMo alloy surfaces. *Wear*, 390-391(May):302–311, 2017.

[194] Anna Di Laura, Harry S. Hothi, Jay M. Meswania, Robert K. Whittaker, Danielle de Villiers, Jozef Zustin, Gordon W. Blunn, John A. Skinner, and Alister J. Hart. Clinical relevance of corrosion patterns attributed to inflammatory cell-induced corrosion: A retrieval study. *Journal of Biomedical Materials Research - Part B Applied Biomaterials*, 105(1):155–164, 2017.

[195] Anne Neville, James Hesketh, Andrew R. Beadling, Michael G. Bryant, and Duncan Dowson. Incorporating corrosion measurement in hip wear simulators: An added complication or a necessity? *Proceedings of the Institution of Mechanical Engineers, Part H: Journal of Engineering in Medicine*, 230(5):406–420, 2016.

[196] ASTM F1875. ASTM F1875: Standard Practice for Fretting Corrosion Testing of Modular Implant Interfaces : Hip Femoral Head-Bore and Cone Taper Interface. *ASTM Standards*, 98(Reapproved 2009):1–6, 2009.

[197] J. Philippe Kretzer, Eike Jakubowitz, Michael Krachler, Marc Thomsen, and Christian Heisel. Metal release and corrosion effects of modular neck total hip arthroplasty. *International Orthopaedics*, 33(6):1531–1536, 2009.

[198] Aleksandra Kocijan, Ingrid Milošev, and Boris Pihlar. Cobalt-based alloys for orthopaedic applications studied by electrochemical and XPS analysis. *Journal of Materials Science: Materials in Medicine*, 15(6):643–650, 2004.

[199] G T Burstein and P C Pistorius. Surface-Roughness and the Metastable Pitting of Stainless-Steel in Chloride Solutions. *Corrosion*, 51(5):380–385, 1995.

[200] Tiziano Bellezze, Giampaolo Giuliani, and Gabriella Roventi. Study of stainless steels corrosion in a strong acid mixture. Part 1: cyclic potentiodynamic polarization curves examined by means of an analytical method. *Corrosion Science*, 130(June 2017):113–125, 2018.

[201] M A Wimmer, C Sprecher, R Hauert, G Täger, and A Fischer. Tribochemical reaction on metal-on-metal hip joint bearings A comparison between in-vitro and in-vivo results. *Wear*, 255:1007–1014, 2003.

[202] A Igual Muñoz, S Mischler J Electrochem, C Soc, A Igual Muñoz, and S Mischler. Interactive Effects of Albumin and Phosphate Ions on the Corrosion of CoCrMo Implant Alloy Interactive Effects of Albumin and Phosphate Ions on the Corrosion of CoCrMo Implant Alloy. *Journal of The Electrochemical Society*, 154(10):C562–C570, 2007.

[203] Shima Karimi, Tirdad Nickchi, and Akram Alfantazi. Effects of bovine serum albumin on the corrosion behaviour of AISI 316L, Co-28Cr-6Mo, and Ti-6Al-4V alloys in phosphate buffered saline solutions. *Corrosion Science*, 53(10):3262–3272, 2011.

[204] A. Wang, A. Essner, and G. Schmidig. The Effects of Lubricant Composition on in Vitro Wear Testing of Polymeric Acetabular Components. *Journal of Biomedical Materials Research - Part B Applied Biomaterials*, 68(1):45–52, 2004.

[205] G D Jay, D E Britt, and C J Cha. Lubricin is a product of megakaryocyte stimulating factor gene expression by human synovial fibroblasts. *The Journal of rheumatology*, 27(3):594–600, mar 2000.

[206] A. Igual Munoz, J. Schwiesau, B. M. Jolles, and S. Mischler. In vivo electrochemical corrosion study of a CoCrMo biomedical alloy in human synovial fluids. *Acta Biomaterialia*, 21:228–236, 2015.

[207] Margareth R.C. Marques, Raimar Loebenberg, and May Almukainzi. Simulated biological fluids with possible application in dissolution testing. *Dissolution Technologies*, 18(3):15–28, 2011.

[208] Barbara Matteoli. *Biomedical Tissue Culture*. InTech, oct 2012.

[209] I. V. Branzoi, M. Iordoc, F. Branzoi, R. Vasilescu-Mirea, and G. Sbarcea. Influence of diamond-like carbon coating on the corrosion resistance of the NITINOL shape memory alloy. *Surface and Interface Analysis*, 42(6-7):502–509, 2010.

[210] Sigmaaldrich. Fetal Bovine Serum (FBS) – What You Need to Know, 2023.

[211] Sachin A. Mali and Jeremy L. Gilbert. Correlating Fretting Corrosion and Micromotions in Modular Tapers: Test Method Development and Assessment. In *Modularity and Tapers in Total Joint Replacement Devices*, pages 259–282. ASTM International, 100 Barr Harbor Drive, PO Box C700, West Conshohocken, PA 19428-2959, dec 2015.

[212] Henning Haschke, Sabrina Y. Jauch-Matt, Kay Sellenschloh, Gerd Huber, and Michael M. Morlock. Assembly force and taper angle difference influence the relative motion at the stem-neck interface of bi-modular hip prostheses. *Proceedings of the Institution of Mechanical Engineers, Part H: Journal of Engineering in Medicine*, 230(7):690–699, 2016.

[213] Henning Haschke, Tobias Konow, Gerd Huber, and Michael M. Morlock. Influence of flexural rigidity on micromotion at the head-stem taper interface of modular hip prostheses. *Medical Engineering & Physics*, 68(xxxx):1–10, jun 2019.

[214] S.Y. Jauch, G. Huber, E. Hoenig, M. Baxmann, T.M. Grupp, and M.M. Morlock. Influence of material coupling and assembly condition on the magnitude of micromotion at the stem–neck interface of a modular hip endoprosthesis. *Journal of Biomechanics*, 44(9):1747–1751, jun 2011.

[215] Adrian Falkenberg, Sara Biller, Michael M. Morlock, and Gerd Huber. Micromotion at the head-stem taper junction of total hip prostheses is influenced by prosthesis design-, patient- and surgeon-related factors. *Journal of Biomechanics*, 98:109424, 2020.

[216] P. L. Reu and T. J. Miller. The application of high-speed digital image correlation. *Journal of Strain Analysis for Engineering Design*, 43(8):673–688, 2008.

[217] Matthew L. Mroczkowski, Justin S. Hertzler, Steven M. Humphrey, Todd Johnson, and Cheryl R. Blanchard. Effect of impact assembly on the fretting corrosion of modular hip tapers. *Journal of Orthopaedic Research*, 24:271–279, 2006.

[218] David Pierre, Viswanathan Swaminathan, Laura Y. Scholl, Kevor TenHuisen, and Jeremy L. Gilbert. Effects of Seating Load Magnitude on Incremental Cyclic Fretting Corrosion in 5°40' Mixed Alloy Modular Taper Junctions. *Journal of Arthroplasty*, 33(6):1953–1961, 2018.

[219] Hani Haider, Joel N. Weisenburger, and Kevin L. Garvin. Simultaneous measurement of friction and wear in hip simulators. *Proceedings of the Institution of Mechanical Engineers, Part H: Journal of Engineering in Medicine*, 230(5):373–388, 2016.

[220] David E. Lunn, Enrico De Pieri, Graham J. Chapman, Morten E. Lund, Anthony C. Redmond, and Stephen J. Ferguson. Current Preclinical Testing of New Hip Arthroplasty Technologies Does Not Reflect Real-World Loadings: Capturing Patient-Specific and Activity-Related Variation in Hip Contact Forces. *Journal of Arthroplasty*, 35(3):877–885, 2020.

[221] A. Panagiotidou, J. Meswania, K. Osman, B. Bolland, J. Latham, J. Skinner, F. S. Haddad, A. Hart, and G. Blunn. The effect of frictional torque and bending moment on corrosion at the taper interface: An in vitro study. *Bone and Joint Journal*, 97-B(4):463–472, 2015.

[222] Eric S. Ouellette, Sachin A. Mali, Jua Kim, Justin Grostefon, and Jeremy L. Gilbert. Design, Material, and Seating Load Effects on In Vitro Fretting Corrosion Performance of Modular Head-Neck Tapers. *Journal of Arthroplasty*, 34(5):991–1002, 2019.

[223] Nadim James Hallab, Carlo Messina, Anastasia Skipor, and Joshua J. Jacobs. Differences in the fretting corrosion of metal–metal and ceramic–metal modular junctions of total hip replacements. *Journal of Orthopaedic Research*, 22(2):250–259, mar 2004.

[224] Fiachra E. Rowan, Amanda Wach, Timothy M. Wright, and Douglas E. Padgett. The onset of fretting at the head-stem connection in hip arthroplasty is affected by head material and trunnion design under simulated corrosion conditions. *Journal of Orthopaedic Research®*, 36(6):1630–1636, jun 2018.

[225] Jeremy L. Gilbert, Manav Mehta, and Bryan Pinder. Fretting crevice corrosion of stainless steel stem-CoCr femoral head connections: Comparisons of materials, initial moisture, and offset length. *Journal of Biomedical Materials Research - Part B Applied Biomaterials*, 88(1):162–173, 2009.

[226] Anna Panagiotidou, Jay Meswania, Jia Hua, Sarah Muirhead-Allwood, Alister Hart, and Gordon Blunn. Enhanced wear and corrosion in modular tapers in total hip replacement is associated with the contact area and surface topography. *Journal of Orthopaedic Research*, 31(12):2032–2039, dec 2013.

[227] Khosro Fallahnezhad, Reza H. Oskouei, Hojjat Badnava, and Mark Taylor. An adaptive finite element simulation of fretting wear damage at the head-neck taper junction of total hip replacement: The role of taper angle mismatch. *Journal of the Mechanical Behavior of Biomedical Materials*, 75(January):58–67, 2017.

[228] Eric S. Ouellette, Aarti A. Shenoy, and Jeremy L. Gilbert. The seating mechanics of head-neck modular tapers in vitro: Load-displacement measurements, moisture, and rate effects. *Journal of Orthopaedic Research*, 36(4):1164–1172, 2018.

[229] S. Y. Jauch-Matt, A. W. Miles, and H. S. Gill. Effect of trunnion roughness and length on the modular taper junction strength under typical intraoperative assembly forces. *Medical Engineering and Physics*, 39:94–101, 2017.

[230] Annelie Rehmer, Nicholas E. Bishop, and Michael M. Morlock. Influence of assembly procedure and material combination on the strength of the taper connection at the head-neck junction of modular hip endoprostheses. *Clinical Biomechanics*, 27(1):77–83, 2012.

[231] Jonathan R. Danoff, Jason Longaray, Raga Rajaravivarma, Ananthkrishnan Gopalakrishnan, Antonia F. Chen, and William J. Hozack. Impaction Force Influences Taper-Trunnion Stability in Total Hip Arthroplasty. *Journal of Arthroplasty*, 33(7):S270–S274, 2018.

[232] Florian Witt, Julian Gührs, Michael M. Morlock, and Nicholas E. Bishop. Quantification of the contact area at the head-stem taper interface of modular hip prostheses. *PLoS ONE*, 10(8):1–15, 2015.

[233] Ulrike Mueller, Therese Bormann, Stefan Schroeder, and J. Philippe Kretzer. Taper junctions in modular hip joint replacements: What affects their stability? *Journal of the Mechanical Behavior of Biomedical Materials*, 116(November 2020):104258, 2021.

[234] Viswanathan Swaminathan and Jeremy L. Gilbert. Fretting corrosion of CoCrMo and Ti6Al4V interfaces. *Biomaterials*, 33(22):5487–5503, 2012.

[235] J Archard. Elastic deformation and the laws of friction. *T. E. Allibone*, (1):190–205, 1957.

[236] Z R Zhou and L Vincent. Mixed fretting regime. *Wear*, 181-183(PART 2):531–536, mar 1995.

[237] S. W. Watson, F. J. Friedersdorf, B. W. Madsen, and S. D. Cramer. Methods of measuring wear-corrosion synergism. *Wear*, 181-183(PART 2):476–484, 1995.

[238] Michael Bryant and Anne Neville. Fretting corrosion of CoCr alloy: Effect of load and displacement on the degradation mechanisms. *Proceedings of the Institution of Mechanical Engineers, Part H: Journal of Engineering in Medicine*, 231(2):114–126, feb 2017.

[239] Harry S. Hothi, Reshid Berber, Robert K. Whittaker, Gordon W. Blunn, John A. Skinner, and Alister J. Hart. The Relationship Between Cobalt/Chromium Ratios and the High Prevalence of Head-Stem Junction Corrosion in Metal-on-Metal Total Hip Arthroplasty. *Journal of Arthroplasty*, 31(5):1123–1127, 2016.

[240] Jeremy L. Gilbert and Dongkai Zhu. A metallic biomaterial tribocorrosion model linking fretting mechanics, currents, and potentials: Model development and experimental comparison. *Journal of Biomedical Materials Research - Part B Applied Biomaterials*, 108(8):3174–3189, 2020.

[241] Sachin A. Mali, Dongkai Zhu, Yangping Liu, and Jeremy L. Gilbert. Fretting crevice corrosion of 316 L stainless steel in physiological phosphate buffered saline: Load, potential and alloy counterface effects. *Tribology International*, 164(July):107198, 2021.

[242] J Goldberg. The electrochemical and mechanical behavior of passivated and TiN/AlN-coated CoCrMo and Ti6Al4V alloys. *Biomaterials*, 25(5):851–864, feb 2004.

[243] F P Bowden and D Tabor. Mechanism of metallic friction. *Nature*, 150(3798):197–199, 1942.

[244] Frank Philip Bowden Tabor. The area of contact between stationary and between moving surfaces. *Royal Society*, 169(938):391–412, 1938.

[245] Stephanie Smith and Jeremy L. Gilbert. Compliant interfaces and fretting corrosion in modular taper junctions: The micromechanics of contact. *Transactions of the Annual Meeting of the Society for Biomaterials and the Annual International Biomaterials Symposium*, 40(February):9, 2019.

[246] Z R Zhou, S Fayeulle, and L Vincent. Cracking behaviour fretting wear of various aluminium alloys during. *Wear*, 155:317–330, 1992.

[247] Stephanie M. Smith and Jeremy L. Gilbert. Interfacial compliance, energy dissipation, frequency effects, and long-term fretting corrosion performance of Ti-6Al-4V/CoCrMo interfaces. *Journal of Biomedical Materials Research - Part A*, 110(2):409–423, 2022.

[248] Dmitry Royhman, Robin Pourzal, Deborah Hall, Hannah J. Lundberg, Markus A. Wimmer, Joshua Jacobs, Nadim J. Hallab, and Mathew T. Mathew. Fretting-corrosion in hip taper modular junctions: The influence of topography and pH levels – An in-vitro study. *Journal of the Mechanical Behavior of Biomedical Materials*, 118(November 2019):104443, 2021.

[249] Colin Y L Woon, Amanda Wach, Timothy M Wright, and Douglas E Padgett. Taper Design, Head Material, and Manufacturer Affect the Onset of Fretting Under Simulated Corrosion Conditions. *The Journal of Arthroplasty*, nov 2019.

[250] Y. Stefani B. Cales. Risks and advantages in standardization of bores and cones for heads in modular hip prostheses. *Journal of Biomedical Materials Research*, 43(1):62–68, 1998.

[251] J K Lord, D J Langton, A V F Nargol, and T J Joyce. Volumetric wear assessment of failed metal-on-metal hip resurfacing prostheses. 272:79–87, 2011.

[252] S Hussenbocus, D Kosuge, L B Solomon, D W Howie, and R H Oskouei. Head-Neck Taper Corrosion in Hip Arthroplasty. *BioMed Research International*, 2015:1–9, 2015.

[253] BSI. ISO 14242-2 Implants for surgery - Wear of total hip joint prostheses - Part 2 : Methods of measurement. *BSI*, 14242(2), 2000.

[254] ISO 4288. Geometric Product Specification (GPS) — Surface texture — Profile method : Rules and procedures for the assessment of surface texture BS EN ISO 4288:1998. *International Standard Organization*, (1), 1998.

[255] BS ISO. BS ISO 4287: Geometric product specification - surface texture: Profile method - Terms, definitions and surface texture parameters. *BSI*, 4287, 1997.

[256] British Standard. Geometrical product specifications (GPS) Ð Surface texture : Profile method ; surfaces having stratified functional properties Ð - Part 2: Height characterization using linear material ratio curve. *BSI*, Part 2(1), 2000.

[257] British Standards Institution. BSI Standards Publication Geometrical product specifications (GPS) — Surface texture : Areal Part 2 : Terms , definitions and surface. 2012.

[258] Andrew R. Beadling, Michael Bryant, Duncan Dowson, and Anne Neville. Tribocorrosion of hard-on-hard total hip replacements with metal and ceramic counterfaces under standard and adverse loading conditions. *Tribology International*, 103:359–367, nov 2016.

[259] Eugene I. Rivin. Advanced 7/24 Taper Toolholder/Spindle Interfaces for High-Speed CNC Machine Tools. In *SAE Technical Papers*, number 724, jun 1998.

[260] Jeff Elliott. A Deeper Look at "Precision" Toolholders, 2017.

[261] Paul H Werner, Harmen B Etema, Florian Wit, Michael M Morlock, and Cees C P M Verheyen. Basic principles and uniform terminology for the head-neck juncton in hip replacement. *HIP International*, 25(2):115–119, 2015.

[262] Michael M. Morlock, Robert Hube, Georgi Wassilew, Felix Prange, Gerd Huber, and Carsten Perka. Taper corrosion: a complication of total hip arthroplasty. *EFORT Open Reviews*, 5(11):776–784, 2020.

[263] Keith Tucker, Martin Pickford, Claire Newell, Peter Howard, Linda P. Hunt, and Ashley W. Blom. Mixing of components from different manufacturers in total hip arthroplasty: Prevalence and comparative outcomes. *Acta Orthopaedica*, 86(6):671–677, 2015.

[264] Ulrike Mueller, Benjamin Panzram, Steffen Braun, Robert Sonntag, and J. Philippe Kretzer. Mixing of Head-Stem Components in Total Hip Arthroplasty. *Journal of Arthroplasty*, 33(3):945–951, 2018.

[265] P.C. Noble H.J. Jones, E. Foley, K. Garrett. The Effect of Femoral Head Material on the Locking Strength and Contact area of Modular Couplings. In *International Society for Technology in Arthroplasty (ISTA) meeting, 32nd Annual Congress, Toronto, Canada, October 2019. Part 2 of 2*, page 48, Toronto, 2020. Orthopaedic Proceesings.

[266] Taylor Hobson. *A Guide to Roundness and Surface Texture - Measurement and Parameters*. Taylor Hobson, Leicester, 1 edition, 2017.

[267] M. H. Yadav and S. S. Mohite. Controlling deformations of thin-walled Al 6061-T6 components by adaptive clamping. *Procedia Manufacturing*, 20:509–516, 2018.

[268] Radu Racasan, Paul Bills, Liam Blunt, Alister Hart, and John Skinner. Method for Characterization of Material Loss from Modular Head-Stem Taper Surfaces of Hip Replacement Devices. In *Modularity and Tapers in Total Joint Replacement Devices*, pages 132–146. ASTM International, 100 Barr Harbor Drive, PO Box C700, West Conshohocken, PA 19428-2959, dec 2015.

[269] Yongsheng Zhao, Xiaolei Song, Ligang Cai, Zhifeng Liu, and Qiang Cheng. Surface fractal topography-based contact stiffness determination of spindle-toolholder joint. *Proceedings of the Institution of Mechanical Engineers, Part C: Journal of Mechanical Engineering Science*, 230(4):602–610, 2016.

[270] Fick Robert and Zimmer. Fick v. Zimmer US, Inc, 2018.

[271] R. B. Cook, C. Maul, and A. M. Strickland. Validation of an Optical Coordinate Measuring Machine for the Measurement of Wear at the Taper Interface in Total Hip Replacement. In *Modularity and Tapers in Total Joint Replacement Devices*, pages 362–378. ASTM International, 100 Barr Harbor Drive, PO Box C700, West Conshohocken, PA 19428-2959, dec 2015.

[272] Maren Bechstedt, Jonathan A. Gustafson, Steven P. Mell, Julian Gührs, Michael M. Morlock, Brett R. Levine, and Hannah J. Lundberg. Contact conditions for total hip head-neck modular taper junctions with microgrooved stem tapers. *Journal of Biomechanics*, 103:109689, 2020.

[273] Phuong Thao Mai, Therese Bormann, Ulrike Müller, Jan Philippe Kretzer, and Jens Gibmeier. Effect of surface topography and residual stress on the taper connection stability in total hip arthroplasty. *Journal of the Mechanical Behavior of Biomedical Materials*, 128(June 2021):105119, 2022.

[274] Mohammad Reza Yavari and Mohd Hasbullah Idris. Effect of surface roughness and taper angle on junction strength of modular biomedical implant. *International Journal of Mechanical and Mechatronics Engineering*, 16(2):42–47, 2016.

[275] Berend Denkena, Christof Hurschler, Benjamin Bergmann, Beate Legutko, Marco Gustav, and Bastian Welke. Influence of surface topography on junction strength of modular hip endoprostheses. *Procedia CIRP*, 110(C):64–69, 2022.

[276] Sophie Le Cann, Erika Tudisco, Mikael J. Turunen, Alessandra Patera, Rajmund Mokso, Magnus Tägil, Ola Belfrage, Stephen A. Hall, and Hanna Isaksson. Investigating the mechanical characteristics of bone-metal implant interface using in situ synchrotron tomographic imaging. *Frontiers in Bioengineering and Biotechnology*, 6(JAN), 2019.

[277] Jonova Thomas, Andrew Chihpin Chuang, Hrishikesh Das, Lianghua Xiong, Piyush Upadhyay, and Dileep Singh. Three-dimensional microstructure of a friction stir welded magnesium/steel interface characterized via high-energy synchrotron X-rays. *Materials Science and Engineering A*, 852(May):143708, 2022.

[278] BSI. Implants for surgery — Partial and total hip joint prostheses Part 4: Determination of endurance properties and performance of stemmed femoral components BS ISO 7206-4:2010+A1:2016 Committee. (July), 2016.

[279] Hongbo Wang and Zhihua Feng. Ultrastable and highly sensitive eddy current displacement sensor using self-temperature compensation. *Sensors and Actuators, A: Physical*, 203:362–368, 2013.

[280] Chris Oberhauser. LDC calculations tool, 2016.

[281] Haisong Xu, Dongbai Sun, and Hongying Yu. Repassivation behavior of 316L stainless steel in borate buffer solution: Kinetics analysis of anodic dissolution and film formation. *Applied Surface Science*, 357:204–213, 2015.

[282] Yu Yan, Anne Neville, and Duncan Dowson. Biotribocorrosion of CoCrMo orthopaedic implant materials-Assessing the formation and effect of the biofilm. *Tribology International*, 40(10-12 SPEC. ISS.):1492–1499, 2007.

[283] Yu Yan, Anne Neville, and Duncan Dowson. Tribo-corrosion properties of cobalt-based medical implant alloys in simulated biological environments. *Wear*, 263(7-12 SPEC. ISS.):1105–1111, 2007.

[284] M. Bryant, J. Rituerto Sin, N. Emami, and A. Neville. Effect of proteins and phosphates on the degradation and repassivation of CoCrMo alloys under tribocorrosion conditions. *Tribology - Materials, Surfaces and Interfaces*, 14(4):207–218, 2020.

[285] M. Baxmann, A. M. Pfaff, C. Schilling, T. M. Grupp, and M. M. Morlock. Biomechanical Evaluation of the Fatigue Performance, the Taper Corrosion and the Metal Ion Release of a Dual Taper Hip Prosthesis under Physiological Environmental Conditions. *Biotribology*, 12(June):1–7, 2017.

[286] Sara Ehsani Majd, Roel Kuijer, Alexander Köwitsch, Thomas Groth, Tannin A. Schmidt, and Prashant K. Sharma. Both hyaluronan and collagen type II keep proteoglycan 4 (lubricin) at the cartilage surface in a condition that provides low friction during boundary lubrication. *Langmuir*, 30(48):14566–14572, 2014.

[287] Craig W. Forsthoefel, Nicholas M. Brown, and Mark L. Barba. Comparison of metal ion levels in patients with hip resurfacing versus total hip arthroplasty. *Journal of Orthopaedics*, 14(4):561–564, 2017.

[288] Mohiuddin SS Tobias A, Ballard BD. Physiology, Water Balance. In *StatPearls*. Treasure Island (FL): StatPearls, 2023.

[289] H. S. Dobbs and M. J. Minski. Metal ion release after total hip replacement. *Biomaterials*, 1(4):193–198, 1980.

[290] Diana Bitar and Javad Parvizi. Biological response to prosthetic debris. *World Journal of Orthopedics*, 6(2):172–189, 2015.

[291] Nadim James Hallab. A review of the biologic effects of spine implant debris: Fact from fiction. *SAS Journal*, 3(4):143–160, 2009.

[292] J. M. Brandt, L. K. Brière, J. Marr, S. J. MacDonald, R. B. Bourne, and J. B. Medley. Biochemical comparisons of osteoarthritic human synovial fluid with calf sera used in knee simulator wear testing. *Journal of Biomedical Materials Research - Part A*, 94(3):961–971, 2010.

[293] DMG and Mori Seiki. CNC Universal Milling Machines: DMU 60 / 80 / 100 monoBLOCK: Classic Series. *dmgmoriseiki*, 2008, 2008.

[294] Bulent Kaya, Cuneyt Oysu, and Huseyin M. Ertunc. Force-torque based on-line tool wear estimation system for CNC milling of Inconel 718 using neural networks. *Advances in Engineering Software*, 42(3):76–84, 2011.

[295] S Groves, D and Vasiljeva, K and Al-Hajjar, M and Fisher, J and Williams. CONTACT AREA IN METAL-ON-POLYETHYLENE AND CERAMIC-ON-POLYETHYLENE TOTAL HIP REPLACEMENTS. *The British Editorial Society of Bone & Joint Surgery*, 99:149—-149, 2017.

[296] S C Scholes and A Unsworth. Comparison of friction and lubrication of di ff erent hip prostheses. *Proceedings of the Institution of Mechanical Engineers, Part H: Journal of Engineering in Medicine*, 214(July 1999):49–57, 2000.

[297] A. Matthies, R. Underwood, P. Cann, K. Ilo, Z. Nawaz, J. Skinner, and A. J. Hart. Retrieval analysis of 240 metal-on-metal hip components, comparing modular total hip replacement with hip resurfacing. *Journal of Bone and Joint Surgery - Series B*, 93 B(3):307–314, 2011.

[298] Philipp Damm, Alwina Bender, and Georg Bergmann. Postoperative changes in in vivo measured friction in total hip joint prosthesis during walking. *PLoS ONE*, 10(3):1–15, 2015.

[299] Colin P. McCarty, Sang Hyun Park, Nathan C. Ho, Sophia N. Sangiorgio, and Edward Ebramzadeh. Taper Material Loss in Total Hip Replacements: Is It Affected by Joint Friction? *Journal of Bone and Joint Surgery*, 104(9):796–804, 2022.

[300] Gamry Instruments. Understanding iR Compensation.

[301] F. Witt, B. H. Bosker, N. E. Bishop, H. B. Ettema, C. C.P.M. Verheyen, and M. M. Morlock. The relation between titanium taper corrosion and cobalt-chromium bearing wear in large-head metal-on-metal total hip prostheses: A Retrieval Study. *Journal of Bone and Joint Surgery - American Volume*, 96(18):e157(1), 2014.

[302] Heiko Meyer, Tina Mueller, Gesine Goldau, Kathrin Chamaon, Marcel Ruetschi, and Christoph H. Lohmann. Corrosion at the cone/taper interface leads to failure of large-diameter metal-on-metal total hip arthroplasties. *Clinical Orthopaedics and Related Research*, 470(11):3101–3108, 2012.

[303] Hamidreza Farhoudi, Khosro Fallahnezhad, Reza H. Oskouei, and Mark Taylor. A finite element study on the mechanical response of the head-neck interface of hip implants under realistic forces and moments of daily activities: Part 1, level walking. *Journal of the Mechanical Behavior of Biomedical Materials*, 75(August):470–476, 2017.

[304] A.NEVILLE F. MOTAMENSALEHI, A. WADE, M.G.BRYANT, R.M.HALL. Tribocorrosion of Metal-on-Metal Hip Implants: In Vitro Corrosion Measurement of Interfaces. *Leeds-Lyon 2018 (Poster)*, 2018.

[305] Ing. Philipp Damm and rer.nat. Alwina Bender. Orthoload Database - Loading of Orthopaedic Implants.

[306] Aarti A. Shenoy and Jeremy L. Gilbert. In vitro test methods for seating and fretting corrosion behavior of modular metal-on-metal acetabular tapers. *Journal of Orthopaedic Research*, 38(5):1089–1100, 2020.

[307] Ville Satopaa, Jeannie Albrecht, David Irwin, and Barath Raghavan. Finding a "Kneedle" in a Haystack: Detecting Knee Points in System Behavior. In *2011 31st International Conference on Distributed Computing Systems Workshops*, pages 166–171. IEEE, jun 2011.

[308] V. Swaminathan, L. Scholl, R. Lee, A. Faizan, M. Thakore, K. TenHuisen, and J. Nevelos. Simultaneous Hip Head-Stem Taper Junction Measurements of Electrochemical Corrosion and Micromotion: A Comparison of Taper Geometry and Stem Material. *Modularity and Tapers in Total Joint Replacement Devices*, pages 321–335, dec 2015.

[309] Hamidreza Farhoudi, Reza H. Oskouei, Ali A.Pasha Zanoosi, Claire F. Jones, and Mark Taylor. An analytical calculation of frictional and bending moments at the head-neck interface of hip joint implants during different physiological activities. *Materials*, 9(12):1–14, 2016.

[310] Sabrina Yvonne Jauch, Gerd Huber, Kay Sellenschloh, Henning Haschke, Marc Baxmann, Thomas M. Grupp, and Michael M. Morlock. Micromotions at the taper interface between stem and neck adapter of a bimodular hip prosthesis during activities of daily living. *Journal of Orthopaedic Research*, 31(8):1165–1171, 2013.

[311] Teruo Murakami, Seido Yarimitsu, Kazuhiro Nakashima, Yoshinori Sawae, and Nobuo Sakai. Influence of synovia constituents on tribological behaviors of articular cartilage. *Friction*, 1(2):150–162, 2013.

[312] S. Radice, S. Liu, R. Pourzal, M. P. Laurent, and M. A. Wimmer. Effects of Bovine Serum Albumin and Hyaluronic Acid on the Electrochemical Response of a CoCrMo Alloy to Cathodic and Anodic Excursions. *Journal of Bio- and Tribo-Corrosion*, 5(4):1–12, 2019.

[313] Yang Liu and Jiawei Wang. Influences of microgap and micromotion of implant–abutment interface on marginal bone loss around implant neck. *Archives of Oral Biology*, 83(February):153–160, 2017.

[314] Vitor Venâncio Moreira Rodrigues, Daniele Sorgatto Faé, Cleber Davi Del Rei Daltro Rosa, Victor Augusto Alves Bento, Mariane Floriano Lopes Santos Lacerda, Eduardo Piza Pellizzer, and Cleidiel Aparecido Araujo Lemos. Is the clinical performance of internal conical connection better than internal non-conical connection for implant-supported restorations? A systematic review with meta-analysis of randomized controlled trials. *Journal of Prosthodontics*, 32(5):382–391, 2023.

[315] Mathew T. Mathew, Shelley Kerwell, Hannah J. Lundberg, Cortino Sukotjo, and Louis G. Mercuri. Tribocorrosion and oral and maxillofacial surgical devices. *British Journal of Oral and Maxillofacial Surgery*, 52(5):396–400, 2014.

[316] K. Apaza-Bedoya, M. Tarce, C. A.M. Benfatti, B. Henriques, M. T. Mathew, W. Teughels, and J. C.M. Souza. Synergistic interactions between corrosion and wear at titanium-based dental implant connections: A scoping review. *Journal of Periodontal Research*, 52(6):946–954, 2017.

[317] Christian M. Schmitt, Getulio Nogueira-Filho, Howard C. Tenenbaum, Jim Yuan Lai, Carlos Brito, Hendrik Döring, and Jörg Nonhoff. Performance of conical abutment (Morse Taper) connection implants: A systematic review. *Journal of Biomedical Materials Research - Part A*, 102(2):552–574, 2014.

[318] P. Westerhoff, F. Graichen, A. Bender, A. Halder, A. Beier, A. Rohlmann, and G. Bergmann. In vivo measurement of shoulder joint loads during activities of daily living. *Journal of Biomechanics*, 42(12):1840–1849, 2009.

[319] Johannes A. Eckert, Ulrike Mueller, Sebastian Jaeger, Benjamin Panzram, and J. Philippe Kretzer. Fretting and Corrosion in Modular Shoulder Arthroplasty: A Retrieval Analysis. *BioMed Research International*, 2016, 2016.

[320] Jonathan O. Wright, Corinn K. Gehrke, Ian R. Penvose, Omar N. Khatib, Murphy A. Mallow, J. Michael Wiater, Brett P. Wiater, and Erin A. Baker. Larger-diameter trunnions and bolt-reinforced taper junctions are associated with less tribocorrosion in reverse total shoulder arthroplasty. *Journal of Shoulder and Elbow Surgery*, 32(1):201–212, 2023.

[321] Maria Crackau, Nicole Märtens, Karsten Harnisch, Alexander Berth, Joachim Döring, Christoph H. Lohmann, Thorsten Halle, and Jessica Bertrand. In vivo corrosion and damages in modular shoulder prostheses. *Journal of Biomedical Materials Research - Part B Applied Biomaterials*, 108(5):1764–1778, 2020.

[322] William M. Mihalko, Markus A. Wimmer, Carol A. Pacione, Michel P. Laurent, Robert F. Murphy, and Carson Rider. How Have Alternative Bearings and Modularity Affected Revision Rates in Total Hip Arthroplasty? *Clinical Orthopaedics and Related Research*, 472(12):3747–3758, 2014.

[323] Alan M. Kop and Eric Swarts. Corrosion of a Hip Stem With a Modular Neck Taper Junction. *The Journal of Arthroplasty*, 24(7):1019–1023, oct 2009.

[324] Kevin C. Ilo, Emma J. Derby, Robert K. Whittaker, Gordon W. Blunn, John A. Skinner, and Alister J. Hart. Fretting and Corrosion Between a Metal Shell and Metal Liner May Explain the High Rate of Failure of R3 Modular Metal-on-Metal Hips. *Journal of Arthroplasty*, 32(5):1679–1683, 2017.

[325] T. David Tarity, Chelsea N. Koch, Jayme C. Burket, Timothy M. Wright, and Geoffrey H. Westrich. Fretting and Corrosion at the Backside of Modular Cobalt Chromium Acetabular Inserts: A Retrieval Analysis. *Journal of Arthroplasty*, 32(3):1033–1039, 2017.

[326] Aarti A. Shenoy, Steven M. Kurtz, and Jeremy L. Gilbert. Nontribological corrosion modes dominate wrought CoCrMo acetabular taper corrosion: A retrieval study. *Journal of Biomedical Materials Research - Part B Applied Biomaterials*, 109(12):2000–2013, 2021.

[327] Harry S. Hothi, Kevin Ilo, Robert K. Whittaker, Antti Eskelinen, John A. Skinner, and Alister J. Hart. Corrosion of Metal Modular Cup Liners. *Journal of Arthroplasty*, 30(9):1652–1656, 2015.

[328] Asim M. Makhdom and Javad Parvizi. Modular versus nonmodular tibial inserts in total knee arthroplasty: What are the differences? *Annals of Translational Medicine*, 5(10):1–4, 2017.

[329] Christina M. Arnholt, Daniel W. MacDonald, Mariya Tohfafarosh, Jeremy L. Gilbert, Clare M. Rimnac, Steven M. Kurtz, Gregg Klein, Michael A. Mont, Javad Parvizi, Harold E. Cates, Gwo-Chin Lee, Arthur Malkani, and Mattheuw Kraay. Mechanically Assisted Taper Corrosion in Modular TKA. *The Journal of Arthroplasty*, 29(9):205–208, sep 2014.

[330] Ricardo Pulido, Benjamin Kester, and Ran Schwarzkopf. Trunnionosis in Total Knee Arthroplasty: Is it a clinical problem? *International Journal of Orthopaedics*, 4(6):837–840, 2017.

[331] William C. McMaster and Jay Patel. Adverse Local Tissue Response Lesion of the Knee Associated With Morse Taper Corrosion. *Journal of Arthroplasty*, 28(2):375.e5–375.e8, 2013.

[332] I. Kutzner, B. Heinlein, F. Graichen, A. Bender, A. Rohlmann, A. Halder, A. Beier, and G. Bergmann. Loading of the knee joint during activities of daily living measured in vivo in five subjects. *Journal of Biomechanics*, 43(11):2164–2173, 2010.

[333] Kyle Snethen, Jorge Hernandez, and Melinda Harman. The effect of manufacturing tolerances on the mechanical environment of taper junctions in modular TKR. *Journal of the Mechanical Behavior of Biomedical Materials*, 97(10):49–57, sep 2019.

[334] MHRA. Off-label use of a medical device, 2014.

[335] G. E. Roter, J. B. Medley, J. D. Bobyn, J. J. Krygier, and F. W. Chan. Stop-dwell-start motion: A novel simulator protocol for the wear of metal-on-metal hip implants. *Tribology Series*, 40:367–376, 2002.

[336] Angela Bermúdez-Castañeda, Anna Igual-Muñoz, and Stefano Mischler. A Crevice Corrosion Model for Biomedical Trunnion Geometries and Surfaces Feature. *Materials*, 14(4):1005, feb 2021.

[337] A. Rack, T. Rack, M. Stiller, H. Riesemeier, S. Zabler, and K. Nelson. In vitro synchrotron-based radiography of micro-gap formation at the implant–abutment interface of two-piece dental implants. *Journal of Synchrotron Radiation*, 17(2):289–294, mar 2010.

[338] Edgar Hornus, Ke Wang, Moreica Pabbruwe, Alan Kop, Chris Jones, Ashraf Salleh, Mobin Salasi, and Mariano Iannuzzi. A new experimental method to simulate dynamic crevice corrosion in modular hip arthroplasty. *Corrosion Science*, 190(March):109704, sep 2021.

Appendix A

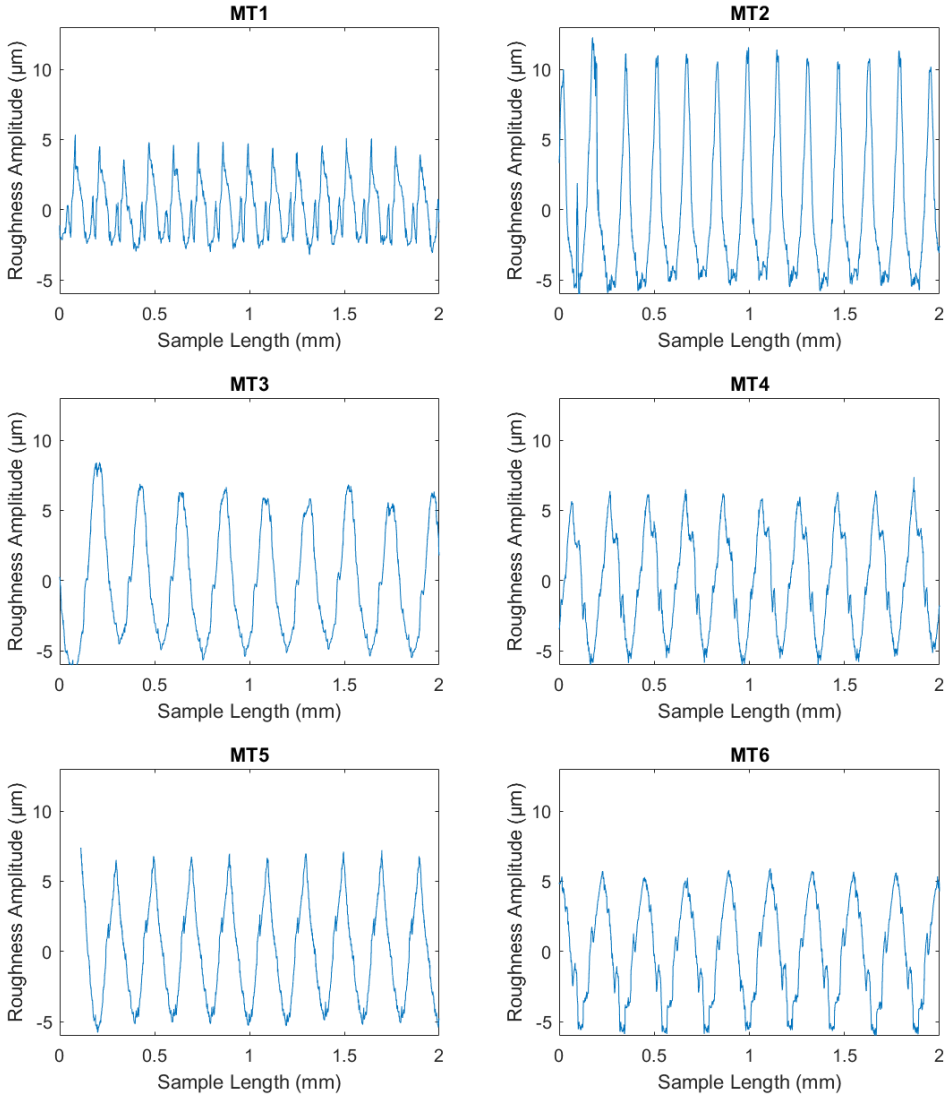

Fig. A.1 Surface roughness profiles MT1-MT6

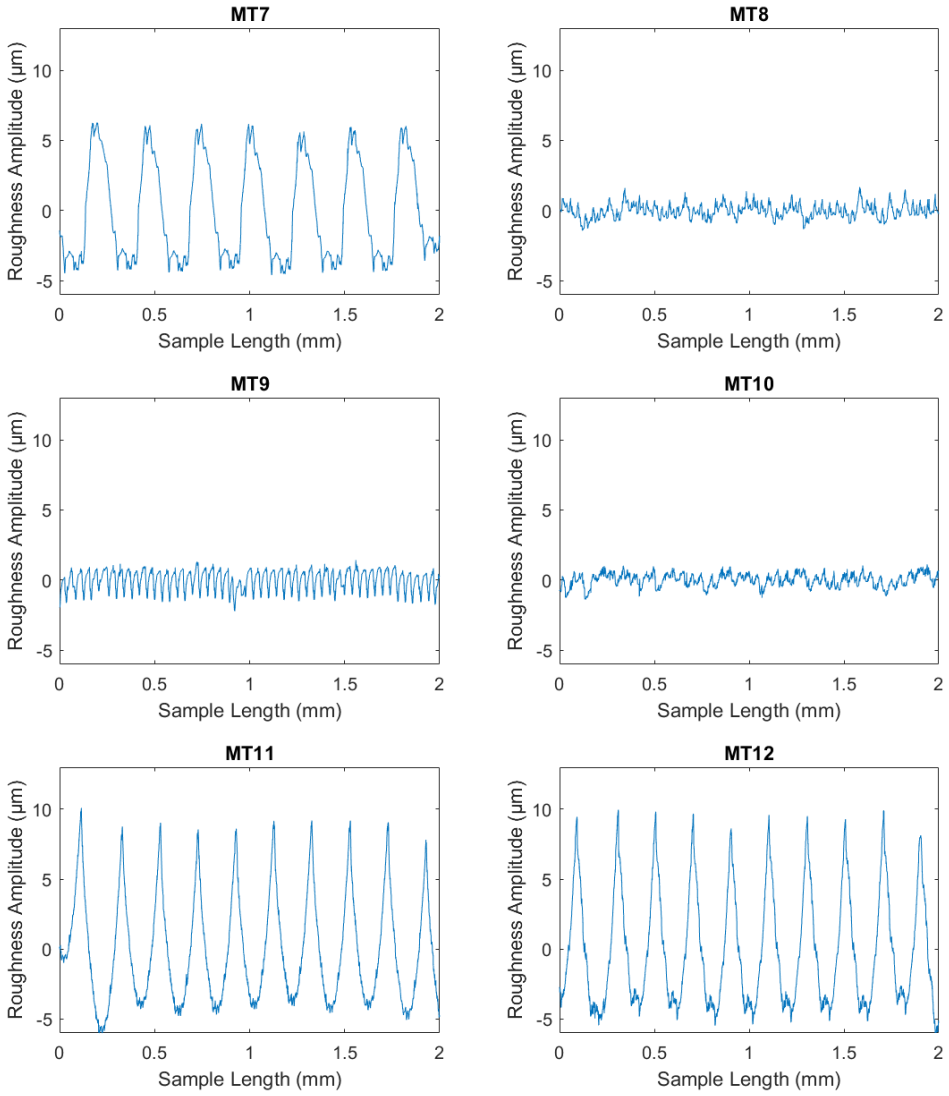

Fig. A.2 Surface roughness profiles MT7-MT12

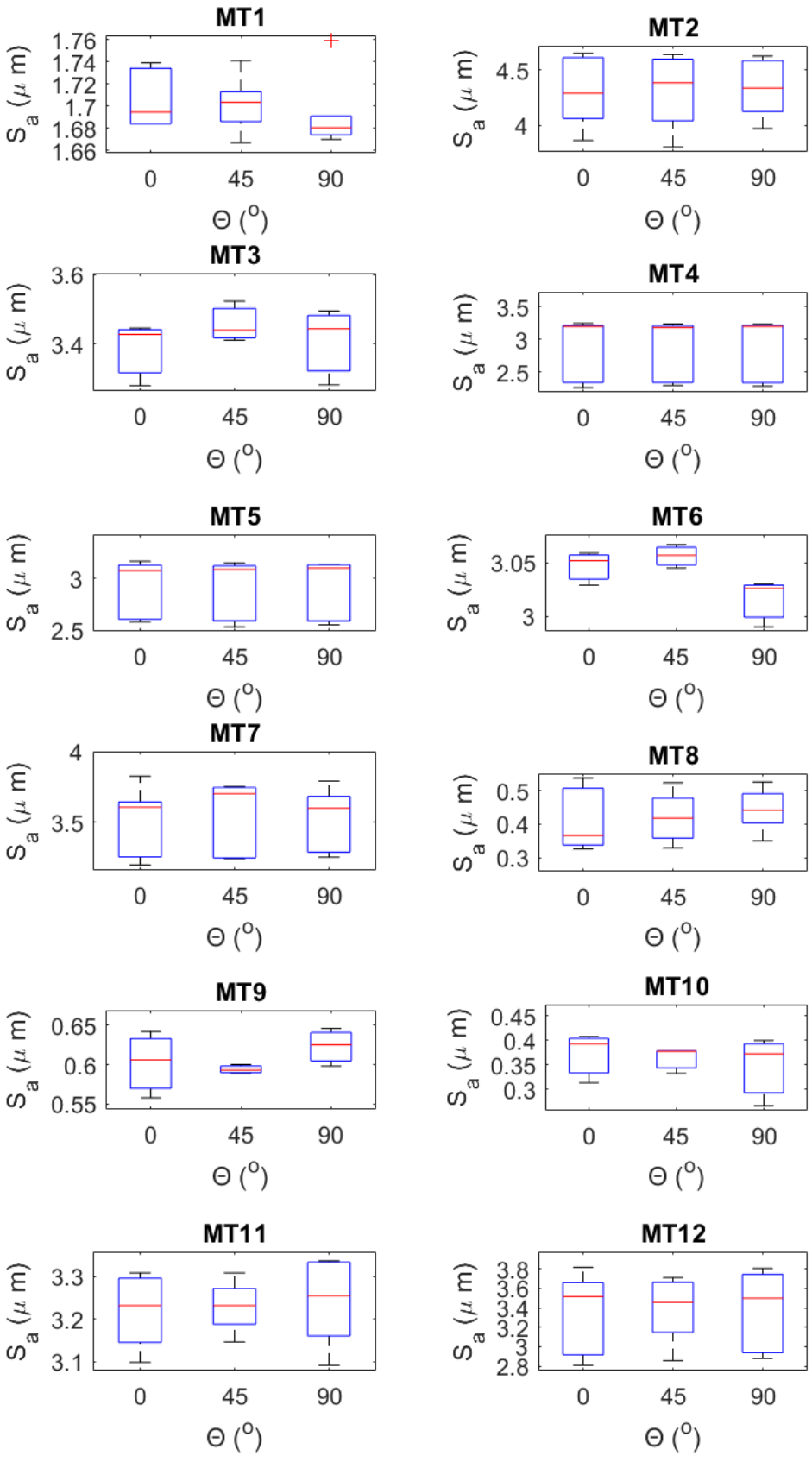

Fig. A.3 Variation in S_a around the taper axis of clinically available THR

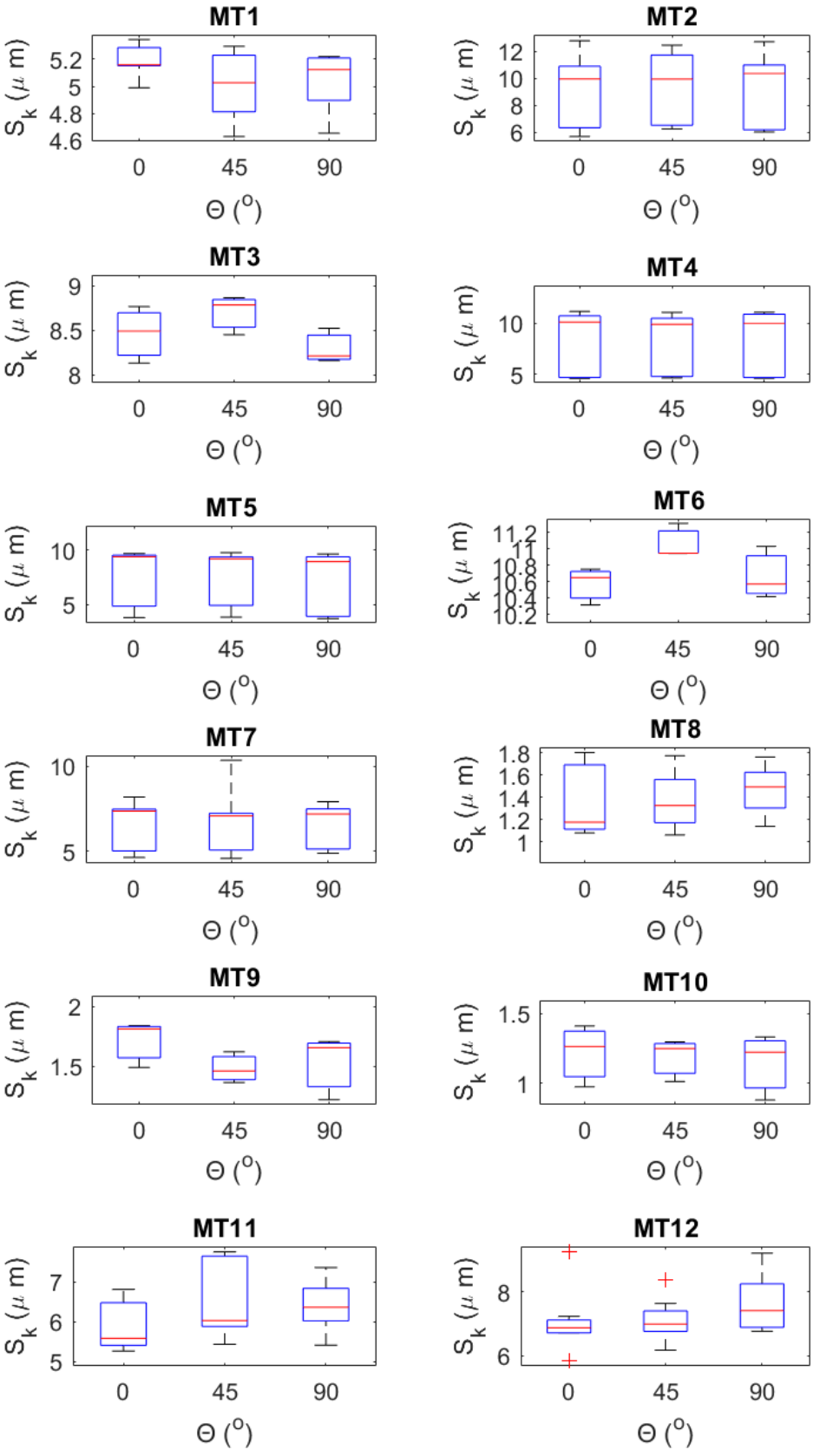

Fig. A.4 Variation in S_k around the taper axis of clinically available THR

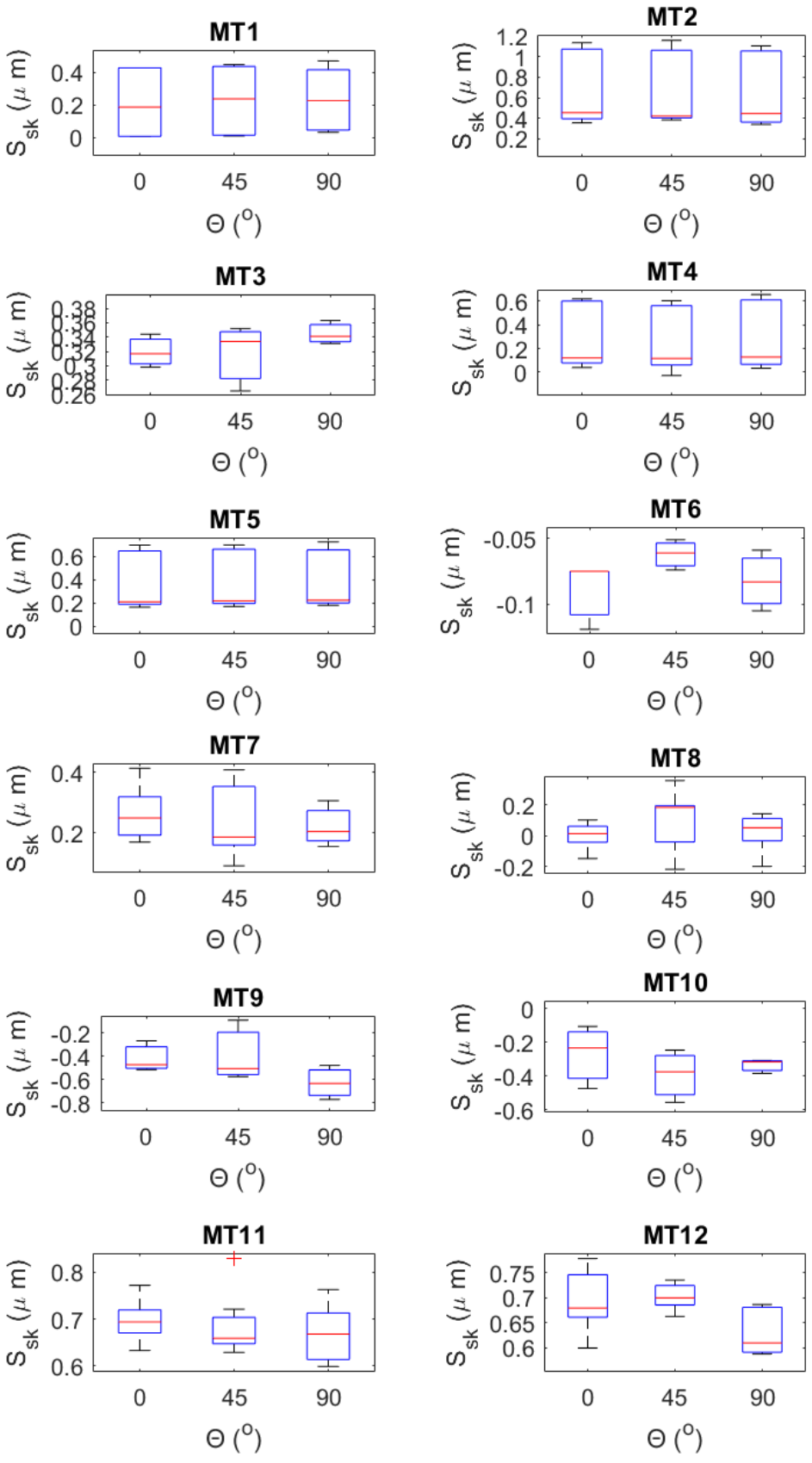

Fig. A.5 Variation in S_{sk} around the taper axis of clinically available THR

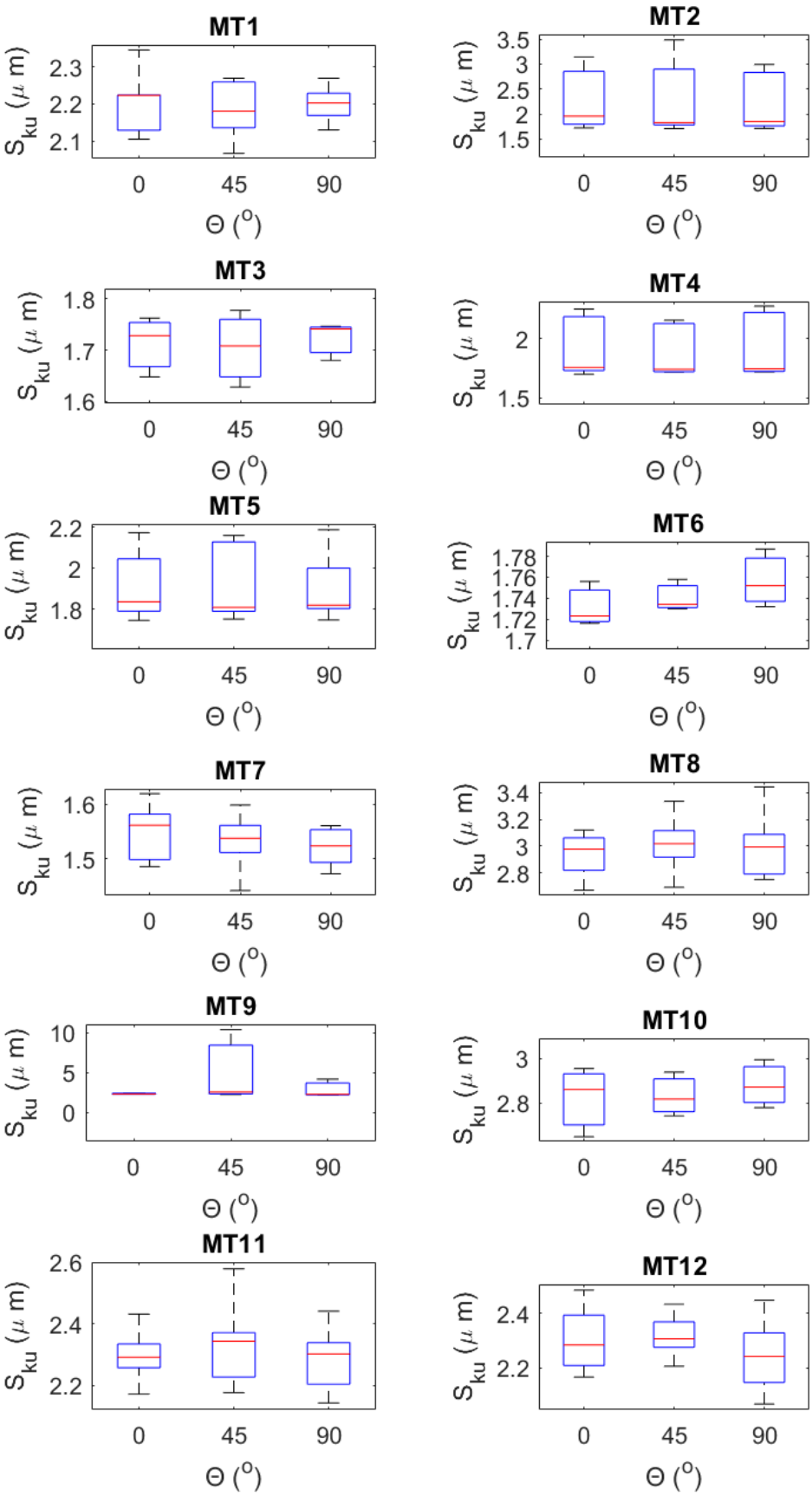
MT1
MT2
MT3
MT4
MT5
MT6
MT7
MT8
MT9
MT10
MT11
MT12
S_{ku} (μ m)
Θ (°)
0
45
90

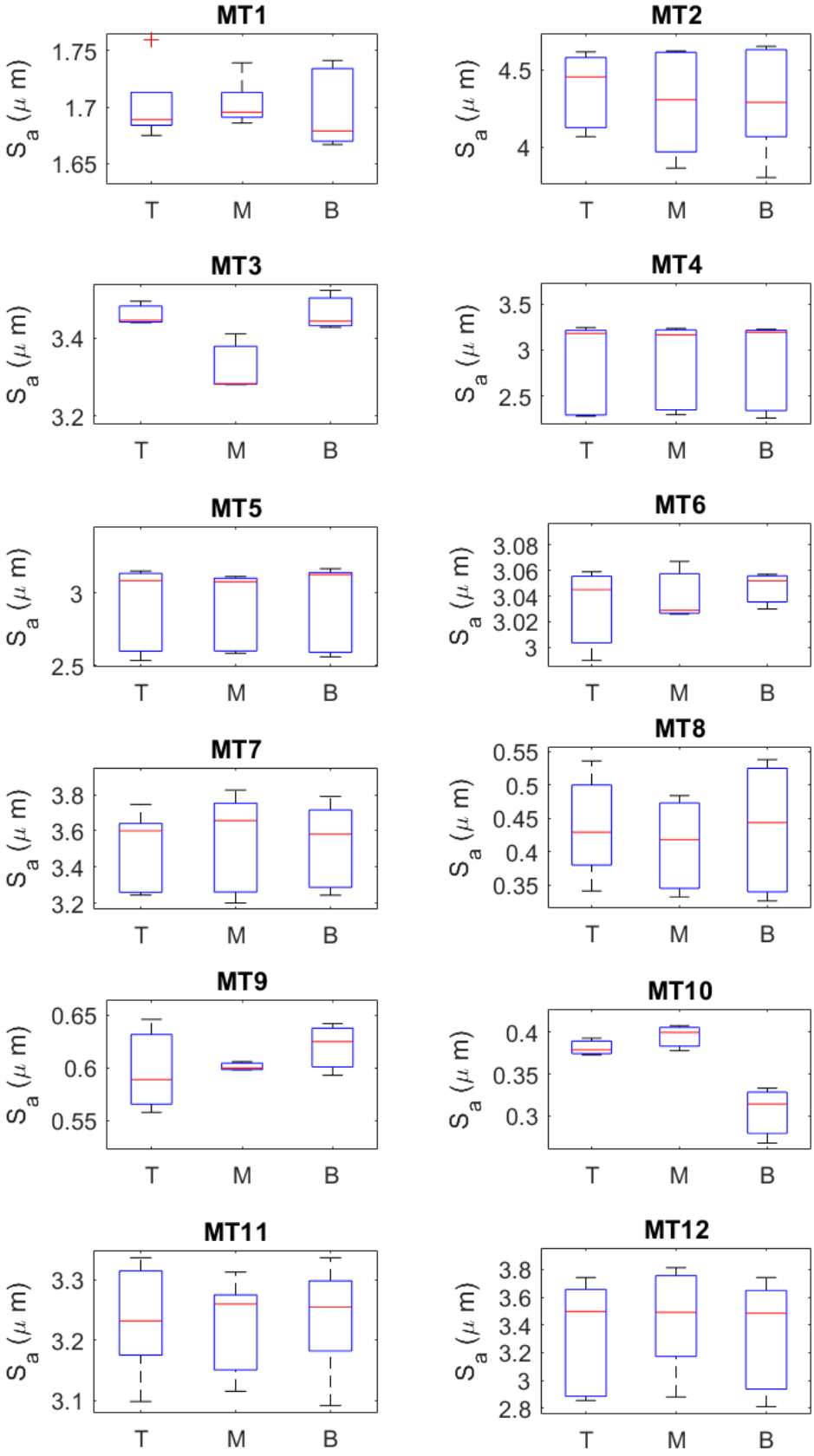

Fig. A.7 Variation in S_a along the taper axis of clinically available THR

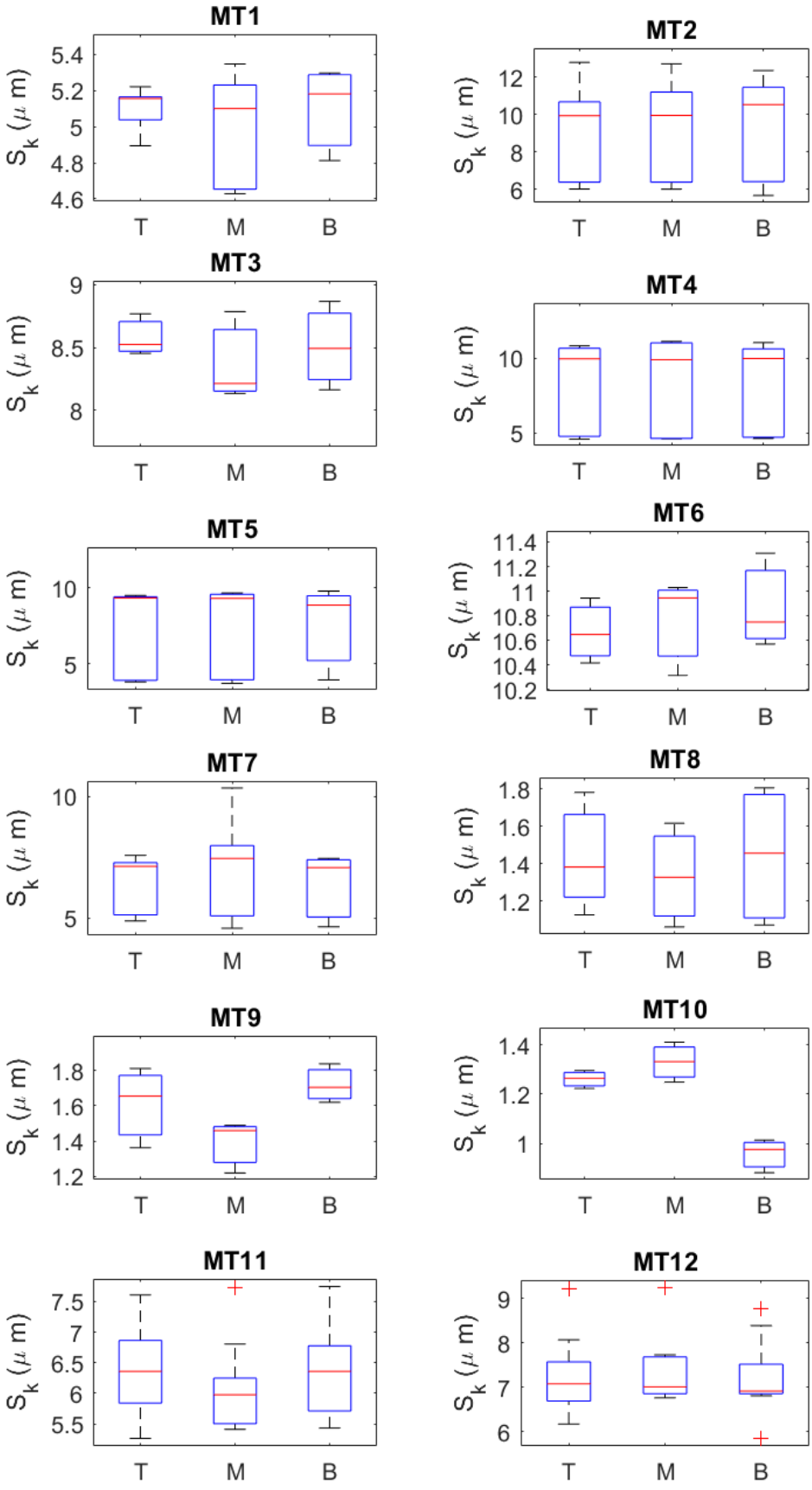
MT1
MT2
MT3
MT4
MT5
MT6
MT7
MT8
MT9
MT10
MT11
MT12
S_k (μ m)
T
M
B

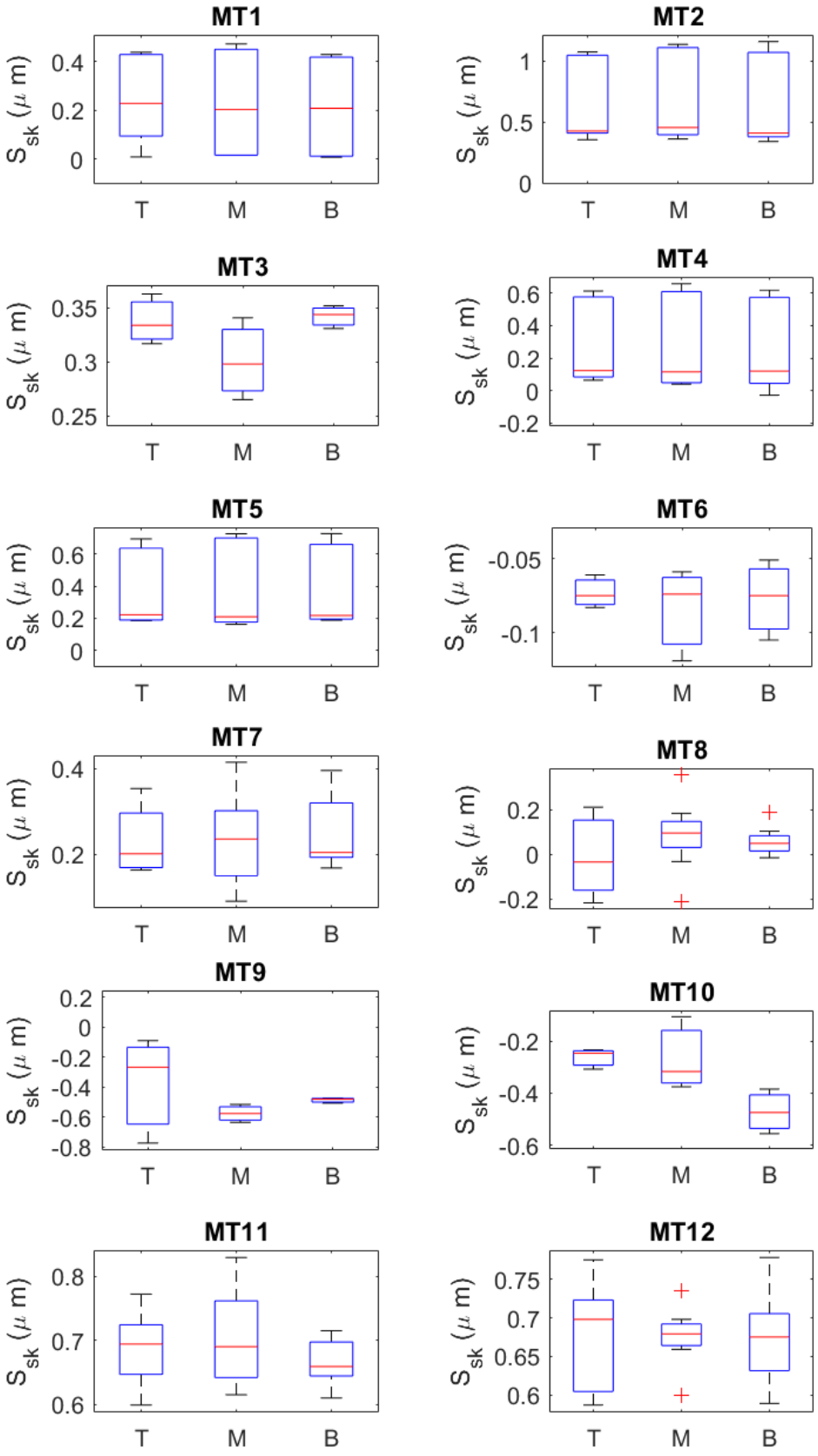

Fig. A.9 Variation in S_{sk} along the taper axis of clinically available THR

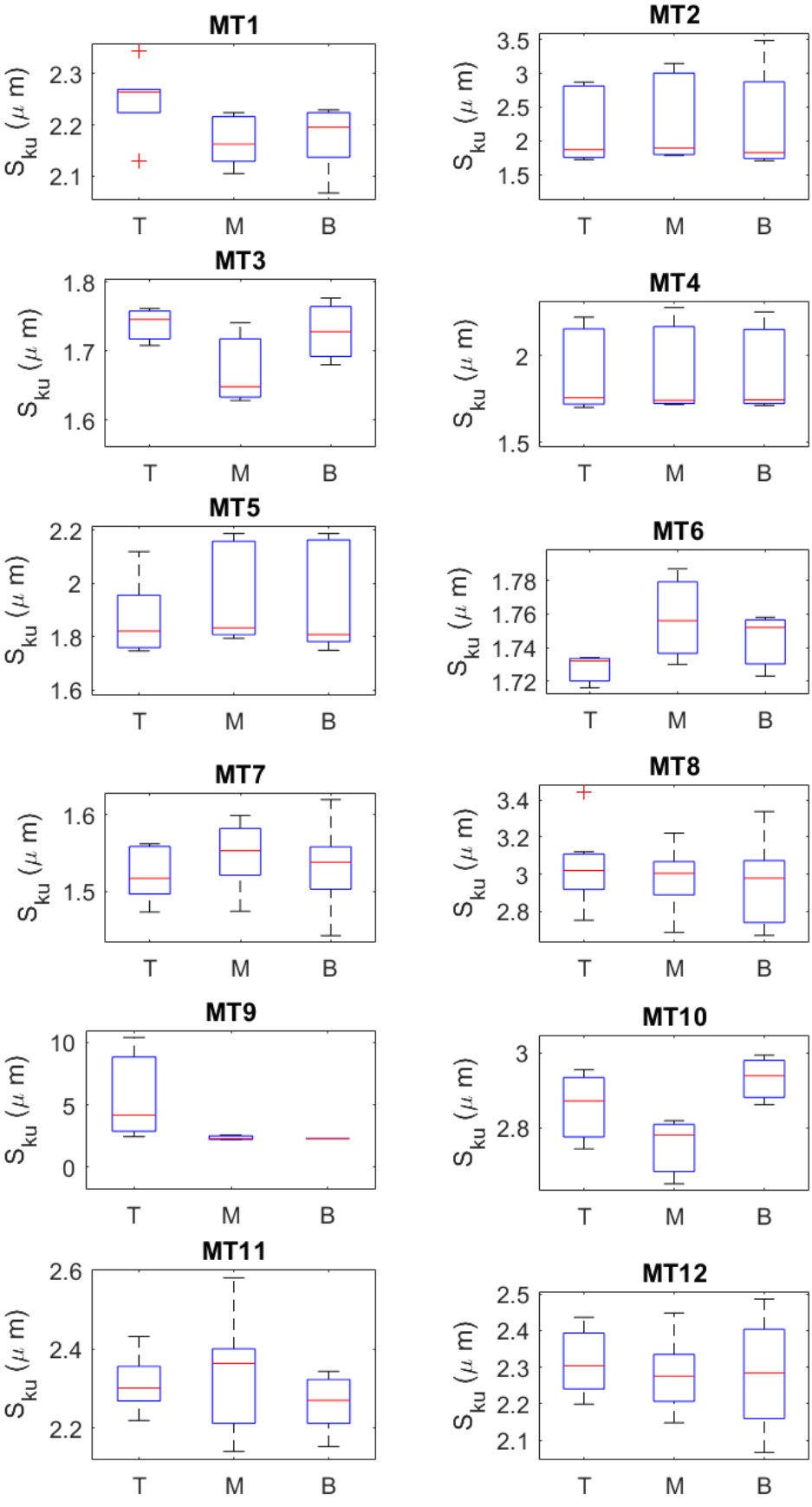
MT1
MT2
MT3
MT4
MT5
MT6
MT7
MT8
MT9
MT10
MT11
MT12
S_{ku} (μ m)
T
M
B

Appendix B

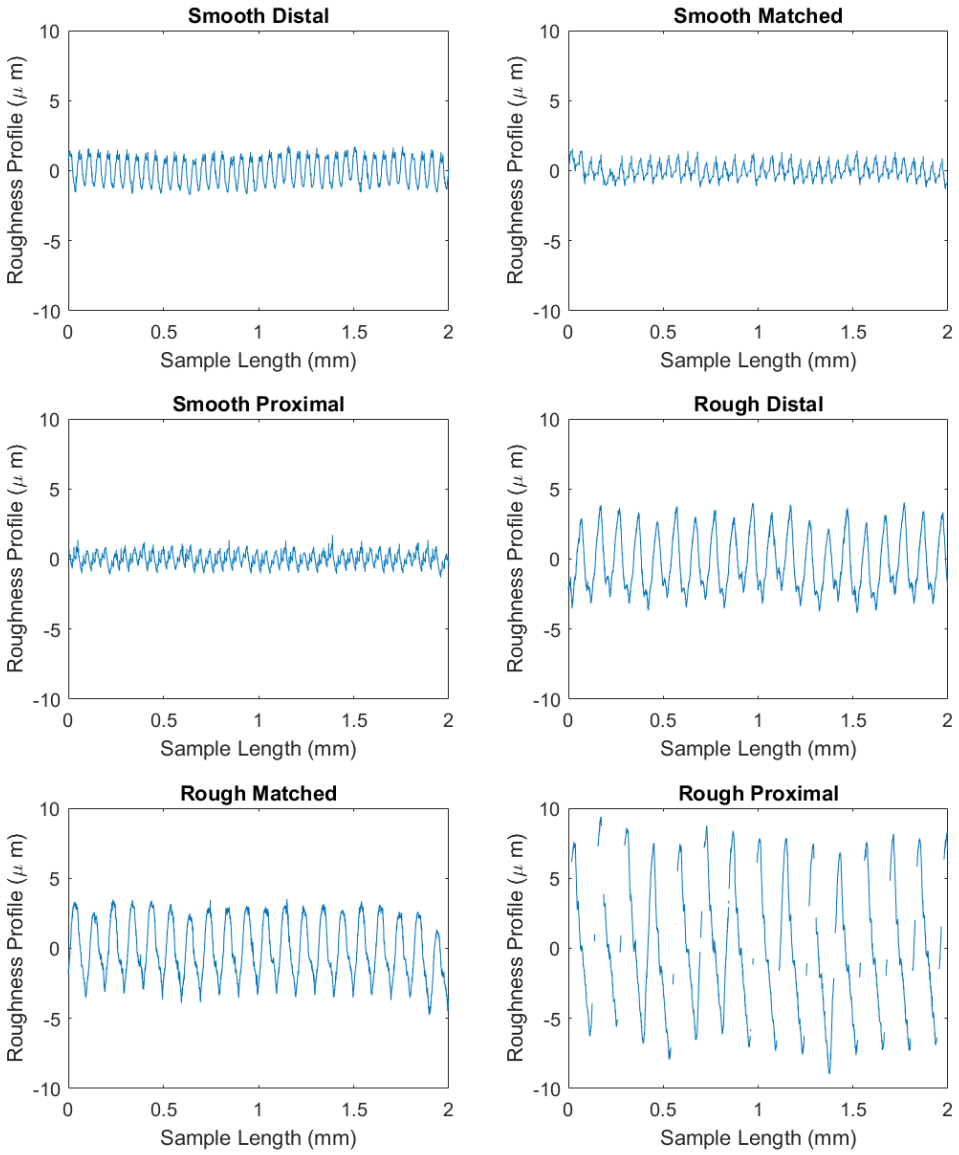

Fig. B.1 Example surface roughness profiles for all samples used throughout this project.

Appendix C

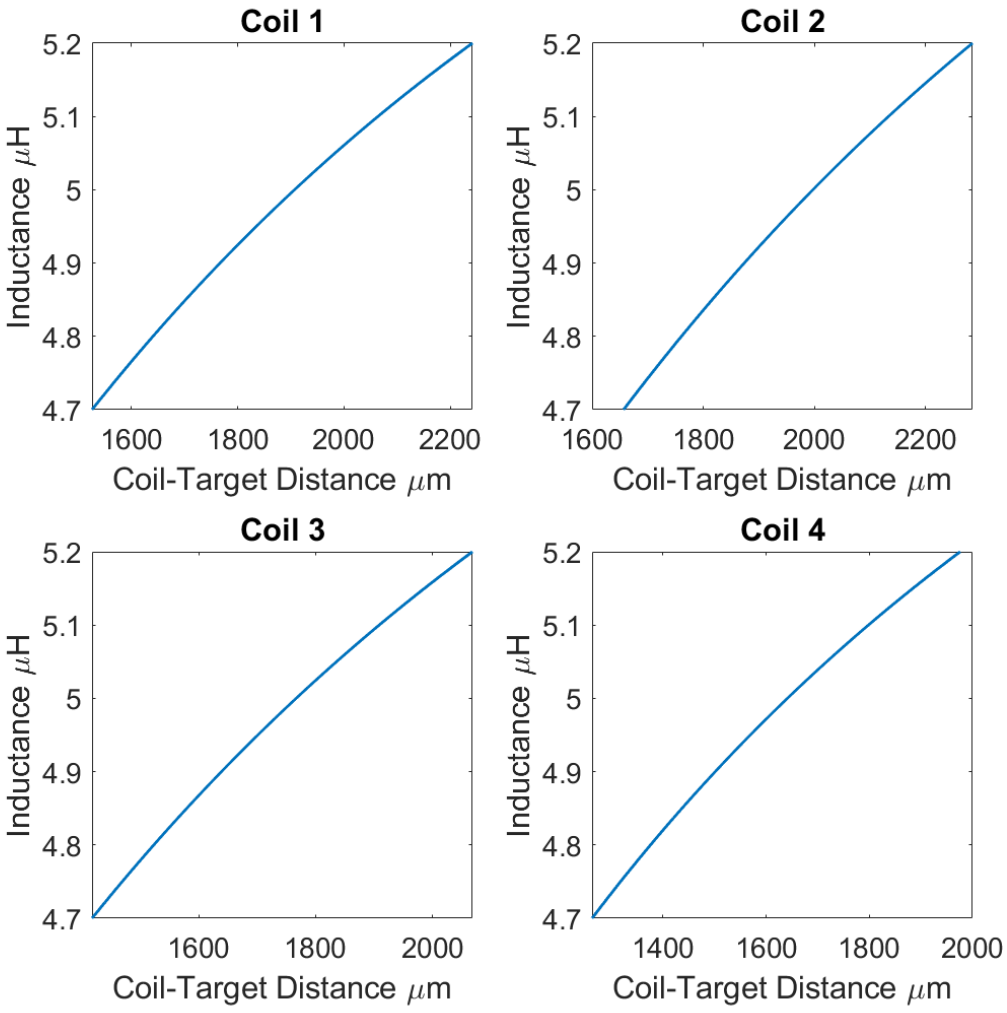

Fig. C.1 Calibration curves relating inductance to target-coil distance for each coil.

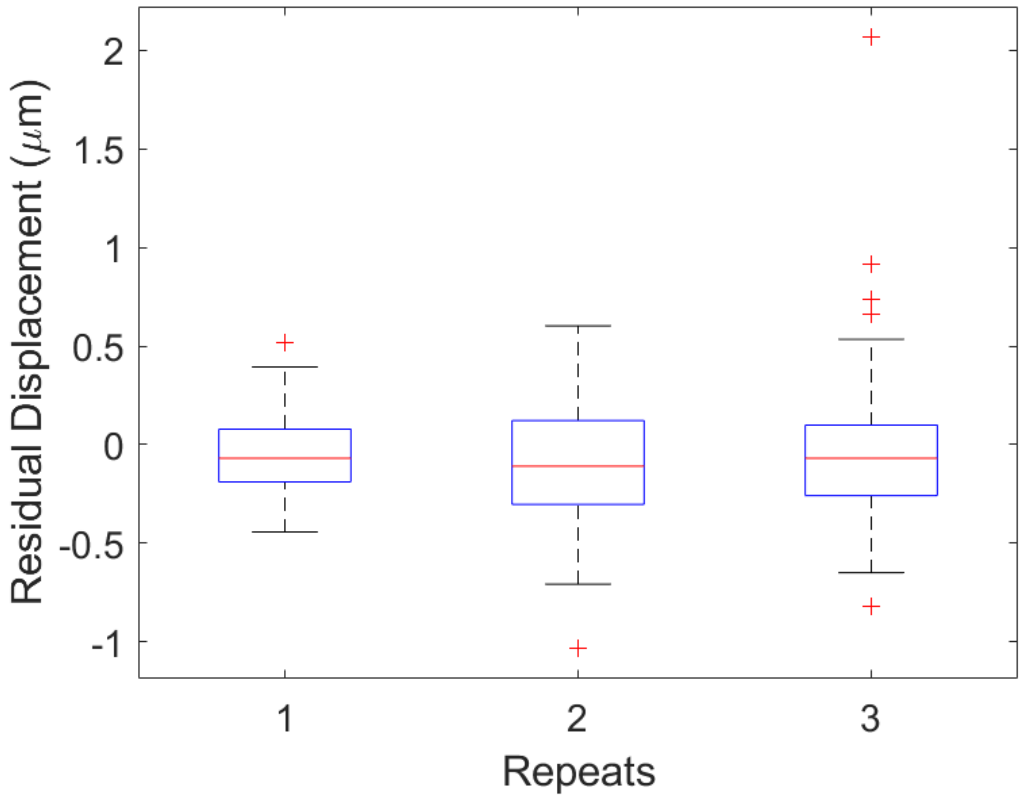

Fig. C.2 Residual displacements measured but the precision positioner stage from that calculated by the relationships relating inductance to displacement shown in Figure C.1. This was done for three repeat tests.

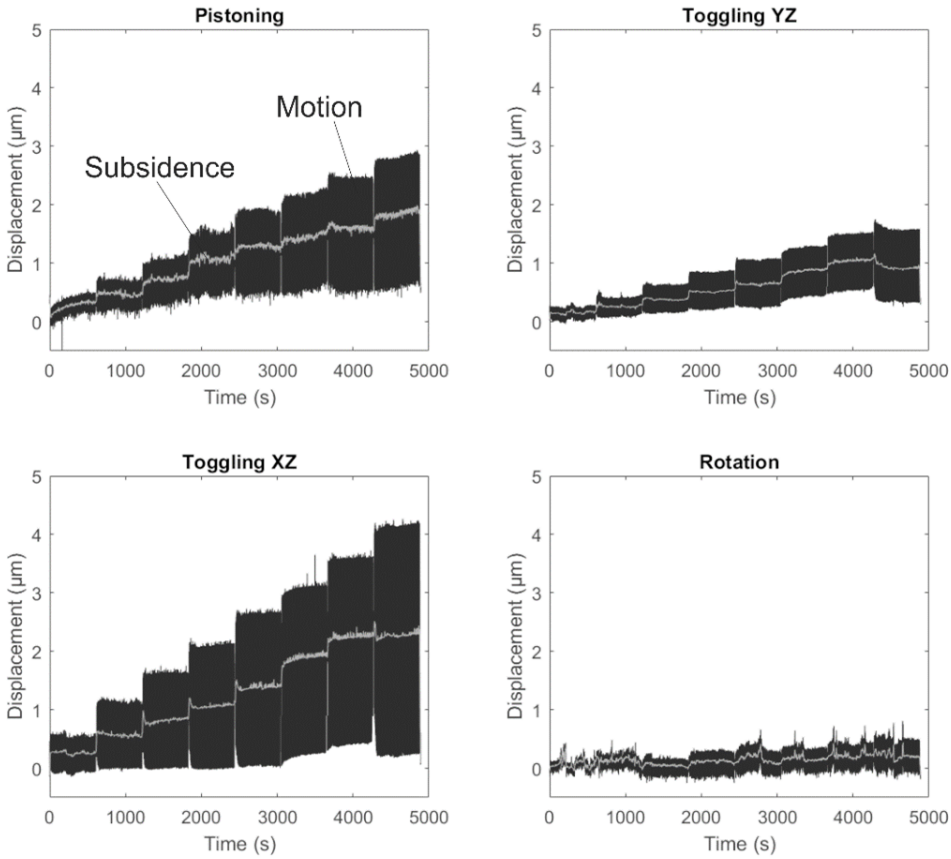

Fig. C.3 Motion captured for measurement of an equivalent monobloc sample. The dark grey represents the total motion and the lighter line following the 'form' of the motion represents subsidence. NB the complete recovery of motion after the final dynamic loading increment due to unloading.

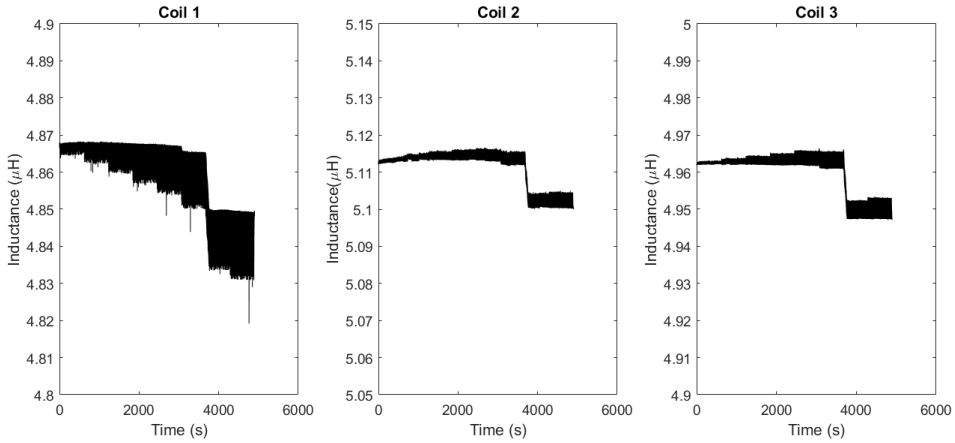

Fig. C.4 Example of the raw motion data captured by the coils 1, 2 and 3.

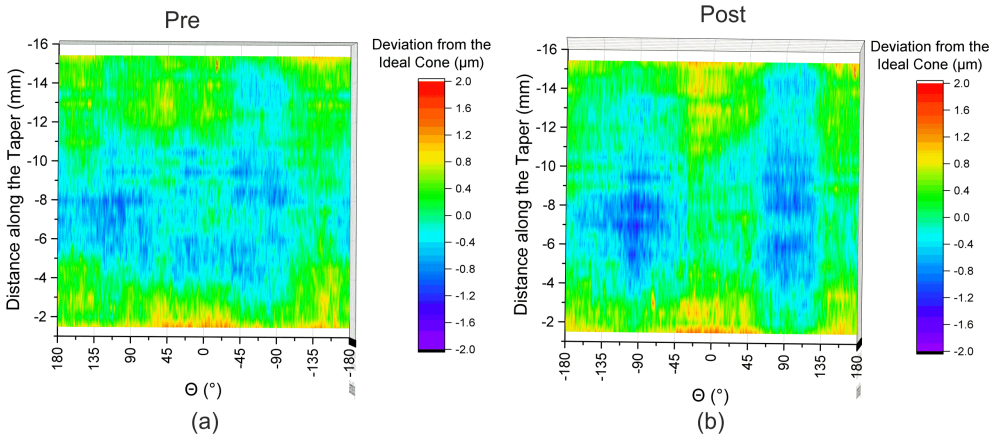

Fig. C.5 Example surface deviation map of a smooth distal sample (a) pre testing as detailed in Chapter 5 and (b) post.

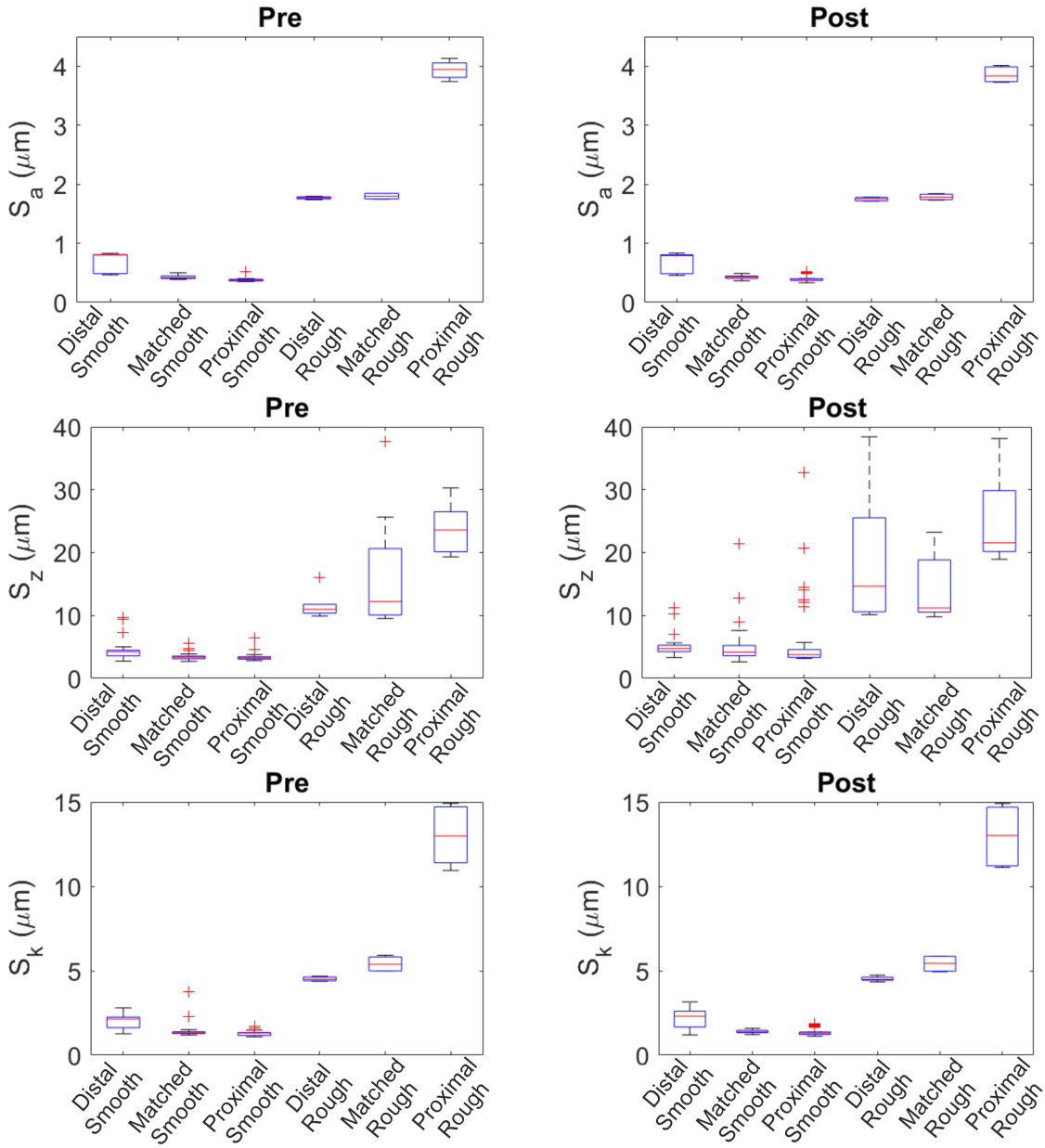

Fig. C.6 Surface topography amplitude parameters prior to testing i.e. 'Pre' compared to 'Post' testing.

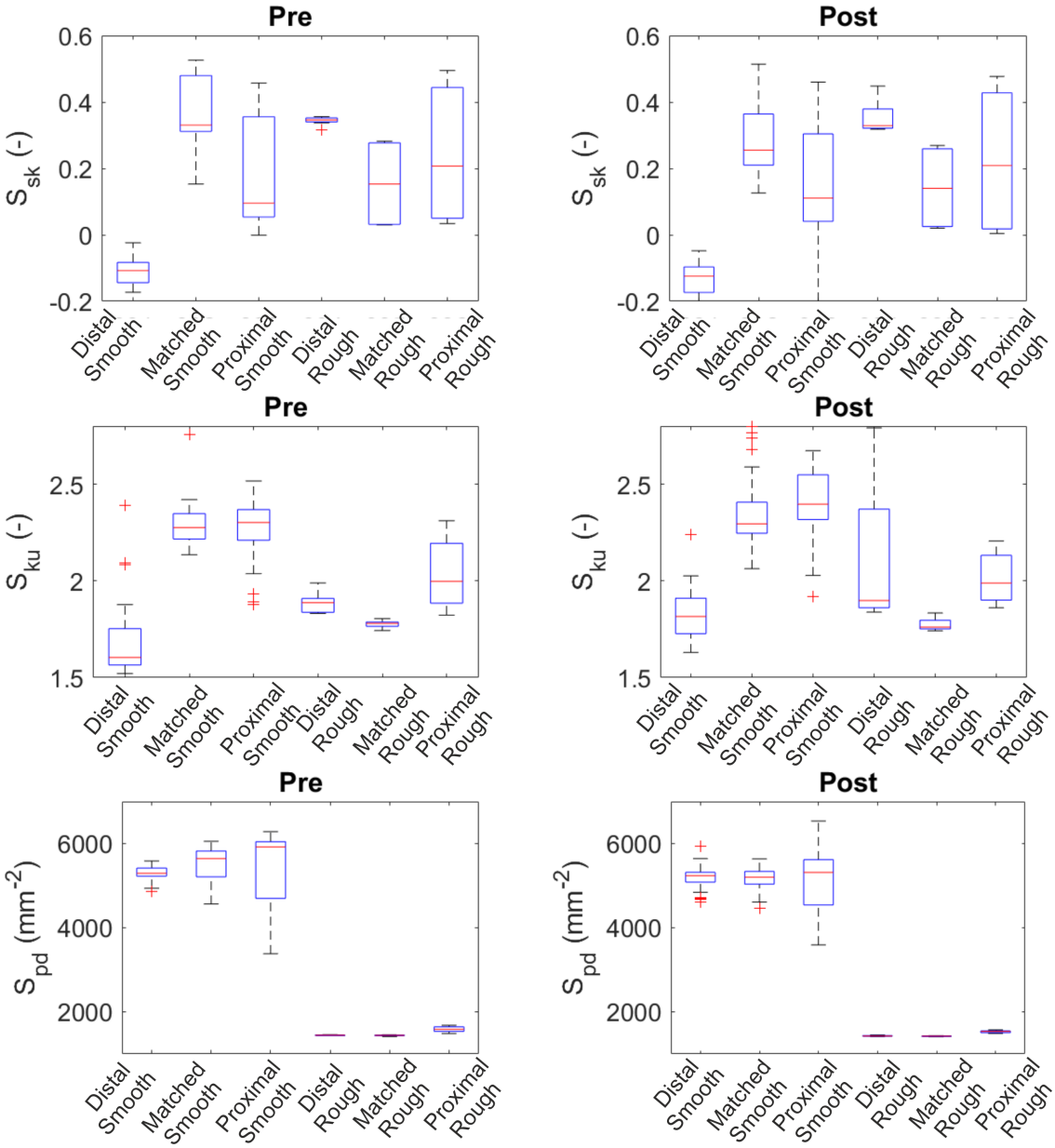

Fig. C.7 Surface topography shape and distribution parameters prior to testing i.e. 'Pre' compared to 'Post' testing.

Appendix D

Copyright Permissions

Fig. D.1 Figure 2.16 copyright permission

ASTM INTERNATIONAL LICENSE
TERMS AND CONDITIONS

Dec 26, 2022

This Agreement between University of Leeds -- Abigail Wade ("You") and ASTM International ("ASTM International") consists of your license details and the terms and conditions provided by ASTM International and Copyright Clearance Center.

The publisher has provided special terms related to this request that can be found at the end of the Publisher's Terms and Conditions.

License Number	5184311480318
License date	Nov 08, 2021
Licensed Content Publisher	ASTM International
Licensed Content Publication	ASTM Book
Licensed Content Title	Corrosion of Modular Tapers in Total Joint Replacements: A Critical Assessment of Design, Materials, Surface Structure, Mechanics, Electrochemistry, and Biology
Licensed Content Date	Dec 1, 2015
Type of Use	Thesis/Dissertation
Requestor type	Student
Format	Electronic
Portion	image/photo
Number of images/photos requested	1

Fig. D.2 Figure 2.21 copyright permission

ASTM INTERNATIONAL LICENSE
TERMS AND CONDITIONS

Dec 26, 2022

This Agreement between University of Leeds -- Abigail Wade ("You") and ASTM International ("ASTM International") consists of your license details and the terms and conditions provided by ASTM International and Copyright Clearance Center.

The publisher has provided special terms related to this request that can be found at the end of the Publisher's Terms and Conditions.

License Number	5184311480318
License date	Nov 08, 2021
Licensed Content Publisher	ASTM International
Licensed Content Publication	ASTM Book
Licensed Content Title	Corrosion of Modular Tapers in Total Joint Replacements: A Critical Assessment of Design, Materials, Surface Structure, Mechanics, Electrochemistry, and Biology
Licensed Content Date	Dec 1, 2015
Type of Use	Thesis/Dissertation
Requestor type	Student
Format	Electronic
Portion	image/photo
Number of images/photos requested	1

Fig. D.3 Figure 2.22 copyright permission

ELSEVIER LICENSE
TERMS AND CONDITIONS

Jan 07, 2023

This Agreement between University of Leeds -- Abigail Wade ("You") and Elsevier ("Elsevier") consists of your license details and the terms and conditions provided by Elsevier and Copyright Clearance Center.

License Number	5463660191945
License date	Jan 07, 2023
Licensed Content Publisher	Elsevier
Licensed Content Publication	Journal of Biomechanics
Licensed Content Title	Hip contact forces and gait patterns from routine activities
Licensed Content Author	G Bergmann,G Deuretzbacher,M Heller,F Graichen,A Rohlmann,J Strauss,G.N Duda
Licensed Content Date	Jul 1, 2001
Licensed Content Volume	34
Licensed Content Issue	7
Licensed Content Pages	13
Start Page	859
End Page	871
Type of Use	reuse in a thesis/dissertation
Portion	figures/tables/illustrations

Fig. D.4 Figure 2.3 copyright permission

JOHN WILEY AND SONS LICENSE
TERMS AND CONDITIONS

Dec 26, 2022

This Agreement between University of Leeds -- Abigail Wade ("You") and John Wiley and Sons ("John Wiley and Sons") consists of your license details and the terms and conditions provided by John Wiley and Sons and Copyright Clearance Center.

License Number	5183731151843
License date	Nov 07, 2021
Licensed Content Publisher	John Wiley and Sons
Licensed Content Publication	Journal of Orthopaedic Research
Licensed Content Title	Wear patterns of taper connections in retrieved large diameter metal-on-metal bearings
Licensed Content Author	Michael Morlock, Markus Michel, Marcel Rütschi, et al
Licensed Content Date	Feb 25, 2013
Licensed Content Volume	31
Licensed Content Issue	7
Licensed Content Pages	7
Type of use	Dissertation/Thesis
Requestor type	University/Academic

Fig. D.5 Figure 2.24 copyright permission

JOHN WILEY AND SONS LICENSE
TERMS AND CONDITIONS

Dec 26, 2022

This Agreement between University of Leeds -- Abigail Wade ("You") and John Wiley and Sons ("John Wiley and Sons") consists of your license details and the terms and conditions provided by John Wiley and Sons and Copyright Clearance Center.

License Number	5183750667769
License date	Nov 07, 2021
Licensed Content Publisher	John Wiley and Sons
Licensed Content Publication	Journal of Orthopaedic Research
Licensed Content Title	Variations in the trunnion surface topography between different commercially available hip replacement stems
Licensed Content Author	William Robert Walsh, William L. Walter, Selin Munir
Licensed Content Date	Oct 15, 2014
Licensed Content Volume	33
Licensed Content Issue	1
Licensed Content Pages	8
Type of use	Dissertation/Thesis
Requestor type	University/Academic

Fig. D.6 Figure 2.25a and b copyright permission

Fig. D.7 Figure 2.25c and d copyright permission

WOLTERS KLUWER HEALTH, INC. ORDER DETAILS

Dec 20, 2022

This Agreement between Abigail Wade ("You") and Wolters Kluwer Health, Inc. ("Wolters Kluwer Health, Inc.") consists of your order details and the terms and conditions provided by Wolters Kluwer Health, Inc. and Copyright Clearance Center.

Order Number	501781497
Order date	Dec 19, 2022
Licensed Content Publisher	Wolters Kluwer Health, Inc.
Licensed Content Publication	Clinical Orthopaedics and Related Research
Licensed Content Title	Insights into Imprinting: How Is the Phenomenon of Tribocorrosion at Head-Neck Taper Interfaces Related to Corrosion, Fretting, and Implant Design Parameters?
Licensed Content Author	Therese Bormann, Ulrike Müller, Jens Gibmeier, et al
Licensed Content Date	Apr 5, 2022
Licensed Content Volume	480
Licensed Content Issue	8
Type of Use	Dissertation/Thesis
Requestor type	University/College
Sponsorship	Commercial
Format	Electronic

Fig. D.8 Figure 2.25 copyright permission

ASTM INTERNATIONAL LICENSE
TERMS AND CONDITIONS

Jan 07, 2023

This Agreement between University of Leeds -- Abigail Wade ("You") and ASTM International ("ASTM International") consists of your license details and the terms and conditions provided by ASTM International and Copyright Clearance Center.

The publisher has provided special terms related to this request that can be found at the end of the Publisher's Terms and Conditions.

License Number	5184311480318
License date	Nov 08, 2021
Licensed Content Publisher	ASTM International
Licensed Content Publication	ASTM Book
Licensed Content Title	Corrosion of Modular Tapers in Total Joint Replacements: A Critical Assessment of Design, Materials, Surface Structure, Mechanics, Electrochemistry, and Biology
Licensed Content Date	Dec 1, 2015
Type of Use	Thesis/Dissertation
Requestor type	Student
Format	Electronic
Portion	image/photo
Number of images/photos requested	1

Fig. D.9 Figure 2.27 copyright permission

ELSEVIER LICENSE
TERMS AND CONDITIONS

Dec 26, 2022

This Agreement between University of Leeds -- Abigail Wade ("You") and Elsevier ("Elsevier") consists of your license details and the terms and conditions provided by Elsevier and Copyright Clearance Center.

License Number	5183690998107
License date	Nov 07, 2021
Licensed Content Publisher	Elsevier
Licensed Content Publication	Corrosion Science
Licensed Content Title	Study of stainless steels corrosion in a strong acid mixture. Part 1: cyclic potentiodynamic polarization curves examined by means of an analytical method
Licensed Content Author	Tiziano Bellezze,Giampaolo Giuliani,Gabriella Roventi
Licensed Content Date	Jan 1, 2018
Licensed Content Volume	130
Licensed Content Issue	n/a
Licensed Content Pages	13
Start Page	113
End Page	125
Type of Use	reuse in a thesis/dissertation

Fig. D.10 Figure 2.28 copyright permission

Fig. D.11 Figure 2.29 copyright permission

ELSEVIER LICENSE
TERMS AND CONDITIONS

Jan 07, 2023

This Agreement between University of Leeds -- Abigail Wade ("You") and Elsevier ("Elsevier") consists of your license details and the terms and conditions provided by Elsevier and Copyright Clearance Center.

License Number	5456700909975
License date	Dec 26, 2022
Licensed Content Publisher	Elsevier
Licensed Content Publication	Medical Engineering & Physics
Licensed Content Title	Influence of flexural rigidity on micromotion at the head-stem taper interface of modular hip prostheses
Licensed Content Author	Henning Haschke,Tobias Konow,Gerd Huber,Michael M. Morlock
Licensed Content Date	Jun 1, 2019
Licensed Content Volume	68
Licensed Content Issue	n/a
Licensed Content Pages	10
Start Page	1
End Page	10
Type of Use	reuse in a thesis/dissertation

Fig. D.12 Figure 2.33 copyright permission

Fig. D.13 Figure **??** copyright permission

WOLTERS KLUWER HEALTH, INC. LICENSE
TERMS AND CONDITIONS

Jan 19, 2023

This Agreement between University of Leeds -- Abigail Wade ("You") and Wolters Kluwer Health, Inc. ("Wolters Kluwer Health, Inc.") consists of your license details and the terms and conditions provided by Wolters Kluwer Health, Inc. and Copyright Clearance Center.

The publisher has provided special terms related to this request that can be found at the end of the Publisher's Terms and Conditions.

License Number	5472631353951
License date	Jan 19, 2023
Licensed Content Publisher	Wolters Kluwer Health, Inc.
Licensed Content Publication	Journal of the American Academy of Orthopaedic Surgeons
Licensed Content Title	Head-Neck Taper Corrosion in Metal-on-Polyethylene Total Hip Arthroplasty: Risk Factors, Clinical Evaluation, and Treatment of Adverse Local Tissue Reactions
Licensed Content Author	David Fitz, Christian Klemt, Wenhao Chen, et al
Licensed Content Date	Jul 17, 2020
Licensed Content Volume	28
Licensed Content Issue	22
Type of Use	Dissertation/Thesis
Requestor type	University/College
Sponsorship	Commercial

Fig. D.14 Figure 2.11 copyright permission

Abigail Wade [mn13aw]

From: Carry Koolbergen <C.Koolbergen@iospress.nl>
Sent: 27 January 2023 13:20
To: Abigail Wade [mn13aw]
Subject: RE: Permissions

Follow Up Flag: Follow up
Flag Status: Flagged

DOI: 10.3233/BME-2010-0616
Journal: Bio-Medical Materials and Engineering, vol. 20, no. 2, pp. 65-75, 2010

Dear Abigail Wade,

We hereby grant you permission to use the below mentioned material in **print and electronic format** at no charge subject to the following conditions:

1. Permission should also be granted by the original authors of the article in question (if possible).
   Address for correspondence: Prof. Dr.-Ing. Georg Bergmann, Julius Wolff Institut, Charité – Universitätsmedizin Berlin, Augustenburger Platz 1, 13353 Berlin, Germany. Tel.: +49 30 450 659081; E-mail: georg.bergmann@charite.de.

2. If any part of the material to be used (for example, figures) has appeared in our publication with credit or acknowledgement to another source, permission must also be sought from that source. If such permission is not obtained then that material may not be included in your publication/copies.

3. Suitable acknowledgement to the source must be made, either as a footnote or in a reference list at the end of your publication, as follows:

   "Reprinted from Publication title, Vol number, Author(s), Title of article, Pages No., Copyright (Year), with permission from IOS Press".
   The publication is available at IOS Press through http://dx.doi.org/[insert DOI]

4. This permission is granted for non-exclusive world **English** rights only. For other languages please reapply separately for each one required.

5. Reproduction of this material is confined to the purpose for which permission is hereby given.

Yours sincerely

Carry Koolbergen (Mrs.)
Contracts, Rights & Permissions Coordinator
Not in the office on Wednesdays

IOS Press | Nieuwe Hemweg 6B, 1013 BG Amsterdam, The Netherlands
Tel.: +31 (0)20 688 3355/ +31 (0) 687 0022 | c.koolbergen@iospress.nl | www.iospress.nl
Twitter: @IOSPress_STM | Facebook: publisheriospress

View the latest IOS Press newsletter here

Fig. D.15 Figure 2.4 copyright permission

ELSEVIER LICENSE
TERMS AND CONDITIONS

Feb 06, 2023

This Agreement between University of Leeds -- Abigail Wade ("You") and Elsevier ("Elsevier") consists of your license details and the terms and conditions provided by Elsevier and Copyright Clearance Center.

License Number	5483281382453
License date	Feb 06, 2023
Licensed Content Publisher	Elsevier
Licensed Content Publication	Biomaterials
Licensed Content Title	Fretting corrosion of CoCrMo and Ti6Al4V interfaces
Licensed Content Author	Viswanathan Swaminathan,Jeremy L. Gilbert
Licensed Content Date	Aug 1, 2012
Licensed Content Volume	33
Licensed Content Issue	22
Licensed Content Pages	17
Start Page	5487
End Page	5503
Type of Use	reuse in a thesis/dissertation
Portion	figures/tables/illustrations

Fig. D.16 Figures 2.36 and 2.39 copyright permissions

Fig. D.17 Figure 2.37 copyright permission

ELSEVIER LICENSE
TERMS AND CONDITIONS

Jun 28, 2023

This Agreement between University of Leeds -- Abigail Wade ("You") and Elsevier ("Elsevier") consists of your license details and the terms and conditions provided by Elsevier and Copyright Clearance Center.

License Number	5577490618705
License date	Jun 28, 2023
Licensed Content Publisher	Elsevier
Licensed Content Publication	Journal of Biomechanics
Licensed Content Title	The transmission of load through the human hip joint
Licensed Content Author	A.S. Greenwald,J.J. O'Connor
Licensed Content Date	Dec 1, 1971
Licensed Content Volume	4
Licensed Content Issue	6
Licensed Content Pages	22
Start Page	507
End Page	528
Type of Use	reuse in a thesis/dissertation
Portion	figures/tables/illustrations

Fig. D.18 Figure 2.2 copyright permission

Fig. D.19 Figure 2.5 copyright permission

ELSEVIER LICENSE
TERMS AND CONDITIONS

Jul 04, 2023

This Agreement between University of Leeds -- Abigail Wade ("You") and Elsevier ("Elsevier") consists of your license details and the terms and conditions provided by Elsevier and Copyright Clearance Center.

License Number	5581771014290
License date	Jul 04, 2023
Licensed Content Publisher	Elsevier
Licensed Content Publication	Clinical Biomechanics
Licensed Content Title	Hip contact forces in asymptomatic total hip replacement patients differ from normal healthy individuals: Implications for preclinical testing
Licensed Content Author	Junyan Li,Anthony C. Redmond,Zhongmin Jin,John Fisher,Martin H. Stone,Todd D. Stewart
Licensed Content Date	Aug 1, 2014
Licensed Content Volume	29
Licensed Content Issue	7
Licensed Content Pages	5
Start Page	747
End Page	751
Type of Use	reuse in a thesis/dissertation

Fig. D.20 Figure 2.5 copyright permission

ELSEVIER LICENSE
TERMS AND CONDITIONS

Oct 24, 2023

This Agreement between University of Leeds -- Abigail Wade ("You") and Elsevier ("Elsevier") consists of your license details and the terms and conditions provided by Elsevier and Copyright Clearance Center.

License Number	5655211004984
License date	Oct 24, 2023
Licensed Content Publisher	Elsevier
Licensed Content Publication	The Journal of Arthroplasty
Licensed Content Title	Head Taper Corrosion Causing Head Bottoming Out and Consecutive Gross Stem Taper Failure in Total Hip Arthroplasty
Licensed Content Author	Michael M. Morlock,Emilie C. Dickinson,Klaus-Peter Günther,Dennis Bünte,Valerie Polster
Licensed Content Date	Nov 1, 2018
Licensed Content Volume	33
Licensed Content Issue	11
Licensed Content Pages	10
Start Page	3581
End Page	3590
Type of Use	reuse in a thesis/dissertation

Fig. D.21 Figure 2.23 copyright permission